THEORETICAL INVESTIGATION OF ROCKING FRAMES UNDER HORIZONTAL SEISMIC EXCITATION WITH APPLICATION TO NUCLEAR FACILITIES

THEORETICAL INVESTIGATION OF ROCKING FRAMES UNDER HORIZONTAL SEISMIC EXCITATION WITH APPLICATION TO NUCLEAR FACILITIES

By

AMITABH DAR, **P.Eng.**

B.Eng., M.M.S., M.A.Sc.
SCE

A Thesis Submitted to the School of Graduate Studies in Partial Fulfillment of the Requirements for the Degree Doctor of Philosophy

McMaster University

Doctor of Philosophy (2023) McMaster University

(Civil Engineering) Hamilton, Ontario

TITLE: THEORETICAL INVESTIGATION OF ROCKING FRAMES UNDER HORIZONTAL SEISMIC EXCITATION WITH APPLICATION TO NUCLEAR FACILITIES

AUTHOR: Amitabh Dar,

B. Eng. (Hons), MMS, MASc, P.Eng.

SUPERVISOR: Dr Wael W. El-Dakhakhni

NUMBER OF PAGES: xxxi, 257

Dedication

To,

My parents

LAY ABSTRACT

Rocking frames, each consisting of a heavy rigid horizontal beam freely supported on unanchored rigid piers, are common to nuclear power plants (NPPs) (e.g., a turbine rotor freely supported by triangular or trapezoidal piers). The support points for the beam on the pier in such frames may be concentric or eccentric with respect to the pier's center of mass as in a triangular or trapezoidal pier configuration. The current Canadian and American nuclear standards do not provide guidance on rocking frames. Support eccentricity variation has not been addressed in the literature. Consequently, the seismic risk of rocking frame configurations, common to NPPs, remains unknown. This thesis addresses this gap by employing an equivalent rocking block model for frames with symmetrical eccentricities, with an equation of motion representing those with unsymmetrical eccentricities; and examining the stability of the two under slide-restrained conditions.

ABSTRACT

The seismic risk of a nuclear power plant (NPP) depends on structures, systems and components (SSCs) that are seismically qualified to a design basis earthquake (DBE) in Canada or a safe shutdown earthquake (SSE) in the United States. On the other hand, there exist some components that are not essential to safety but their seismic interaction with seismically-qualified SSCs adversely affects the seismic risk of such SSCs. Rocking frames consisting of a rigid beam freely supported by piers (e.g., a 150 Ton spare turbine rotor, or a 100 Ton idle steam generator resting on triangular or trapezoidal rigid piers) are common to NPPs. Seismic interaction of such frames with seismically-qualified safety components or their host structure may be detrimental to nuclear safety as witnessed in the 2013 Arkansas Nuclear One accident where the drop of a 500 Ton stator adversely impacted the severe core damage frequency of the entire plant, negatively affecting the nuclear risk. In order to ensure nuclear safety, it is essential to quantify the risk of a heavy component's drop owing to a rocking frame's instability caused by design basis accidents including seismic. A rocking frame's beam support may be concentric or eccentric with respect to the pier's center of mass depending on it's geometry, for example, triangular or trapezoidal respectively. The current nuclear standards, ASCE 43-19 and CSA N289.1-2018 are silent about rocking frames. Literature has also not addressed the eccentricity variation. This thesis addresses the gap on seismic qualification of rocking frames by, establishing an equivalent rocking block for rocking frames with symmetrical support eccentricities, obtaining the response of frames with unsymmetrical support eccentricities and finally examining the stability of the two types of frames under slide restrained conditions.

ACKNOWLEDGEMENTS

In 2009, I went back to academics almost twenty-five years after my bachelor's degree by enrolling in the part time Master's program at McMaster University. During the Master's degree, Dr Wael El-Dakhakhni encouraged me to continue further and aim for the doctoral program which I started in 2015. The encouragement from my supervisors, Dr Wael El-Dakhakhni and Dr Dimitrios Konstantinidis (former co-supervisor) was catalytic to my academic journey. I sincerely thank both of them. I am also thankful to all the professors with whom I completed my courses. Education at McMaster University has been a great experience. I appreciate the constructive feedback from the supervisory committee members Drs. Lydell Wiebe and Mohamed Ezzeldin, and the previous members Drs Tracy Becker and John Luxat.

Thanks are due to Bruce Power, for supporting my education program concurrent with my employment. I sincerely acknowledge the constant inspiration by my colleague Jim Hanna and support from Section Managers Shaun Abbas and Patrick Protomanni. I am indebted to Cathy Sprague, Executive Vice President (Human Resources), and, Gary Newman, Chief Engineer and Senior Vice President (Engineering), Bruce Power for their approvals of my education program.

Thanks are due to my wife Anuradha for her love, affection, and support in taking care of the home and family. I am also thankful to my daughters Apoorva and Arpita for their understanding on my academic schedule taking priority over family time. I dedicate this thesis to my late parents, both of whom had careers in the field of education.

LIST OF ACRONYMS

ANO	Arkansas Nuclear One
CG	Center of gravity
COR	Coefficient of Restitution
CSA	Canadian Standards Association
COF	Coefficient of Friction
COFD	Coefficient of Friction Demand
DBA	Design Basis Accident
DBE	Design Basis Earthquake
EPRI	Electrical Power Research Institute
FEA	Finite Element Analysis
FRS	Floor Response Spectrum
NBK	Newmark, Blume and Kapur
NPP	Nuclear Power Plant
NVHC	Normalized Velocity squared Horizontal Component
NVVC	Normalized Velocity squared Vertical Component
PGA	Peak Ground Acceleration
PSA	Peak Spectral Acceleration
RS	Right Scale (corresponds to the right vertical axis in a chart)

SA	Spectral Acceleration
SDOF	Single Degree of Freedom
SPRA	Seismic Probabilistic Risk Assessment
SRSH	Slide restrained Rocking induced Separation under Horizontal Excitation
SSC	Structures, Systems and Components
SSE	Safe Shutdown Earthquake
TH	Time History
USNRC	United States Nuclear Regulatory Commission
ZPA	Zero Period Acceleration

LIST OF SYMBOLS

α	Slenderness parameter of a symmetrical block. Slenderness parameter of an unsymmetrical block or the pier in a frame, i.e., inclination angle (from the vertical) of its radius from the near pivot. Slenderness parameter for the generalized rotation pier in a two-pier frame.
α'	Additional slenderness parameter of an unsymmetrical block or the pier in a frame, i.e., inclination angle of its radius from the far pivot.
α_T	Slenderness parameter of the beam in a rocking frame
α_{eq}	Slenderness parameter of an equivalent block of two-pier frame with symmetrical eccentricity
α^*	Effective system slenderness causing minimum acceleration demand, $g \tan \alpha^*$, to initiate rocking
b	Half width of a symmetrical pier or a block. Horizontal distance of an unsymmetrical block's CG from the nearest pivot. Horizontal distance of an unsymmetrical pier's CG from the interior pivot in a frame.
β	Inclination of the beam's support point's radius, R_1, from the vertical in a frame.
β'	Inclination of the beam's support point's radius, R_1' from the vertical in a frame.
$\delta_1, \delta_2, \delta_3$	Inner angles of the contact polygon in a two-pier frame
D	Longer diagonal of the contact polygon

g	Gravitational acceleration
h	Height of an individual block's CG's or that of the pier in a frame.
I_o	Mass moment of inertia of a symmetrical block about the pivot. Mass moment of inertia of an unsymmetrical block about its near pivot.
$I_{o'}$	Mass moment of inertia of an unsymmetrical block about its far pivot.
I_{on}	Normalized mass moment of inertia of the generalized rotation pier in a two-pier frame, I_o/mR^2
I_{TB}	Mass moment of inertia of the beam about its contact point with the generalized rotation pier
I_T	Mass moment of inertia of the beam about its CG
l	Distance between the two inner contact points of a beam in a two-pier frame
l_B	Distance between the inner pivot of a pier with the outer pivot of the other in a two-pier frame
l_c	Distance between the centroids of piers in a two-pier frame
l_T	Distance between the outer pivot of the beam at one end and the inner pivot at the other, in a two-pier frame
M_T	Mass of the beam in a two-pier frame
m	Mass of the generalized rotation pier in a two-pier frame
m'	Mass of the pier other than the generalized rotation pier in a two-pier frame

μ	The ratio of the horizontal distance of an unsymmetrical block's CG from its positive rotation pivot with the base width
η	Eccentricity parameter of the outer contact point of the beam in a two-pier frame
η'	Eccentricity parameter of the inner contact point of the beam in a two-pier frame
η_s and η_s'	Those values of η and η' that leads to symmetrical eccentricities
p	Size, or frequency parameter of a rocking block
p_{eq}	Size parameter of an equivalent block of a frame with symmetrical eccentricity
p_p	Size, or frequency parameter of an unsymmetrical block under positive rotation
p_n	Size, or frequency parameter of an unsymmetrical block under negative rotation
q	Ratio of the beam mass and the total mass of piers in a multi-pier frame
q_I	Ratio of the mass moments of inertia of an unsymmetrical pier in a two-pier frame about its nearest and farthest pivots from its CG
q_T	Ratio of the masses of the beam and the generalized rotation pier in a two-pier frame
q_{IT}	I_{TB}/I_o

q_L	b/l_c
q_{LT}	$2q_L^2/(1+2\eta\, q_L)(1+(\eta-\eta')\, q_L)$
q_m	m'/m
q_{OT}	I_T/I_o
q_R	R'/R
q_{RT}	R_T/R
R	Distance of a block's CG from the nearest pivot. In a two-pier frame, it is the CG of a pier from the inner pivot.
R'	Distance of a block's CG from its farthest pivot. In a two-pier frame, it is the CG of a pier from the exterior pivot.
R_1	Distance of the beam's outer contact point with the pier from the pier's pivot towards the interior in a two-pier frame
R_1'	Distance of the beam's inner contact point with the pier from the pier's pivot towards the exterior in a two-pier frame
R_{eq}	Radius of the equivalent block system for a frame with symmetrical eccentricity
R_{ratio}	R_1/R_{eq} in a frame with symmetrical eccentricity
R_T	Radius of the beam in the rocking frame: the distance between its CG and the contact point with the generalized rotation pier
u_B	Horizontal displacement of the beam

v_B	Vertical displacement of the beam
u_g	Ground displacement
ψ	Inertial parameter of a two-pier frame
τ	Torsional parameter of a two-pier frame
θ	Rotation of an unsymmetrical block about its near pivot from the CG. Also, the rotation of a pier in a two-pier frame about its inner pivot which is the generalized rotation of the frame.
θ'	Rotation of an unsymmetrical block abouts it farthest pivot from the CG. Rotation of the pier about the outer pivot in a two-pier frame.
θ_T	Rotation of the beam in a two-pier frame
θ^*	Effective system rotation
ν	R_1/R
ν'	R_1'/R
ξ	Height of the topmost point of a block or pier divided by the height of the CG.

TABLE OF CONTENTS

TABLE OF FIGURES

LIST OF TABLES

DECLARATION OF ACADAMEIC ACHIEVEMENT

This thesis is written in accordance with the guidelines given by the School of Graduate Studies, McMaster university. The Thesis follows the acceptance criteria for a "Sandwich PhD Thesis" given in Section 1.3 and 5.0 of the guide. The thesis is a compilation of three papers along with introductory and conclusion chapters. Out of the three, one has been published in a peer reviewed journal and the rest two are to be submitted. The third paper is large and can be divided into two distinct papers. In essence, this thesis consists of four papers. The work presented in this thesis has been performed solely by Amitabh Dar with technical and editorial feedback from supervisor(s) as described below. The original contribution of the author to each of the three manuscripts are as follows:

Chapter 2: Dar A, Konstantinidis D, El-Dakhakhni W. Seismic response of rocking frames with top support eccentricity. *Earthquake Engineering and Structural Dynamics* 2018; **47**(12): 2496– 2518. https://doi.org/10.1002/eqe.3096.

Status: Published.

The main idea of the paper emerged from A. Dar's thought process and observations in the industry on application of rocking frames in the field. The entire work was carried out by A. Dar with technical guidance provided by Dr. D. Konstantinidis and review feedback by Dr W.W. El-Dakhakhni. The manuscript was prepared by A. Dar and reviewed by Dr. D. Konstantinidis for technical and editorial comments.

Chapter 3: Dar A. Dynamic analysis of two-pier rocking frames with eccentric top supports and beam rotation

Status: To be submitted.

The main idea of the paper emerged from A. Dar's thought process and observations in the industry on application of rocking frames with top support eccentricities. The entire work was carried out by A. Dar with review feedback provided by Dr. D. Konstantinidis and Dr. W.W. El-Dakhakhni. The manuscript was prepared by A. Dar and reviewed by Dr. D. Konstantinidis and Dr W.W. El-Dakhakhni.

Chapter 4: Dar A. Seismic stability of rocking frames under horizontal excitation.

Status: To be submitted as two papers: 1. Stability of a rocking block, and, 2. Stability of a frame. Since a rocking frame with symmetrical eccentricity can be represented by an equivalent block, these two papers required research on the stability of a slide restrained block first and then its progression into rocking frames with symmetrical and unsymmetrical eccentricities.

The main idea of the two papers emerged from A. Dar's thought process and observations in the industry on the stability of slide restrained rocking blocks and frames in the field. The entire work was carried out by A. Dar with review feedback by Dr W.W. El-Dakhakhni. The manuscripts were prepared by A. Dar and reviewed by Dr W.W. El-Dakhakhni.

CHAPTER 1

INTRODUCTION

1.1 Background and Motivation

The seismic risk of a nuclear power plant (NPP) depends on a host of safety related structures, systems, and components (SSCs) that are seismically qualified to a design basis earthquake (DBE) in Canada [1] and a Safe Shutdown Earthquake (SSE) in the Unites States [2]. A set of such SSCs, that are required to bring a NPP to safe shutdown state and maintain it for at least 72 hours following a prescribed seismic event, is known as *success path*, and the document that lists such components is known as Safe Shutdown Equipment List (SSEL) [2]. The seismic risk of a NPP depends on fragilities of the success path SSCs. Although the modern standards [3, 4] recommend anchoring of the success path SSCs, there are several components that cannot be anchored to the structure owing to their frequent movements. In a seismic event such components behave essentially like rocking blocks. Apart from the success path SSCs, there are several unanchored components that are not essential to safety but their seismic interaction with the safety related SSCs may directly impact the NPP's overall nuclear risk [2]. Unreinforced masonry radiation shielding walls, tool cabinets, scaffolds are some examples of such components that essentially behave as rocking blocks.

Apart from individual rocking blocks, assemblages of heavy rigid components such as rocking frames are quite common to NPPs that are utilized to store heavy components in between or during outages. Figure 1-1 shows some applications of rocking frames consisting of a rigid beam freely supported by unanchored piers. Figure 1-1 (a) and (b) respectively show a ~150 Ton turbine rotor on triangular and trapezoidal piers. Figure 1-1 (c), (d), and (e) show ~100 Ton idle

steam generators resting on a series of piers. Turbine rotors and steam generators are examples of heavy components whose accidental drop can pose serious risk to a NPP's nuclear safety as witnessed in the 2013 Arkansas Nuclear One (ANO) accident where a 500 Ton stator was dropped while being transported from one place to the other [5]. An investigation by the United States Nuclear Regulatory Commission (USNRC) [5] revealed that the accident had a direct impact on nuclear risk of the entire NPP owing to the extensive damage to the turbine building, tripping of a running unit and flooding of electrical components due to a fire main's rupture. Although the ANO accident was not caused by a seismic event, the accidental drop may be caused by a design basis accident (DBA) including seismic.

Figure 1-1 (f) shows schematics of a man bridge supported by triangular piers beside a fuel bay full of irradiated water. Although such applications are temporary (lasting only for a few weeks), they are not devoid of radiation risk posed by dropping of the frame into the pool of water and exposing the nuclear fuel to the atmosphere. Figure 1-1 (g) shows an emergency power generator trailer resting on a rocking frame during maintenance. Here, an active emergency component is at risk of damage due to its disengagement from supports. Each rocking frame example shown in Figure 1-1 is a potential threat to nuclear safety and therefore, their seismic risk is required to be evaluated. In addition, following the Fukushima Daiichi nuclear power plant accident in 2011, caused by the 2011 Tohoku earthquake, the seismic re-evaluation efforts of nuclear facilities warranted quantification of seismic risk of such components. Modern North American nuclear standards [3, 4] do not provide any guidance on rocking frames. Consequently, seismic risk of rocking frames in NPPs remains unknown. This thesis establishes a methodology for successfully assessing rocking frames with varying support eccentricities on symmetrical and unsymmetrical piers as explained in the next section.

1.2 Support Eccentricity in Rocking Frames

The contact point of the rotor with a triangular pier (Figure 1-1 (a)) is concentric with the pier's center of gravity (CG) whereas for the trapezoidal pier (Figure 1-1 (b)), the contact points are eccentric to the pier CG. Thus, for a triangular pier, there is no support eccentricity, but for a rectangular pier, it would be the maximum, and for a trapezoidal pier, in between the two limits. Figure 1-2 (a) shows the definition of support eccentricity, η, defined in this thesis as the distance of the support point from the pier CG divided by it half width, b. In rocking motion, the top pivots are the beam support points, whereas the bottom pivots are the pier support points. As evident, a vertically symmetrical pier with symmetrical eccentricity results in equal distances between the two opposite pivots, $R_1 = R_1'$. Figure 1-2 (b) shows a rocking frame with rectangular piers analyzed by Makris and Vassiliou [6] where the support eccentricity is maximum, $\eta = 1$. The authors established an equivalent rocking block model whose response is the same as of the frame and derived its coefficient of restitution (COR) to account of the loss of energy upon impact. They proved that the seismic response of such frames is less than that of a solitary pier; thus, establishing that a heavier frame is more stable than a lighter one. In contrast to this, Dar et al. [7], in a preliminary study, found that the response of rocking frames with $\eta = 0$, such as the one shown in Figure 1-2 (c), is worse than that of a solitary pier, proving that the eccentricity plays an important role in the response of a rocking frame. Figure 1-2 (d) shows rocking frame with eccentricity in between the two limits, $0 \leq \eta \leq 1$, which is the focus of this thesis.

Figure 1-2(b) to (d) show rocking frames supported by symmetrical piers with symmetrical eccentricity resulting in $R_1 = R_1'$. Also shown is the *contact polygon* in thick dashes grey lines that connects the pivot points. For a continued rocking motion, assuming no sliding, the sides of the

contact points being kinematically constrained, remain invariant. Since the opposite sides of the contact polygon are equal, the beam remains horizontal in rocking motion. Figure 1-2 (e) shows the schematics of a turbine rotor supported by stem blocks attached to two trapezoidal piers that are unsymmetrical about their CG axis. Here, since $R_1 \neq R_1'$, it is a case of unsymmetrical eccentricities. Figure 1-2 (f) shows an idealized representation of this configuration where, since $R_1 \neq R_1'$, the top beam does not remain horizontal during rocking motion. Figure 1-2 (g) shows another variation in a rocking frame with symmetrical piers but unsymmetrical eccentricities. Thus, a rocking frame may have symmetrical or unsymmetrical piers subjected to symmetrical or unsymmetrical eccentricities. The literature [6] presents only one type of rocking frame with maximum eccentricity on symmetrical piers. This thesis explores all other types of rocking frames depicted in Figure 1-2 (d), (e) and (f). Although the pier geometries shown are trapezoidal or rectangular, the formulation presented in this thesis addresses any geometry.

1.3 Modes of Failure

Rocking frames analyzed by Makris and Vassiliou [6] for $\eta = 1$ and Dar et al. [7] for $\eta = 0$ can be represented by an equivalent rocking block whose response is the same as that of the frame. Thus, the instability of rocking frame with symmetrical eccentricities depends on the overturning of an equivalent block. In addition, sliding of the beam or the pier will cause instability of the frame. However, for a continued frame action, the contact polygon must remain intact, necessitating no sliding. Figure 1-2 (h) shows symbolic representation of shear keys (depicted as recesses), for a rocking frame with trapezoidal piers similar to those assumed by Makris and Vassiliou [6] for rectangular piers. In such cases, sliding is not permitted. However, under such slide-restrained conditions, the beam can still lift-off or separate owing to the beam-pier contact

point's vertical acceleration being even less than -g (e.g., if the pier contact point moves downward with acceleration $-1.2g$, the beam being unanchored to the pier will not be able to follow it and separate). Thus, restraining sliding and considering only overturning as the failure mode is no guarantee of stability. A rocking frame may not overturn or undergo sliding, and yet its beam may separate. Therefore, under the slide-restrained condition, this thesis identifies and investigates a novel mode of instability, *Slide-restrained Rocking-induced Separation under Horizontal excitation*, or, the SRSH failure mode for rocking frames with symmetrical and unsymmetrical eccentricities. Since a frame with symmetrical eccentricities can be represented by a rocking block, this thesis first explores the SRSH failure mode for a rigid block and then progresses with rocking frames.

1.4 Literature Review

Following the seminal work by Housner [8], several studies [9-17] focused on obtaining the response of a rigid rocking block to seismic excitation. Some studies tried to obtain the response of a rigid block by considering it as a single-degree-of-freedom (SDOF) oscillator [18-19], including the methodology given in the nuclear standard ASCE 43-05 [3]. Such methodologies were evaluated and found to produce erroneous results [20-22] concluding that a rocking spectrum, rather than a response spectrum based on a SDOF oscillator, is the true representation of the peak response of a rigid block to seismic excitation [20]. Regarding the separation of a rigid block during rocking motion, Pompei et al [14] investigated the phenomenon of separation of a *falling* block under free vibration and determined that the separation is a possibility only in wide blocks. Considering slender blocks, the authors investigated a *rising* block under pulse excitation and determined that the separation of a slender block is impossible because sliding precedes, or

safeguards against, separation. However, the authors did not investigate a falling block under slide-restrained conditions subjected to the excitation that augments its fall. Since the separation happens when a block accelerates downwards, it is imperative to investigate a block's response to the excitation that augments is fall. To the best of the author's knowledge, there is no evidence in the literature of research that focused on a falling block analysis. Zhang and Makris [16] investigated a realistic scenario under slide restrained condition from the 1906 San Francisco earthquake; overturning of a train under sine pulse excitation. The authors did report a high coefficient of friction demand (COFD) and opined that it did not result in sliding due to the engagement of wheels with rails. However, the authors surmised overturning as the only mode of failure without looking into the SRSH mode. The cycloidal pulses investigated by the authors included pure sine or cosine pulse but without the pre-excitation low-amplitude-and-low-frequency half sine pulse that often precedes the main cycloidal pulse in a real earthquake record as shown in Figure 1-2 (k). This case is revisited in this thesis in CHAPTER 4.

Apart from a single rocking block, assemblages of rigid blocks have been studied. DeJong and Dimitrakopoulos [23] explained that how an equivalent single block can represent various assemblages, including simple rocking frames similar to that in Figure 1-2(b). Several other types assemblages have been studied by Lee [24], Ikushima and Nakazawa [25], Allen et al. [26], Psycharis [27], Spanos et al. [28], Konstantinidis and Makris [29], Kounadis et al. [30], and Minafo et al. [31]. Shake table test studies were made by Wittich and Hutchinson to investigate the seismic response of asymmetric rocking single-body structures [32] and dual-body systems [33]. Investigations on the impact of two parameters, size and slenderness, on the response of a pier or a frame led to the opinion that these are two competing parameters [34-36]. An example of rocking frames considered in this thesis is inspired by the large size bridge pier investigated in [37]. Most

of the studies on a rocking block are focused on rectangular piers. Investigation on cylindrical piers behavior was investigated in [38].

Other than [6] and [7], there have been studies on rocking frames [39-42]. Drosos et al. [39] carried out shake table tests on multidrum columns and portals. Vassiliou et al.[40] provided an approximate finite element model of deformable rocking frames. Dimitrakopoulos and Giouvanidis [41] focused on piers of asymmetric frames with unequal heights but without any consideration to support eccentricities. Diamantopoulos and Fragiadakis [42] proposed finite element modelling of rocking frames with symmetrical piers as a SDOF oscillator with negative stiffness based on the equivalent block model and its equation of motion presented in [6]. The authors did not discuss the impact of eccentricity on the rocking response of frames, neither the instability of frames due to beam separation. However, they indicated that, in order to create an approximate finite element model, it is essential to formulate the equation of motion of a frame resembling that of a single block.

Studies on rocking frames as seismic isolation systems [6, 43-47] focused on the horizontal and vertical displacements of the beam. Horizontal acceleration at the top of a rocking frame was obtained in [44] but without investigating the impact of its variation along with support eccentricity on the overall response. None of these studies explored the vertical acceleration of the beam under horizontal excitation leading to separation.

The studies listed above are commonly referenced in the thesis chapters depending on their applicability to the topic of discussion.

1.5 Earthquake records

The design response spectrum for the NPPs is given in the USNRC Regulatory Guide 1.60 Revision 1 [48] and Revision 2 [49]. Both revisions are based on the popularly known NBK spectrum named after its creators Newmark, Blue and Kapur [50] focusing on the west coast events. Revision 2 adds additional requirements to address the high frequency content of the east coast earthquake records. An evaluation of the west and the east coast events was carried out by Dar et al. [51] concluding that the west coast events being comparatively richer over low frequency range carry inherent conservatism over their eastern counterparts in the context of the rocking response of a rigid block. The authors considered an east coast event with the zero-period acceleration almost twice the west coast one and found the rocking response to the east coast event to be lower. Therefore, the earthquake records considered in this thesis will be based on the similarity of their response spectrum with that in Revision 1 of the USNRC guide [48]. The numerical response to earthquake records was obtained by utilizing AdamsBDF solver [52].

1.6 Research Objectives

Seismic response of rocking frames with rectangular supports have been analyzed in the literature but without investigating the impact of varying eccentricity, shape geometry and varying load under eccentric support condition. Separation of the beam in rocking frames under slide-restricted conditions subjected to horizontal excitation has not been explored in the literature. The nuclear standard, ASCE 43 [3], allows consideration of horizontal and vertical excitations separately. Therefore, the focus of this thesis is on horizontal excitation.

The main objective of this dissertation is to obtain the response of rocking frames, common in NPPs, under varying eccentricities and investigate their instability under slide restricted conditions. This objective can further be subdivided into the following:

1.6.1 Rocking frame with symmetrical support eccentricity on symmetrical piers:

Investigate if frames with symmetrical support eccentricity on symmetrical piers (as shown in Figure 1-2 (d)) can be represented by an equivalent rocking block. If possible, establish the parameters of an equivalent block and its COR. Obtain the response of equivalent block to pulse excitations and earthquake records. Investigate the sensitivity of the response to eccentricity.

1.6.2 Rocking frames with unsymmetrical support eccentricities on unsymmetrical and symmetrical piers

Investigate the dynamics of rocking frames with unsymmetrical eccentricities as shown in Figure 1-2 (f) and (g). Determine if such frames can be represented by an equivalent block or the equation of motion can be presented in a format that resembles summation of several rocking blocks. Derive the CORs for the unsymmetrical piers and the rocking frames with unsymmetrical eccentricities. Obtain the rocking frame's response to earthquake records and investigate its sensitivity to eccentricity. Also, explore if a rocking frame on unsymmetrical piers can be turned into the one with symmetrical eccentricity by maneuvering the eccentricities to make $R_1 = R_1'$. Thus, this investigation would involve the following:

1. Rocking frames with unsymmetrical eccentricity on unsymmetrical piers.

2. Rocking frames with unsymmetrical eccentricity on symmetrical piers.

3. Rocking frames with symmetrical eccentricity on unsymmetrical piers.

1.6.3 Stability of rocking frames under horizontal excitation.

Since rocking frames with symmetrical eccentricity can be represented by an equivalent block, investigate separation or lift-off of a rocking block under slide restrained conditions and then investigate separation of the beam in a frame. This part of the research can be further subdivided into two parts.

1.6.3.1 Investigation on separation of a slide-restrained single rigid block under horizontal pulse excitation

Investigate a slender falling block's response to a pulse excitation that makes the block rise to its peak rotation and then accelerates it in the opposite direction augmenting its fall. The low-amplitude-low-frequency excitation pulse (that precedes the main sine pulse in Figure 1-2 (k)) would make the block rise and the main pulse will augment its fall under slide restrained conditions. Determine such hybrid pulse excitations that would result in separation of a slide restrained slender block. Derive closed-form solutions to hybrid pulse excitations. Obtain the response of rectangular and trapezoidal blocks to such pulse excitations by numerical analysis and verify the response obtained through closed form solutions. Study the sensitivity of the COFD to the vertical acceleration of the block.

1.6.3.2 Investigation on separation of the beam in rocking frames

Investigate separation of the beam in frames with symmetrical eccentricities subjected to hybrid pulse excitation and compare its response with that of a single block. Obtain the

horizontal and vertical accelerations of the beam along with the displacements for pulse excitations and earthquake records. Formulate equations to predict the horizontal and vertical accelerations, and, the COFD of the beam for frames with symmetrical eccentricity. Compare the equations' outcome of the numerical response to earthquake records in form of time history and rocking spectra. Study the impact of eccentricity on the vertical and horizontal accelerations of the beam through rocking spectra based on variation of eccentricity. Explore the possibility of separation for frames with unsymmetrical eccentricity with unsymmetrical and symmetrical piers.

1.7 Thesis Organization

The thesis consists of five chapters. The first chapter contains introduction that includes research objectives. The second, third and the fourth chapters contain articles (papers) that follow the research objectives established in the first chapter. The fifth chapter contains conclusion of the research. Below is the brief description of each chapter.

1. Chapter 1 contains information on the applications of rocking frames in NPPs carrying heavy load, nuclear risk due to the accidental drop of such components and the motivation behind the entire thesis. Chapter 1 also includes literature review, research objectives and the overall description of the entire thesis.
2. Chapter 2 contains investigation of rocking frames with symmetrical eccentricity on symmetrical piers. It establishes the parameters of an equivalent rocking block that can represent the frame. The COR for such frames is derived and response of frames to pulse excitation and earthquake records is obtained. This chapter also investigates the sensitivity of a rocking frame's response to the variation in eccentricity.

3. Chapter 3 investigates rocking frames with unsymmetrical eccentricity on unsymmetrical and symmetrical piers. It is discovered that such frames cannot be represented by a single rocking block. However, the equation of motion is derived in form of combination of equivalent blocks with time varying dynamic parameters. The CORs for unsymmetrical piers and for the entire frame are derived. This chapter also explores the applicability of eccentricity as a manipulative tool to convert an unsymmetrical eccentricity configuration into the one with symmetrical eccentricity. Response to earthquake records of frames with unsymmetrical eccentricity is obtained and their sensitivity to eccentricity is studied.

4. Chapter 4 explores the possibility of separation of an individual slender block under slide restrained conditions subjected to pulse excitations. Equations of hybrid pulse excitations and their closed form solutions for slender blocks are derived. The closed form solutions for horizontal and vertical accelerations are verified with numerically obtained responses to the pulse excitation. Responses of symmetrical eccentricity frames with rectangular and trapezoidal piers are obtained. Sensitivity of the COFD to the vertical acceleration of a block is studied.

5. Rocking induced isolation of the beam in a frame with symmetrical eccentricities under horizontal excitation and its effectiveness are also studied. Horizontal and vertical accelerations of the beam in a frame with symmetrical eccentricity are obtained and semi-empirical equations for such accelerations and the COFD are formulated. The outcome of equations is compared with the numerically obtained responses for frames with symmetrical eccentricity to earthquake records. The equations' outcome is also compared with the

numerically obtained solutions to earthquake records for frames with unsymmetrical eccentricities on unsymmetrical and symmetrical piers.

6. Chapter 5 provides summary of the research, key findings and describes the overall application of the research in the field that aligns with the research objectives. Recommendations for future research are also presented.

7. APPENDIX A provides supplementary information related to analysis covered in Chapter 3.

Disclaimer

The opinions and conclusions expressed in this thesis are of the author, Amitabh Dar, and do not reflect the official position of the author's employer, Bruce Power.

1.8 References

1. CSA. CSA N291. *Requirements for nuclear safety-related structures*. Rexdale, Ontario, Canada: Canadian Standards Association, 2019.
2. EPRI. NP-6041-SL-Revision 1. *A Methodology for Assessment of Nuclear Power Plant Seismic Margin*. Palo Alto, CA: Electric Power Research Institute, 1991.
3. American Society of Civil Engineers. ASCE 43-19 – *Seismic Design Criteria for Structures, Systems and Components in Nuclear Facilities*, Reston, 2019.
4. CSA. CSA N89.3. *Design procedures for seismic qualification of nuclear power plants*. Rexdale, Ontario, Canada: Canadian Standards Association, 2020.
5. USNRC. Arkansas Nuclear One – *NRC augmented inspection team follow-up inspection report 05000313/2013012 and 05000368/2013012; preliminary red and yellow findings*. United States Regulatory Commission's letter to Ankansas Nuclear One. 2014, March 24. Retrieved May 9, 2021, from www.nrc.gov: https://www.nrc.gov/docs/ML1408/ML14083A409.pdf
6. Makris N, Vassiliou MF. Planar rocking response and stability analysis of an array of free-standing columns capped with a freely supported rigid beam. *Earthquake Engineering and Structural Dynamics* 2013; **42**(3):431-449.
7. Dar A, Konstantinidis D, El-Dakhakhni WW. Impact of slenderness on the seismic response of rocking frames in Ontario nuclear power plants. *5th International Structural Specialty Conference*, London, Ontario, Canadian Society for Civil Engineering, 2016.

8. Housner GW. The behavior of inverted pendulum structures during earthquakes. *Bulletin of the Seismological* Society of America 1963; **53**(2):403–417.
9. Aslam M, Scalise DT, Godden WG. Earthquake rocking response of rigid bodies. *Journal of the Structural Division* 1980; **106**(2):377-392.
10. Spanos PD, Koh AS. Rocking of rigid blocks due to harmonic shaking. *Journal of Engineering Mechanics* 1984;**110**(11):1627-1642.
11. Konstantinidis D, Makris N. The dynamics of a rocking block in three dimensions. Proc., *8th Hellenic Society for Theoretical and Applied Mechanics Int. Congress on Mechanics*, Hellenic Society for Theoretical and Applied Mechanics, Athens, Greece, 2007.
12. Yim CK, Chopra A, Penzien J. Rocking response of rigid blocks to earthquakes. *Earthquake Engineering and Structural Dynamics* 1980; **8**(6):565–587.
13. Makris N, Roussos Y. *Rocking response and overturning of equipment under horizontal pulse-type motions*, Report No. 1998/05. Berkeley, 1998.
14. Pompei, A., Scalia, A., & Sumbatyan, M. A. Dynamics of rigid block due to horizontal ground motion. *Journal of Engineering Mechanics*, 1998; **7**(124), 713-717.
15. Shao Y, Tung C. Seismic response of unanchored bodies. *Earthquake Spectra* 1999; **15**(3):523–536.
16. Zhang, J.and Makris, N. (2001). Rocking response of free-standing blocks under cycloidal pulses, *Journal of Engineering Mechanics* 2001; **127**(5), 473-483
17. Konstantinidis D, Makris N. Experimental and analytical studies on the response of 1/4-scale models of freestanding laboratory equipment subjected to strong earthquake shaking. *Bulletin of Earthquake Engineering*, 2010; **8**(6):1457–1477.
18. Priestley M, Evison R, Carr AJ. Seismic response of structures free to rock on their foundations. *Bulletin of the New Zealand National Society for Earthquake Engineering* 1978; 11(3):141–150.
19. Wesley DA, Kennedy RP, Richter PJ. Analysis of the seismic collapse capacity of unreinforced masonry wall structures. *Proceedings of the 7th World Conference on Earthquake Engineering*, Istanbul, Turkey, 1980.
20. Makris N, Konstantinidis D. The rocking spectrum and the limitations of practical design methodologies. *Earthquake Engineering and Structural Dynamics*, 2003; 32(2):265–289.
21. Dar A, Konstantinidis D, El-Dakhakhni W. Requirement of rocking spectrum in Canadian nuclear standards. Transactions, *22nd International Structural Mechanics in Reactor Technology Conference (SMiRT22)*, San Francisco, CA, 2013.
22. Dar A, Konstantinidis D, El-Dakhakhni WW. Evaluation of ASCE 43-05 seismic design criteria for rocking objects in nuclear facilities. *Journal of Structural Engineerin*g 2016; 142(11).
23. DeJong MJ, Dimitrakopoulos EG. Dynamically equivalent rocking structures. *Earthquake Engineering and Structural Dynamics* 2014; **43**:1543–1563.
24. Lee TH. Nonlinear dynamic analysis of a stacked fuel column subjected to boundary motion. *Nuclear Engineering and Design* 1975; **32**:337-350.
25. Ikushima, Nakazawa T. A seismic analysis method for a block column gas-cooled reactor core. *Nuclear Engineering and Design* 1979; **55**:331-342.
26. Allen RH, Oppenheim IJ, Parker AR, Bielak J. On the dynamic response of rigid body assemblies. *Earthquake Engineering and Structural Dynamics* 1986;**14**:861-876.

27. Psycharis IN. Dynamic behaviour of rocking two-block assemblies. *Earthquake Engineering and Structural Dynamics* 1990; **19**:555-575.
28. Spanos PD, Roussis PC, Nikolaos P. Dynamic analysis of stacked rigid blocks. *Soil Dynamics and Earthquake Engineering* 2001; **21**:559-578.
29. Konstantinidis D, Makris N. Seismic response analysis of multidrum classical columns. *Earthquake Engineering and Structural Dynamics* 2005; **34**:1243–1270.
30. Kounadis AN, Papadopoulos GJ, Cotsovos DM. Overturning instability of a two-rigid block system under ground excitation. *ZAMM Z. Angew. Math. Mech.* 2012; **92**(7):536 – 557.
31. Minafo G, Amato G, Stella L. Rocking behaviour of multi-block columns subjected to pulse-type ground motion accelerations. *The Open Construction and Building Technology Journal* 2016; **10**(Suppl 1: M9): 150-157.
32. Wittich CE, Hutchinson TC. Shake table tests of stiff, unattached, asymmetric structures. *Earthquake Engineering and Structural Dynamics* 2015; **44**(14):2425-43.
33. Wittich CE, Hutchinson TC. Shake table tests of unattached, asymmetric, dual-body systems. *Earthquake Engineering and Structural Dynamics* 2017; **46**(9):1391–1410.
34. Makris N, Vassiliou M. Sizing the slenderness of free-standing rocking columns to withstand earthquake shaking. *Archive of Applied Mechanics* 2012; **82**(10):1497–1511.
35. Makris N, Kampas G. Size Versus Slenderness: Two Competing Parameters in the Seismic Stability of Free-Standing Rocking Columns. *Bulletin of Seismological Society of America* 2016; **106**(1):104-122.
36. Makris N, Vassiliou M. Are Some Top-Heavy Structures More Stable? *Journal of Structural Engineering* 2014; **140**(5).
37. Beck JL, Skinner RI. The seismic response of a reinforced concrete bridge pier designed to step. *Earthquake Engineering and Structural Dynamics* 1974; **2**:343-358.
38. Vassiliou, M. F., Burger, S., Egger M, B., Bachmann, J., Broccardo, M., & Stojadinovic, B. The three-dimensional behavior of inverted pendulum cylindrical structures during earthquakes. *Earthquake Engineering & Structural Dynamics* 2017; **46**(14): 2261–2280.
39. Drosos V, Anastasopoulos I. Shaking table testing of multidrum columns and portals. *Earthquake Engineering and Structural Dynamics* 2014;**43**(11):1703-23.
40. Vassiliou MF, Mackie KR, Stojadinović B. A finite element model for seismic response analysis of deformable rocking frames. *Earthquake Engineering and Structural Dynamics* 2017;**46**(3):447-66.
41. Dimitrakopoulos, E. G., Giouvanidis, A. I. Seismic Response Analysis of the Planar Rocking Frame. *J. Eng. Mech* 2015;**141**(7).
42. Diamantopoulos, S., Fragiadakis, M. Modeling of rocking frames under seismic loading. *Earthquake Engng Struct Dyn,* 2021;**51**(1):109-128.
43. Bachmann, J. A., Vassiliou, M. F., & Stojadinović, B. Dynamics of rocking podium structures. *Earthquake Engng Struct. Dyn*. 2017; **46**, 2499– 2517. doi:10.1002/eqe.2915
44. Chen, Y.-H., Liao, W.-H., Lee, C.-L., & Wang, Y.-P. Seismic isolation of viaduct piers by means of a rocking mechanism. *Earthquake Engng. Struct. Dyn.,* 2006;**35**(6),713-736.
45. Cheng, C.-W., & Chao, C.-H. (2017). Seismic behavior of rocking base-isolated structures. *Engineering Structures*, **139**, 46-58.
46. Lu, L.-Y., & Hsu, C.-C. Experimental study of variable-frequency rocking bearings for near-fault seismic isolation. *Engineering Structures,* 2013;**46**,116-129.

47. Makris, N. Dynamics of Rocking Isolation . *Recent Advances in Earthquake Engineering in Europe - 16th European Conference on Earthquake Engineering*, 2018;**46**:289-307. Thessaloniki: Springer.
48. USNRC. *Design Response Spectra for Seismic Design of Nuclear Power Plants*, Regulatory Guide 1.60, Revision 1. Washington, D.C.: United States Nuclear Regulatory Commission, 1973.
49. USNRC. *Design Response Spectra for Seismic Design of Nuclear Power Plants*, Regulatory Guide 1.60, Revision 2. Washington DC: United States Regulatory Commission, 2014.
50. Newmark, N. M., Blume, J. H., & Kapur, K. K. Seismic Design Spectra for Nuclear Power Plants. *Journal of the Power Division*, 1973;99(2), 287-303.
51. Dar A, Konstantinidis D, El-Dakhakhni WW. Seismic qualification of rocking objects in Canadian nuclear power plants. *Proceedings of the 10th National Conference in Earthquake Engineering*, Earthquake Engineering Research Institute, Anchorage, AK, 2014.
52. Mathcad 15.0 [Computer software]. Parametric Technology Corporation, Needham, MA.

1.9 Figures

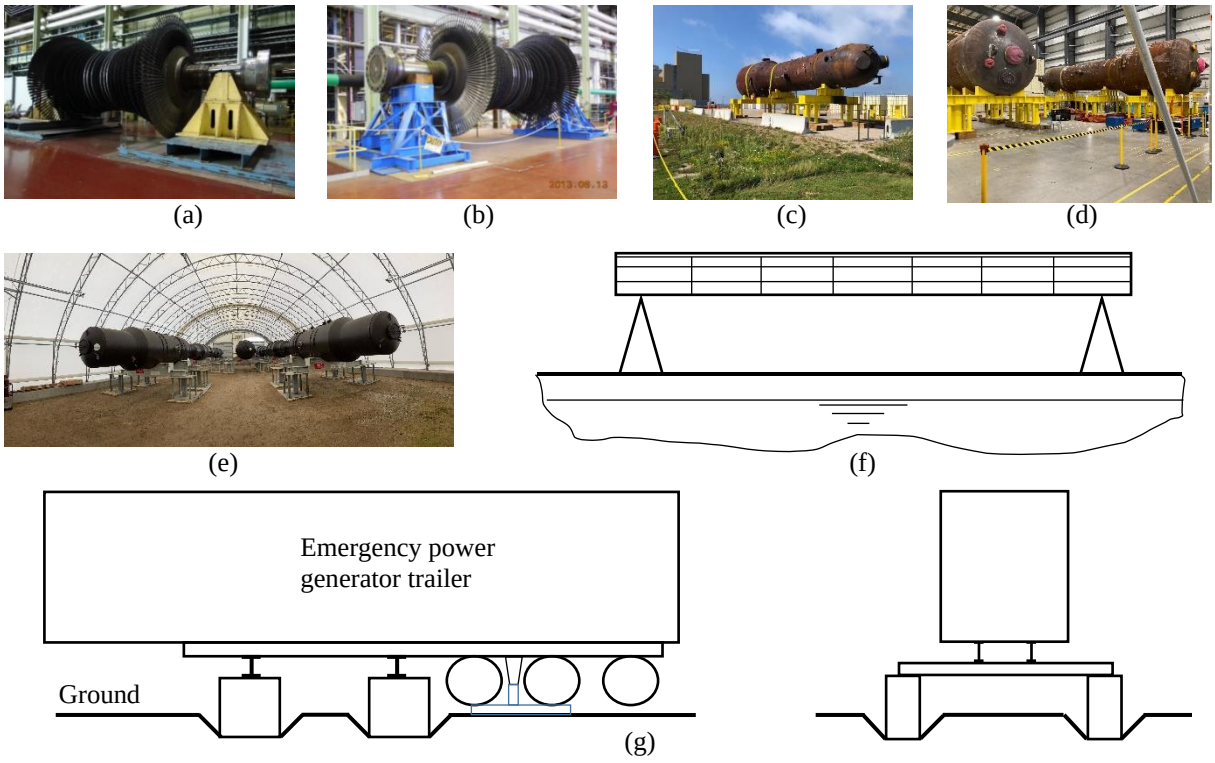

Figure 1-1: Rocking frame examples in NPPs: (a) and (b) turbine rotors supported by symmetrical and unsymmetrical piers. (c), (d), and (e), steam generators in storage. (f), schematic representation of the 4 Ton 40 feet span man-bridge geometry beside the fuel bay pool resting on two triangular steel piers, (g) emergency power generator resting on concrete piers with steel beams during maintenance. Photo Curtsey: Bruce Power (Ontario).

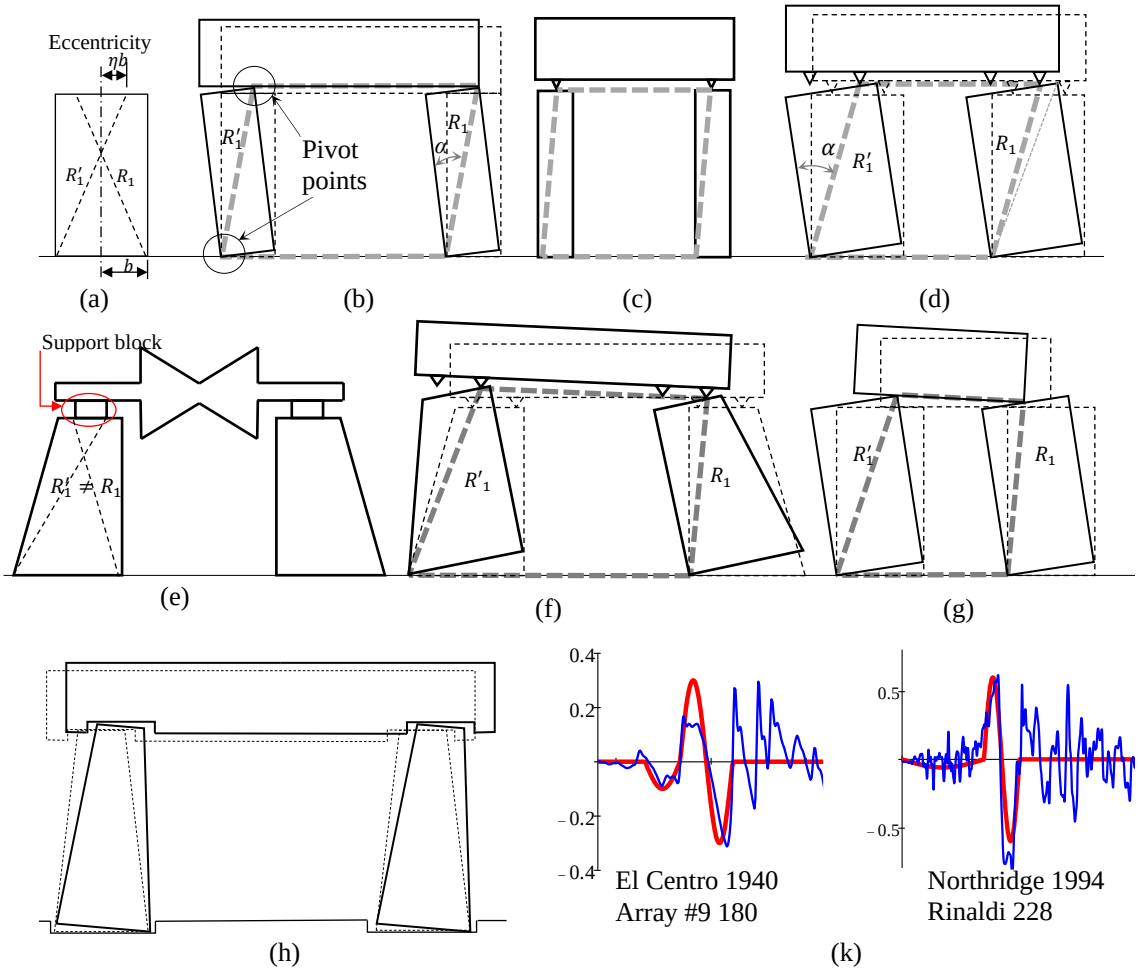

Figure 1-2: (a) support eccentricity. (b) rocking frame having symmetrical piers with pivot points at the pier corners, (c) at pier centers, and (d) in between the two. (e) turbine rotor support geometry with unsymmetrical piers and, (f) idealized presentation of unsymmetrical piers with support eccentricity. (g) support eccentricity on symmetrical pier. (h) rocking frame on trapezoidal piers with shear keys. (k) low-amplitude-low-frequency pre-excitation pulse before the main pulse in earthquake record.

CHAPTER 2

SEISMIC RESPONSE OF ROCKING FRAMES WITH TOP SUPPORT ECCENTRICITY

The contents of this chapter have been published in the following article:

Dar A, Konstantinidis D, El-Dakhakhni W. Seismic response of rocking frames with top support eccentricity. *Earthquake Engineering and Structural Dynamics* 2018; **47**(12): 2496– 2518. https://doi.org/10.1002/eqe.3096

2.1 Abstract

The seismic response of rocking frames that consist of a rigid beam freely supported on rigid freestanding rectangular piers has received recent attention in the literature. Past studies have investigated the special case where, upon planar rocking motion, the beam maintains contact with the piers at their extreme edges. However, in many real scenarios, the beam-to-pier contact lies closer to the center of the pier, affecting the overall stability of the system. This paper investigates the seismic response of rocking frames under the more general case which allows the contact edge to reside anywhere in-between the center of the pier and its extreme edge. The study introduces a rocking block model that is dynamically equivalent to a rocking frame with vertically symmetric piers of any geometry. The impact of top eccentricity (i.e., the distance of the contact edge from the pier's vertical axis of symmetry) on the seismic response of rocking frames is investigated under pulse excitations and earthquake records. It is concluded that the stability of a top-heavy rocking frame is highly influenced by the top eccentricity. For instance, a rocking frame with contacts at the extreme edges of the piers can be more seismically stable than a solitary block that is identical to one of the frame's piers, while a rocking frame with contacts closer to the centers of the piers is less stable. The concept of critical eccentricity is introduced, beyond which the

coefficient of restitution contributes to a greater reduction in response of a frame than that of its pier.

2.2 Introduction

Assemblages of unanchored components that can be modeled as rocking frames are observed in various types of structures ranging from ancient Greek temples [1-3] to present day nuclear power plants [4]. The top row of Figure 2-1 shows examples of typical rocking frames in nuclear power plants, while the bottom row shows schematic representations of various types of rocking frames. Concerns about the seismic stability of such components have arisen during seismic re-evaluation efforts of nuclear facilities following the Fukushima Daiichi nuclear power plant accident in 2011, caused by the 2011 Tohoku earthquake. Studies on the seismic response of rocking frames have been scarce, and current nuclear standards offer very limited guidance on solitary rocking components and no guidance on rocking frames. Therefore, the real risk due to the seismic performance of rocking frames in nuclear facilities remains unknown.

To obtain the response of a rocking frame, it is convenient to represent it by an equivalent rigid rocking block the response of which is the same as that of the frame. Following the pioneering work by Housner [5], numerous studies [6-12 and references therein] have investigated the response of a rigid rocking block to seismic excitation. Attempts to represent a rigid block by a single-degree-of-freedom oscillator [13-14], including the design criterion given in the nuclear standard ASCE 43-05 [15], and to obtain its peak response from a response spectrum have been evaluated and shown to be highly inaccurate when compared to the results of nonlinear response history analysis [16-18].

The dynamics of rigid-block assemblages has also been studied. DeJong and Dimitrakopoulos [19] demonstrated the dynamic equivalency of various assemblages, including simple rocking frames similar to that in Figure 2-2(a), to single blocks. Several other types of block assemblages have been studied by Lee [20], Ikushima and Nakazawa [21], Allen et al. [22], Psycharis [23], Spanos et al. [24], Konstantinidis and Makris [25], Kounadis et al. [26], Minafo et al. [27] and Bachmann et al. [28]. Wittich and Hutchinson carried out extensive shake table test studies to investigate the seismic response of asymmetric rocking single-body structures [29] and dual-body systems [30].

Figure 2-2 (a) shows the rocking frame investigated by Makris and Vassiliou [3], consisting of rigid unanchored prismatic rectangular piers freely supporting a top rigid beam, having uniformly distributed mass, with sufficient friction at all contact points to prevent sliding. In the undisplaced configuration of such frames, the top surfaces of piers are in full contact with the beam (Figure 2-2 (a), dashed outline). During rocking motion, the piers uplift at their base, and the beam rests on the top edges, referred to hereinafter as *corners* (of the piers' cross sections), opposite to the pivot corners at the bases of the piers. Upon impact, the contact point shifts from the left to the right top corner of the pier. Makris and Vassiliou [3] showed that the response of this type of rocking frame is equal to that of a dynamically equivalent rocking block, shown in Figure 2-2 (b), which has the same slenderness (represented by angle α) as the piers but is larger in size. Since a larger block is seismically more stable than a smaller block with the same slenderness, a size effect noted by Housner [5], the authors concluded that top-heavy rocking frames are more stable in comparison to their lighter counterparts.

A variation of the rocking frame analyzed by Makris and Vassiliou [3] was studied by Dar et al. [31] and revisited by Dar et al. [4] in the context of nuclear power plants. This type of rocking frame is shown in Figure 2-1(e), with its idealized representation in Figure 2-1(f). In this case, the contact point between the beam and each pier remains fixed (at pier center) during rocking motion. For this type of frame, the equivalent rocking block was not only larger but also slenderer (lower α) than a solitary pier. Using a small set of ground motion records, this frame was found to be less stable than a solitary pier.

In this paper, the location of the top support is defined in terms of the top eccentricity, η, which varies between the two extremes: $\eta = 0$ (top center) to $\eta = 1$ (top corner). The mass distributions of the piers and the top beam are assumed uniform, but not equal to each other. All piers of a rocking frame are considered to have the same shape and size. Figure 2-3(a) shows a rocking frame in clockwise rocking motion, where, as in Figure 2-1(a), (b) and (c), the contact point between the beam and a typical pier lies between the pier corner and its center. As shown later, the seismic response of the rocking frame in Figure 2-3(a) is the same as that of the pier-mass assembly in Figure 2-3 (b), where, a lumped mass (equal to the top beam mass divided by the number of piers) at the top of the pier (with width $2b$ and height $2h$) is located at a distance ηb from the center of the pier. In Figure 2-3 (c), the slenderness parameter of the pier-mass assembly remains the same as that of the solitary pier, i.e. $\alpha_{eq} = \alpha$ (the case studied by Makris and Vassiliou [3]), but in Figure 2-3 (b) it is less than that of the solitary pier ($\alpha_{eq} < \alpha$). However, the size of the pier-mass assembly is larger than the size of the solitary pier ($R_{eq} > R$). Makris and Vassiliou [3] perceived the pier-mass assembly as a large rectangular pier, shown with a solid outline in Figure 2-3 (c), with size $\hat{R}$. The center of gravity, $\overline{CG}$, in Figure 2-3 (c) is on the pier diagonal, while in Figure 2-3 (b) it is

not. As explained by Housner [5] and later by Makris and Roussos [10], to maintain stability for a given excitation, the right combination of α and R is required. Deficiency in the former must be compensated by an augmentation of the latter. Thus, these two parameters are considered as complementary to each other in the context of this paper. However, there are other cases where they have been considered as "competing" [33].

The location of the center of gravity is not only influenced by η but also by the geometry of the piers (e.g., tapered piers, as shown in Figure 2-1(a) and (b)). Makris and Vassiliou [3] analyzed rocking frames with rectangular piers. Konstantinidis and Makris [25] considered trapezoidal (linearly tapered) piers but only for deriving the coefficient of restitution of a single column. Apart from studying the impact of η on the rocking response of frames, the current study also considers piers of any vertically symmetrical geometry. Figure 2-4(a) and 4(b) show rocking frames with trapezoidal piers, where the top mass would never align with the line joining the bottom pivot and the location of the CG (represented by the horizontal dotted line), even if the top mass sits at the pier corner during rocking motion. This would result in $\alpha_{eq} < \alpha$ but $R_{eq} > R$ (similar to Figure 2-3(b)). Figure 2-4 (c) and (d) are similar to bridges (with unanchored piers) where the deck is freely supported by bearings (on piers) which are not expected to transfer the deck load exactly at the top corners of the piers. A rocking frame like the one in Figure 2-2 with damaged top pier corners would be conceptually similar to the frame in Figure 2-4 (c). Thus, it is very rare that realistically the top lumped mass would not result in reduced slenderness parameter ($\alpha_{eq} < \alpha$). Hence the stability of the top-heavy rocking frames requires investigation beyond the one carried out by Makris and Vassiliou [3, 34].

This paper investigates the dynamics of rocking frames with top eccentricity on piers of any vertically symmetrical geometry. It is shown that such a rocking frame can be represented by a dynamically equivalent rocking-block model. Parameters representing the slenderness, size, and restitution coefficient of the equivalent rocking block are derived. The dynamics of such frames is investigated through nonlinear response analysis of equivalent rocking blocks subject to various pulse excitations and earthquake records, using a state-space formulation [16] and utilizing the AdamsBDF solver [35].

2.3 Review of a Rocking Block

Figure 2-5 shows a rigid rectangular block of uniformly distributed mass m with width $2b$, mass moment of inertia I_o about the pivot point O, and its center of gravity at height h and distance R (hereinafter referred to as the *radius* of rotation) from the pivot point. The total height of the block is ξh. The block is subjected to base horizontal acceleration $\ddot{u}_g$. The equation of motion for this block is [9]:

$$\ddot{\theta} = -p^2 \left\{ \sin[\alpha \, \mathrm{sgn}(\theta) - \theta] + \frac{\ddot{u}_g}{g} \cos[\alpha \, \mathrm{sgn}(\theta) - \theta] \right\} \tag{2-1}$$

where, $\mathrm{sgn}(\cdot)$ is the *signum* function, g is the gravitational acceleration, α is the block slenderness parameter, and $p = \sqrt{mgR/I_o}$ is the so-called frequency parameter, which is the frequency of a pendulum created by suspending the rocking block upside down from O or O'. The variable ξ is equal to 2 for the rectangular block in Figure 2-5 but varies for a non-rectangular vertically symmetrical geometry with uniform mass distribution. For a rectangular block, $I_o = (4/3)mR^2$ and $p = \sqrt{3g/4R}$.

The energy lost during the impact is accounted for through the use of a coefficient of restitution, which requires that angular velocity immediately after impact is reduced from that immediately before impact. In the absence of experimental data, the value of the coefficient of restitution, e, in rocking analysis is usually taken as the value required to sustain pure rocking motion, which is derived by conservation of angular moment at the instants before and after the impact. The post-impact velocity, $\dot{\theta}_2$, is obtained by multiplying the pre-impact velocity, $\dot{\theta}_1$, by e, given by [5]

$$e = 1 - \frac{3}{2}\sin^2\alpha \tag{2-2}$$

2.4 Rocking Frame with Eccentrically Loaded Piers

Figure 2-6(a) shows the geometry of a rectangular rocking block pier for the rocking frame shown in Figure 2-3(a). Sufficient friction at all contact points is assumed to prevent sliding. The equations presented below are in terms of the total height (ξh) and are applicable to any vertically symmetrical geometry with the base width greater or equal to the top width. The top contact point of the pier with the beam is denoted as B (or B' for negative rotation) at a distance ηb from the top centre, where η varies from 0 to 1. Figure 2-6(b) shows the point load from the top beam considered as a lumped point mass $m_t = M_T/N$, where M_T is the mass of the top beam and N is the number of piers. The following geometrical relationships (from Figure 2-6 (a)) are important for later analysis:

$$\begin{gathered} R_1\cos\beta = \xi R\cos\alpha; \quad R_1\sin\beta = (1+\eta)R\sin\alpha; \\ R_1^2 = R^2\left[(1+\eta)^2\sin^2\alpha + \xi^2\cos^2\alpha\right] \end{gathered} \tag{2-3}$$

Since the top beam is rigid and experiences no rotation, its relative horizontal and vertical displacements are the same as those of point B, which are (for $\theta > 0$)

$$u_B = (1+\eta)b - R_1 \sin(\beta - \theta) \tag{2-4}$$

$$v_B = R_1 \cos(\beta - \theta) - \xi h \tag{2-5}$$

with the corresponding velocities

:

$$\dot{u}_B = R_1 \cos(\beta - \theta)\, \dot{\theta} \tag{2-6}$$

$$\dot{v}_B = R_1 \sin(\beta - \theta)\, \dot{\theta} \tag{2-7}$$

Similarly, the relative horizontal and vertical displacements and velocities of the infinitesimal mass dm (see Figure 2-6 (a)), at distance R_{dm} and angle α_{dm}, are

$$u_{dm} = R_{dm}[\sin \alpha_{dm} - \sin(\alpha_{dm} - \theta)] \tag{2-8}$$

$$v_{dm} = R_{dm}[\cos(\alpha_{dm} - \theta) - \cos \alpha_{dm}] \tag{2-9}$$

$$\dot{u}_{dm} = R_{dm} \cos(\alpha_{dm} - \theta)\, \dot{\theta} \tag{2-10}$$

$$\dot{v}_{dm} = R_{dm} \sin(\alpha_{dm} - \theta)\, \dot{\theta} \tag{2-11}$$

Since the rocking frame system is conservative between impacts, Lagrange's Equation can be written as

$$\frac{d}{dt}\left(\frac{dL}{d\dot{\theta}}\right) - \frac{dL}{d\theta} = 0 \tag{2-12}$$

where $L = T - V$ is the Lagrangian, T is the kinetic energy, and V is the potential energy, of the system. For pure horizontal ground motion with the ground velocity denoted as $\dot{u}_g$, the piers rotate about the pivot point but the top mass M_T only translates vertically and horizontally. Considering

the total horizontal and vertical velocities of the top mass as $\dot{u}_B^t = \dot{u}_B + \dot{u}_g$ and $\dot{v}_B^t = \dot{v}_B$, and of the mass dm as $\dot{u}_{dm}^t = \dot{u}_{dm} + \dot{u}_g$ and $\dot{v}_{dm}^t = \dot{v}_{dm}$, the kinetic energy of the system is given by

$$T = \frac{1}{2}N\int\left[\left(\dot{u}_{dm} + \dot{u}_g\right)^2 + \dot{v}_{dm}^2\right]dm + \frac{1}{2}M_T\left[\left(\dot{u}_B + \dot{u}_g\right)^2 + {\dot{v}_B}^2\right] \tag{2-13}$$

from which, using $\dot{\theta}_T = \dot{\theta}(d\theta_T/d\theta)$ gives

$$\begin{aligned} T = \frac{1}{2}N\left[\dot{\theta}^2\int R_{dm}^2 dm + \dot{u}_g^2\int dm + 2\dot{\theta}\dot{u}_g\int R_{dm}\cos(\alpha_{dm}-\theta)dm\right] + \cdots \\ + \tfrac{1}{2}M_T\left[R_1^2\dot{\theta}^2 + {\dot{u}_g}^2 + 2R_1\cos(\beta-\theta)\dot{\theta}\dot{u}_g\right] \end{aligned} \tag{2-14}$$

The term $R_{dm}\cos(\alpha_{dm}-\theta)dm$ is the moment of mass dm about the axis OO'. Hence its integral is the total mass m times the perpendicular distance of the CG from OO', i.e., $mR\cos(\alpha-\theta)$. By definition, the first integral in Equation (2-14) is the moment of inertia about the pivot O, I_o, giving

$$T = \frac{1}{2}N\left[I_o\dot{\theta}^2 + m\dot{u}_g^2 + 2mR\cos(\alpha-\theta)\dot{\theta}\dot{u}_g\right] + \frac{1}{2}M_T\left[R_1^2\dot{\theta}^2 + \dot{u}_g^2 + 2R_1\cos(\beta-\theta)\dot{\theta}\dot{u}_g\right] \tag{2-15}$$

With the ground set as the reference, the potential energy of the rocking frame is

$$V = NmgR[\cos(\alpha-\theta) - \cos\alpha] + M_T g[R_1\cos(\beta-\theta) - \xi h] \tag{2-16}$$

Substituting the expressions for T and V into (12), with $m_t = M_T/N$, leads to the equation of motion for $\theta > 0$:

$$(I_o + m_t R_1^2)\ddot{\theta} = -mR\left[g\sin(\alpha-\theta) + \ddot{u}_g\cos(\alpha-\theta)\right] - m_t R_1\left[g\sin(\beta-\theta) + \ddot{u}_g\cos(\beta-\theta)\right] \tag{2-17}$$

The above is the same as the equation of motion of the solitary block pier (Eq. (1)) with additional terms on both sides added for the lumped mass m_t at point B in Figure 2-6 (b). The terms related to m_t amount to the equation of motion of a forced inverted pendulum of mass m_t

with its equilibrium slanted at angle β. This shows that the dynamic behavior of a single block pier with lumped mass m_t is equivalent to that of the entire rocking frame.

Defining the mass ratio $q = m_t/m$ and an inertia parameter $\psi = 1 + qmR_1^2/I_o$, and with the help of Equation (2-3), Equation (2-17) can be written as

$$\psi I_o\ddot{\theta} = -mR\{g[(1+(\eta+1)q)\sin\alpha\cos\theta - (1+\xi q)\cos\alpha\sin\theta] \ldots \\ +\ddot{u}_g[(1+(\eta+1)q)\sin\alpha\sin\theta + (1+\xi q)\cos\alpha\cos\theta] \tag{2-18}$$

Consider two parameters defined as a constant λ and an angle α_{eq} with the following equalities

$$\lambda\sin\alpha_{eq} = [1+(\eta+1)q]\sin\alpha \tag{2-19}$$

$$\lambda\cos\alpha_{eq} = (1+\xi q)\cos\alpha \tag{2-20}$$

Substituting Equations (2-19) and (2-20) into Equation (2-18) and incorporating the *signum* function (to account for positive and negative rotations) gives

$$\ddot{\theta} = -p_{eq}^2\left\{\sin\left[\alpha_{eq}\mathrm{sgn}(\theta)-\theta\right] + \frac{\ddot{u}_g}{g}\cos\left[\alpha_{eq}\mathrm{sgn}(\theta)-\theta\right]\right\} \tag{2-21}$$

where, α_{eq}, λ, and p_{eq}, obtained from Equations (2-19) and (2-20) are

$$\alpha_{eq} = \tan^{-1}\left(\frac{1+(\eta+1)q}{1+\xi q}\tan\alpha\right) \tag{2-22}$$

$$\lambda = \sqrt{(1+(\eta+1)q)^2\sin^2\alpha + (1+\xi q)^2\cos^2\alpha} \tag{2-23}$$

$$p_{eq}^2 = \frac{m(1+q)gR_{eq}}{I_{eq}} = \frac{\lambda}{\psi}p^2 \tag{2-24}$$

$$R_{eq} = \frac{\lambda}{1+q}R \tag{2-25}$$

$$I_{eq} = \psi I_o \tag{2-26}$$

$$\psi = 1 + \frac{qm}{I_o}R_1^2 = 1 + \frac{q}{I_{on}}\left[(1+\eta)^2\sin^2\alpha + \xi^2\cos^2\alpha\right] \tag{2-27}$$

and $I_{on} = I_o/mR^2$ (or ${r_o}^2/R^2$, where r_o is the radius of gyration of the pier about the pivot point) is defined as the normalized moment of inertia. For a rectangular block, $I_{on} = 4/3$.

Equation (2-21) is the same as Equation (2-1) but with equivalent rocking block parameters p_{eq} and α_{eq}. The equivalent rocking block represents the entire frame of Figure 2-3(a) with any number of piers and one rigid top beam. The set of Equations (2-22) to (2-27) define various relationships necessary to compute p_{eq} and α_{eq}. It is noted that Equations (2-22) to (2-27) are applicable to a typical block pier of any vertically symmetrical geometry, as shown in Figure 2-7(a), having uniform density with the center of gravity at height h from the base. In Figure 2-7 (a), η cannot have any value other than ϕ because of the top curved surface and the horizontal distance between the top pivot points being less than that between the bottom ones. The top load eccentricity, in a trapezoidal pier with the configuration shown in Figure 2-7 (b), under horizontal excitation, may vary in the range $0 \leq \eta \leq \phi$. Table 2-1 contains equivalent parameters for a trapezoidal block including its two extremes: a triangle ($\phi = 0$) to a rectangle ($\phi = 1$). The last column of Table 2-1 provides equivalent parameters for a cylindrical block. Although it is known [36] that the rocking response of a cylindrical block to ground motion is highly unlikely to be purely planar, its parameters have been included here with the assumption that the top and the base of a cylindrical pier are square shaped (with sides equal to the diameter of the cylinder = $2b$) having much smaller thicknesses compared to the pier height.

Table 2-2 gives a summary of various parameters obtained in this study for a rocking frame with piers of any vertically symmetrical geometry and also compares them with those of frames having rectangular piers for the two extremes of η, i.e., $\eta_{min} = 0$ and $\eta_{max} = 1$, which match with the expressions derived by Dar et al. [4] and Makris and Vassiliou [3] respectively.

To assess the impact of increasing q for $\eta = 1$, the limit of Equation (2-25) as q approaches infinity is

$$\lim_{q\to\infty} \frac{1+2q}{1+q} R = 2R \tag{2-28}$$

Equation (2-28), which was derived by Dar et al. [4], is in agreement with the definition of the parameter R_{eq}. Makris and Vassiliou [3] gave the correct expression for p_{eq}^2 at η =1 which is alternatively obtained from Equation (2-24) as

$$p_{eq}^2 = \frac{1+2q}{1+3q} p^2 \tag{2-29}$$

However, from the above, they derived the expression for equivalent radius $\hat{R}$ as

$$\hat{R} = \frac{3g}{4p_{eq}^2} = \frac{1+3q}{1+2q} R \tag{2-30}$$

Figure 2-3(c) shows the equivalent rectangle in solid lines with the same p_{eq} as of the pier-mass assembly but with radius $\hat{R}$. The parameters, α_{eq} and p_{eq}, derived in this study and Makris and Vassiliou [3], both, represent a rocking rigid pier-mass assembly rather than a rectangular block. The expression for $\hat{R}$ above is more representative of a perception resulting in an equivalent rectangular block, whereas R_{eq} represents the system.

Figure 2-8(a) shows the variation in the normalized radius of rotation with q for $\eta = 1$, which is independent of α, that asymptotes to 2. Figure 2-8 (b) shows that the normalized radius, R_{eq}/R, increases with the increase in q for $\eta = 0$. Considerable difference is observed between R_{eq}/R for $\alpha = 0.1$ and $\alpha = 0.5$. Figure 2-8 (c) shows the variation in the normalized frequency parameter, p_{eq}/p. Significant difference is noted for $\eta = 0$ between the two values of α. For $\eta =$

1, p_{eq}/p is independent of α (Table 2-2, last column) and is the minimum of all cases signifying that the size of the equivalent block is maximum when $\eta = 1$. Figure 2-8 (d) shows that the normalized slenderness α_{eq}/α decreases as q increases for $\eta = 0$. However, for $\eta = 1$, it remains constant at unity. Thus, Figure 2-8 illustrates how for $\eta < 1$, as the top mass increases, the slenderness parameter decreases but the size increases.

2.5 Lumped mass approach

Figure 2-6(b) shows that the center of gravity of the pier and top mass assembly lies on the line joining CG and B. The proportion of segment 'c' with 'd' would be the same as of the ratio of the lumped mass and the total mass. The following relationships emerge for a rectangular pier with $\xi = 2$

$$\frac{c}{d} = \frac{q}{1+q} = \frac{h1}{h} = \frac{b1}{\eta b}, \quad \bar{h} = h\left(1 + \frac{q}{1+q}\right), \quad \text{and} \quad \bar{b} = b\left(1 + \frac{\eta q}{1+q}\right) \tag{2-31}$$

Considering $R_{eq}^2 = \bar{h}^2 + \bar{b}^2$ and substituting $h = R\cos\alpha$ and $b = R\sin\alpha$ gives

$$R_{eq} = \frac{R}{1+q}\sqrt{(1 + (1+\eta)q)^2 \sin^2\alpha + (1+2q)^2\cos^2\alpha} \tag{2-32}$$

Equation (2-32) is the same as Equation (2-25) with $\xi = 2$. Similarly, $I_{eq} = I_o + m_t R_1^2$ with the lumped mass approach. Resolving I_{eq} and considering $p_{eq}^2 = \bar{m}gR_{eq}/I_{eq}$ gives the same expression as in Equation (2-24) with $\xi = 2$. This shows that a solitary block with the lumped mass (top beam mass divided by the number of piers) leads to the same dynamic properties as those of the equivalent rocking block representing the dynamic behavior of the entire rocking frame. From here onwards, the lumped mass model is considered for further analysis.

2.6 Coefficient of Restitution

Impact damping is accounted for through the coefficient of restitution, which is computed herein following Housner's assumption that the vertical impulse that arises upon impact is located at the succeeding pivot point, and therefore angular momentum about this point is conserved. Figure 2-9(a) shows with a dotted line a rigid block of any vertically symmetrical geometry with the base wider than the top. For the convenience of identifying the vertical and horizontal components of the tangential velocity of the top mass, a rectangular shape is also shown in Figure 2-9 (a) with solid lines, illustrating a pier and top mass assembly with clockwise angular velocity $\dot{\theta}_1$ just before impact. At first, the top mass is not considered in this derivation. The center of gravity of the arbitrary geometry is shown as CG at a distance R from the pivot point. The tangential velocity of an infinitesimally small mass dm at a distance r_1 (with angle β_1 from the vertical) from the pivot point O' is $v_t = r_1\dot{\theta}_1$.

Since the clockwise rotation is positive, the corresponding angular momentum of the mass dm about the pivot point O (see Figure 2-9 (a)) just before the impact is

$$\begin{aligned} dH_{O_{\text{before}}} &= -r_1 r_2 \dot{\theta}_1 dm = -r_1(2b\sin\beta_1 - r_1)\,\dot{\theta}_1 dm = (r_1^2 - 2b\,r_1\sin\beta_1)\,\dot{\theta}_1 dm \\ &= [r_1^2 - 2b(b-x)]\dot{\theta}_1 dm \end{aligned} \tag{2-33}$$

where r_2 and x are defined as shown in Figure 2-9 (a). Integrating over the entire body gives

$$H_{O_{\text{before}}} = \left(\int r_1^2\, dm - 2b^2 \int dm + 2b \int x\, dm\right)\dot{\theta}_1 \tag{2-34}$$

In the above equation, the first term inside the bracket is the moment of inertia about O', and the last term is zero by definition of the center of gravity because x is the perpendicular distance from CG. Equating $H_{O_{\text{before}}}$, with the angular momentum about the pivot point O after the impact,

$H_{O_{\text{after}}} = I_o\dot{\theta}_2$, and recognizing $I_{O'} = I_O$ for a vertically symmetrical body, leads to the same expression as derived by Housner [5] for a rectangular block

$$(I_o - 2mbR\sin\alpha)\dot{\theta}_1 \;=\; I_o\dot{\theta}_2 \tag{2-35}$$

Substituting, $b = R\sin\alpha$ leads to the coefficient of restitution for the individual pier (without the top mass)

$$e_G = \frac{\dot{\theta}_2}{\dot{\theta}_1} \;=\; 1 - \frac{2}{I_{on}}\sin^2\alpha \tag{2-36}$$

For a rectangular block, substituting the normalized moment of inertia $I_{on} = 4/3$ leads to Equation (2-2). For a trapezoidal block, considering its parameters as defined by Konstantinidis and Makris [25]: bottom width = $2b$, top width = $2c$, and height = $2h$, and thus substituting $\phi = c/b$ and $\xi = 2$ in the expression given for I_{on} of a trapezoidal block (Table 2-1), Equation (2-36) leads to the same expression as given in Equation (11) in Konstantinidis and Makris [25].

Next, the contribution of the top mass is considered. Before impact, the top point mass is at B (Figure 2-9 (a)). During impact, it smoothly shifts from B to B', depicted in Figure 2-9 (b) and (c). Figure 2-9 (b) shows the top mass when it is just short of landing at B' (in grey color). For calculating the angular momentum about pivot point O of the top mass just before landing at B', the mass is considered to be exactly at B' (where the impulsive force is assumed during impact). Adding the effect of the top mass (its angular moment about the pivot point O) to both sides in Equation (2-35) gives,

$$\dot{\theta}_1(I_o - 2mbR\sin\alpha) + m_t v_{h1}\xi h \;-\; m_t v_{v1}(1+\eta)b = \;\dot{\theta}_2\, I_o + \; m_t v_{h2}\xi h + \; m_t v_{v2}(1+\eta)b \tag{2-37}$$

Equation (2-37) can also be derived from the methodology given in [3] by considering the changes in horizontal and vertical linear momentum of the top beam as $M_T\xi h\left(\dot{\theta}_1 - \dot{\theta}_2\right)$ and

$M_T b(1+\eta)\left(\dot{\theta}_1+\dot{\theta}_2\right)$ applicable at the respective distances ξh and $b(1+\eta)$, from O. Substituting $v_{h1}=\xi h\dot{\theta}_1$ and $v_{v1}=b(1+\eta)\dot{\theta}_1$ before impact, and $v_{h2}=\xi h\dot{\theta}_2$ and $v_{v2}=b(1+\eta)\dot{\theta}_2$ after impact, in Equation (2-37) and considering $h=R\cos\alpha$ and $b=R\sin\alpha$ leads to the coefficient of restitution for the equivalent rocking block representing a pier-top-mass assembly with any vertically symmetrical geometry pier:

$$E_{eq}=\frac{\dot{\theta}_2}{\dot{\theta}_1}=\frac{1}{\psi}\left\{e_G+\frac{q}{I_{on}}\left[(\xi\cos\alpha)^2-\left((1+\eta)\sin\alpha\right)^2\right]\right\} \tag{2-38}$$

where e_G is given by Equation (2-36) and ψ by Equation (2-27). Table 2-2 shows that for $\xi=2$ and $\eta=0$ and 1, Equation (2-38) leads to the same expression as derived by Dar et al. [4] and Makris and Vassiliou [3] respectively. Equations (2-37) and (2-38) are valid for a pier of any geometry (shown with a dotted outline in Figure 2-9 (a)) symmetrical about a vertical axis passing through its centroid with the base wider than its top.

For $q=0$, i.e. without any top mass, the coefficient of restitution given by Equation (2-38) would be the same as e_G given in Equation (2-36). Figure 2-10 shows that the equivalent coefficient of restitution E_{eq}, obtained from Equation (2-38), for a rectangular block with $\alpha=0.2$ increases for $\eta=0$ and decreases for $\eta=1$ as q increases. This means that there is a value of η for which the coefficient of restitution remains equal to that of the solitary rocking pier without any top mass (in this case, $e=0.941$ from Equation (2-2)), which is represented by the horizontal line in Figure 2-10. Equating Equations (2-2) and (2-38) leads to an expression for the *critical eccentricity*, η_{cr}, for a rectangular block ($\xi=2$):

$$\eta_{cr} = 2\cos\alpha\sqrt{\frac{3}{1+3\cos^2\alpha}} - 1 \tag{2-39}$$

Applying the same concept to a block of any pier of vertically symmetrical geometry (Equations (2-36) and (2-38)) leads to the critical eccentricity given below

$$\eta_{Gcr} = \xi\cos\alpha\sqrt{\frac{1}{I_{on}-\sin^2\alpha}} - 1 \tag{2-40}$$

It is noted that Equations (2-39) and (2-40) are independent of q. This is a useful feature that may be used to determine the location of beam supports on a pier or the dimensions of a trapezoidal pier where (at $\eta > \eta_{cr}$) the coefficient of restitution contributes to a greater reduction in response in comparison to that of a solitary pier.

2.7 Size and Slenderness Relationships for Stability

Stability is defined herein as the state whereby the normalized rotation, θ/α, is less than unity. Housner [5] presented stability relationships as functions of the size (p) and slenderness (α) of a rectangular slender block, and the excitation characteristics for various types of excitations: (1) rectangular pulse, (2) half-sine pulse, and (3) white noise (assumed earthquake excitation). The overturning vulnerability of a rectangular block to half-sine pulse excitation was refined by Makris and Roussos [10], who highlighted the multivaluedness of the overturning spectrum. The response to a rectangular pulse was further analyzed by Makris and Vassiliou [32], who noted that the rectangular pulse having the strongest overturning potential among all types of pulse excitations, can be considered to determine the minimum slenderness required (for a given size) for pulselike ground motions considered therein. They derived the size-slenderness relationship as a function of

the excitation characteristics of the rectangular pulse assuming that the velocity required to overturn the block at rest is the same as that required to overturn it from any rotation. The derivation given in Makris and Vassiliou [32] is revisited below without any assumption on the required velocity to overturn the block.

2.7.1 Stability of slender rectangular blocks subjected to rectangular pulse excitation

We proceed by examining the free-rocking response of a block (just after the expiration of a rectangular pulse) as it rotates from $\theta(t) = \theta_t$ and $\dot{\theta}(t) = \dot{\theta}_t$ to a point where it teeters on the edge of overturning, where $\theta = \alpha$ and $\dot{\theta} = 0$. Equating the change in potential energy, $mgR[1 - \cos(\alpha - \theta_t)]$, to the change in kinetic energy, $I_o\dot{\theta}_t^2/2$, leads to the minimum velocity required (referred to hereinafter as the *overturning velocity*) to bring a rigid body from any rotation θ_t to overturning as

$$\dot{\theta}_t = p\sqrt{2[1 - \cos(\alpha - \theta_t)]} \tag{2-41}$$

Considering a slender block and applying small angle approximation leads to the overturning velocity at any rotation θ_t as

$$\dot{\theta}_t = p(\alpha - \theta_t) \tag{2-42}$$

The response of a rectangular slender block to a rectangular acceleration pulse for positive rotation with amplitude a_p, was shown by Housner [5] to be:

$$\frac{\theta}{\alpha} = \left(\frac{a_p}{\alpha g} - 1\right)(\cosh pt - 1) \tag{2-43}$$

Housner [5] observed that "for each α, there is a time [pulse duration, T_p] during which the acceleration can generate velocity sufficient to overturn the block." Equating the velocity in

Equation (2-42) at the expiry of the rectangular pulse of duration T_p, with that obtained from Equation (2-43) at time T_p leads to

$$pT_p = -\ln\left(1 - \frac{\alpha g}{a_p}\right) \tag{2-44}$$

It is evident from Equation (2-44) that infinite size ($p = 0$) is required to maintain stability for zero slenderness ($\alpha = 0$). With mathematical manipulation, Equation (2-44) leads to the following expression, given as Equation (9) in [5],

$$pT_p = \cosh^{-1}\left(1 + \frac{1}{2\frac{a_p}{\alpha g}\left(\frac{a_p}{\alpha g} - 1\right)}\right) \tag{2-45}$$

For an infinite size block ($p \to 0$), Equation (2-44) leads to an acceleration pulse with infinite amplitude. The minimum slenderness required for rectangular pulse excitations is obtained from Equation (2-44) as

$$\alpha_{min} = \frac{a_p}{g}(1 - e^{-pT_p}) \tag{2-46}$$

While this expression for the minimum slenderness was hypothesized in [32] based solely on dimensional and physical arguments, it is derived herein formally based on the exact solution of a slender rocking block subjected to rectangular pulse excitation.

2.7.2 Stability of slender rectangular blocks subjected to half-sine pulse excitation

The response of a slender rocking block to the half-sine pulse excitation $-a_p \sin(\omega_p t + \Psi)$, where, $a_p \sin\Psi = g \sin\alpha$, was presented by Housner [5] and confirmed by Makris and Roussos [10] as

$$\frac{\theta-\alpha}{\alpha}=\frac{1}{1+\left(\frac{\omega_p}{p}\right)^2}\left[\frac{\omega_p}{p}\frac{\sinh pt}{\tan\Psi}-\left(\frac{\omega_p}{p}\right)^2\cosh pt-\frac{\sin\left(\omega_p t+\Psi\right)}{\sin\Psi}\right] \tag{2-47}$$

Housner [5] assumed overturning at the end of the half-sine pulse and obtained the size-slenderness relationship leading to overturning. However, similar to what was observed by Housner [5] for a rectangular pulse excitation, overturning occurs when the block attains sufficient velocity (Eq. (42)) at the end of the pulse, during free vibration [10]. Obtaining the velocity, $\dot{\theta}_t$, from the above equation and equating it with Equation (2-42) leads to

$$\left(\cos\Psi-\frac{\omega_p}{p}\sin\Psi\right)\left\{\sinh\left[\frac{p}{\omega_p}(\pi-\Psi)\right]+\cosh\left[\frac{p}{\omega_p}(\pi-\Psi)\right]\right\}+1=0 \tag{2-48}$$

This equation is the same as Equation (3.8) derived in Makris and Roussos [10]; however, the approach adopted here is more straightforward. Substituting $\sin\Psi=\alpha g/a_p$ and $\tan\Psi=\alpha g/\sqrt{a_p^2-(\alpha g)^2}$ in Equation (2-48) leads to the following implicit relationship between $\alpha g/a_p$ and ω_p/p,

$$\frac{\omega_p}{p}=\frac{a_p}{\alpha g}e^{-\frac{p}{\omega_p}\left[\pi-\sin^{-1}\left(\frac{\alpha g}{a_p}\right)\right]}+\frac{\sqrt{a_p^2-(\alpha g)^2}}{\alpha g} \tag{2-49}$$

Equation (2-49) is a result of linear approximation for a slender block and does not correctly predict the required value of p, for a given α, in comparison to the non-linear solution of Equation (2-1). An approximate equation was given by Makris and Roussos [10]:

$$\frac{a_p}{\alpha g}=1+\frac{1}{2}\frac{\omega_p}{p} \tag{2-50}$$

From observation of Figure 4 in [10] and from results of the nonlinear analysis carried out in this study, it was found that for $\omega_p/p > 0.32$, the digit '1' in Equation (2-50) can be replaced by 0.84 to more accurately approximate the non-linear solution for slender rectangular blocks. Thus, the required p to maintain stability for any half-sine pulse excitation, expressed as p_{Req}, leads to the following expression:

$$p_{Req} = \frac{\omega_p}{2\left(\frac{a_p}{\alpha g} - 0.84\right)}, \qquad \text{for } \omega_p > 0.32p \tag{2-51}$$

Similar to the observation made based on Equation (2-44), the above equation also leads to the fact that, for $\alpha = 0$, infinite size ($p = 0$) is required to maintain stability.

2.8 Response of Rocking Frames to Pulse Excitations

In this study, the stability of top-heavy rocking frames is compared to that of solitary piers by considering five examples: three with rectangular piers and two with trapezoidal piers. Equivalent block parameters given in [3] are utilized to obtain the response of rocking frames. Table 2-3 lists parameter values for three rectangular prismatic solitary piers along with characteristics of rectangular and half-sine acceleration pulse excitations. Table 2-3 also gives the expected stability response based on Equations (2-44) and (2-51) for rectangular and half-sine pulse respectively. Example 1 consists of a typical pier ($2h = 3$ m), as one of the frames evaluated by Dar et al. [4]. Example 2 is inspired by the size of the bridge pier in Beck and Skinner [37], and Example 3 is the same rocking frame as that considered by Makris and Vassiliou [3]. Table 2-4 provides details of two types of trapezoidal piers for the rocking frame shown in Figure 2-1(b), having the idealized geometry shown in Figure 2-7(b), as well as details of the pulse excitations. This section considers

the first two examples of frames with rectangular piers from Table 2-3 and the two examples of frames with trapezoidal piers from Table 2-4.

For a given frame, there are two independent parameters that represent the top loading characteristics: η and q. This study considers practical values observed in examples drawn from the field and the literature, with η taken as 0 and 1 with a relatively smaller value of q for narrow piers, whereas for wide piers, a larger variation in η is feasible with a large value of q. Table 2-5 gives details of rocking frames consisting of the pier in Example 1 (Table 2-3) with $q = 0.75$, for two boundary conditions, $\eta = 0$ and $\eta = 1$, along with the excitation pulses and the 'Expected Stability Response', while Table 2-6 provides similar details for Example 2 with $q = 4$ for several values of η, including $\eta = \eta_{cr}$.

The maximum value of p required to survive the prescribed pulse excitation, obtained from Equation (2-44), is denoted as p_{Req} in Table 2-3, Table 2-5, and Table 2-6, for the applicable slenderness parameters, α or α_{eq}, depending on the position of the top mass on the pier. The normalized size parameter, p_{eq}/p_{Req}, representing the ratio between the available size versus what is required to maintain stability, is also given in Table 2-3, Table 2-5, and Table 2-6. Thus $p_{eq}/p_{Req} < 1$ would mean expected stable response because the parameter p is inversely proportional to size. The actual (as compared to expected) response to excitation is obtained by solving Equation (2-1). Overturning instability is assumed to occur when $\theta/\alpha_{eq} > 1$.

2.8.1 Response of rocking frame of Example 1 to pulse excitations

The rocking frame of Example 1 is subjected to the base excitations given in Table 2-3: a rectangular acceleration pulse with amplitude $a_p = 1.5g \tan\alpha$ and duration $T_p = 0.45$ s, and half-sine pulse excitation with $a_p = 1.5\ g \tan\alpha$ and $\omega_p = 4.418$ rad/s. As seen in Table 2-3 for the

solitary pier of Example 1, since the parameter p is less than its maximum required value ($p_{eq}/p_{Req} < 1$), for both pulses, a stable response is expected. Figure 2-11(a) and (b) show no overturning and hence confirm the expected response to be stable for the solitary pier of Example 1. For the equivalent rocking block of a frame with the top mass at the corner ($\eta = 1$), in Table 2-5, the slenderness remains unaffected, and because $p_{eq}/p_{Req} < 1$, stable response is expected for both types of pulse excitations. The curves denoted as '$\eta = 1$ Corner' in Figure 2-11 (a) and (b) confirm this observation. In contrast, for the top central mass ($\eta = 0$) condition, as given in Table 2-5, $p_{eq}/p_{Req} > 1$ and overturning is expected without any impact. Figure 2-11 (a) and (b) indeed confirm overturning for $\eta = 0$. For the limiting case (with $p = p_{Req}$) the response should be marginally stable, i.e., the equivalent block would be on the verge of overturning. The curves denoted as '$\eta = 0$ Central Req' in Figure 2-11 (a) and (b) confirm this observation.

The above observations demonstrate that the stability of the rocking frame can be predicted by simply comparing the size of the equivalent rocking block with that of the size required to survive excitation for rectangular and half-sine pulse excitations. From the observations, it is concluded that the combination of slenderness and size required for a stable response depends on the type of excitation and the eccentricity.

2.8.2 Response of rocking frame in Example 2 to pulse excitations

As proof of concept, Makris and Vassiliou [3] investigated the response of a freestanding rocking bridge bent with dimensions typical of those of highway overpasses and other bridges in Europe and the USA with deck-to-pier mass ratio of $q = 4$. Although the response of modern bridges (whether made of steel or reinforced concrete) is not described by pure planar rocking, existing historical bridges with masonry piers may experience this type of response. The rocking

frames shown in Figure 2-4 can be considered as idealized representations of rocking bridges with rigid decks. The weight of the deck is transferred to the top of the piers through bearings that are generally located close to, but not exactly at, the top pier corners (Figure 2-4 (c) or (d)). The piers are likely to be very slender in the longitudinal direction of the frame but less slender in the transverse direction. Hence, as shown in Figure 2-4 (d), in the longitudinal direction the top mass may be transferred at the center of the piers, while in the transverse direction it may be transferred somewhere between the corner and the center. In the transverse direction, the assemblage of a pier with the top deck (assumed rigid) would be more similar to the stack of two rocking blocks [23,24], which is beyond the scope of this study. However, the idealized configuration of a bridge (assuming a rigid deck) in the longitudinal direction is fundamentally that of a series of rocking piers with the deck on top, which is the focus of this study. The location of bearings is represented by η.

For the rocking frame in Example 2, various values of eccentricity are considered, resulting in different equivalent size and slenderness values, as listed in Table 2-6, subject to rectangular pulse ($a_p = 1.5g\tan\alpha$ and $T_p = 2$ s) and half-sine pulse ($a_p = 1.5g\tan\alpha$ and $\omega_p = 0.981$ rad/s) excitations. Figure 2-12 shows the responses of the equivalent blocks for various values of η to the two pulse excitations. As shown in Figure 2-12 (a) and (b), the peak response of the equivalent block with the maximum eccentricity ('$\eta = 1$ Corner') is less than that of the solitary block ('Solitary') implying that the top-heavy rocking frame is more stable than a solitary pier. However, as the eccentricity reduces, the response increases. In Table 2-6, critical eccentricity is given as 0.698 (~0.7), meaning that for $\eta > 0.698$, the contribution of the coefficient of restitution to the reduction in response is greater than that for $\eta < 0.698$. It is observed in this case that $\eta = 0.8$ is approximately the eccentricity threshold where the peak response of the equivalent block is almost

the same as that of the solitary pier. For $\eta = 0$, the equivalent block overturns. In this example also, as seen in others, the size of the equivalent block for $\eta = 0$ is smaller (larger p) than what is required by the excitation resulting in overturning in both cases. The response on the verge of overturning, denoted as '$\eta = 0$ Central Req' for the parameter p_{Req}, is shown in Figure 2-12 (a) and (b).

2.8.3 Response of rocking frame with trapezoidal piers to pulse excitations

Geometrical parameters of the two cases of trapezoidal piers (with ϕ = 0.25 and 0.5) given in Table 2-4, supporting a turbine rotor as shown in Figure 2-1(b) (and schematics in Figure 2-7(b)), are calculated by utilizing the relationships given in Table 2-1. Equations (2-44) and (2-51) are not applicable to stocky piers and hence the expected responses are not reported in Table 2-4. Turbine rotors are much heavier than their supporting pedestals leading to large values of q (between 10 and 20). Also, it is assumed here that shear keys are present at the pivot points of the piers, preventing sliding from occurring. The normalized response of equivalent rocking blocks to such rocking frames is obtained for the square and half-sine pulse excitations detailed in Table 2-4, for, ϕ = 0.25 and 0.5, q = 10 and 20, and $\eta = \phi,\ 0.8\phi, 0.5\phi$, and 0. In Figure 2-13, the top and bottom rows show the normalized responses of piers with $\phi = 0.25$ and 0.50, respectively, to the pulse excitations, arranged in two sets of columns pertaining to rectangular-pulse excitation on the left and half-sine pulse excitation on the right. Each set of columns contains responses for $q = 10$ on its left and $q = 20$ on its right side. The coefficient of restitution, e_G, for the stocky (large α) solitary piers given in Table 2-4, comes out to be negative and hence is considered as zero. However, for the loaded frame, with $q = 10$ or 20, even with the maximum value of η ($= \phi$), the equivalent block becomes slenderer than the solitary one and hence its coefficient of restitution,

obtained from Equation (2-38), is finite. Therefore, as can be seen in Figure 2-13, for both types of pulse excitations, the rocking response of the solitary piers is entirely suppressed after the first impact, but the loaded piers (that do not overturn) sustain rocking motion, albeit due to a small coefficient of restitution in all cases the response decays very quickly. The response shown in Figure 2-13 demonstrates that a top-heavy frame with trapezoidal piers is less stable than a solitary pier even for the maximum value of η considered. The normalized response in the bottom row is lower than that in the top row for all cases of η and both types of excitations. Thus, the increase in ϕ, i.e., the pier shape being closer to rectangular, leads to greater stability of the frame. Increasing q tends to have a minimal effect in the response for larger values of η, but for low η there is a marked increase in response with increasing q, leading to overturning.

2.8.4 Variation of η over q and ϕ

In all examples considered in this section, it is observed that the rocking frames are the least stable for $\eta = 0$ and the most stable for $\eta = 1$, or ϕ (in the case of trapezoidal piers), for all cases of q: 0.75, 4, 10 and 20. These examples demonstrate that the responses of top heavy frames follow similar trends with variation in η for all values of q

2.9 Response of Eccentrically Loaded Rocking Frames to Earthquake Excitations

The rocking response of eccentrically loaded rocking frames analyzed as equivalent rocking blocks, subjected to various earthquake ground motions was obtained by solving Equation (2-1). Table 2-7 shows the earthquake records considered in this study. Since η varies between 0 and 1, each value of η for a rocking frame with a given q leads to a unique combination of α_{eq} and p_{eq}, obtained from the expressions in Table 2-2.

2.9.1 Indirect influence of η on the peak response to earthquake excitation through size, slenderness parameter and coefficient of restitution

Figure 2-14(a) shows the variation in the normalized parameters p_{eq}/p and α_{eq}/α with η for the pier of Example 2 in Table 2-3 and with $q = 4$. At $\eta = 0$, p_{eq} attains a maximum (i.e., minimum size), and α_{eq} attains a minimum; hence, as observed in Section 2.8, the response of the equivalent rocking block is expected to be the largest in comparison to that for all other values of η. However, as seen below, this is not always the case. This is because of two reasons: (1) The coefficient of restitution increases with increasing q for $\eta < \eta_{cr}$ (given in the fourth row of Table 2-6) but decreases with increasing q for $\eta > \eta_{cr}$, and (2) The earthquake records do not follow predictable variation over time in terms of amplitude and/or frequency and hence any closed form solution to predict the response (e.g., equations in Section 2.7) is inapplicable. The loss of energy decreases with decreasing η, when $\eta < \eta_{cr}$.

Figure 2-14 (b) shows the variation in the coefficient of restitution, E_{eq} (Table 2-2) for Example 2 in Table 2-3. Also shown is the coefficient of restitution for a solitary pier (horizontal line), obtained from Equation (2-2) and denoted as $e(\alpha)$. As discussed earlier, and shown in Figure 2-14 (b), at η_{cr}, $e(\alpha) = E_{eq}$. The graph shows that the curve $e(\alpha_{eq})$, i.e., Eq. (2) using α_{eq} , deviates from E_{eq}, illustrating that it is not appropriate to merely use α_{eq} in Eq. (2) to obtain the coefficient of restitution to sustain pure rocking. For $\eta = 1$, $e(\alpha_{eq}) = e(\alpha)$, which is not correct, as demonstrated by Makris and Vassiliou [3]. The decrease in E_{eq} (increase in energy loss) for $\eta > \eta_{cr}$ also contributes to the decrease in response at $\eta = 1$.

Figure 2-14 (c) shows the response of the equivalent block in Example 2 to the 1971 San Fernando PCD 164 record. It is seen that for $\eta = 1$ the peak response of the equivalent block is

less than that of the solitary pier, but for $\eta = 0.8$ and 0.4 the peak responses of the equivalent block and solitary pier are close to one another. For $\eta = 0$ the peak response of the equivalent block is significantly larger than that of the solitary pier, but the maximum peak response is obtained for $\eta = 0.2$. Thus, this section concludes that, at $\eta = 0$, the response to an earthquake excitation may not necessarily be the maximum unlike that for the pulse excitations observed in Section 2.8. However, if the coefficient of restitution is considered to be equal to that of the solitary pier regardless of η (instead of the value for E_{eq} from Table 2-2), Figure 2-14 (d) shows that the peak response is maximum for $\eta = 0$ and minimum for $\eta = 1$.

2.9.2 Peak response of rocking frames to earthquake records

In order to study the impact of η on the response of a rocking frame, the peak normalized response (θ/α_{eq}) of the equivalent rocking block is obtained for various values of η (varying from 0 to 1 with an increment of 0.02) for different earthquake motions. Figure 2-15 shows θ/α_{eq} for the equivalent block of the rocking frame in Example 1 of Table 2-3 with $q = 0.75$ subjected to four earthquake records: San Francisco, Helena, Alaska and Napa Valley, ordered with increasing PGA from left to right. Overturning is assumed to occur when $\theta/\alpha_{eq} = 1$, although it is known that a rocking block may survive normalized rotation $\theta/\alpha_{eq} > 1$ [38]. The response of the solitary pier (i.e., without any top mass) is shown as the solid grey horizontal line. As can be seen, although the solitary pier response increases with the PGA (from left to right) up to the third graph, it decreases in the fourth one. This is in agreement with the observations made in [25] that there is no strong correlation between the peak response of the solitary pier and the PGA. The normalized response of the rocking frame tends to increase with decreasing η. For the San Francisco record, the normalized response of the pier with the top corner mass ($\eta = 1$) is less than that of the solitary

block, but for nearly all other values of η, it is not so. For $\eta = 0.94$, i.e., only with 6% variation in eccentricity, the response is more than that of a solitary pier. This behavior demonstrates that, generically, the 'top-heavy' frames (even with a low value of $q = 0.75$) are not necessarily more stable than the solitary pier except for η close to 1.0. For the Helena record, the rocking frame is more stable than the solitary pier for $\eta > 0.4$, with a single exception at $\eta = 0.42$. In this graph, for $\eta < 0.18$, the rocking frame is in all cases less stable than the solitary pier. For the Alaska record, the response of the rocking frame is less than that of the solitary pier at $\eta = 1$ but increases with decreasing η, resulting in overturning in the range $0.3 < \eta < 0.7$. For the Napa Valley record, the rocking frame overturns in the majority of cases with few exceptions. However, the response for those exceptions follows an increasing trend with decreasing η.

Figure 2-16 shows the normalized response of the rocking frames corresponding to Examples 2 and 3 in Table 2-3, with $q = 4$, for the Imperial Valley, Parkfield, Erzincan, Loma Prieta, Northridge, and San Fernando records, in increasing order of PGA from left to right. The top and bottom rows show the responses for the rocking frames of Example 2 and 3 respectively. As seen in both the rows, the response of the solitary pier and of the rocking frame, again, do not follow a consistent trend with increasing PGA. For all records (both rows), the response of the rocking frame is lower than that of the solitary pier for large values of η, but it is higher for small values of η except in three cases in the bottom row (3rd, 4th, and 5th columns) where the solitary block overturns (the grey horizontal line is not shown, as the response exceeds the graph limits). Out of these three cases, the response to the Erzincan and Loma Prieta records exhibit some peculiar characteristics that are discussed below.

In both rows, the responses of the rocking frames exhibit an increasing trend with reduction in η except for the Erzincan record in the bottom row (3rd column), where, the peak normalized

response demonstrates an increasing trend with decreasing η up to $\eta = 0.64$ and thereafter it starts decreasing with decreasing η reaching its minimum at $\eta = 0.34$, for which the response is even lower than that for $\eta = 1$. This exception to the general trend of decreasing response with increasing η showcases the sensitivity of the rocking problem to the kinematic characteristics of the ground motion, pointed out in previous studies. For example, through the concept of the *rocking spectrum*, Makris and Konstantinidis [16] demonstrated that, while there is a clear trend of decreasing rocking response with increasing block size, individual exceptions arise. Such exceptions are prominently seen in response to the Loma Prieta record in the bottom row (4^{th} column), where, despite overturning at $\eta = 0.94$, sporadic cases of stable response are visible for lower values of η. However, these exceptions do follow an increasing trend with decreasing η. This case also demonstrates the fact that even 6% reduction in η may result in a catastrophic response, while the rocking frame is stable for $\eta = 1$.

From the comparison of Figure 2-15 and Figure 2-16, it is seen that the response of top-heavy frames exhibits similar trends for low and high values of q (0.75 in Figure 2-15, and 4 in Figure 2-16) in comparison to that of a solitary pier. Thus, the behavior of a relatively lighter frame is expected to be qualitatively the same as of the heavier frame with respect to the variation in η. Also, the response of such frames is highly dependent on the location of top beam supports, as illustrated in the bottom row of Figure 2-16 for Loma Prieta record where 6% reduction in η causes a large variation in response, resulting in overturning. This shows that even if for $\eta = 1$, a stable response is obtained for a rocking frame, minor damage to the top pier corner (due to aging or some other reason) may result in overturning. This is an important observation to be considered especially while evaluating existing frames, such as Greek temples or unanchored (e.g., historic masonry) bridges. Such sensitivity of the response to η can also significantly influence the fragility

of rocking frames in a nuclear power plant. For the design of rocking frames, as shown in Figure 2-1(b) for supporting a rotor, the concept of critical eccentricity can be useful in determining the dimensions of a trapezoidal pedestal.

2.10 Conclusions

This study investigated the behavior of unanchored freestanding rocking frames, consisting of piers having uniformly distributed mass supporting a rigid beam. The effect of the boundary conditions of the contact points between the piers and the rigid beam on the response of the rocking frame was studied. The size and slenderness parameters (p_{eq} and α_{eq}) of an equivalent rocking block, the response of which is equal to that of a rocking frame, were established. Various different types of prismatic and non-prismatic vertically symmetric geometries were considered for the piers, including rectangular, trapezoidal, triangular, and cylindrical.

It was concluded that that the response of a top-heavy rocking frame is markedly affected by the location of the points that serve as pivots between the top beam and the piers when the frame is rocking. This location is characterized through an eccentricity parameter, η, which varies between 0 and 1, representing the two extremes of the contact point between the pier and beam being at the top center and the top corner, respectively. The closed form solutions for the response of an equivalent rocking block (for frames with slender piers) to rectangular-pulse and half-sine pulse base excitations were revisited, utilizing a simpler approach than the one reported in the literature. It is noted that the peak response of such equivalent blocks to the defined pulse loading depends on a combination of α_{eq} and p_{eq}. In comparison to a rectangular solitary pier (without a top beam) with slenderness α and frequency parameter p, any eccentricity other than η = 1 results in a reduction in the slenderness parameter ($\alpha_{eq} < \alpha$) but increase in size ($p_{eq} < p$) of the

equivalent block. To maintain the stability of the equivalent block whose equivalent slenderness parameter (α_{eq}) is reduced, its size has to be larger than the size required for a particular pulse excitation, i.e., $p_{eq} < p_{Req}$. Thus, the size and slenderness parameters are found to be complementary to each other.

To investigate the effect of eccentricity, η, the study further examined the normalized peak rotation of three examples of rocking frames with rectangular piers to a suite of earthquake records. It was found that the coefficient of restitution of an equivalent block depends on η, and hence its peak response to the earthquake records is influenced by the location of the top beam supports on the pier. The concept of critical eccentricity η_{cr} was introduced, below which the coefficient of restitution of an equivalent rocking block increases with increasing beam-to-pier mass ratio but decreases for $\eta > \eta_{cr}$. Rocking frames consisting of rectangular flat-top piers in full contact with the top rigid beam ($\eta = 1$) are found to be more stable than a solitary pier, confirming the observation of Makris and Vassiliou [3]; but rocking frames are found to be less stable than the solitary piers as the bearing points move inward toward the centerline ($\eta = 0$) of the pier. The peak response is influenced by the combination of the size and slenderness parameters along with the coefficient of restitution of the equivalent rocking block representing the frame. How the sensitivity of the response of rocking frames to η affects the fragility of the frame can be a subject of future research. Piers that are vertically unsymmetrical or wider at the top in comparison to their base are beyond the scope of this paper and left for future investigation.

2.11 Acknowledgments

The authors acknowledge Bruce Power for providing resources to write this paper as a part of the first author's academic program at McMaster University. The partial support of the Natural

Sciences and Engineering Research Council of Canada (NSERC) is acknowledged. The opinions and conclusions expressed in this paper are of the authors and do not reflect the official position of Bruce Power or NSERC.

2.12 References

1. Drosos V, Anastasopoulos I. Shaking table testing of multidrum columns and portals. *Earthquake Engineering and Structural Dynamics* 2014;**43**(11):1703-23.
2. Vassiliou MF, Mackie KR, Stojadinović B. A finite element model for seismic response analysis of deformable rocking frames. *Earthquake Engineering and Structural Dynamics* 2017;**46**(3):447-66.
3. Makris N, Vassiliou MF. Planar rocking response and stability analysis of an array of free-standing columns capped with a freely supported rigid beam. *Earthquake Engineering and Structural Dynamics* 2013; **42**(3):431-449.
4. Dar A, Konstantinidis D, El-Dakhakhni WW. Impact of slenderness on the seismic response of rocking frames in Ontario nuclear power plants. *5th International Structural Specialty Conference,* London, Ontario, Canadian Society for Civil Engineering, 2016.
5. Housner GW. The behavior of inverted pendulum structures during earthquakes. *Bulletin of the Seismological* Society of America 1963; **53**(2):403–417.
6. Aslam M, Scalise DT, Godden WG. Earthquake rocking response of rigid bodies. *Journal of the Structural Division* 1980; **106**(2):377-392.
7. Spanos PD, Koh AS. Rocking of rigid blocks due to harmonic shaking. *Journal of Engineering Mechanics* 1984;**110**(11):1627-1642.
8. Konstantinidis D, Makris N. The dynamics of a rocking block in three dimensions. Proc., *8th Hellenic Society for Theoretical and Applied Mechanics Int. Congress on Mechanics*, Hellenic Society for Theoretical and Applied Mechanics, Athens, Greece, 2007.
9. Yim CK, Chopra A, Penzien J. Rocking response of rigid blocks to earthquakes. *Earthquake Engineering and Structural Dynamics* 1980; **8**(6):565–587.
10. Makris N, Roussos Y. *Rocking response and overturning of equipment under horizontal pulse-type motions*, Report No. 1998/05. Berkeley, 1998.
11. Shao Y, Tung C. Seismic response of unanchored bodies. *Earthquake Spectra* 1999; **15**(3):523–536.
12. Konstantinidis D, Makris N. Experimental and analytical studies on the response of 1/4-scale models of freestanding laboratory equipment subjected to strong earthquake shaking. *Bulletin of Earthquake Engineering*, 2010; **8**(6):1457–1477.
13. Priestley M, Evison R, Carr AJ. Seismic response of structures free to rock on their foundations. *Bulletin of the New Zealand National Society for Earthquake Engineering* 1978; **11**(3):141–150.
14. Wesley DA, Kennedy RP, Richter PJ. Analysis of the seismic collapse capacity of unreinforced masonry wall structures. *Proceedings of the 7th World Conference on Earthquake Engineering,* Istanbul, Turkey, 1980.

15. American Society of Civil Engineers. *ASCE 43-05 – Seismic Design Criteria for Structures, Systems and Components in Nuclear Facilities*, Reston, 2005.
16. Makris N, Konstantinidis D. The rocking spectrum and the limitations of practical design methodologies. *Earthquake Engineering and Structural Dynamics* 2003; **32**(2):265–289.
17. Dar A, Konstantinidis D, El-Dakhakhni W. Requirement of rocking spectrum in Canadian nuclear standards. *Transactions, 22nd International Structural Mechanics in Reactor Technology Conference (SMiRT22)* San Francisco, CA, 2013.
18. Dar A, Konstantinidis D, El-Dakhakhni WW. Evaluation of ASCE 43-05 seismic design criteria for rocking objects in nuclear facilities. *Journal of Structural Engineering* 2016; **142**(11).
19. DeJong MJ, Dimitrakopoulos EG. Dynamically equivalent rocking structures. *Earthquake Engineering and Structural Dynamics* 2014; **43**:1543–1563.
20. Lee TH. Nonlinear dynamic analysis of a stacked fuel column subjected to boundary motion. *Nuclear Engineering and Design* 1975; **32**:337-350.
21. Ikushima, Nakazawa T. A seismic analysis method for a block column gas-cooled reactor core. *Nuclear Engineering and Design* 1979; **55**:331-342.
22. Allen RH, Oppenheim IJ, Parker AR, Bielak J. On the dynamic response of rigid body assemblies. *Earthquake Engineering and Structural Dynamics* 1986;**14**:861-876.
23. Psycharis IN. Dynamic behaviour of rocking two-block assemblies. *Earthquake Engineering and Structural Dynamics* 1990; **19**:555-575.
24. Spanos PD, Roussis PC, Nikolaos P. Dynamic analysis of stacked rigid blocks. *Soil Dynamics and Earthquake Engineering* 2001; **21**:559-578.
25. Konstantinidis D, Makris N. Seismic response analysis of multidrum classical columns. *Earthquake Engineering and Structural Dynamics* 2005; **34**:1243–1270.
26. Kounadis AN, Papadopoulos GJ, Cotsovos DM. Overturning instability of a two-rigid block system under ground excitation. *ZAMM Z. Angew. Math. Mech.* 2012; **92**(7):536 – 557.
27. Minafo G, Amato G, Stella L. Rocking behaviour of multi-block columns subjected to pulse-type ground motion accelerations. *The Open Construction and Building Technology Journal* 2016; **10**(Suppl 1: M9): 150-157.
28. Bachmann JA, Vassiliou MF, Stojadinović B. Dynamics of rocking podium structures. *Earthquake Engineering and Structural Dynamics* 2017 (in press).
29. Wittich CE, Hutchinson TC. Shake table tests of stiff, unattached, asymmetric structures. *Earthquake Engineering and Structural Dynamics* 2015; **44**(14):2425-43.
30. Wittich CE, Hutchinson TC. Shake table tests of unattached, asymmetric, dual-body systems. *Earthquake Engineering and Structural Dynamics* 2017; **46**(9):1391–1410.
31. Dar A, Konstantinidis D, El-Dakhakhni WW. Seismic response of masonry rocking frames in nuclear power plants. T*ransactions, 23rd International Structural Mechanics in Reactor Technology Conference (SMiRT23)*, Manchester,2015.
32. Makris N, Vassiliou M. Sizing the slenderness of free-standing rocking columns to withstand earthquake shaking. *Archive of Applied Mechanics* 2012; **82**(10):1497–1511.
33. Makris N, Kampas G. Size Versus Slenderness: Two Competing Parameters in the Seismic Stability of Free-Standing Rocking Columns. *Bulletin of Seismological Society of America* 2016; **106**(1):104-122.
34. Makris N, Vassiliou M. Are Some Top-Heavy Structures More Stable? *Journal of Structural Engineering* 2014; **140**(5).

35. Mathcad 15.0 [Computer software]. Parametric Technology Corporation, Needham, MA.
36. Vassiliou, M. F., Burger, S., Egger M, B., Bachmann, J., Broccardo, M., & Stojadinovic, B. The three-dimensional behavior of inverted pendulum cylindrical structures during earthquakes. *Earthquake Engineering & Structural Dynamics* 2017; **46**(14): 2261–2280.
37. Beck JL, Skinner RI. The seismic response of a reinforced concrete bridge pier designed to step. *Earthquake Engineering and Structural Dynamics* 1974; **2**:343-358.
38. Zhang, J.and Makris, N. (2001). Rocking response of free-standing blocks under cycloidal pulses, *Journal of Engineering Mechanics* 2001; **127**(5), 473-483.

2.13 Tables

Table 2-1 Normalized moment of inertia, $\boldsymbol{I_{on}}$, and coefficient of restitution, $\boldsymbol{e}$, for a vertically symmetrical rocking piers.

Parameter	Trapezoid	Triangle	Rectangle	Cylindrical
	$0 < \phi < 1$	$\phi = 0$	$\phi = 1$	
ξ	$\frac{3(1+\phi)}{1+2\phi}$	3	2	2
${}^{*}I_{on} = \frac{{r_0}^2}{R^2}$	$\frac{\sin^2\alpha}{6}\left[7+\phi^2+\frac{(1+3\phi)}{(1+\phi)}\xi^2\cot^2\alpha\right]$	$\frac{1}{6}(7+2\cos^2\alpha)$	$\frac{4}{3}$	$\frac{1}{12}(15+\cos^2\alpha)$
e	$1-\frac{2}{I_{on}}\sin^2\alpha$	$1-\frac{12}{7+9\cot^2\alpha}$	$1-\frac{3}{2}\sin^2\alpha$	$1-\frac{24\sin^2\alpha}{15+\cos^2\alpha}$

[†] r_0 is the radius of gyration of the pier about the pivot point.

Table 2-2: Equivalent block parameters for a rocking frame in this study and others.

	Vertically symmetrical piers (any geometry) This study $0 \le \eta \le 1$	Rectangular Piers ($\xi = 2$)	
		Dar et al. [4] $\eta = 0$	M&V [3] $\eta = 1$
α_{eq}	$\tan^{-1}\left(\frac{1+(1+\eta)q}{1+\xi q}\tan\alpha\right)$	$\tan^{-1}\left(\frac{1+q}{1+2q}\tan\alpha\right)$	α
λ	$\sqrt{(1+(1+\eta)q)^2\sin^2\alpha+(1+\xi q)^2\cos^2\alpha}$	$\sqrt{(1+q)^2\sin^2\alpha+(1+2q)^2\cos^2\alpha}$	$(1+2q)$
ψ	$1+\frac{q}{I_{on}}\left[(1+\eta)^2\sin^2\alpha+\xi^2\cos^2\alpha\right]$	$1+\frac{3}{4}q[1+3\cos^2\alpha]$	$(1+3q)$
R_{eq}	$\frac{\lambda}{1+q}R$	R	
I_{eq}	ψI_o	$I_o\left[1+\frac{3}{4}q(1+3\cos^2\alpha)\right]$	
p_{eq}	$p\sqrt{\lambda/\psi}$	$p\left[\frac{\sqrt{(1+q)^2\sin^2\alpha+(1+2q)^2\cos^2\alpha}}{1+\frac{3}{4}q(1+3\cos^2\alpha)}\right]^{\frac{1}{2}}$	$p\left[\frac{1+2q}{1+3q}\right]^{\frac{1}{2}}$
$E_{eq}{}^{\dagger}$	$\frac{1}{\psi}\left[e_G+\frac{q}{I_{on}}\left[\xi^2\cos^2\alpha-(1+\eta)^2\sin^2\alpha\right]\right]$	$\frac{e+\frac{3}{4}q(5\cos^2\alpha-1)}{1+\frac{3}{4}q(1+3\cos^2\alpha)}$	$\frac{e+3q\cos 2\alpha}{1+3q}$

$^{\dagger}I_{on} = {r_o}^2/R^2$, where, r_o is the radius of gyration of the pier about the pivot point.

Table 2-3: Parameters of three examples of slender solitary rectangular prismatic piers ($\boldsymbol{\xi = 2}$) and expected stability response under rectangular and half-sine pulse excitations.

Example	h (m)	b (m)	R (m)	α (rad)	p (rad/s)	e	Rectangular pulse $a_p = 1.5\,g\tan\alpha$				Half-sine pulse $a_p = 1.5\,g\tan\alpha$			
							T_p (s)	p_{Req} (Eq 2-44) (rad/s)	$\frac{p}{p_{Req}}$	Expected stability response	ω_p (rad/s)	p_{Req} (Eq 2-51) (rad/s)	$\frac{p}{p_{Req}}$	Expected stability response
1	1.5	0.145	1.507	0.096	2.209	0.986	0.45	2.441	0.90	Stable	4.418	3.347	0.66	Stable
2	30	6	30.594	0.197	0.490	0.942	2	0.549	0.89	Stable	0.981	0.743	0.66	Stable
3	4.5	0.75	4.562	0.165	1.27	0.96	-	-	-	-	-	-	-	--

Table 2-4: Parameters of solitary trapezoidal pier and pulse excitations

ϕ	ξ	ξh (m)	h (m)	b (m)	R (m)	α (rad)	p (rad/s)	e_G	Rectangular pulse		Half-sine pulse	
									a_p	T_p(s)	a_p	ω_p(rad/s)
0.25	2.5	2.4	0.96	1.5	1.781	1.001	2.092	0	$1.5\,g\tan\alpha$	0.2	$1.5\,g\tan\alpha$	8.366
0.50	2.25	2.4	1.067	1.5	1.841	0.953	2.044	0	$1.5\,g\tan\alpha$	0.2	$1.5\,g\tan\alpha$	8.177

Table 2-5: Parameters of equivalent block of Example 1 ($\boldsymbol{q = 0.75}$) and expected stability response under pulse excitations.

Top mass location	η	α_{eq} (rad)	p_{eq} (rad/s)	e_{eq}	Rectangular pulse $a_p = 1.5\ g \tan\alpha$, $T_p = 0.45$ s			Half-sine pulse $a_p = 1.5\ g \tan\alpha$, $\omega_p = 4.418$ rad/s		
					p_{Req} (rad/s)	$\frac{p_{eq}}{p_{Req}}$	Expected stability response	p_{Req} (rad/s)	$\frac{p_{eq}}{p_{Req}}$	Expected stability response
Corner	1	0.096	1.938	0.983	2.441	0.79	Stable	3.347	0.58	Stable
Center	0	0.068	1.94	0.992	1.397	1.39	Unstable	1.696	1.14	Unstable

Table 2-6: Parameters of equivalent block of Example 2 ($\boldsymbol{q = 4}$) and expected response under pulse excitations.

η	α_{eq} (rad)	p_{eq} (rad/s)	e_{eq}	Rectangular pulse $a_p = 1.5\ g \tan\alpha$, $T_p = 2$ s			Half-sine pulse $a_p = 1.5\ g \tan\alpha$, $\omega_p = 0.981$ rad/s		
				p_{Req} (rad/s)	$\frac{p_{eq}}{p_{Req}}$	Expected Stability response	p_{Req} (rad/s)	$\frac{p_{eq}}{p_{Req}}$	Expected response
1	0.197	0.408	0.925	0.549	0.74	Stable	0.743	0.55	Stable
0.9	0.189	0.4083	0.931	0.507	0.80	Stable	0.672	0.61	Stable
0.8	0.18	0.4087	0.938	0.467	0.88	Stable	0.608	0.67	Stable
$\eta_{cr} = 0.698$	0.171	0.409	0.944	0.43	0.95	Stable	0.549	0.75	Stable
0	0.111	0.411	0.977	0.231	1.78	Unstable	0.264	1.56	Unstable

Table 2-7: Details of earthquake records.

Earthquake	Year	Station	Record	PGA (g)
San Francisco, CA	1957	Golden Gate Bridge	SANFRAN/GGP100	0.112
Helena, MT	1935	Carroll College	A-HMC-270	0.173
Iniskin, AK	2016	NSMP Stn 8039,	East	0.211
Napa Valley, CA	2014	Huichica Creek	Chan 3: 90	0.293
Imperial Valley, CA	1979	117 El Cento Array #9	I-ELC180	0.313
Parkfield, CA	1966	1013 CHOLAME #2	N65E	0.476
Erzincan, Turkey	1992	Erzincan	NS	0.515
Loma Prieta, CA	1989	LGPC	LGP 000	0.563
Northridge, CA	1994	Rinaldi	RRS 228	0.838
San Fernando, CA	1971	Pacoima Dam	PCD 164	1.160

2.14 Figures

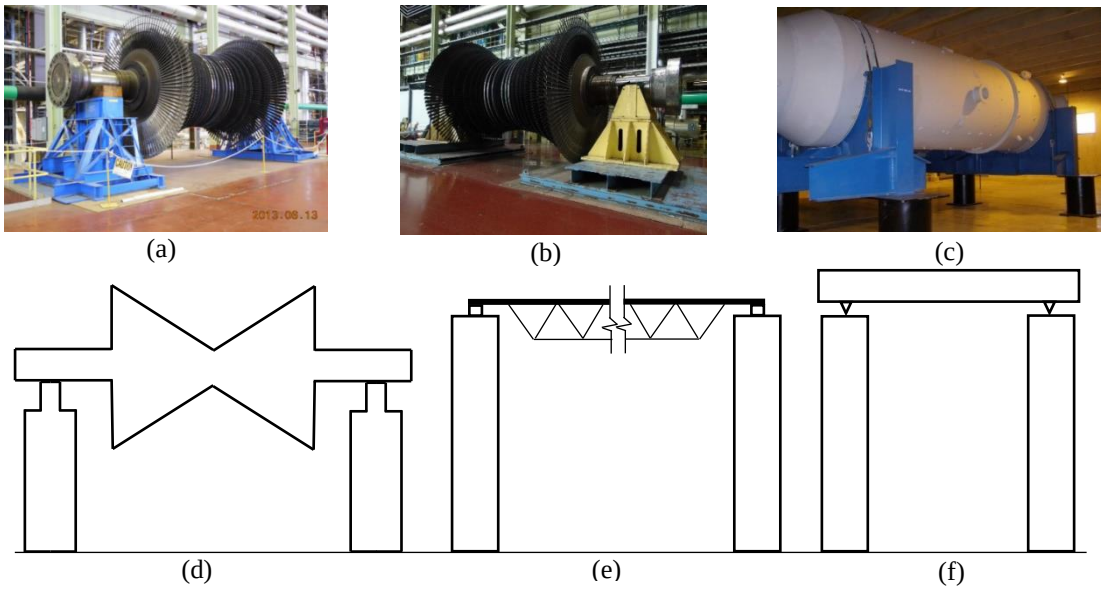

Figure 2-1: Top: examples of rocking frames in a nuclear power plant: (a) turbine rotor on trapezoidal pedestals with top stems, (b) turbine rotor on triangular pedestals, (c) steam generator in storage on cylindrical pedestals [Photo courtesy: Bruce Power, Ontario]. Bottom: schematic representations of (d) turbine rotor on rigid rectangular pedestals with top stems, (e) unreinforced masonry enclosure, (f) idealized representation of the frame in (e).

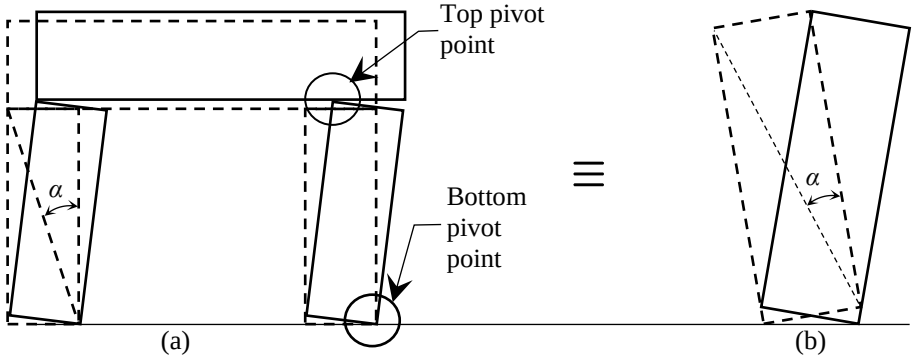

Figure 2-2: (a) Rocking frame with pivot points at the pier corners, and (b) equivalent rocking block.

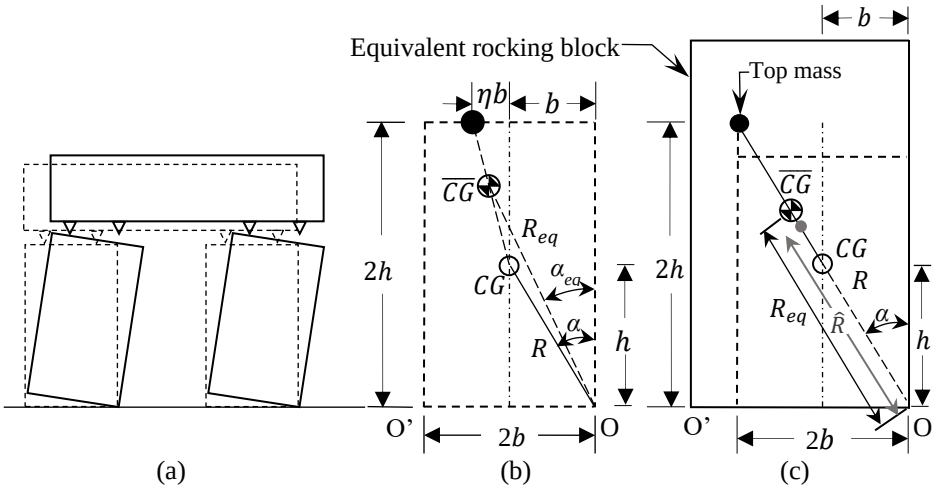

Figure 2-3 Schematics of rocking frames with unsymmetrical eccentricities (a) turbine rotor with unsymmetrical piers (b) simplified representation, and, (c) symmetrical piers

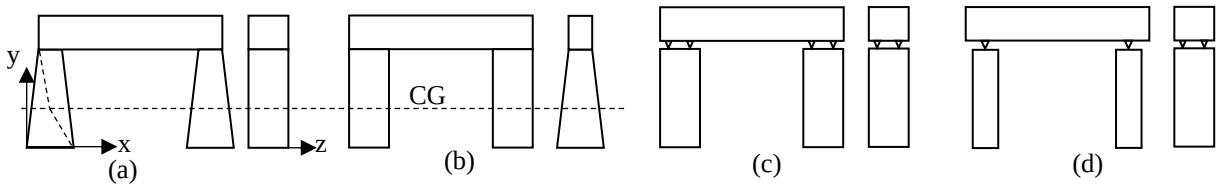

Figure 2-4 Rocking frames with top beams supported by: flat trapezoidal piers in (a) and (b); bearings on rectangular piers (similar to unanchored bridges) in (c) and (d).

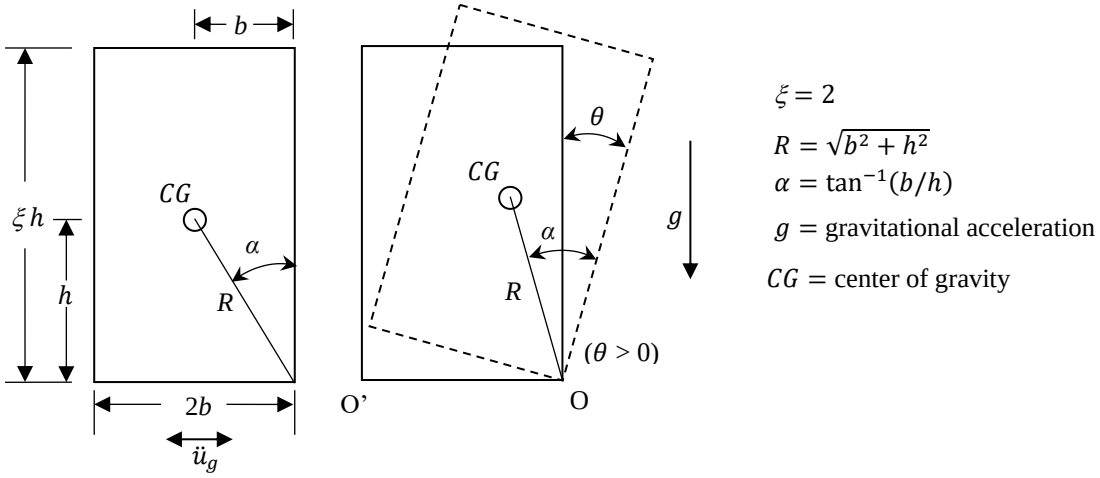

Figure 2-5 Schematic of a freestanding rigid block in rocking motion.

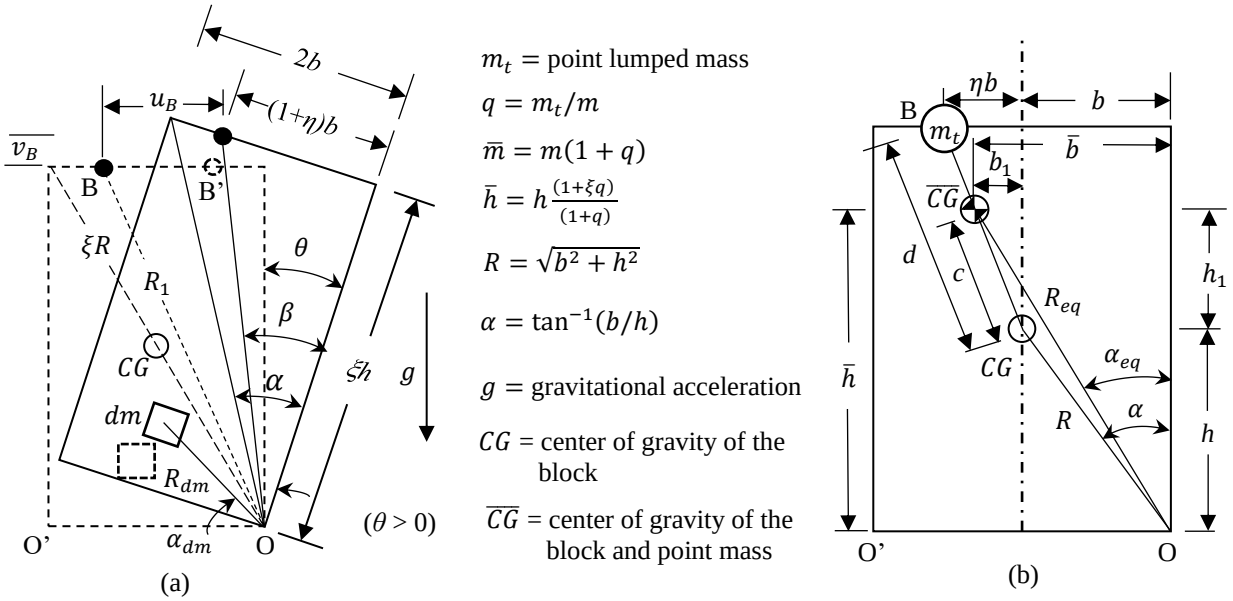

Figure 2-6 (a) Geometry of rocking pier with the top beam contact at point B for positive (and B' for negative) rotation, and (b) rocking pier with a lumped mass at B.

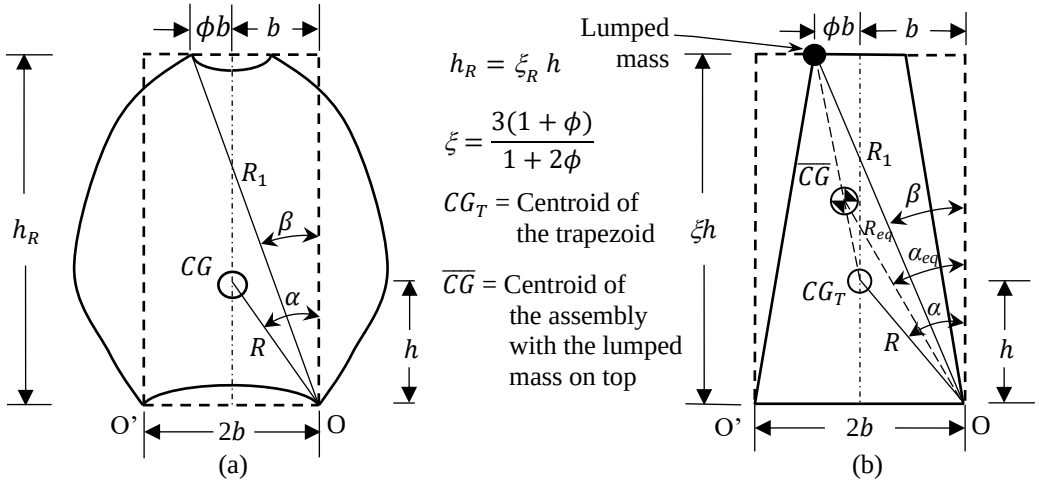

Figure 2-7 Rocking block having uniformly distributed mass, symmetrical about the vertical axis, and having wider base than top: (a) any geometry, and (b) trapezoidal shape.

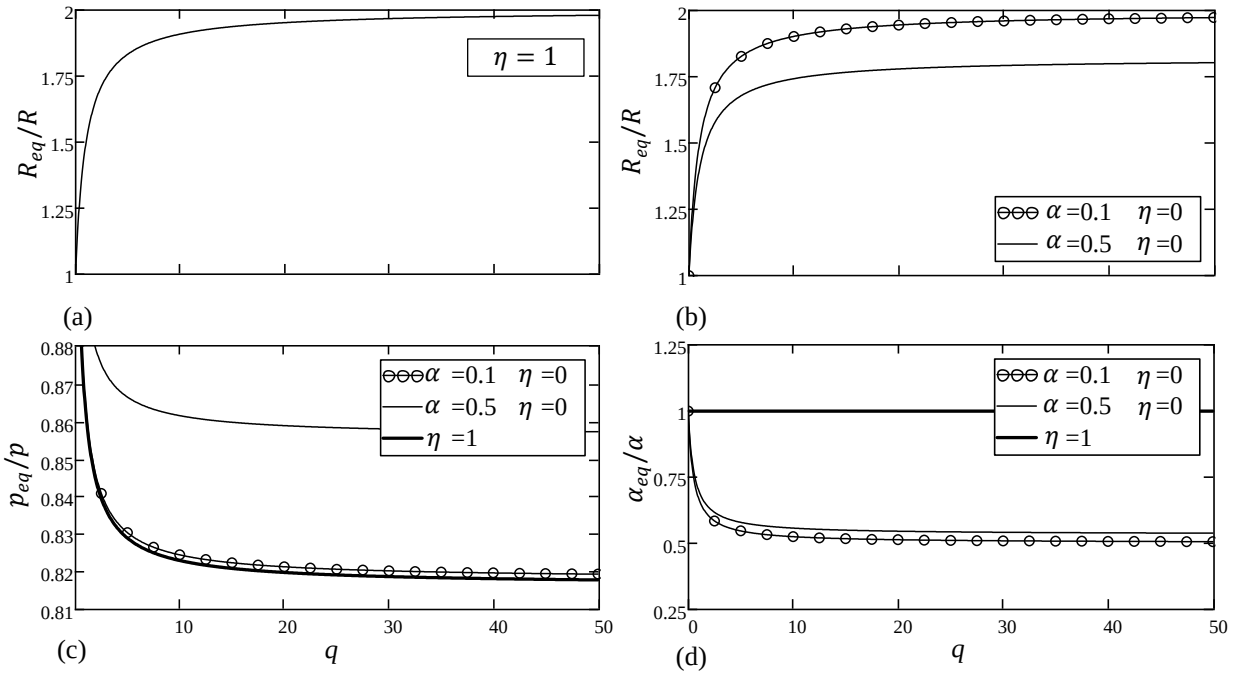

Figure 2-8 Variation of the equivalent rectangular block's parameters with mass ratio q..

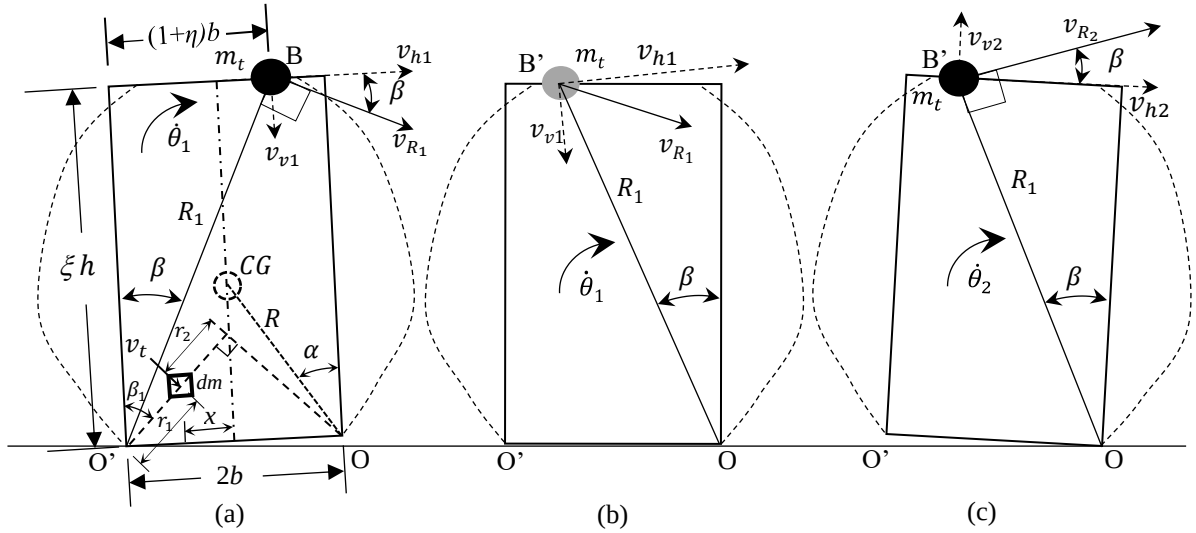

Before impact:

$v_{R_1} = R_1\dot{\theta}_1$

$v_{h1} = v_{R_1}\cos\beta = \xi h\dot{\theta}_1$

$v_{v1} = v_{R_1}\sin\beta = (1+\eta)b\dot{\theta}_1$

Just before striking point O

After impact:

$v_{R_2} = R_1\dot{\theta}_2$

$v_{h2} = \xi h\dot{\theta}_2$

$v_{v2} = (1+\eta)b\dot{\theta}_2$

Figure 2-9 Geometry of rocking pier with the lumped mass at: (a) B, before, (b) B', just before, and (c) B', after impact. An alternative vertically symmetrical geometry is shown with dotted outline.

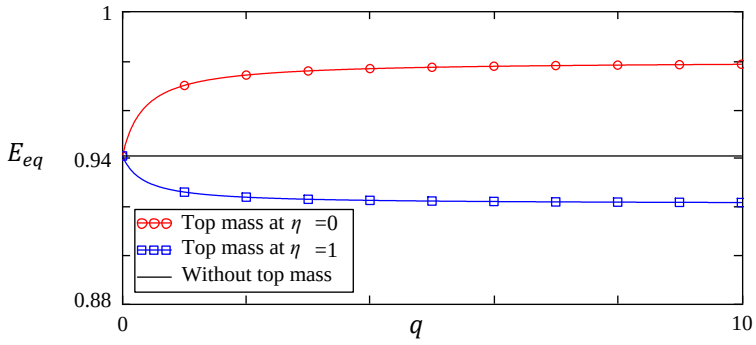

Figure 2-10 Equivalent coefficient of restitution for a rectangular pier (ξ=2) for $\alpha = 0.2$ rad.

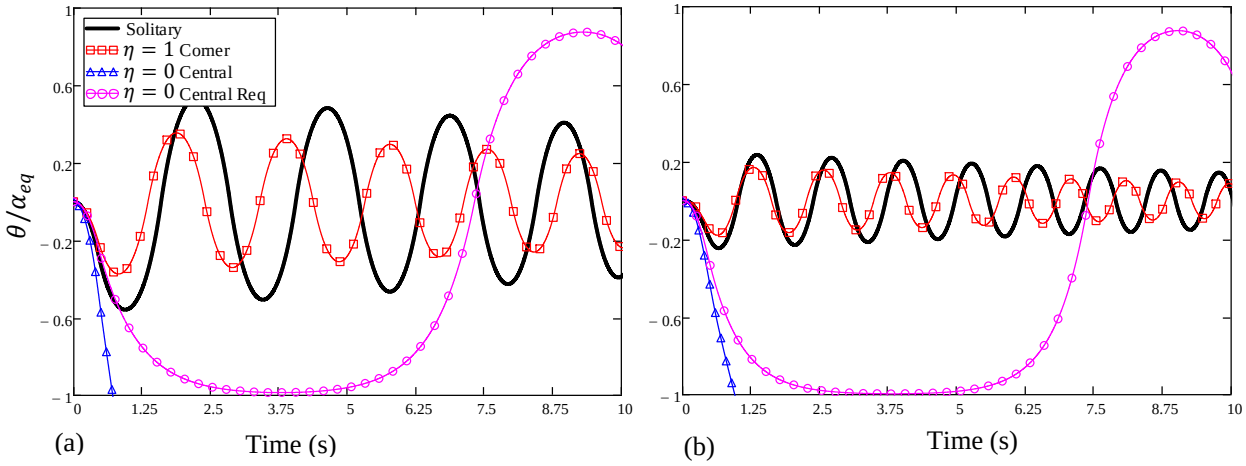

Figure 2-11 Normalized response of the rocking frame in Example 1 to pulse excitation with amplitude $a_p = 1.5\ g \tan\alpha$: (a) rectangular pulse with duration $T_p = 0.45$ s, (b) half-sine pulse with $\omega_p = 4.418$ rad/s.

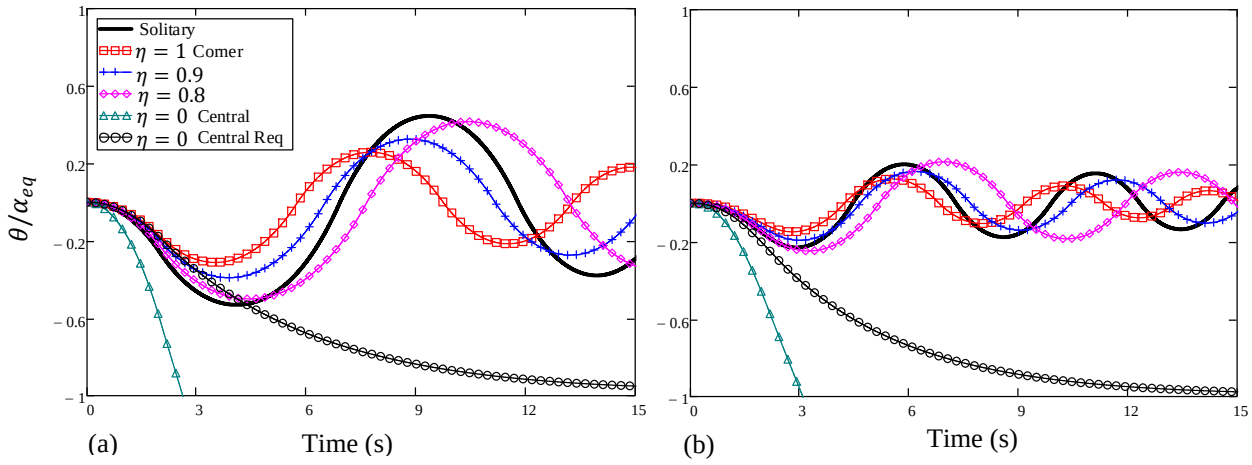

Figure 2-12 Normalized response of rocking frame in Example 2 (Table 2-6) to pulse excitation with $a_p = 1.5\ g \tan\alpha$: (a) rectangular pulse with duration $T_p = 2$ s (b) half-sine pulse with $\omega_p = 0.981$ rad/s.

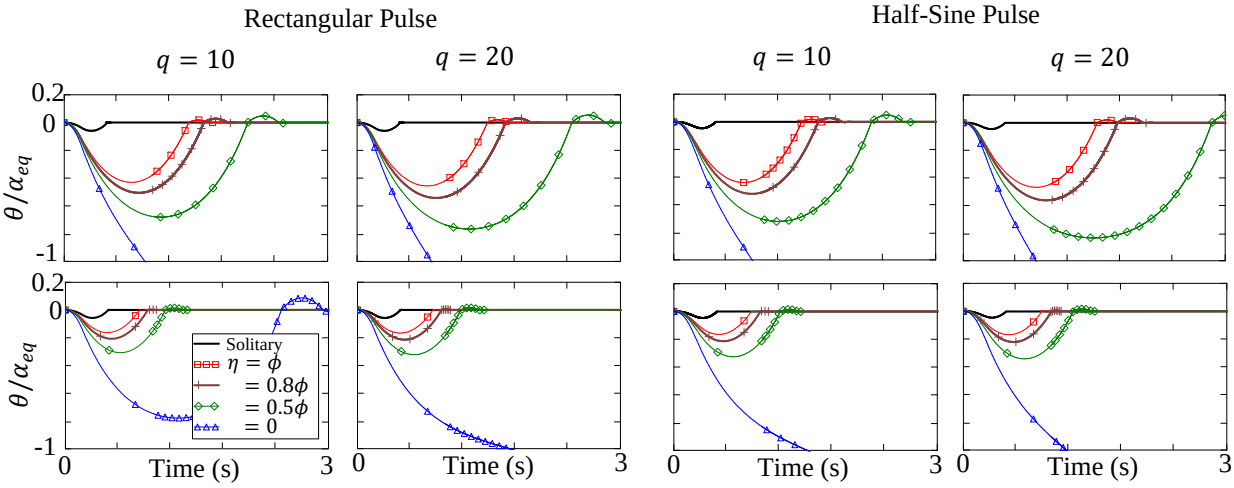

Figure 2-13 Normalized response of rocking frames with trapezoidal piers (Table 2-4), to rectangular and half-sine pulse excitations in the two left and two right columns respectively, with $q = 10$ and $q = 20$, for 3s duration. *Top row:* $\phi = 0.25$. *Bottom row:* $\phi = 0.50$

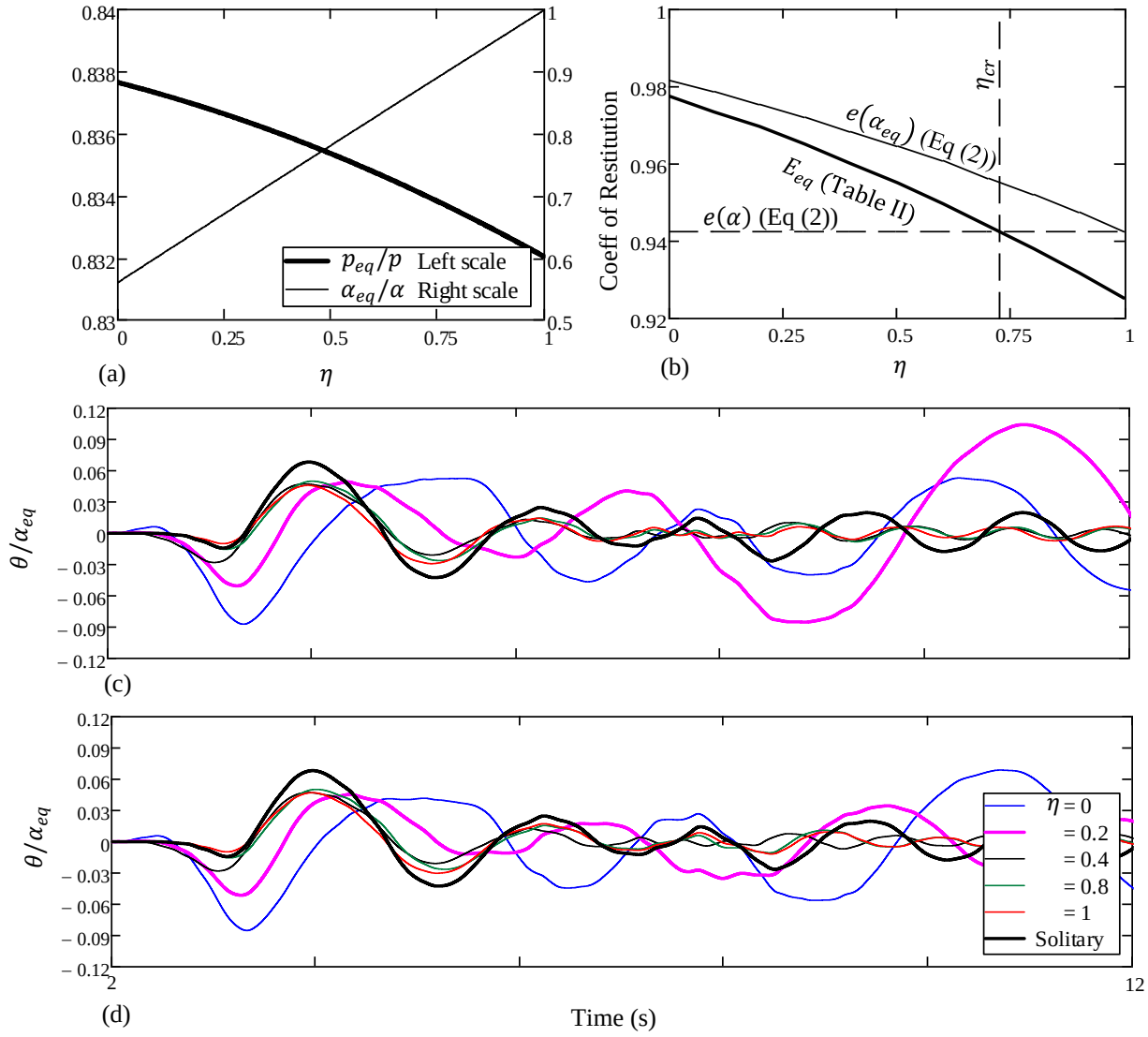

Figure 2-14 Impact of variation in η on equivalent parameters of the pier in Example 2 (Table 2-3) with $q = 4$: (a) p_{eq}/p and α_{eq}/α, and (b) coefficient of restitution. Normalized response to San Fernando PCD164: (c) with coefficient of restitution values as applicable for each η, and (d) with the same coefficient of restitution as that of the solitary pier.

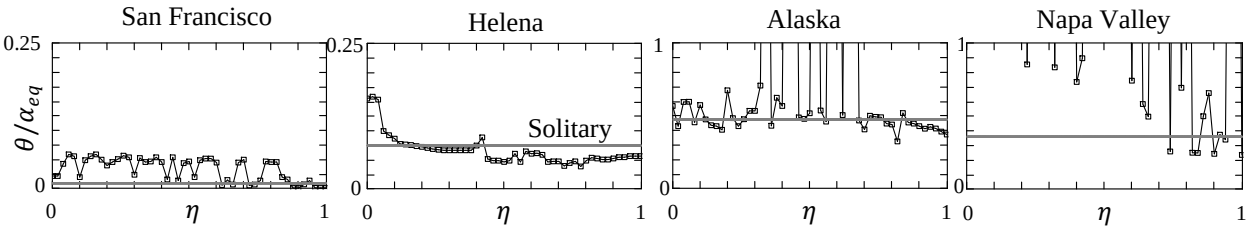

Figure 2-15 Normalized peak rotation of the rocking frame in Example 1 (Table 2-3) with $q = 0.75$ as a function of η for four earthquake records. Each point represents the peak response of the equivalent rocking block with a unique combination of p_{eq}, α_{eq}, and coefficient of restitution, E_{eq} for every η. The response of a solitary block (without any top mass) is shown as the horizontal solid grey line.

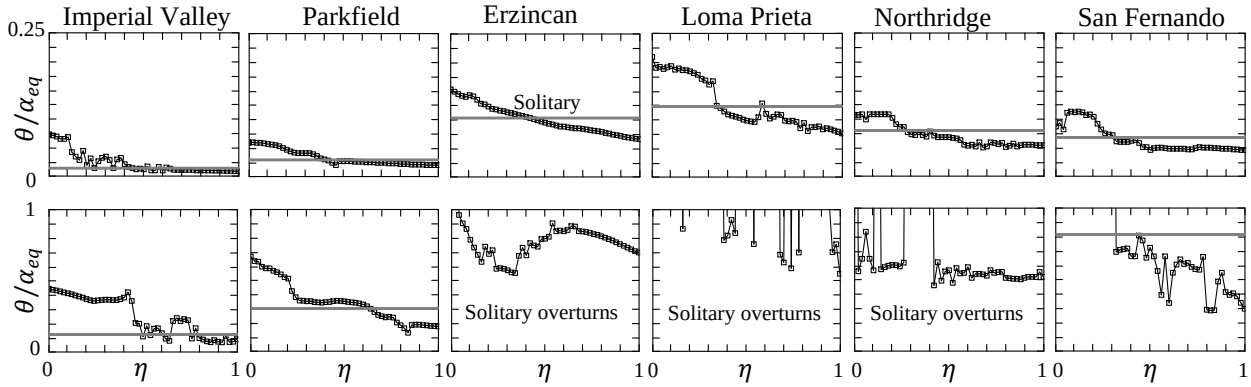

Figure 2-16 Normalized peak rotation θ/α_{eq} of the equivalent rocking block as a function of eccentricity η with $q = 4$ for Example 2 (top row) and Example 3 (bottom row) subject to various earthquake records (Table 2-7).

CHAPTER 3

DYNAMIC ANALYSIS OF TWO-PIER ROCKING FRAMES WITH ECCENTRIC TOP SUPPORTS AND BEAM ROTATION

3.1 Abstract

The seismic response analysis of a rocking frame consisting of a rigid beam freely supported by vertically symmetrical rigid piers has been studied in the literature. The stability of such rocking frames has been shown to be highly dependent on the locations of the beam-to-pier pivot points. In the case of rocking frames with equal pier heights, when the distance between the beam-to-pier pivot point and the diagonally opposite pier-to-ground pivot point is equal for the two piers; the beam does not undergo rotation during seismic excitation and this scenario is referred to in this study as *symmetrical top supports*. However, unsymmetrical top supports are common in practical applications of rocking frames, including nuclear power plants. This study focuses on practical two-pier rocking frames, where the piers are not symmetrical about their vertical axes, but there is a vertical axis of symmetry (a mirror plane) for the entire rocking frame, as a system. It is shown that the top-support eccentricity can be utilized as a manipulative tool to maintain the beam horizontal during seismic excitation by converting an unsymmetrical top support condition to a symmetrical one. For such cases, dynamic characteristics of an equivalent block whose response is the same as of the frame have been established. For the general case, it is found that the rocking frame response can be obtained by considering a combination of several equivalent blocks with time dependent dynamic characteristics. It is found that eccentricity significantly influences instability caused by excess *effective system rotation*, a concept developed in this study. Response

of frames with unsymmetrical piers to earthquake records is obtained and compared with that of a solitary unsymmetrical pier. Coefficients of restitution for an unsymmetrical pier for rotations about two opposite pivots are established. Rocking frames are utilized in nuclear power plants specially to support heavy loads. An accidental drop of such load has been reported to directly impact the nuclear risk. This study provides tools to obtain the response of rocking fames subjected to unsymmetrical support conditions that can be utilized to ascertain the seismic risk of such frames.

3.2 Introduction

The seismic interaction of unanchored components with seismically qualified systems in a nuclear power plant (NPP) can be detrimental to nuclear safety [1]. Unreinforced masonry (prone to rocking) inside a NPP has been identified as one of the major contributors to seismic risk [2] and is considered as a "conservative surrogate for concrete structures" for assessing safety because if a (200 or 300 mm thick) rocking masonry does not overturn in a seismic event, other structures fixed at the base will be safe [3]. An assemblage of unanchored objects, such as a rocking frame in a NPP, requires attention beyond that of an individual unanchored object during a seismic event [4-8]. Figure 3-1(a) and (b) show rocking frames consisting of turbine rotors (weighing ~150 Ton) freely supported by symmetrical and unsymmetrical piers respectively in a NPP. Figure 3-1 (c) to (e) show large steam generators (weighing ~100 Ton) supported by piers. Figure 3-1 (f) illustrates the geometry of a ~12m span 4 Ton man bridge resting on triangular piers beside the fuel bay in a NPP during maintenance. Figure 3-1 (g) shows an emergency power generator trailer lifted on piers while undergoing modifications. An accidental drop of heavy components such as a turbine rotor in Figure 3-1 (a) is detrimental to the life of workers and a potential cause of serious structural

damage, whereas the drop of the man-bridge into the fuel bay (Figure 3-1 (f)) may expose the spent fuel causing radiation hazard to the surroundings. As witnessed in Arkansas Nuclear One (ANO) accident [9], a heavy turbine stator was dropped while being moved from one location to the other. The investigation by the United States Nuclear Regulatory Commission (USNRC) [9] delved into the domino effect of the accident that caused not only serious structural damage but multiple events such as breach of a fire main causing flooding of electrical components resulting in tripping of another running unit. A detailed risk evaluation concluded that the core damage frequency of the entire NPP was impacted. Therefore, to ascertain nuclear risk in terms of the core damage frequency, the risk due to the fall of heavy components supported by rocking frames is required to be known. Nuclear standards, such as ASCE 43-19 [10] provide limited guidance on the analysis of an individual rocking component and no guidance on rocking assemblages. As a result, the true seismic risk of rocking frames in nuclear facilities remains unknown.

Representing a rocking frame by an equivalent rocking block is a convenient way of obtaining its response through a rocking spectrum. The seminal work by Housner [11] led to numerous studies [12-18] that examined the behavior of a rigid rocking block subjected to seismic excitation. Attempts were made since then to represent a rigid rocking block by a damped oscillator [19-20] and obtain its peak response from a response spectrum. However, such attempts have been shown to be highly unreliable when compared to results obtained by solving the nonlinear equation of motion of a rocking block [21-23].

Several studies have investigated the response of rocking assemblages. DeJong and Dimitrakopoulos [24] demonstrated the dynamic equivalency of various assemblages, including simple rocking frames, to single blocks. Dimitrakopoulos and Giouvanidis [25] presented the

equations of motion of a rocking frame with symmetrical support conditions on piers of unequal heights but without considering top support eccentricity. The authors observed that the response due to asymmetric condition is not much different from that of the symmetric frame. This observation is examined in this study and found that while it may be true for a particular case considered in [25], it cannot be generalized to all frames especially with eccentric support conditions. Diamantopoulos and Fragiadakis [26] established a finite element model based on the equation of motion presented in [6] representing a rocking frame as single-degree-of-freedom (SDOF) oscillator with negative stiffness subject to approximations accompanying an acceptable error below the slenderness threshold, $\alpha \leq 0.3$. However, the authors did not consider the impact of variation in top support eccentricity. Neither did they comment on non-slender systems. Other types of block assemblages have been studied by Lee [27], Ikushima and Nakazawa [28], Allen et al. [29], Psycharis [30], Spanos et al. [31], Konstantinidis and Makris [32], Kounadis et al. [33], Minafo et al. [34] and Bachmann et al. [35]. Shake table tests were carried out by Wittich and Hutchinson for asymmetric rocking single-body [36] and dual-body systems [37]. However, the dynamics of a rocking frame having piers of equal height with unsymmetrical top support condition has not been investigated in the literature, which is the focus of this study.

Figure 3-2 shows examples with symmetrical top support condition of a typical pier illustrated in Figure 3-2 (a) where the distances between diagonally opposite pivot points are equal ($R_1' = R_1$). Such condition is defined as *symmetrical eccentricity*, i.e., the distance of the support point from the pier center being equal on either side of the CG axis. Figure 3-2 (b) shows the rocking frame studied by Makris and Vassiliou [6]. The dashed lines depict the frame at rest, whereas the solid lines illustrate it in rocking motion towards right (positive rotation), where the beam is

supported at pier corners. The authors established the parameters of an equivalent block whose seismic response is the same as that of the frame concluding that a heavier beam frame is more stable than that a lighter one. For the rocking frame in Figure 3-2 (c), where the beam is supported at pier centers, Dar et al. [4] demonstrated that a heavier beam adversely impacts the stability for some selected earthquake records. Figure 3-2 (d) shows the rocking frame investigated by Dar et al. [5] where the support points of the beam are located in between the corners and the centers of the piers. The authors concluded that the stability of the frame highly depends on the eccentricity, as defined in Figure 3-2 (a)). For all configurations in Figure 3-2, the beam is horizontal when the frame is at rest as a result of equal pier heights; in rocking motion, the distances of the top pivot points from the bottom pivot points are equal ($R_1 = R_1'$ in Figure 3-2 (d)), leading to symmetrical eccentricity. The fundamental difference between the configuration in Figure 3-2 (b) and those in Figure 3-2 (c) and (d) is that, in the former, the center of gravity (CG) of the pier (depicted by the red dot), the top pivot point, and the bottom pivot points are collinear, whereas in the latter cases they are not. This is the reason that, in the configurations shown in Figure 3-2 (c) and (d), a heavier beam in certain cases renders the frame assembly less stable than a lighter beam, contrary to the observation by Makris and Vassiliou [6]. It is assumed that sliding does not occur in any of the configurations in Figure 3-2; therefore, the distances between the top and bottom pivot points of the piers (thick dashed grey lines, referred hereinafter as the *contact polygon*) remain invariant during the rocking motion. Also, the left and right sides of the *contact polygon*, being equal in length because of symmetry, remain parallel to each other, resulting in both piers rotating by the same angle. Consequently, the beam remains horizontal during rocking motion.

Figure 3-3 shows examples of rocking frames with unequal distances between pivot points ($R_1' \neq R_1$) leading to *unsymmetrical top support* scenario or *unsymmetrical eccentricities*. Figure 3-2 (a) shows the schematics of a turbine rotor in a NPP supported by stems (support blocks, rigidly attached to the pier as shown in Figure 3-1(b)) on top of unsymmetrical piers. The piers are unsymmetrical but the entire frame as a system is mirrored about its axis of symmetry. For simplicity, the configuration in Figure 3-3 (b) shows piers without stems. Similar to Figure 3-2, assuming no sliding, the lengths of all sides of the *contact polygon* in Figure 3-3 do not vary during rocking motion about a given set of pivot points. Upon impact, the contact polygon switches to its mirror image. Thus, rotations of all sides of contact polygon depend on one chosen generalized rotation. Therefore, such rocking frame is essentially a SDOF system. Since the left and the right sides of the contact polygon are unequal ($R_1 \neq R_1'$), the piers experience unequal rotation, causing the beam to rotate. This is similar to the planar four-bar linkage mechanism with the bottom bar being fixed, a widely studied SDOF system in engineering dynamics (e.g., O'Reilly [38]). In a preliminary study Dar et al [39] showed that in case of unsymmetrical piers, the two opposite sides of the contact polygon can be made equal to each other ($R_1 = R_1'$) by maneuvering eccentricities; thus, converting the frame into an equivalent block system. Figure 3-3 (c) shows a rocking frame in rocking motion with symmetrical piers but with unsymmetrical eccentricities, a situation reported in [7] in the context other than the NPPs. In this case, the beam experiences rotation despite the piers being symmetrical.

This study investigates the dynamic analysis of rocking frames shown in Figure 3-3 (with two mirror-image but individually unsymmetrical piers of equal height) with unsymmetrical top support condition. Response of frames with unsymmetrical eccentricities to earthquake records is

derived and compared with that of a solitary unsymmetrical pier. Since an unsymmetrical solitary pier's geometry is different in two directions of rotation, its coefficient of restitution (COR) in either direction has been established. For the unsymmetrical eccentricity condition, the COR of the frame is derived. Response to earthquake records for symmetrical and unsymmetrical eccentricities are compared. The chosen earthquake records are compatible with the seismic design basis of NPPs prescribed in the USNRC regulatory guide 1.60 [40, 41] based on the design response spectrum given by Newmark, Blume and Kapur [42].

3.3 Review of a Rocking Block

This section reviews the dynamics of a solitary rocking block. As the subject is well covered in the literature, the discussion below focuses only on highlighting aspects relevant to this study. Figure 3-4(a) shows a rigid rectangular block having uniformly distributed mass m with mass moment of inertia I_o about the pivot point O, width $2b$, height ξh, its CG at height h and distance R (hereinafter referred to as the *radius* of rotation) from the pivot point. The block is subjected to base horizontal acceleration $\ddot{u}_g$. It is assumed that the only mode or response is rocking, i.e., sliding, rock-sliding, and lift-off are excluded. Figure 3-4 (b) shows the rectangular block in positive rotation, θ, about the pivot point O. The equation of motion of the rocking block is [15]:

$$\ddot{\theta} = -p^2 \left\{ \sin[\alpha \, \mathrm{sgn}(\theta) - \theta] + \frac{\ddot{u}_g}{g} \cos[\alpha \, \mathrm{sgn}(\theta) - \theta] \right\} \tag{3-1}$$

where, $\mathrm{sgn}(\cdot)$ is the *signum* function, g is the gravitational acceleration, α is the block slenderness parameter, and $p = \sqrt{mgR/I_o}$ is the so-called frequency parameter [16]. The variable ξ is equal to 2 for the rectangular block [5] with $I_o = (4/3)mR^2$ and $p = \sqrt{3g/4R}$. The parameter, p, is also referred to as the size parameter. Larger the R, smaller is the p. Some of the examples

exhibiting the range of p in a NPP are: large heat exchangers ($p \cong 1$ rad/s) [16], electrical transformers ($p \cong 2$ rad/s) [16] and a radiation shielding block wall ($p \cong 4$).

Figure 3-4 (c) shows a non-rectangular vertically unsymmetrical block under positive rotation θ. The block has uniformly distributed mass m, base width μb, height, ξh, and its center of gravity at b and height, h, from the pivot point O, and. In this case, the frequency parameter is different for positive and negative rotations: $p_p = \sqrt{mgR/I_o}$, for $\theta > 0$, and, $p_n = \sqrt{mgR'/I_{o'}}$, for $\theta < 0$, where R' and I_o, are the radius of rotation and the mass moment of inertia respectively with respect to the pivot point O'. The equation of motion for the vertically unsymmetrical block is [39]

$$\begin{aligned} \ddot{\theta} &= -p_p^2 \left\{ \sin[\alpha - \theta] + \frac{\ddot{u}_g}{g} \cos[\alpha - \theta] \right\} \text{ for } \theta > 0 \\ \ddot{\theta} &= -p_n^2 \left\{ \sin[-\alpha' - \theta] + \frac{\ddot{u}_g}{g} \cos[-\alpha' - \theta] \right\} \text{ for } \theta < 0 \end{aligned} \tag{3-2}$$

A coefficient of restitution is utilized to account for the energy lost during the impact resulting in reduced angular velocity immediately after impact, $\dot{\theta}_2$, from that immediately before impact, $\dot{\theta}_1$. In rocking analysis, conservation of angular momentum about the new pivot point at the instants before and after the impact, leads to the value of the coefficient of restitution, e_G. For any symmetrical geometry [5],

$$e_G = \frac{\dot{\theta}_2}{\dot{\theta}_1} = 1 - \frac{2}{I_{on}} \sin^2 \alpha \tag{3-3}$$

where, I_{on} is the normalized moment of inertia ($I_{on} = I_o/(mR^2) = r_o^2/R^2$), where $r_o = \sqrt{I_o/m}$, is the radius of gyration of the block. For a rectangular block, substituting the normalized moment of inertia, $I_{on} = 4/3$, leads to the coefficient of restitution given by Housner [11].

Instability of a rocking block due to overturning occurs when $\theta/\alpha > 1$ or, $\theta/\alpha' > 1$. In other words, the overturning instability occurs when the bock's potential energy is at its maximum.

3.4 Rocking Frame with Unsymmetrical Eccentricities

Figure 3-5(a) illustrates a rocking frame with unsymmetrical piers (about their vertical axes) symmetrically oriented about a vertical axis passing through the center of the beam. Sufficient friction is assumed at all contact points and no sliding is envisaged. Clockwise rotation is considered as positive. The concept developed in this study is applicable to any pier geometry as long as the piers are of equal height, and mirror images of each other (i.e., system level symmetry). Since trapezoidal piers are mostly used in rocking frames supporting a typical rotor, the trapezoidal shape has been considered here. The frame is shown with solid lines when at rest and with dashed lines when in rocking motion. The distances between the CGs of the beam, the left pier, and the right pier from their respective pivot points are R_T, R, and R', and the inclination angles are α_T, α, and α'. Figure 3-5 (b) shows the frame in rocking motion with positive rotation displaced by the ground displacement, u_g with respect to Figure 3-5 (a). Figure 3-6(a) shows the generic configuration of a trapezoidal pier, whereas Table 3-1 lists various parameters of this configuration along with their comparison with those in [5]. Figure 3-6 (b) shows the details of the left pier of Figure 3-5 (a), while Figure 3-6 (c) shows it with a positive rotation in solid black lines. As shown in Figure 3-5 (b) and Figure 3-6 (c), the beam will be supported by the left support, i.e. point B (black dot), under positive rotation. Figure 3-6 (b) shows point B at a distance ηb from the CG; where, η is the ratio of block's support point's (B) distance from the pier CG and the CG's distance from the pivot O = b. Under negative rotation, the beam will be supported at point B$'$ (grey dot), at a distance $\eta' b$ from the CG, where, η' is the ratio of the distance of B$'$ from CG and b. Thus, η

and η' are two eccentricity parameters that represent support points' distances from the CG of the pier. The distance of point B and B′ from the corresponding pivot points, O and O', are, R_1 and R_1', at angles, β and β' from vertical, respectively.

The masses of the three rigid bodies of the rocking frame: left pier, right pier and beam, considered as m, m' and M_T, respectively are assumed to be uniformly distributed. The moments of inertia of the left pier about point O, the right pier about O', and the beam about the left support of the left pier (point B in Figure 3-6 (b)) are, I_o, $I_{o'}$ and I_{TB}, respectively. The moment of inertia of the beam about its CG is I_T. Figure 3-5(a) shows the distance between the beam interior supports as l and others dimensions important for the analysis that follows. Figure 3-5 (b) shows the sides of the contact polygon in thick grey dashed lines, which rotate but their lengths remain invariant. Since there is no sliding, this configuration is the same as that of a typical four-bar linkage mechanism.

The generalized rotation is assigned to the pier containing smaller of the two vertically inclined sides of the contact polygon, R_1 and R_1'. Thus, for the geometry shown in Figure 3-5 (b), the left pier rotation is considered as generalized rotation. Since the sides of the contact polygon are invariant, the rotations of the beam and right pier, θ' and θ_T, respectively, are kinematically constrained; hence the entire frame is a SDOF system. The top side of the contact polygon, i.e., the distance between the left supports of the beam at each pier, is $l_T = l + (\eta + \eta')b$. The distance of the CG of the beam from the exterior left support is $l/2 + (\eta + \eta')b$. The bottom side, i.e., the distance between the two pivot points on the ground is l_B . The left side is R_1 and the right side is R_1' . For negative rotations, i.e., to the left, the contact polygon would be the mirror image of that shown in Figure 3-5 (b) and hence, while positive θ is the positive rotation of the left pier, the

negative θ would be the negative rotation of the right pier. Thus, a plot of θ would represent combined rotation of two piers: positive for the right and negative for the left. Hence solving the rocking frame for the generalized rotation θ will lead to the solution in both directions. While the sides of the contact polygon remain invariant, it changes its shape due the variation in diagonal, D, which is a function of the generalized rotation, θ. Hence, all angles in the sequel are expressed as a function of D. The flow chart in Figure 3-7 explains the process adapted for the analysis. As the first step given therein, the following relationships are established that will be useful in further analysis.

$$\begin{gathered} D = \sqrt{R_1^2 + l_B^2 + 2 l_B R_1 \sin(\beta - |\theta|)} \\ b = R\sin\alpha, \;\; R'\sin\alpha' = (\mu - 1)b, \;\; h = R\cos\alpha = R'\cos\alpha' \\ R_1\cos\beta = R_1'\cos\beta' = \xi h, \\ R_1\sin\beta = (1+\eta)b, \;\; R_1'\sin\beta' = (\mu - 1 + \eta')b \\ R_1 = \nu R, \text{ where, } \nu = \sqrt{(1+\eta)^2\sin^2\alpha + \xi^2\cos^2\alpha} \\ R_1' = \nu' R, \text{ where, } \nu' = \sqrt{(\mu - 1 + \eta')^2\sin^2\alpha + \xi^2\cos^2\alpha} \\ l_B = l_C + (\mu - 1)b, \;\; l_T = l_C + (\eta - \eta')b \end{gathered} \tag{3-4}$$

Solving all angles in terms of θ for the four-bar linkage mechanism (contact polygon in Figure 3-5(b)) with cosine rule leads to

$$\begin{gathered} \delta_1 = \tan^{-1}\left[\frac{R_1\cos(\beta - |\theta|)}{l_B + R_1\sin(\beta - |\theta|)}\right], \;\; \delta_2 = \cos^{-1}\left[\frac{D^2 + R_1^{'2} - l_T^2}{2DR_1^{'}}\right] \\ \delta_3 = \cos^{-1}\left[\frac{D^2 + l_T^2 - R_1'^2}{2Dl_T}\right] \end{gathered} \tag{3-5}$$

Since $R_1' > R_1$, under positive rotation of the left pier, the right pier rotation will also be positive but smaller than that of the left pier, and the beam rotation will always be negative and vice versa. Therefore, the diagonal D and the angle, δ_1, are obtained for the absolute value of the rotation and

the signs of θ' and θ_T are assigned after evaluation of internal angles. Rotations of the right pier and of the beam are given as

$$\theta' = \operatorname{sgn}\theta\left(\delta_1 + \delta_2 + \beta' - \frac{\pi}{2}\right) \qquad \theta_T = -\operatorname{sgn}\theta\,(\delta_3 - \delta_1) \tag{3-6}$$

It is essential to establish the first and second derivatives of angles, θ' and θ_T, with respect to θ since these are required into the analysis presented later. The four-bar linkage mechanism shown in Figure 3-6(d) leads to the following relationship [38]:

$$\begin{aligned} a\mathbf{e_x} + b\mathbf{e_y} = L_1\left(\cos\theta_1\,\mathbf{e_x} + \sin\theta_1\,\mathbf{e_y}\right) - L_2\left(\cos\theta_2\,\mathbf{e_x} + \sin\theta_2\,\mathbf{e_y}\right) \\ -L_3\left(\cos\theta_3\,\mathbf{e_x} + \sin\theta_3\,\mathbf{e_y}\right) \end{aligned} \tag{3-7}$$

Applying the above to the contact polygon in Figure 3-5(b) and substituting $a = l_B$, $b = 0$, $L_1 = R_1$, $L_2 = l_T$, $L_3 = R_1'$, leads to the following.

$$a = R_1\cos\theta_1 - l_T\cos\theta_2 - R_1'\cos\theta_3\,, \quad 0 = R_1\sin\theta_1 - l_T\sin\theta_2 - R_1'\sin\theta_3 \tag{3-8}$$

Where, $$\theta_1 = \frac{\pi}{2} + \beta - \theta, \quad \theta_2 = \pi - \theta_T, \quad \theta_3 = \frac{\pi}{2} + \beta' - \theta'$$

Therefore, $$\dot{\theta} = -\dot{\theta}_1, \quad \dot{\theta}_T = -\dot{\theta}_2, \quad \dot{\theta}' = -\dot{\theta}_3, \quad \ddot{\theta} = -\ddot{\theta}_1, \quad \ddot{\theta}_T = -\ddot{\theta}_2, \quad \ddot{\theta}' = -\ddot{\theta}_1 \tag{3-9}$$

Differentiating Equation (3-6) with respect to time [38] gives

$$\dot{\theta}_2 = \left[\frac{R_1\sin(\theta_1 - \theta_3)}{l_T\sin(\theta_2 - \theta_3)}\right]\dot{\theta}_1, \quad \dot{\theta}_3 = \left[\frac{R_1\sin(\theta_2 - \theta_1)}{R_1'\sin(\theta_2 - \theta_3)}\right]\dot{\theta}_1 \tag{3-10}$$

$$\ddot{\theta}_2 = \frac{d}{dt}\left(\frac{R_1\sin(\theta_1-\theta_3)}{l_T\sin(\theta_2-\theta_3)}\right)\dot{\theta}_1 + \frac{R_1\sin(\theta_1-\theta_3)}{l_T\sin(\theta_2-\theta_3)}\ddot{\theta}_1, \quad \ddot{\theta}_3 = \frac{d}{dt}\left(\frac{R_1\sin(\theta_2-\theta_1)}{R_1'\sin(\theta_2-\theta_3)}\right)\dot{\theta}_1 + \frac{R_1\sin(\theta_2-\theta_1)}{R_1'\sin(\theta_2-\theta_3)}\ddot{\theta}_1 \tag{3-11}$$

Since $\dot{\theta}_2 = (d\theta_2/d\theta_1)\dot{\theta}_1$, the terms inside the square brackets in Equation (3-10) are the first derivatives of angles with respected to θ_1. From Equation (3-9), $\dot{\theta}_2/\dot{\theta}_1 = \dot{\theta}_T/\dot{\theta} = d\theta_T/d\theta$. Thus,

the first derivatives of the right pier and the beam rotations with respect to the generalized rotation including the incorporation of $\mathrm{sgn}(\theta)$ are

$$\frac{d\theta'}{d\theta} = \left[\frac{R_1 \cos(\theta_T - \theta + \mathrm{sgn}(\theta)\beta)}{R_1' \cos(\theta_T - \theta' + \mathrm{sgn}(\theta)\beta')}\right], \quad \frac{d\theta_T}{d\theta} = \mathrm{sgn}(\theta)\left[\frac{R_1 \sin[\theta' - \theta + \mathrm{sgn}(\theta)(\beta - \beta')]}{l_T \cos(\theta_T - \theta' + \mathrm{sgn}(\theta)\beta')}\right] \tag{3-12}$$

followed by the second derivatives as

$$\begin{aligned} \frac{d^2\,\theta'}{d\theta^2} &= \frac{d\theta'}{d\theta}\left[\tan(\theta_T - \theta' + \mathrm{sgn}(\theta)\beta')\left(\frac{d\theta_T}{d\theta} - \frac{d\theta'}{d\theta}\right) - \tan(\theta_T - \theta + \mathrm{sgn}(\theta)\beta)\left(\frac{d\theta_T}{d\theta} - 1\right)\right] \\ \frac{d^2\,\theta_T}{d\theta^2} &= \frac{d\,\theta_T}{d\theta}\left[\tan(\theta_T - \theta' + \mathrm{sgn}(\theta)\beta')\left(\frac{d\theta_T}{d\theta} - \frac{d\theta'}{d\theta}\right) + \cot\big(\theta' - \theta + \mathrm{sgn}(\theta)(\beta - \beta')\big)\left(\frac{d\theta'}{d\theta} - 1\right)\right] \end{aligned} \tag{3-13}$$

Equations (3-9) to (3-13) achieve Step 2 in the flow chart in Figure 3-7. The horizontal and vertical displacements and corresponding velocities of point B, as illustrated in Figure 3-6(b) and (c), are,

$$\begin{aligned} u_B = (1+\eta)b - R_1 \sin(\beta - \theta), \quad v_B = R_1 \cos(\beta - \theta) - \xi h \\ \dot{u}_B = \dot{u}_g + R_1 \cos(\beta - \theta)\,\dot{\theta}, \quad \dot{v}_B = R_1 \sin(\beta - \theta)\,\dot{\theta} \end{aligned} \tag{3-14}$$

Figure 3-5(a) shows the horizontal and vertical displacements of the beam's CG (dotted grey circle) as u_{CT} and v_T from its position at rest (solid black circle). The sign of beam rotation, θ_T would be negative (opposite to that of θ) and hence the horizontal distance of its CG from point B in is shown as $R_T \sin(\alpha_T + \theta_T)$ in Figure 3-5 (a) and (b). Similarly, the vertical distance, shown as h_T, would be $R_T \sin(\alpha_T + \theta_T)$. As shown in Figure 3-5 (b), since the CGs of all individual elements move towards right in the horizontal direction, the ground motion can be directly added. Adding the horizontal ground motion, u_g, the total horizontal and vertical translations of the CG of the beam and their corresponding velocities are,

$$\begin{gathered} u_T = u_g + u_{CT} = u_g + u_B + R_T[\sin(\alpha_T + \theta_T) - \sin\alpha_T] \\ v_T = v_B + h_T - h_o = R_1\cos(\beta - \theta) - \xi h + R_T[\cos(\alpha_T + \theta_T) - \cos\alpha_T] \\ \dot{u}_T = \dot{u}_g + R_1\cos(\beta - \theta)\dot{\theta} + R_T\cos(\alpha_T + \theta_T)\,\dot{\theta}_T \\ \dot{v}_T = R_1\sin(\beta - \theta)\,\dot{\theta} - R_T\sin(\alpha_T + \theta_T)\,\dot{\theta}_T \end{gathered} \tag{3-15}$$

from which, using $\dot{\theta}_T = \dot{\theta}(d\theta_T/d\theta)$ gives

$$\begin{gathered} \dot{u}_T^2 + \dot{v}_T^2 = \left[R_1^2\dot{\theta}^2 + R_T^2\dot{\theta}_T^2 + 2R_1R_T\dot{\theta}^2\frac{d\theta_T}{d\theta}\cos(\alpha_T + \theta_T + \beta - \theta) + \dot{u}_g^2\right] + \cdots \\ 2\dot{u}_g\dot{\theta}\left[R_1\cos(\beta - \theta) + R_T\cos(\alpha_T + \theta_T)\frac{d\theta_T}{d\theta}\right] \end{gathered} \tag{3-16}$$

The relative horizontal and vertical displacements, and corresponding velocities of the CG of the pier (Figure 3-6 (b)), are

$$\begin{gathered} u_m = u_g + R[\sin\alpha - \sin(\alpha - \theta)], \quad v_m = R[\cos(\alpha - \theta) - \cos\alpha] \\ \dot{u}_m = \dot{u}_g + R\cos(\alpha - \theta)\,\dot{\theta}, \quad \dot{v}_m = R\sin(\alpha - \theta)\,\dot{\theta} \end{gathered} \tag{3-17}$$

The equations for the right pier would be the same as Equation (3-17) containing the terms corresponding to the right pier: u', R', α', θ', $\dot{u}'$, $\dot{v}'$, and, $\dot{\theta}'$, and are not repeated for brevity. Langrage's equation for the system with the generalized coordinate, θ, is

$$\frac{d}{dt}\left(\frac{dL}{d\dot{\theta}}\right) - \frac{dL}{d\theta} = 0 \tag{3-18}$$

where, $L = T - V$ is the Lagrangian, where T is the kinetic energy, and V is the potential energy, of the system. Equation (3-18) achieves Step 3 in Figure 3-7. The kinetic energy of the system is given by

$$T = \frac{1}{2}[\dot{u}_m^2 + \dot{v}_m^2] + \frac{1}{2}[\dot{u}'^2_m + \dot{v}'^2_m] + \frac{1}{2}M_T\left[\dot{u}_T{}^2 + \dot{v}_T{}^2\right] + \frac{1}{2}I_T\dot{\theta}_T^2 \tag{3-19}$$

Expanding Equation (3-19) with the help of Equations (3-16) and (3-17),gives

$$
\begin{aligned}
T = {} & \tfrac{1}{2}[I_o\dot{\theta}^2 + m\dot{u}_g^2 + 2mR\cos(\alpha-\theta)\dot{\theta}\dot{u}_g]_{Left\ pier} + \\
& \tfrac{1}{2}\left[I_{o'}\dot{\theta'}^2 + m'\dot{u}_g^2 + 2m'R'\cos(\alpha'-\theta')\dot{\theta}'\dot{u}_g\right]_{\text{Right Pier}} + \\
& \tfrac{1}{2}I_T\dot{\theta}_T^2 + \tfrac{1}{2}M_T R_T^2\dot{\theta}_T^2 + \\
& \tfrac{1}{2}M_T\left[R_1^2\dot{\theta}^2 + 2R_1R_T\dot{\theta}^2\frac{d\theta_T}{d\theta}\cos(\alpha_T+\theta_T+\beta-\theta) + \dot{u}_g^2\right] + \\
& + \tfrac{1}{2}M_T\left\{2\dot{u}_g\dot{\theta}\left[R_1\cos(\beta-\theta) + R_T\cos(\alpha_T+\theta_T)\frac{d\theta_T}{d\theta}\right]\right\}
\end{aligned}
\tag{3-20}
$$

Since $dV/d\dot{\theta} = 0$, substituting $I_T + M_T R_T^2 = I_{TB}$ in Equation (3-20) turns the first term in Equation (3-18) into

$$
\begin{aligned}
\left[\frac{d}{dt}\left(\frac{dT}{d\dot{\theta}}\right) - \frac{dT}{d\theta}\right] = {} & [I_o\ddot{\theta} + mR\cos(\alpha-\theta)\ddot{u}_g]_{\text{Left pier}} + \dots \\
& \left[I_{o'}\ddot{\theta}\left(\frac{d\theta'}{d\theta}\right)^2 + I_{o'}\dot{\theta}^2\left(\frac{d\theta'}{d\theta}\right)\frac{d^2\theta'}{d\theta^2} + m'R'\cos(\alpha'-\theta')\frac{d\theta'}{d\theta}\ddot{u}_g\right]_{\text{Right pier}} + \\
& M_T R_1^2\ddot{\theta} + I_{TB}\left[\ddot{\theta}\left(\frac{d\theta_T}{d\theta}\right)^2 + \dot{\theta}^2\left(\frac{d\theta_T}{d\theta}\right)\frac{d^2\theta_T}{d\theta^2}\right] + \\
& M_T R_1 R_T\left[2\ddot{\theta}\frac{d\theta_T}{d\theta}\cos(\alpha_T+\theta_T+\beta-\theta)\right] + \\
& M_T R_1 R_T\dot{\theta}^2\left[\frac{d^2\theta_T}{d\theta^2}\cos(\alpha_T+\theta_T+\beta-\theta) + \left(\frac{d\theta_T}{d\theta}\right)\sin(\alpha_T+\theta_T+\beta-\theta)\left[1-\left(\frac{d\theta_T}{d\theta}\right)\right]\right] + \\
& M_T\ddot{u}_g\left[R_1\cos(\beta-\theta) + R_T\cos(\alpha_T+\theta_T)\frac{d\theta_T}{d\theta}\right]
\end{aligned}
\tag{3-21}
$$

Using the beam's vertical displacement, v_T, from Equation (3-15) and that for the left and right piers (v_m) from Equation (3-17) gives potential energy of the system as

$$
\begin{aligned}
V = {} & mgR[\cos(\alpha-\theta) - \cos\alpha] + m'gR'[\cos(\alpha'-\theta') - \cos\alpha'] + \\
& M_T g\{R_1\cos(\beta-\theta) - \xi h + R_T[\cos(\alpha_T+\theta_T) - \cos\alpha_T]\}
\end{aligned}
\tag{3-22}
$$

Equations (2-20) to (3-22) fulfill Step 4 in Figure 3-7. Substituting Equations (3-21) and (3-22) in Equation (3-18) gives the equation of motion for the rocking frame as

$$\ddot{\theta}\left[[I_o + M_T R_1^2] + \left[I_{o'}\left(\frac{d\theta'}{d\theta}\right)^2 + I_{TB}\left(\frac{d\theta_T}{d\theta}\right)^2\right] + \left[2M_T R_1 R_T \frac{d\theta_T}{d\theta}\cos(\alpha_T + \theta_T + \beta - \theta)\right]\right] =$$
$$-g\left[mR\sin(\alpha - \theta) + m'R'\sin(\alpha' - \theta')\frac{d\theta'}{d\theta} + M_T\left[R_1\sin(\beta - \theta) - R_T\sin(\alpha_T + \theta_T)\frac{d\theta_T}{d\theta}\right]\right]$$
$$-\ddot{u}_g\left[mR\cos(\alpha - \theta) + m'R'\cos(\alpha' - \theta')\frac{d\theta'}{d\theta} + M_T\left[R_1\cos(\beta - \theta) + R_T\cos(\alpha_T + \theta_T)\frac{d\theta_T}{d\theta}\right]\right] \quad (3\text{-}23)$$
$$-\dot{\theta}^2\left[I_{o'}\left(\frac{d\theta'}{d\theta}\right)\frac{d^2\theta'}{d\theta^2} + I_{TB}\left(\frac{d\theta_T}{d\theta}\right)\frac{d^2\theta_T}{d\theta^2}\right]$$
$$-\dot{\theta}^2\left[M_T R_1 R_T\left[\frac{d^2\theta_T}{d\theta^2}\cos(\alpha_T + \theta_T + \beta - \theta) + \left(\frac{d\theta_T}{d\theta}\right)\sin(\alpha_T + \theta_T + \beta - \theta)\left[1 - \left(\frac{d\theta_T}{d\theta}\right)\right]\right]\right]$$

Equation (3-23) fulfills Step 5 in Figure 3-7. Before going further into the analysis, it is important to understand the physical interpretation of Equation (3-23) which otherwise appears to be a mere collection of mathematical symbols (as required by Step 6 in Figure 3-7). Physical manifestation of Equation (3-23) can be understood through the solution of the rocking frame system having symmetrical piers with equal top support eccentricity given by Dar et al. [5] where the beam remains horizontal in rocking motion. Considering identical piers ($I_o = I_{o'}, \alpha = \alpha'$, $m = m',\ R = R'$) leads to $\theta_T = 0$ and Equation (3-23) turns into

$$\ddot{\theta}[2I_o + M_T R_1^2] = -2mgR\left[\sin(\alpha - \theta) + \frac{\ddot{u}_g}{g}\cos(\alpha - \theta)\right] - gM_T R_1\left[\sin(\beta - \theta) + \frac{\ddot{u}_g}{g}\cos(\beta - \theta)\right] \quad (3\text{-}24)$$

Equation (3-24) is the same as Equation (17) in [5] with the number of piers, $N = 2$. The multiple of 2 with I_o on the left side of Equation (3-24) and with the first term in square brackets on the right side implies that the two piers merge or overlap and the beam mass acts as a lumped mass at the contact point. This scenario is illustrated in Figure 3-8(a) as a combination of three equivalent configurations. The configuration on the left shows the frame, the one in the middle shows it under positive and negative rotations with merged piers and the one on the right shows merged piers supporting the beam as a two-block rocking system where the top block remains horizontal during rocking motion. Due to the vertical symmetry of the piers, their mirror images

(left pier in solid blue and the right pier in red dashed lines) can be superimposed. Since the entire system is a combination of two blocks and because the top block remains horizontal, it can be treated as a lumped mass [5] as shown in Figure 3-8(b), where, the dynamic parameters, emanating from the system's center of mass (CM) location, equivalent slenderness, α_{eq}, and radius, R_{eq}, define an equivalent rocking block system whose response is the same as that of the frame. The parameters, and α_{eq} and R_{eq}, remain invariant during rocking motion that lead to the equivalent size parameter, p_{eq} listed in Table 3-2. The equivalent block system was perceived as an equivalent rectangular block of radius $\hat{R} = 3g/4p_{eq}^2$ for $\eta = 1$ by Makris and Vassiliou in [6]. Although the authors did not use this parameter except mentioning it, it does not convey the correct message because for $q = \infty$, $R_{eq} = 2R$ (Table 3-2) and $I_{on} = 1$, whereas $\hat{R} = 1.5$ and for rectangular shape $I_{on} = 4/3$. Thus, the perceived rectangular block concept does not lead to correct analysis. The configuration in Figure 3-8(c) illustrates unsymmetrical piers but with symmetrical eccentricities. Meaning, $R_1 = R_1'$ but with $I_o \neq I_{o'}$. Since $R_1 = R_1'$, the rotations of the two piers would be equal resulting in beam remaining horizontal, i.e., $\theta = \theta'$ and $\theta_T = 0$, and in an overall symmetrical merged pier. Thus, in Figure 3-8(a), (b), and (c), the rocking frame can be represented by an equivalent rocking block system with time independent parameters.

The case under consideration in this study is shown in Figure 3-8(d), where, $R_1 \neq R_1'$, $\theta \neq \theta'$ and $\theta_T \neq 0$. In this case the piers do overlap but with the right pier's mathematically transformed shape to suit the generalized rotation coordinate, θ; a *scaling* effect caused by Jacobians: $d\theta'/d\theta$ and $d\theta_T/\, d\theta$. The instantaneous work done by the right pier (moment of inertia = $I_{o'}$), subject to the angular acceleration, $\ddot{\theta}'$, in rotating by angle, $d\theta'$, would be $\ddot{\theta}' I_{o'} d\theta'$, or, $\ddot{\theta}'(I_{o'} d\theta'/d\theta)d\theta$,

which is the same as the instantaneous work done caused by acceleration, $\ddot{\theta}'$, on the *scaled* moment of inertia ($I_{o'}d\theta'/d\theta$), corresponding to rotation $d\theta$. At an instant, treating $d\theta'/d\theta$ as a constant, the scaled moment of inertia would cause a mathematical shape distortion in the beam and the right pier, depicted in Figure 3-8(e) in dashed lines. The concept behind the distorted shape due to scaling by Jacobians is explained in APPENDIX A. Substituting, $\ddot{\theta}' = \ddot{\theta}(d\theta'/d\theta) + \dot{\theta}^2(d^2\theta'/d\theta^2)$ in $I_{o'}(d\theta'/d\theta)\ddot{\theta}'$, leads to the two terms associated with $I_{o'}$ for the right pier on the right hand side of Equation (3-21) in square brackets with the suffix "Right Pier". Since the area will also be scaled in the same proportion, the mass term, m', also carries the scaling multiplier, $d\theta'/d\theta$. The beam shape is scaled by $d\theta_T/\,d\theta$. Thus, the entire systems can be represented by merged piers and the top mass subjected to tangential and centripetal forces and the moment caused by beam rotation as depicted in Figure 3-8(e). It is to be noted that the beam contact point is on the supporting arm, R_1 (left pier), corresponding to the generalized rotation. For the rotation towards left, the mirror image of Figure 3-8(e) is applicable. Thus, Figure 3-8(e) is similar to a particular configuration of a two rectangular stacked blocks system consisting of a *narrow* block supporting a *wide* block. In the case of negative pier rotation, the bottom block mirrors and shifts to the right pier location along with the mirrored beam. Two blocks stacked system has been dealt with in detail in [33]. It can be shown that Equations (81) and (82) from [33], with substitution of equivalent symbols used in this study, lead to Equation (3-23). The proof of equivalence between the two stacked blocks system configurations in [33] and the system depicted in Figure 3-8(e) is given in APPENDIX A. Alternatively, the entire concept can also be understood by considering a combination of piers and lumped beam mass with applicable forces. Figure 3-8(e) shows angular accelerations, $\ddot{\theta}$, $\ddot{\theta}'$, and $\ddot{\theta}_T$, for the left and right piers, and the beam, respectively.

Since the beam is a rotating rigid body pivoting on top of another (the pier), it would experience centripetal and tangential accelerations due to two rotations: 1) its own and 2) that of the pier. The centripetal acceleration on the beam due to its own rotation is $R_T\dot{\theta}_T^2$ and the centripetal and tangential accelerations due to the pier rotation are, $R_1\dot{\theta}^2$and $R_1\ddot{\theta}$ respectively. Including the ground acceleration and the self weight, four moments are caused at point B due to: 1) the beam's rotational acceleration, $\ddot{\theta}_T$, 2) the pier's centripetal ($R_1\dot{\theta}^2$), and 3) tangential acceleration ($R_1\ddot{\theta}$), and 4) ground and gravitational accelerations. The moment at B after scaling by $d\theta_{\mathrm{T}}/d\theta$ comes out to be

$$\tau_B = \tau_{B1} + \tau_{B2} + \tau_{B3} + \tau_{B4}$$

Where,

$$\tau_{B1} = -I_{TB}\,\ddot{\theta}_T\frac{d\theta_{\mathrm{T}}}{d\theta} = -I_{TB}\frac{d\theta_{\mathrm{T}}}{d\theta}\left[\ddot{\theta}\left(\frac{d\theta_{\mathrm{T}}}{d\theta}\right) + \dot{\theta}^2\left(\frac{d^2\theta_{\mathrm{T}}}{d\theta^2}\right)\right]$$

$$\tau_{B2} = M_T R_1 R_T\frac{d\theta_{\mathrm{T}}}{d\theta}\left[\sin(\alpha_T + \theta_T + \beta - \theta)\,\dot{\theta}^2\right] \tag{3-25}$$

$$\tau_{B3} = -M_T R_1 R_T\frac{d\theta_{\mathrm{T}}}{d\theta}\left[\cos(\alpha_T + \theta_T + \beta - \theta)\ddot{\theta}\right]$$

$$\tau_{B4} = M_T g R_T\frac{d\theta_{\mathrm{T}}}{d\theta}\left[\sin(\alpha_T + \theta_T) - \frac{\ddot{u}_g}{g}\cos(\alpha_T + \theta_T)\right]$$

The moment, τ_B, along with the other forces acting on the lumped mass is shown in Figure 3-8 (f). The sum of moments about O due to the left and the right pier (scaled by $d\theta'/d\theta$) is

$$\tau_P = -I_o\ddot{\theta} - mgR\left(\sin(\alpha-\theta) + \frac{\ddot{u}_g}{g}\cos(\alpha-\theta)\right) - I_o'\left(\frac{d\theta'}{d\theta}\right)\left[\ddot{\theta}\left(\frac{d\theta'}{d\theta}\right) + \dot{\theta}^2\left(\frac{d^2\theta'}{d\theta^2}\right)\right]$$
$$-m'gR'\left(\frac{d\theta'}{d\theta}\right)\left(\sin(\alpha'-\theta') + \frac{\ddot{u}_g}{g}\cos(\alpha'-\theta')\right) \tag{3-26}$$

The moment about O, caused by the forces on the lumped mass shown in Figure 3-8(f), does not require further scaling by Jacobians. Summing up the moments about O through Equations

(3-25), (3-26), and those caused by the forces acting on the lumped mass in Figure 3-8(f), leads to Equation (3-23). Because the shapes of the merged pier and the beam vary with time, there is no time-independent equivalent block for the rocking frame with unsymmetrical eccentricities ($R_1 \neq R_1'$). The deformed shapes of the right pier and the beam have been exaggerated in Figure 3-8(e) and (f) for clarity.

Although, Equation (3-23) does not represent an equivalent block, it can be manipulated into a combination of several parts resembling Equation (3-1), as explained below catering to Step 7 in Figure 3-7. Since angles $\theta'$and θ_T are functions of θ, the rotation of the left pier, terms related to the right pier and beam ($I_{o'}$, I_{TB}, etc) can be expressed in terms of those of the left pier by considering their respective ratios. Defining the dimensionless ratios, $q_I = I_{o'}/I_o$, $q_{IT} = I_{TB}/I_o$, $q_T = M_T/m$, $q_m = m'/m$, $q_R = R'/R$, $q_{RT} = R_T/R$, recalling $I_{on} = I_o/mR^2$, and rearranging Equation (3-23) with the help of Equation (3-4) leads to

$$
\begin{aligned}
&\ddot{\theta} I_o \left[\left[1 + q_T \nu^2 \tfrac{mR^2}{I_o}\right]_1 + \left[q_I \left(\tfrac{d\theta'}{d\theta}\right)^2\right]_2 + \left[q_{IT} \left(\tfrac{d\theta_T}{d\theta}\right)^2\right]_3 + \left[2\nu q_T q_{RT} \tfrac{mR^2}{I_o} \tfrac{d\theta_T}{d\theta} \cos(\alpha_T + \theta_T + \beta - \theta)\right]_4\right] = \\
&-mg \left[R \sin(\alpha - \theta) + R \tfrac{\ddot{u}_g}{g} \cos(\alpha - \theta) + q_T R_1 \left[\sin(\beta - \theta) + \tfrac{\ddot{u}_g}{g} \cos(\beta - \theta)\right]\right]_1 \\
&-m' g R' \tfrac{d\theta'}{d\theta} \left[\sin(\alpha' - \theta') + \tfrac{\ddot{u}_g}{g} \cos(\alpha' - \theta')\right]_2 \\
&-q_T q_{RT} \tfrac{d\theta_T}{d\theta} mgR \left[\sin(-\alpha_T - \theta_T) + \tfrac{\ddot{u}_g}{g} \cos(\alpha_T + \theta_T)\right]_3 \\
&-\dot{\theta}^2 I_o \left[q_I \left(\tfrac{d\theta'}{d\theta}\right) \tfrac{d^2\theta'}{d\theta^2} + q_{IT} \left(\tfrac{d\theta_T}{d\theta}\right) \tfrac{d^2\theta_T}{d\theta^2} + \nu q_T q_{RT} \tfrac{mR^2}{I_o} \left[\tfrac{d^2\theta_T}{d\theta^2} \cos(\alpha_T + \theta_T + \beta - \theta) + \left(\tfrac{d\theta_T}{d\theta}\right) \sin(\alpha_T + \theta_T + \beta - \theta) \left[1 - \left(\tfrac{d\theta_T}{d\theta}\right)\right]\right]\right]_4
\end{aligned}
\tag{3-27}
$$

The terms on the left and the right sides of Equation (3-27) have been grouped in square brackets with suffixes to identify their association with one another. The first term (with suffix 1) on both sides of Equation (3-27) is the same as in Equations (17) in [5] (or Equations (2-17) in Chapter 2). Substituting $R_1 \sin\beta = (1+\eta)b = (1+\eta)\, R \sin\alpha$ and $R_1 \cos\beta = \xi R \cos\alpha$ from

Equation (3-4), and considering $\lambda_L \sin\alpha_L = \big(1 + q_T(1+\eta)\big)\sin\alpha$ and $\lambda_L \cos\alpha_L = (1 + q_T\xi)\cos\alpha$, leads to the first term in the right hand side of Equation (3-27) as

$$\lambda_L mgR\left[\sin(\alpha_L - \theta) + \frac{\ddot{u}_g}{g}\cos(\alpha_L - \theta)\right] \tag{3-28}$$

Where, $\alpha_L = \tan^{-1}\left(\frac{1+(1+\eta)q_T}{1+q_T\xi}\tan\alpha\right)$, and $\lambda_L = \sqrt{(1+(1+\eta)q_T)^2\sin^2\alpha + (1+q_T\xi)^2\cos^2\alpha}$

Similarly, substituting $R'\cos\alpha' = R\cos\alpha$, $R'\sin\alpha' = (\mu-1)R\sin\alpha$, $m' = q_m m$, in the second term in the right hand side of Equation (3-27) leads to

$$\lambda_R mgR\frac{d\theta'}{d\theta}\left[\sin(\alpha_R - \theta') + \frac{\ddot{u}_g}{g}\cos(\alpha_R - \theta')\right] \tag{3-29}$$

Where, $\alpha_R = \tan^{-1}\big((\mu-1)\tan\alpha\big)$, and $\lambda_R = q_m\sqrt{(\mu-1)^2\sin^2\alpha + \cos^2\alpha}$

Substituting equations (3-28) and (3-29) in to Equation (3-27), recognizing $\cos(\alpha_T + \theta_T) = \cos(-\alpha_T - \theta_T)$, and, introducing equivalent parameters, p_L, p_R, p_T, α_L, α_R and α_T along with $\mathrm{sgn}(\theta)$ leads to

$$\begin{aligned}\ddot{\theta} = &-p_L^2\left[\sin\big(\mathrm{sgn}(\theta)\alpha_L - \theta\big) + \tfrac{\ddot{u}_g}{g}\cos\big(\mathrm{sgn}(\theta)\alpha_L - \theta\big)\right]\\ &-p_R^2\left[\sin\big(\mathrm{sgn}(\theta)\alpha_R - \theta'\big) + \tfrac{\ddot{u}_g}{g}\cos\big(\mathrm{sgn}(\theta)\alpha_R - \theta'\big)\right]\\ &-p_T^2\left[\sin\big(-\mathrm{sgn}(\theta)\alpha_T - \theta_T\big) + \tfrac{\ddot{u}_g}{g}\cos\big(-\mathrm{sgn}(\theta)\alpha_T - \theta_T\big)\right] - \frac{\tau}{\psi}\dot{\theta}^2..\end{aligned} \tag{3-30}$$

Where, $p = \frac{mgR}{I_o}$, $p_L^2 = \frac{\lambda_L}{\psi}p^2$, $p_R^2 = \frac{\lambda_R}{\psi}\frac{d\theta'}{d\theta}p^2$ and $p_T^2 = \frac{q_T q_{RT}}{\psi}\frac{d\theta_T}{d\theta}p^2$

$$\psi = 1 + q_I\left(\frac{d\theta'}{d\theta}\right)^2 + q_{IT}\left(\frac{d\theta_T}{d\theta}\right)^2 + \frac{q_T\nu}{I_{on}}\left[\nu + 2q_{RT}\frac{d\theta_T}{d\theta}\cos(\mathrm{sgn}(\theta)\alpha_T + \theta_T + \mathrm{sgn}(\theta)\beta - \theta)\right]$$

$$\tau = q_I\left(\frac{d\theta'}{d\theta}\right)\frac{d^2\theta'}{d\theta^2} + q_{IT}\left(\frac{d\theta_T}{d\theta}\right)\frac{d^2\theta_T}{d\theta^2} + \ldots$$
$$\frac{\nu q_T q_{RT}}{I_{on}}\left[\frac{d^2\theta_T}{d\theta^2}\cos(\mathrm{sgn}(\theta)\alpha_T + \theta_T + \mathrm{sgn}(\theta)\beta - \theta) + \left(\frac{d\theta_T}{d\theta}\right)\sin(\mathrm{sgn}(\theta)\alpha_T + \theta_T + \mathrm{sgn}(\theta)\beta - \theta)\left[1 - \left(\frac{d\theta_T}{d\theta}\right)\right]\right]$$

The three bracketed terms in Equation (3-30), by comparison to Equation (3-1), represent three equivalent rocking blocks with their respective equivalent parameters, p_L, α_L, p_R, α_R, and, p_T, α_T. The fourth term represents the centripetal acceleration emanating from the velocity term. The derivatives of θ' and θ_T are given in Equations (3-12) and (3-13). It can be concluded that at any given instant, for a known value of θ, the above equation will represent an equivalent block (similar to what was observed by Dar et al. [5]) but with an additional term dependent on $\dot{\theta}$, and the geometries of the right pier and the beam. The parameters of the equivalent block (size and slenderness) would vary with time. Therefore, although a time independent equivalent block does not exist for a rocking frame with beam rotation, as observed by DeJong and Dimitrakopoulos [24], a numerical solution of Equation (3-30) can be obtained by adapting the procedure laid out in the sequel.

3.5 Eccentricity as a Tool to Obtain an Equivalent Block

This section caters to Step 8 of the flow chart in Figure 3-7.

Figure 3-9(a), (b) and (c) show a rocking frame with symmetrical eccentricities in rocking motion, the pier geometry, and the equivalent lumped mass and pier system respectively. In Figure 3-9(b), the horizontal distances from points B to O and B' to O' of the top support points are equal; $(\mu - 1 + \eta')b = (1 + \eta)b$, depicting it as a case of symmetrical eccentricities. This leads to, $\eta = (\mu - 2 + \eta')$, $R_1 = R_1'$, $\beta' = \beta$, $\theta = \theta'$, $d\theta'/d\theta = 1$, $\theta_T = 0$, and $d\theta_T/d\theta = 0$. Thus, all terms related to θ_T and $\dot{\theta}$ disappear from Equation (3-23), leading to

$$\ddot{\theta}(I_o + I_{o'} + M_T R_1^2) = -\begin{bmatrix} mgR\left\{\sin(\alpha - \theta) + \cos(\alpha - \theta)\frac{\ddot{u}_g}{g}\right\} + m'gR'\left\{\sin(\alpha' - \theta) + \cos(\alpha' - \theta)\frac{\ddot{u}_g}{g}\right\} + .. \\ M_T g R_1\left[\sin(\beta - \theta) + \cos(\beta - \theta)\frac{\ddot{u}_g}{g}\right] \end{bmatrix} \quad (3\text{-}31)$$

Equation (3-29) is the sum of individual equations of two piers and the top mass located at R_1 from the pivot point O for positive rotation. Making appropriate substitutions with the help of Equation (3-4), and considering $\lambda \sin\alpha_{eq} = \big(1 + q_m(\mu - 1) + q_T(1+\eta)\big)\sin\alpha$, and, $\lambda\cos\alpha_{eq} = (1 + q_m + q_T\xi)\cos\alpha$, the relationship in Equation (3-29) turns into

$$\ddot{\theta} = -p_{eq}^2\left\{\sin\left[\alpha_{eq}\mathrm{sgn}(\theta) - \theta\right] + \frac{\ddot{u}_g}{g}\cos\left[\alpha_{eq}\mathrm{sgn}(\theta) - \theta\right]\right\} \tag{3-32}$$

Where,

$$\alpha_{eq} = \tan^{-1}\left(\frac{1 + (\mu-1)q_m + (1+\eta)q_T}{1 + q_m + q_T\xi}\tan\alpha\right)$$

$$p_{eq}^2 = \frac{\breve{m}gR_{eq}}{I_{eq}} = \frac{\lambda}{\psi}\,p^2, \qquad \breve{m} = m(1 + q_m + q_T), \qquad R_{eq} = \frac{\lambda}{1 + q_m + q_T}R,$$

$$I_{eq} = \psi I_o, \qquad I_{on} = I_o/mR^2$$

$$\psi = (1 + q_I + q_T mR_1^2/I_o) = 1 + q_I + \frac{q_T}{I_{on}}\left[(1+\eta)^2\sin^2\alpha + \xi^2\cos^2\alpha\right]$$

$$\lambda = \sqrt{(1 + (\mu-1)q_m + (1+\eta)q_T)^2\sin^2\alpha + (1 + q_m + q_T\xi)^2\cos^2\alpha}$$

Equation (3-32) provides parameters of an equivalent block whose rotation is the same as the rotation of the system. Thus, eccentricity can be utilized as a manipulative tool to achieve $R_1 = R_1'$, so that the top beam does not undergo rotation. It is noted that the piers need not have the same mass or geometry, but the contact points of the top mass are to be equidistant from their respective pivot points O and O'. If the piers are symmetrical and equal in mass, then $q_I = 1$, $q_m = 1$, $q_T = 2q$, and $\eta = \eta'$. Substituting these into above equations leads to the equations for symmetrical piers as given in [5]. Table 3-2 lists the comparison between parameters of equivalent rocking block in this study for symmetrical eccentricities with those in [5]. The results obtained in this section were published in [39] but without the derivation that is given above. The condition $(\mu - 1 + \eta') = (1 + \eta)$ leads to equal eccentricity on either side of the CG of the merged pier as derived in the next section.

3.5.1 Merged piers with equal mass but unequal moment of inertia

Equation (3-31) reveals that two piers merge together as depicted in Figure 3-9(c). Figure 3-9 (c) shows the merged piers with the common portion highlighted. Thus, a new single pier is formed with top point mass, M_T, moment of inertia, $I_p = I_o + I_{o'}$ and other dimensional properties: $b_p = \mu b/2$, $\eta_p = (2/\mu)(1+\eta) - 1$, and the radius of the merged pier, $R_p = \sqrt{b_p^2 + h^2} = (R/2)\sqrt{(\mu \sin\alpha)^2 + 4(\cos\alpha)^2}$. The eccentricity, η_p, is equal on both side of the pier's CG. The normalized moment of inertia for the merged pier would be $I_{pn} = r_{op}^2/R_p^2$, where, r_{op}, is the radius of gyration of the merged pier. Considering piers of equal mass, m, the effective size parameter would be $p_p = \sqrt{2mgR_p/I_p}$, the beam-piers mass ratio, $q = M_T/2m$, and $r_{op} = \sqrt{I_p/2m} = r_o\sqrt{(1+q_I)/2}$. The CG of the merged pier (black dot) would be in the middle of the two CGs of individual piers, improving the stockiness, $\alpha_p > \alpha$, where, $\alpha_p = \tan^{-1}[(\mu/2)\tan\alpha]$. Substituting, the normalized moment of inertia, I_{pn} and the slenderness parameter α_p, of the merged pier in Equation (3-3) gives the coefficient of restitution of the merged pier as

$$e_p = 1 - \frac{\mu^2 \sin^2\alpha}{(1+q_I)I_{on}} \tag{3-33}$$

Coefficient of restitution for rocking frames of symmetrical eccentricities with symmetrical piers is given by Equation (38) of [5] (Chapter 2) which is reproduced below.

$$e = \frac{1}{\psi}\left(e_G + \frac{q}{I_{on}}(\xi^2(\cos\alpha)^2 - (\eta+1)^2\sin\alpha^2)\right) \tag{3-34}$$

Where, $\psi = \left[1 + \frac{q}{I_{on}}(\xi^2(\cos\alpha)^2 + (\eta+1)^2\sin\alpha^2)\right]$, and the rest of the quantities are for the pier: e_G is the coefficient of restitution of a symmetrical pier given by Equation (3-3), q is the mass

of the beam per pier, I_{on} is the normalized moment of inertia, α is slenderness parameter and η represents eccentricity.

Equation (3-32) applies to symmetrical piers. However, two unsymmetrical piers of equal mass that merge together constitute a symmetrical one with mass $2m$, giving $q = M_T/2m$. Substituting parameters for the merged pier in Equation (3-32) such as, $e_G = e_p$, $\eta = \eta_p$, $I_{on} = I_{pn}$ and, $\alpha = \alpha_p$, with further mathematical manipulation leads to the following equation of coefficient of restitution of merged pier.

$$e_{sm} = \frac{1}{\psi_{sm}}\left(e_p + \frac{2q}{(1+q_I)I_{on}}(\xi^2(\cos\alpha)^2 - (\eta+1)^2\sin\alpha^2)\right) \quad (3\text{-}35)$$

Where,

$$\psi_{sm} = 1 + \frac{2q}{(1+q_I)I_{on}}(\xi^2(\cos\alpha)^2 + (\eta+1)^2\sin\alpha^2)$$

If $q_I = 1$, and, $\mu = 2$, Equation (3-35) turns into Equation (3-34) applicable to symmetrical piers. The derivation of the above equation is given in APPENDIX A.

3.6 Minimum Acceleration Required to Initiate Rocking

This section corresponds to Step 9 in Figure 3-7. Applying principle of virtual work for a generalized rotation, $\delta\theta$, in Figure 3-5(b) gives

$$\delta W = M_T\ddot{u}_g\delta u_T + m\ddot{u}_g\delta u_m + m'\ddot{u}_g\delta u_{m'} - M_T g\delta v_T - mg\delta v_m - m'g\delta v_{m'} \quad (3\text{-}36)$$

Where,

$$u_B = \frac{du_B}{d\theta}\delta\theta,\ \ \delta u_m = \frac{du_m}{d\theta}\delta\theta,\ \ \delta v_B = \frac{dv_B}{d\theta}\delta\theta,\ \ \delta v_m = \frac{dv_m}{d\theta}\delta\theta,\ \ \delta u_T = \frac{du_T}{d\theta}\delta\theta,\ \ \delta v_T = \frac{dv_T}{d\theta}\delta\theta$$

$$\delta u_{m'} = \frac{du_{m'}}{d\theta}\delta\theta \qquad \delta v_{m'} = \frac{dv_{m'}}{d\theta}\delta\theta$$

For $\theta = \theta_T = \theta' = 0$, and $\delta W = 0$, with the help of Equations (3-14) and (3-15), Equation (3-36) turns into

$$M_T\ddot{u}_g\left[R_1\cos(\beta)+R_T\cos(\alpha_T)\left[\frac{R_1\sin(\beta-\beta')}{l_T\cos(\beta')}\right]\right]+m\ddot{u}_gR\cos\alpha+m'\ddot{u}_gR'\cos\alpha'\frac{R_1\cos(\beta)}{R_1'\cos(\beta')}=$$
$$M_Tg\left[R_1\sin(\beta)-R_T\sin(\alpha_T)\left[\frac{R_1\sin(\beta-\beta')}{l_T\cos(\beta')}\right]\right]+mgR\sin\alpha+m'gR'\sin\alpha'\frac{R_1\cos(\beta)}{R_1'\cos(\beta')} \quad (3\text{-}37)$$

Making appropriate substitutions from Equation (3-4) , leads to

$$\ddot{u}_gR\cos\alpha\left[\ 1+q_m+q_T\xi+q_TR_T\frac{\cos(\alpha_T)}{R\cos\alpha}\left[\frac{R_1\sin(\beta-\beta')}{l_T\cos(\beta')}\right]\ \right]=$$
$$gR\sin\alpha\left[1+(\mu-1)q_m+q_T(1+\eta)-q_TR_T\frac{\sin(\alpha_T)}{R\sin\alpha}\left[\frac{R_1\sin(\beta-\beta')}{l_T\cos(\beta')}\right]\right] \quad (3\text{-}38)$$

This leads to the minimum ground acceleration required to initiate uplift as

$$\ddot{u}_g=g\tan\alpha^* \quad (3\text{-}39)$$

Where,

$$\alpha^*=\tan^{-1}\left[\frac{b_0^*}{h_0^*}\right] \quad (3\text{-}40)$$

$$b_0^*=b\left[1+(\mu-1)q_m+(1+\eta)q_T-q_T\frac{R_T\sin(\alpha_T)}{R\sin\alpha}\left[\frac{R_1\sin(\beta-\beta')}{l_T\cos(\beta')}\right]\right]$$

$$h_0^*=h\left[1\ +\ q_m\ +q_T\xi+q_T\frac{R_T\cos(\alpha_T)}{R\cos\alpha}\left[\frac{R_1\sin(\beta-\beta')}{l_T\cos(\beta')}\right]\right]$$

Equation (3-40) gives the effective slenderness of the system at zero rotation. Considering $\beta=\beta'$ leads to the case of symmetrical eccentricities giving $\alpha^*=\alpha_{eq}$ of Equation (3-32). Equation (3-40) also implies that at $\theta=0$, the system is equivalent to a block with effective half width and half height as, b_0^* and h_0^*, respectively.

3.7 Effective Overturning Condition for the Rocking Frame

This section corresponds to Step 10 in Figure 3-7. Stability limit is reached when potential energy is maximum. Differentiating potential energy in Equation (3-22) and equating it to zero leads to the static equilibrium equation as

$$mgR[\sin(\alpha-\theta)] + m'gR'\left[\sin(\alpha'-\theta')\frac{d\theta'}{d\theta}\right] + M_T g\left\{R_1\sin(\beta-\theta) - R_T\sin(\alpha_T+\theta_T)\frac{d\theta_T}{d\theta}\right\} = 0 \quad (3\text{-}41)$$

With the help of Equation (3-4), the above leads to

$$\sin\alpha\left(\cos\theta + q_m\frac{d\theta'}{d\theta}(\mu-1)\cos\theta' + (1+\eta)q_T - q_T\frac{R_T\sin\alpha_T}{R\sin\alpha}\frac{d\theta_T}{d\theta}\cos\theta_T\right) = \cos\alpha\left((1+q_T\xi)\sin\theta + q_m\frac{d\theta'}{d\theta}\sin\theta' + q_T\frac{R_T\cos\alpha_T}{R\cos\alpha}\frac{d\theta_T}{d\theta}\right) \quad (3\text{-}42)$$

Considering the terms in brackets as $\cos\theta^*$ and $\sin\theta^*$ results in

$$\sin\alpha\cos\theta^* - \cos\alpha\sin\theta^* = 0 \;\Rightarrow\; \sin(\alpha-\theta^*) = 0 \quad (3\text{-}43)$$

Where,
$$\theta^* = \tan^{-1}\frac{\left((1+q_T\xi)\sin\theta + q_m\frac{d\theta'}{d\theta}\sin\theta' + q_T\sin\theta_T\frac{R_T\cos\alpha_T}{R\cos\alpha}\frac{d\theta_T}{d\theta}\right)}{\left(\cos\theta + q_m\frac{d\theta'}{d\theta}(\mu-1)\cos\theta' + (1+\eta)q_T - q_T\cos\theta_T\frac{R_T\sin\alpha_T}{R\sin\alpha}\frac{d\theta_T}{d\theta}\right)} \quad (3\text{-}44)$$

The rotation, θ^*, a function of θ, in Equation (3-44) is defined here as *effective* rotation of the system, leading to the maximum potential energy. For convenience, this condition is defined as *effective overturning*, representing the instability of the system, when $|\theta^*| = \alpha$. The appearance of Equation (3-43), resembles that of a single rocking block overturning at $|\theta^*| = \alpha$. In the response calculation, θ^* can be numerically monitored to identify the unstable condition while solving Equation (3-30). For a symmetrical pier case, $R_1 = R_1'$, results in $\theta = \theta'$, $\theta_T = 0$, $d\theta_T/d\theta = 0$ and $d\theta'/d\theta = 1$. Substituting these in Equation (3-44) gives

$$\tan(\theta^*) = \frac{(1+q_m+q_T\xi)}{(1+(\mu-1)q_m+(1+\eta)q_T)}\tan\theta = \frac{\tan\alpha}{\tan\alpha_{eq}}\tan\theta \quad (3\text{-}45)$$

Where, α_{eq} is as defined in Equation (3-32). Equation (3-45) reveals that in a symmetrical case the frame will *overturn* when $\theta = \alpha_{eq}$, which leads to $\tan(\theta^*) = \tan\alpha$. Meaning the overturning condtion of $\theta = \alpha_{eq}$ is the same as the system rotation $\theta^* = \alpha$. This is verified by numerical analysis later.

3.8 Maximum Coefficient of Restitution of Rocking Frames with Unsymmetrical Eccentricities

This section corresponds to Step 11 in Figure 3-7. The COR derived herein is based on conservation of angular momentum about a pivot point before and after impact [11]. Figure 3-10(a) shows an unsymmetrical pier of mass, m, in rocking motion with positive (clockwise) velocity in solid lines and negative velocity in dashed lines pivoting about O' and O respectively. For this pier the COR for impact at point O, due to positive velocity is termed as, e_G^+, and, at O' due to negative velocity, e_G^-. The piers in Figure 3-10(b) and (c) respectively depict the left and right piers of the frame in Figure 3-5(a) (just before impact) which are mirror images of each other having mass m and m'. Figure 3-10(b) is addressed as left pier and Figure 3-10(c) as right. The pier in Figure 3-10(b) is similar to that shown in solid line in Figure 3-10(a), with positive velocity pivoting about O' and about to strike O; implying, the COR for the two will be equal. The pier in Figure 3-10(c), pivoting about O and about to strike O' with positive velocity is similar to the pier shown with dashed lines in Figure 3-10(a); meaning, for equal mass piers, i.e., $m = m'$, the COR for the case in Figure 3-10(c) for positive velocity is the same as of the pier in dashed lines with negative velocity (counter clockwise) in Figure 3-10(a).

In the analysis below, both piers in Figure 3-10(b) and (c) are considered with positive rotation. Both cases of Figure 3-10(b) and (c) are dealt with independently, where, pre-impact velocity is addressed as, $\dot{\theta}_1$, and post impact velocity as, $\dot{\theta}_2$. Center of gravity is marked as CG in both cases. Since clockwise rotation is positive, the angular momentum of an infinitesimal element of mass dm in Figure 3-10(b) (or the left pier) with velocity $v_t = r_1\dot{\theta}_1$about the new pivot point O, just before the impact, is

$$dH_{OL_{\text{before}}} = -r_2 v_t dm = -r_1 r_2 \dot{\theta}_1 dm$$
$$= -r_1(\mu b \sin\beta_1 - r_1)\,\dot{\theta}_1 dm = \left[r_1^2 - \mu b\big((\mu-1)b - x\big)\right]\dot{\theta}_1 dm \tag{3-46}$$

where r_2 and x are defined as shown in Figure 3-10(a), and $r_1 \sin\beta_1 = (\mu-1)b - x$. Integrating over the entire body gives

$$H_{OL_{\text{before}}} = \left(\int r_1^2\, dm - \mu(\mu-1)b^2 \int dm + \mu b \int x\, dm\right)\dot{\theta}_1 \tag{3-47}$$

In the above equation, since x is the perpendicular distance from the CG, the last term is zero by definition of the center of gravity, and the first term inside the bracket is the moment of inertia about O'. Hence, for the pier mass, m,

$$H_{OL_{\text{before}}} = (I_{o'} - \mu(\mu-1)mbR\sin\alpha)\dot{\theta}_1 \tag{3-48}$$

Equating $H_{OL_{\text{before}}}$ with the angular momentum after impact, $H_{OL_{\text{after}}} = I_o\dot{\theta}_2$, leads to the COR for the pier about to strike point O in Figure 3-10(b) denoted as e_{GL}, or, of the pier in Figure 3-10(a) with solid lines about to strike point O with positive velocity, denoted as e_G^+ for a solitary pier, as given below.

$$e_{GL} = \frac{\dot{\theta}_2}{\dot{\theta}_1} = \left(q_I - \frac{\mu(\mu-1)}{I_{on}}\sin^2\alpha\right) \qquad e_G^+ = e_{GL} \tag{3-49}$$

Similarly, it can be shown that for the block in Figure 3-10(c) (or the right pier), its angular momentum before impact $H_{OR_{\text{before}}}$ about point O' is

$$dH_{O'R_{\text{before}}} = -r_1 r_2 \dot{\theta}_1 dm = [r_1^2 - \mu b(b-x)]\dot{\theta}_1 dm = [r_1^2 - \mu b(b-x)]\dot{\theta}_1 dm \tag{3-50}$$

$$H_{O'R_{\text{before}}} = \left(\int r_1^2\, dm - \mu b^2 \int dm + \mu b \int x\, dm\right)\dot{\theta}_1 = (I_o - \mu m' bR \sin\alpha)\dot{\theta}_1$$

Where, m', is the pier mass. Equating the above with the after-impact angular momentum of the pier in Figure 3-10(c) (or the right pier) about the pivot point O', $H_{O'R_{\text{after}}} = I_{o'}\dot{\theta}_2$, leads to the COR of the right pier about to strike point O' in Figure 3-10(c), e_{GR}. For $q_m = 1$, e_{GR} will be equal to the COR of the pier in Figure 3-10(a) with dashed lines about to strike point O' with negative velocity, denoted as e_G^-, as given below.

$$e_{GR} = \frac{\dot{\theta}_2}{\dot{\theta}_1} = \frac{1}{q_I}\left(1 - \frac{\mu q_m}{I_{on}}\sin^2\alpha\right), \qquad e_{GR}|_{q_m=1} = e_G^- \tag{3-51}$$

For $q_m = 1$, Equations (3-49) and (3-51) represent positive and negative coefficients of an unsymmetrical pier in Figure 3-10(a). With $q_I = q_m = 1$, and, $\mu = 2$, they lead to Equation (36) in [5] (Equation (2-36) in CHAPTER 2). The two coefficients of restitution, e_G^+ and e_G^-, applicable upon impact with positive and negative velocities, will be utilized later in obtaining the response of a solitary pier to a given excitation.

3.8.1 Frames with two mirror-image piers

Figure 3-11(a) shows a typical four-bar linkage mechanism with the bar *a* having angular velocity ω_A, bar *b*1 having angular velocity ω_B, bar *c* having angular velocity ω_C, while the distance between the two bottom hinges, *d*, is fixed. Two velocity vectors, v_a and v_c, at the two ends of *b*1 are perpendicular to *a* and *c* and tangential to the circles with radii, r_a and r_c, centered at the instantaneous center of rotation, I_C. The angular velocities ω_A and ω_C are inversely proportional to the distance of the bottom hinges from point O_{AC} [43], leading to

$$\frac{\omega_C}{\omega_A} = \frac{O_{AC}O_{AD}}{O_{AC}O_{CD}} \tag{3-52}$$

Figure 3-11(b) shows bar $b1$ with velocity vectors v_a and v_c resolved into longitudinal and transverse components, v_{aX}, v_{cX}, v_{aT}, and v_{cT}. By definition of the instantaneous center of rotation, $v_a = r_a\omega_B$, and $v_c = r_c\omega_B$. From this relationship it can be shown that the axial components of the two velocity vectors are equal ($v_{aX} = v_{cX}$). Figure 3-11(c) shows the axial components of the velocity vectors depicting pure translation in axial direction. Taking algebraic average of the two transverse velocity vectors leads to equal transverse velocity vectors at two ends resulting in pure transverse translation depicted in Figure 3-11(d). Algebraically subtracting this average from the transverse components leads to equal and opposite velocity vectors at two ends causing pure rotation shown in Figure 3-11(e). Thus, the motion of the bar $b1$ in Figure 3-11(b) can be broken into pure axial and transverse translations in Figure 3-11(c) and (d), and, pure rotation in Figure 3-11(e) (Figure 3-11(b)=(c) + (d) + (e)). The angular velocity of the top bar is derived below.

$$v_X = v_{aX} = v_{cX},$$
$$v_T = \frac{1}{2}[v_{aT} + v_{cT}],\ \ v_R = v_{aT} - v_T = -[v_{cT} - v_T],\ \ \omega_B = \frac{2}{b1}v_R \tag{3-53}$$

Figure 3-11(f) shows the rocking frame approaching impact. The piers rotate clockwise and the beam anticlockwise. The beam sways to the right and experiences impact, as shown in Figure 3-11(g), and continues to sway to the right after impact. The instantaneous center of rotation, I_C, of the beam is shown with the help of broken radii (similar to the top bar motion in Figure 3-11(a)). During impact, the beam disengages from the piers with velocities $\boldsymbol{v_{L1}}$ and $\boldsymbol{v_{R1}}$ (thus breaking the

four-bar linkage mechanism for an infinitesimally small time) to re-engage instantly, switching its pivot points (forming a four-linkage mechanism as a mirror image of the previous one), and resulting in impulses on the piers due to the impact. For clockwise pier rotation in Figure 3-11(f) and (g), $\dot{\theta}_{T1}$ would be anticlockwise indicating that the downward velocity on the left pier (vertical component of $\boldsymbol{v_{L1}}$) would be larger. The velocity vectors shown dashed lines in Figure 3-11(f) at contact locations point downward towards right and are not parallel. Whereas in Figure 3-11(g), they point upwards.

Figure 3-12(a) shows the piers of a rocking frame in clockwise rotation about their pivot points, O' and O, just before impact. The two piers are mirror images of each other and have unsymmetrical supports (where $\mu - 1 + \eta' \neq \eta + 1$). The two support points at the top are depicted as dark dots B' and B on the left and right piers, respectively. At the time of impact, the instantaneous configuration of the rocking frame would be the same as that at rest, with the beam horizontal (because the piers ae of equal height). From Equation (3-52), and Figure 3-11(a), for the horizontal top bar, the point, O_{AC}, would be at infinity, and hence equidistant from the two pivot points, leading to

$$\dot{\theta}_1 = \dot{\theta}_1' \qquad \left[\frac{v_{L1}}{v_{R1}}\right]_{\text{just before impact}} = \frac{R_1'}{R_1} \tag{3-54}$$

The above is also clear by geometry in Figure 3-5(a); at $\theta = 0$, $\theta' = \theta_T = 0$. Equation (3-12) would yield $d\theta'/d\theta = 1$, and hence, $\dot{\theta}' = \dot{\theta}$ because $R_1' \cos\beta' = R_1 \cos\beta$ from Equation (3-4). Equal angular velocities of piers would be valid throughout the duration of impact, i.e., just before, during, and just after the impact. Figure 3-12(a) shows the velocity vectors on the left and the right piers just before impact, v_{L1} and v_{R1}. During impact, as shown in Figure 3-12(b), the beam moves

from the assembly with velocities v_{L1} and v_{R1}, with axial and transverse velocities, v_{A1} and v_{T1} and angular velocity, $\dot{\theta}_{T1}$, from one set of pivots (dark dots B' and B) to instantaneously land at the other (grey dots B and B'). The distance between the top pivot points is l_T and between the internal support points is l, as shown in Figure 3-12(b). From Equation (3-53) and Figure 3-11(c), (d) and (e), the longitudinal components of v_{L1} and v_{R1}, would be equal to v_{A1} (Figure 3-12(b)), whereas, the algebraic average of their transverse components would be equal to v_{T1}. From Equation (3-4), $R_1' \cos\beta' = R_1 \cos\beta$, $R_1' \sin\beta' = (\mu - 1 + \eta')b$, $R_1 \sin\beta = (1+\eta)b$, $b = R \sin\alpha$ and with the help of Equation (3-53), the following relationships emerge for various beam velocities: pure-translation longitudinal (v_{A1}), pure-translation transverse (v_{T1}), pure-rotation transverse (v_{O1}), and resulting angular ($\dot{\theta}_{T1}$).

$$v_{Lh1} = v_{L1}\cos\beta' = R_1'\dot{\theta}_1\cos\beta', \quad v_{Rh1} = v_{R1}\cos\beta = R_1\dot{\theta}_1\cos\beta$$

$$v_{Lh1} = v_{Rh1}, \quad v_{A1} = R_1'\dot{\theta}_1\cos\beta' = R_1\dot{\theta}_1\cos\beta \tag{3-55}$$

$$v_{Lv1} = v_{L1}\sin\beta' = R_1'\dot{\theta}_1\sin\beta', \quad v_{Rv1} = v_{R1}\sin\beta = R_1\dot{\theta}_1\sin\beta$$

Pure vertical translational velocity, the average of vertical velocities (negative sign for the downward direction) in Figure 3-12(a), comes out to be

$$v_{T1} = -\frac{1}{2}[v_{Lv1} + v_{Rv1}] = -\frac{1}{2}\left[R_1'\dot{\theta}_1\sin\beta' + R_1\dot{\theta}_1\sin\beta\right] = -\frac{1}{2}[\mu + \eta + \eta']b\dot{\theta}_1 \tag{3-56}$$

In order to obtain the rotational velocity, the average velocity coefficient, $\frac{1}{2}[\mu + \eta + \eta']b$, can be subtracted from either $R_1' \sin\beta' = (\mu - 1 + \eta')b$ or $R_1 \sin\beta = (1+\eta)b$. One would be the negative of the other. Per Equation (3-53), the velocity causing pure rotation is given as

$$v_{O1} = -R_1'\dot{\theta}_1 \sin\beta' + \frac{1}{2}b[\mu + \eta + \eta']\dot{\theta}_1 = -\frac{1}{2}b[\mu + \eta' - \eta - 2]\dot{\theta}_1 \tag{3-57}$$

Because $\frac{l_T}{2}\dot{\theta}_{\mathrm{T1}} = v_{O1}$

$$\dot{\theta}_{\mathrm{T1}} = -\frac{1}{l_T}b[\mu + \eta' - \eta - 2]\dot{\theta}_1 \tag{3-58}$$

Figure 3-12(c) shows the piers just after impact, rotating with angular velocity, $\dot{\theta}_2$ and $\dot{\theta}_2'$, about their respective pivot points, O for the left, and O' for the right pier, giving rise to upward velocity vectors ($v_{L2} = R_1\dot{\theta}_2$ and $v_{R2} = R_1'\dot{\theta}_2'$) acting at the top pivot points shown as grey dots at B and B'. As shown in Figure 3-12(c), after the impact, the vertical velocity components' direction would be opposite to that before impact, but the vertical velocity on the right pier would be more than the left one in order to continue the anticlockwise rotation. Following the similar process as above, the post impact velocities come out to be (post impact velocity are upwards, hence positive),

$$v_{Lh2} = v_{L2}\cos\beta = R_1\dot{\theta}_1\cos\beta, \quad v_{Rh2} = v_{R2}\cos\beta' = R_1'\dot{\theta}_1\cos\beta'$$

$$v_{Lh2} = v_{Rh2}, \quad v_{A2} = R_1'\dot{\theta}_2\cos\beta' = R_1\dot{\theta}_2\cos\beta$$

$$v_{T2} = \frac{1}{2}\left[R_1'\dot{\theta}_2\sin\beta' + R_1\dot{\theta}_2\sin\beta\right] = \frac{1}{2}b[\mu + \eta + \eta']\dot{\theta}_2 \tag{3-59}$$

$$v_{O2} = R_1\dot{\theta}_2\sin\beta - v_{T2} = (1+\eta)b - \frac{1}{2}b[\mu + \eta + \eta']\dot{\theta}_2 = -\frac{1}{2}b[\mu + \eta' - \eta - 2]\dot{\theta}_2$$

$$\dot{\theta}_{T2} = -\frac{1}{l_T}b[\mu + \eta' - \eta - 2]\dot{\theta}_2$$

The impact caused by the beam on the piers is computed below by dividing it into two parts: impact due to pure translation, and, pure rotation.

3.8.2 Impact due to pure translation

As shown in Figure 3-12(b), during impact the beam lands on the new set of pivots, B and B', shown as grey dots along with the pairs of horizontal and vertical components of impact forces acting on the beam and piers as F_{ILx} and F_{ILy} at the left, and, F_{IRx} and F_{IRy} at the right end. From the impulse-momentum theorem in the horizontal direction of the beam,

$$\int F_{ILx}\,dt + \int F_{IRx}\,dt = M_T(v_{A1} - v_{A2}) = M_T\xi h\left(\dot{\theta}_1 - \dot{\theta}_2\right) \tag{3-60}$$

The vertical translational downward velocity, v_{T1}, in Equation (3-56), originates from the beam leaving the points, B' on the left and B on the right pier, depicted as black dots in Figure 3-12(a). The velocity, v_{T1}, is the same throughout the length of the beam and considered to be acting at the beam's center of mass. However, per Figure 3-11(d), it acts at the center of supports of the rod of length $b1$. Meaning, the support locations, B' and B will have equal pure translational velocities implying that the mid-distance between the two can be considered as the center of supports. But the support locations are not equidistant from the beam's center of mass. Considering the left support B' at a distance $r_{TL} = l/2 = l_C/2 - \eta' b$ from the center of mass and the right support, B, at $r_{TR} = l_C/2 - \eta' b + (\eta + \eta')b = l_C/2 + \eta b$ leads to the eccentricity between the center of supports from the beam's center of mass as

$$e_T = \frac{r_{TR} - r_{TL}}{2} = \frac{\frac{l_C}{2} + \eta b - \frac{l_C}{2} + \eta' b}{2} = \frac{(\eta + \eta')b}{2} \tag{3-61}$$

Since, the center of mass would be at an eccentricity, e_T, from the center of supports, in Figure 3-12(a), the linear momentum $M_T v_{T1}$ acting at the center of the beam will be accompanied with a counter clockwise angular momentum, $M_T v_{T1} e_T$. Similarly, this will be the case with the post

impact scenario in Figure 3-12(c) where, the velocity will be negative but with the eccentricity on the opposite side of that in Figure 3-12(a). Hence the net effect would cause a counterclockwise angular momentum, $M_T v_{T2} e_T$. Upon impact in Figure 3-12(b), two impulses at each contact point on piers would emerge, $\int F_{1TLy}\, dt$, and, $\int F_{1TRy}\, dt$, respectively on the left and the right pier. The sum of the vertical impulses $\int \left(F_{1TLy} + F_{1TRy}\right) dt = M_T(v_{T1} + v_{T2})$. Multiplying both sides by e_T leads to the fact that the summation of impulse will be acting at e_T towards left of the beam's center of mass causing an angular momentum equal and opposite to that caused by the beam, i.e., clockwise. However, the eccentricity of e_T towards left would mean that the summation of the two impulses would be equidistant from the two support points where they act individually. This concludes that the two vertical impact forces will be equal, $F_{1TLy} = F_{1TRy}$ and validates the assumption made in [6] on the equality of the impulses on piers caused by the vertical impact of a beam descending with constant velocity. This means that even in the frames with symmetrical eccentricities, the top beam does rotate for an infinitesimally small amount of time during impact but is brought back to be horizontal by the action of the impulse at an eccentricity that counteracts the angular momentum accompanying the beam. Considering $F_{1TLy} = F_{ITy}$, the sum of the two impulses is expressed hereinafter as $2\int F_{ITy}\, dt$. The sum of vertical impulses (since v_{T1} is negative and v_{T2} positive, $v_{T1} - v_{T2}$ will result in addition of velocity but with an overall negative sign due to downward motion), will be equal to the change in vertical momentum

$$2\int F_{ITy}\, dt = M_T(v_{T1} + v_{T2}) = -\frac{1}{2} M_T b(\mu + \eta + \eta')\left(\dot{\theta}_1 + \dot{\theta}_2\right) \tag{3-62}$$

3.8.3 Impact due to pure rotation

Pure rotational velocity, $\dot{\theta}_{\mathrm{T1}}$, would give rise to only the upward force, F_{IOy}, at only left pier due to anticlockwise direction (there is no impact due to pure rotation at the right end since the tangential motion is upwards). Impulse due to pure rotation is obtained by equating the angular momentum caused by the impulse with the difference between the angular momenta of the beam about its centroid before and after the impact. Since the beam's angular velocity direction is

anticlockwise before and after the impact, $\dot{\theta}_{T2}$ is subtracted from $\dot{\theta}_{T1}$ in the equation below. Because the angular velocity is anticlockwise, impact is caused only on the left pier. The impulse at the beam's left end times the distance from its centroid is the angular momentum due to impulse. Substituting $\dot{\theta}_{\mathrm{T1}}$ and $\dot{\theta}_{\mathrm{T2}}$, from Equations (3-58) and (3-59), and $l_T = l + (\eta + \eta')b$ (Figure 3-12(b)), the upward impulse on the beam comes out to be

$$\left[\int F_{IOy}\, dt\right]\left[\frac{l}{2} + b(\eta + \eta')\right] = I_T\left[\dot{\theta}_{\mathrm{T1}} - \dot{\theta}_{\mathrm{T2}}\right]$$

$$\int F_{IOy}\, dt = \frac{2I_T}{l_C^2\left(1 + 2\eta\frac{b}{l_C}\right)\left[1 + (\eta - \eta')\frac{b}{l_C}\right]} b[\mu + \eta' - \eta - 2]\left(\dot{\theta}_1 - \dot{\theta}_2\right) \tag{3-63}$$

Where, I_T is the mass moment of inertia of the beam about its own CG. Equation (3-63) represents the impulse experienced by the beam. The impulse on the pier would be negative of the above,

$$\left[\int F_{IOy}\, dt\right]_{\mathrm{PIER}} = -\frac{2I_T}{l_C^2\left(1 + 2\eta\frac{b}{l_C}\right)\left[1 + (\eta - \eta')\frac{b}{l_C}\right]} b[\mu + \eta' - \eta - 2]\left(\dot{\theta}_1 - \dot{\theta}_2\right) \tag{3-64}$$

3.8.4 Conservation of Angular Momentum

In order to calculate the angular momentum of the system, a reference point P is chosen at a horizontal distance, *d*, from the left pier pivot (Figure 3-12). The angular momentum of the left pier about point P is equal to $\boldsymbol{H_o} + (\boldsymbol{d} \times m\boldsymbol{V_o})$, where $\boldsymbol{H_o}$ is the angular mass momentum of the left pier about point O, $\boldsymbol{V_o}$ is the velocity vector of the point O and $\boldsymbol{d}$ is the distance vector from O to P (If $|\boldsymbol{H_o}|$ is considered as $I_o\dot{\theta}$, where, I_o, is the geometrical moment of inertia, then the mass, m, is to be considered as area). Since $\boldsymbol{V_o} = 0$, the angular momentum of the left pier about point

P is $\boldsymbol{H_O}$. Similarly, the angular momentum of the right pier about point P is equal to its angular momentum about its pivot point O'. Thus, angular momentum about point P of any element of the system is equal to the angular momentum about any pier pivot points.

For applying the conservation of angular momentum, only the piers are considered. The effect of the beam is included in form of various impulses caused during impact. The free body diagram of the piers in Figure 3-12(b) illustrates this concept. Considering conservation of angular momentum of the piers before, during and after the impact gives

$$\boldsymbol{H_{P_{\text{after}}} = H_{P_{\text{before}}} + H_{during}}$$

Since, $\boldsymbol{H_{OP} = H_O}$, and, $\boldsymbol{H_{O'P} = H_{O'}}$, as explained above (3-65)

$$\boldsymbol{H_{OL_{\text{after}}} + H_{OR_{\text{after}}} = H_{OL_{\text{before}}} + H_{OR_{\text{before}}} + H_{\text{during}}}$$

Substituting appropriate terms in Equation (3-65) from the free body diagram of the piers in Figure 3-12,

$$\begin{aligned}\left[(I_O + I_{O'})\dot{\theta}_2\right] = (I_{o'} - \mu(\mu-1)mbR\sin\alpha)\dot{\theta}_1 + (I_o - \mu m' bR\sin\alpha)\dot{\theta}_1 + \xi h(\textstyle\int F_{ILx}\,dt + \int F_{IRx}\,dt) \; + \\ \left[(1+\eta)b\left(\textstyle\int F_{ITy} + F_{IOy}\right)dt + (\mu - 1 + \eta')b\int F_{ITy}\,dt\right]\end{aligned} \tag{3-66}$$

Defining $q_L = b/l_C$, $q_{OT} = I_T/I_o$ and $q_{LT} = \frac{2q_L^2}{(1+2\eta\, q_L)[1+(\eta-\eta')\, q_L]}$ and manipulation with the help of Equation (3-4), (3-60), (3-62), and (3-64), gives

$$I_o\dot{\theta}_2\left[1+q_I+\frac{q_T}{4I_{on}}(4\xi^2\cos^2\alpha+(\mu+\eta+\eta')^2\sin\alpha^2)+(1+\eta)q_{OT}q_{LT}[\mu+\eta'-\eta-2]\right]=..$$

$$I_o\dot{\theta}_1\left[\begin{array}{c}1+q_I-\left(\mu q_m+\mu(\mu-1)\right)\frac{\sin^2\alpha}{I_{on}}+\frac{q_T}{4I_{on}}(4\xi^2\cos^2\alpha-(\mu+\eta+\eta')^2\sin\alpha^2)\\-q_{OT}q_{LT}(1+\eta)[\mu+\eta'-\eta-2]\end{array}\right] \quad (3\text{-}67)$$

Which leads to the equation of COR

$$\check{e}=\frac{\dot{\theta}_2}{\dot{\theta}_1} \quad (3\text{-}68)$$

$$\Rightarrow\ \check{e}=\frac{1}{\check{\psi}}\left(e_{GL}+q_Ie_{GR}+\frac{q_T}{4I_{on}}(4\xi^2\cos^2\alpha-(\mu+\eta+\eta')^2\sin\alpha^2)-(1+\eta)q_{OT}q_{LT}(\mu+\eta'-\eta-2)\right)$$

Where, $\check{\psi}=\left[1+q_I+\frac{q_T}{4I_{on}}(4\xi^2\cos^2\alpha+(\mu+\eta+\eta')^2\sin\alpha^2)+(1+\eta)q_{OT}q_{LT}(\mu+\eta'-\eta-2)\right]$ and e_{GL} and e_{GR} are defined in Equations (3-49) and (3-51) respectively.

$$e_{GL}+q_Ie_{GR}=\left(q_I-\frac{\mu(\mu-1)}{I_{on}}\sin^2\alpha\right)+1-\frac{\mu q_m}{I_{on}}\sin^2\alpha=1+q_I-\frac{\sin^2\alpha}{I_{on}}\left(\mu q_m+\mu(\mu-1)\right) \quad (3\text{-}69)$$

For piers with equal mass, the COR of the frame will be the same in both directions because of the frame's symmetry as a system.

3.8.5 Coefficient of Restitution for Symmetrical Eccentricities

Equidistant support points condition represented by the equation $\mu-1+\eta'=\eta+1$ leads to the following.

If $\mu-1+\eta'=\eta+1$, then, $\mu+\eta'=\eta+2$ and $\mu+\eta+\eta'=2\eta+2$. Meaning $\frac{1}{4}(\mu+\eta+\eta')^2=\frac{4}{4}(\eta+1)^2=(\eta+1)^2$. If $\mu-1+\eta'=\eta+1$ then $\mu+\eta'-\eta-2=0$. Substituting these in Equation (3-68) leads to

$$e_s = \frac{\dot{\theta}_2}{\dot{\theta}_1} = \frac{1}{\psi_s}\left(e_{GL} + q_I e_{GR} + \frac{q_T}{I_{on}}(\xi^2 \cos^2\alpha - (\eta+1)^2 \sin\alpha^2)\right) \quad (3\text{-}70)$$

Where, $\psi_s = \left[1 + q_I + \frac{q_T}{I_{on}}(\xi^2 \cos^2\alpha + (1+\eta)^2 \sin\alpha^2)\right]$.

Further detailed explanation on this particular case can be found in APPENDIX A.

For symmetrical piers with equal mass, $m = m'$, and $q = M_T/(m+m')$, Substituting $q_I = 1$, $q_m = 1$, and $q_T = 2q$ into Equation (3-68) leads to E_{eq} derived in Equation (38) in [5]. Further substituting $\eta = 1$ leads to the COR derived for symmetrical piers with $\eta = 1$ as in [6] where an assumption was made that the impact forces on top of symmetrical piers are equal. Equation (3-68) with suggested substitutions validates this assumption.

3.8.6 Merged piers for Symmetrical Eccentricities and Equal Mass

The merged pier is depicted in Figure 3-9. Considering, $q_T = 0$ (i.e., absence of the beam) and $q_m = 1$, and, substituting $e_{GL} + q_I e_{GR}$, from Equation (3-69) into Equation (3-70), leads to the COR of the solo merged pier as

$$e_{Gp} = \frac{1}{1+q_I}(e_{GL} + q_I e_{GR}) = 1 - \frac{\mu^2 \sin\alpha^2}{(1+q_I)I_{on}} \quad (3\text{-}71)$$

The above is the same as in Equation (3-33). For a frame, considering $q = M_T/2m = q_T/2$, and substituting Equation (3-71) into Equation (3-70) leads to the COR for the merged pier and beam mass combination that represents the rocking frame,

$$e_{sm} = \frac{1}{\psi_{sm}}\left(e_{Gp} + \frac{2q}{I_{on}(1+q_I)}\left(\xi^2 \cos^2\alpha - (\eta+1)^2 \sin\alpha^2\right)\right) \quad (3\text{-}72)$$

where $$\psi_{sm} = 1 + \frac{q_T}{(1+q_I)I_{on}}(\xi^2 \cos^2\alpha + (1+\eta)^2 \sin\alpha^2)$$

The above equation is the same as Equation (3-35).

3.9 Procedure to Obtain Solution of Equation (3-30)

Application of Equation (3-30) in either direction of rotation, positive or negative, is possible only when $q_m = 1$. For piers with unequal mass, $q_m \neq 1$, Equation (3-30) would result in two equations based on various ratios (q_m, q_I etc) for positive and negating generalized rotation: 1) for the left pier, and 2) for the right pier. Similarly, there would be two CORs for positive and negative pre-impact angular velocities. Practical rocking frames in the field consist of equal pier masses ($q_m = 1$). Hence, the examples considered in this study are for $q_m = 1$. The solution to Equation (3-30) can be obtained with the following procedure:

1. Cast Equation (3-30) in $\dot{\mathbf{y}} = f(\mathbf{y}, t)$ format where $\mathbf{y} = [\theta, \dot{\theta}]$.

2. Solve Equation (3-30), utilizing an appropriate solver by considering minimum acceleration required to initiate rocking as $g\tan\alpha^*$, where, α^* is defined by Equation (3-40). The solution is applicable between two impacts. Upon impact the pre-impact part of the solution is selected discarding the rest and a new solution begins with the new boundary conditions: zero rotation and post-impact angular velocity which is obtained by multiplying the pre-impact velocity with the applicable COR. The total solution is the sum of piece-meal solutions between impacts. Per Equation (3-54), at the instant of impact the angular velocities of the two piers would be equal and after multiplication with the coefficient of restitution, would lead to equal initial velocities for the next cycle of rocking

up till the next impact. Equation (3-30) is numerically solved through the state-space formulation [21] on Mathcad [44] in the next section.

3. Terminate the numerical solution when the instability condition given by Equation (3-44) is met; effective system rotation, $|\theta^*| = \alpha$.

The purpose of this study is to assess the impact of eccentricities on the response of rocking frames with unsymmetrical top supports in comparison to the symmetrical condition. Therefore, first, the COR of frames with symmetrical eccentricities (Equation (3-35)) is applied to all cases of eccentricity to the Example 1 frame in Table 3-3. After that, the COR for unsymmetrical eccentricities will be applied to both examples of Table 3-3.

3.10 Response to Earthquake Records

This section corresponds to Step 12 of the flow chart in Figure 3-7, that is studying the impact of varying eccentricities on a frame's response to earthquake records. The beam support configuration in a frame may result in unsymmetrical loading of unsymmetrical and symmetrical piers. Therefore, two shapes are considered: unsymmetrical trapezoidal and rectangular. Table 3-3 lists geometrical properties and dynamic parameters of two examples of rocking frames: Example 1 is similar to that in Figure 3-3(a) with trapezoidal piers and a rotor shaped top beam identical to field example, whereas, Example (2) is similar to that in Figure 3-3(c), with rectangular piers having similar properties to that considered in [7]. Table 3-3 depicts the geometrical parameters necessary for the analysis. Both piers in the frame are of equal mass; $q_m = 1$. Parameters that are independent of, and, dependent on, eccentricities have been identified by shading them differently. Table 3-4 lists the details of earthquake records chosen for this study.

Figure 3-13(a) shows symmetrical eccentricity configuration on an unsymmetrical pier with stem support, where, $1 + \eta = \mu - 1 + \eta'$. Here, the values of η and η' that lead to a symmetrical eccentricity configuration are defined as, η_s and η'_s, respectively that resulting in $R_1 = R'_1$. Figure 3-13(b) shows unsymmetrical eccentricity configuration. Figure 3-13 (c) shows idealized representation of symmetrical eccentricity configuration without the stem support. Since the contribution of the top stem on the moment of inertia of the pier is minimal, it has been ignored. This also ensures that pier geometry remains identical for a suite of eccentricity combinations. In order to study the impact of eccentricities on response, the configuration in Figure 3-13(c) will be utilized with $\eta = \eta_s$ combined with $\eta' = \eta'_s$, $2\eta'_s$, $4\eta'_s$, and, $\eta'_{max} = 1$. For the rectangular pier example (Figure 3-3(c)) only one set of eccentricities, $\eta = 0$ and $\eta' = 1$, is applicable. Since $q_m = 1$, the CORs for the unsymmetrical solitary pier, are given in Table 3-3 as e_G^+ and e_G^-, obtained from Equations (3-49) and (3-51) applicable upon impact with positive and negative angular velocities respectively. For the solitary rectangular pier in Example 2, $e_G^+ = e_G^-$.

3.10.1 Response of symmetrical eccentricity configuration (Figure 3-14)

Figure 3-14 shows the response of rocking frame in Example 1 with symmetrical eccentricities ($\eta = \eta_s$ and $\eta' = \eta'_s$) with $q_T = 20$ (COR = 0.879) for three earthquake records: Loma Prieta LGP 000, San Fernando PCD 254 and Napa Valley Crockett - Carquinez Br. The time history of these records and the compatibility of their response spectra (RS) with the design basis earthquake (DBE) of NPPs [40, 41] are illustrated in the bottom two rows of Figure 3-14. As evident from the response spectrum in the bottom row, frequency contents of these records vary from lower frequency peak spectral acceleration (PSA) on left to the higher one on right. The frequency parameter, p, connects to the timing (or frequency) of application of acceleration [45]. Larger the

timing of acceleration application, greater is the possibility of overturning. Thus, a lower frequency excitation is expected to cause a larger response. The top row shows the responses in terms of generalized rotation, θ, obtained by solving Equations, (3-30), (3-32), and, θ^* obtained from the combination of Equations (3-30) and (3-44). As expected, the peak responses decrease with the increase in the higher frequency content of the excitation from left column to the right. The equivalent block response (θ) from Equation (3-32) and that for the general case from Equation (3-30) are identical and overlap each other, whereas, the system rotation, θ^* comes out to be more than θ in all cases. The second row from top shows the normalized rotation responses, θ/α_{eq}, θ/α^*, and θ^*/α obtained from Equation (3-32), Equations (3-30) and (3-40), and, Equations (3-30) and (3-44) respectively. As evident, all normalized responses are identical to each other despite being obtained from different set of equations. Thus, the second row demonstrates the significance of normalized effective rotation, θ^*/α, as a representative of instability. It also validates the conclusion drawn earlier that all three normalized rotations are equal for a symmetrical eccentricity case.

3.10.2 Response of unsymmetrical eccentricity configuration (Figure 3-15 and Figure 3-16)

Figure 3-15 depicts the influence of eccentricity on the response of rocking frame in Example 1 (Table 3-3), subjected to the three earthquake records: Loma Prieta in the top two rows, SF PCD 254 in the two middle rows and the Napa Valley record in the two bottom rows. Three types of beam loadings varying from the left column to the right are: $q_T = 4, 8, 20$. In each set of rows, the upper row is considered as the first row. In all cases, eccentricity $\eta = \eta_s$, whereas, η' varies as η'_s, $2\eta'_s$, $4\eta'_s$, and, $\eta'_{max} = 1$. Corresponding CORs for the symmetrical eccentricity condition applicable to various values of q_T, as depicted on top of each column, are 0.868, 0.875 and 0.879.

In the top two rows, peak rotations, $\theta \approx 0.2$ and $\theta^*/\alpha \approx 0.6$, indicate a reasonably substantial response to Loma Prieta record (the lowest frequency record among the three). In the left column of the top row, all responses are almost identical except that of the solitary pier which is comparatively quite small. In the middle column, the responses for $\eta' = 4\eta'_s$, and, η'_{max} are much more than other responses and in the right column, the response for η'_{max} is much larger than any other response. This row depicts that as the beam weight increases, the response increases for higher eccentricities. The second row illustrates the normalized effective rotation (θ^*/α) response. In the first column of second row, the symmetrical eccentricity case response is maximum and quite close to the response for $\eta' = 2\eta'_s$. In the second and third columns, the maximum eccentricity (η_{max}) response curve has the highest peak. Thus, in this row, it is observed that the highest eccentricity results in the maximum response at $q_T = 8$ and 20, which is the range for turbine rotors in a NPP. This is in contrast to the generalized observation in [25] that the response of asymmetric frames is almost the same as that of the symmetric frames.

The middle two rows depict an overall lower response ($\theta < 0.05$ and $\theta^*/\alpha \approx 0.1$) in all cases in comparison to the top two rows. It is expected because the frequency content of SF PCD 254 is somewhat in the middle of the three record as depicted in Figure 3-14. The first of the middle two rows depicts the solitary pier response to be the highest in all columns. In the second of the middle two rows, responses of all cases of eccentricity are not too far from one another. However, the response due to highest eccentricity, $\eta_{max} = 1.$ is more than all others in the second and third columns. Thus, in this case as well, higher loading accompanied with higher eccentricity leads to larger response.

The bottom two rows depict the lowest of all responses owing to the comparatively higher frequency content of the Napa record. In the first of the bottom two rows all responses (θ) are quite close to one another. However, in the bottom most row, a distinct order exists among the normalized effective rotation (θ^*/α) of all cases of eccentricity in all columns where the response magnitude follows the increasing order of eccentricity. In all columns, the highest eccentricity leads to the highest and the lowest eccentricity to the lowest response. However, the magnitude of all responses reduces as the beam becomes heavier from left to right columns.

The top four rows in Figure 3-15 conclude that higher eccentricity leads to larger response at higher loading. The maximum eccentricity, $\eta' = 1$, worsens the response. The bottom set of two rows concludes that at low rotations, higher eccentricity leads to higher response for all loadings.

Figure 3-16 illustrates the response of rocking frames in Example 1 and 2 to Northridge Rinaldi and Aegion Greece records respectively. The first two columns from left show the response to the Northridge Rinaldi record, whereas the last two columns show the response to the Aegion record. In the set of two columns for Example 1, the first is for $q_T = 4$ and the second represents $q_T = 20$. In the set of last two columns for Example 2, the first is for $q_T = 0.5$ and the second for $q_T = 4$. The three rows below the sets of columns depict the COR curves for both examples, followed by the respective time histories and response spectra of the two records exhibiting their similarity to the DBE of NPPs [40, 41]. The COR for Example 1 is the highest for the symmetrical eccentricity case. As eccentricity increases the COR decreases. However, the COR increases with increase in the beam mass turning almost into a constant at $q_T = 1$. For Example 2, the COR increases with increasing beam mass.

For Example 1 (left two columns), the first column in the first row (from top) shows effective overturning ($\theta^*/\alpha = 1$) in all cases except those with higher eccentricities, $\eta' = 4\eta'_s$, and, η'_{max}.. In the second column, only two curves ($\eta' = 4\eta'_s, \eta'_{max}$) survive the excitation while the rest overturn. The order of the peak response magnitude in both columns is opposite to that of eccentricity, i.e., the lowest eccentricity leads to the highest and the highest eccentricity leads to the lowest response, for Example 1. The second row illustrates rotational responses to all eccentricities, including the solitary pier response, which is the lowest of all. The response trend is identical to that in the first row. The third row depicts only the surviving cases of eccentricities common to both cases, $\eta' = 4\eta'_s$, and, η'_{max}, where the other pier response, θ', and the beam response, θ_T, are also illustrated. Although the eccentricity case, $\eta' = 2\eta'_s$, also survives for $q_T = 4$, but is not shown for clarity. As shown, the response curve for θ', is almost the same as for θ, because the beam rotation is small, meaning the beam remains almost horizontal similar to the symmetric eccentricity case. However, there is a marked difference between the overall response of the case with symmetric eccentricity versus higher eccentricity. While the symmetric eccentricity case overturns, the higher eccentricity cases survive. Therefore, a small rotation of the beam does not guarantee the response similar to that of a frame with symmetric eccentricity.

The set of right two columns depict the response of Example 2 (Table 3-3) with rectangular piers having the configuration shown in Figure 3-3(c), where only one combination of eccentricities is possible, $\eta = 0$ and $\eta' = 1$. Here the two beam loadings are considered as, $q_T = 0.5$ and 4. The CORs for the two cases are mentioned as 0.968 and 0.973. The first row depicts increased response with increased loading. The second row depicts the same but with solitary pier response to be close to the frame response for $q_T = 0.5$ in the first cycle. In the third row, the right

pier rotation (or, other than the generalized rotation), θ', is almost the same as the first one, θ, and the beam rotation is small. However, the beam rotation relative to that of the frame is higher than that shown for the Rinaldi record response in the first two columns. In this case again, it is seen that the higher loading leads to higher response.

This section demonstrated that although eccentricity at lower beam loading may improve the response in some cases, it worsens the same at higher loadings. The overall response depends on combination of loading, pier configuration, coefficient of restitution and eccentricity. There is no direction correlation of eccentricity with response.

3.11 Summary, Conclusions and Recommendations

This study carried out analysis of rocking frames with unsymmetrical piers of equal height and established its equation of motion for two types of top support eccentricities: symmetrical and unsymmetrical, assuming no sliding. The study also focused on physical interpretation of the equation of motion leading to the discovery that a rocking frame with equal height piers is essentially a SDOF two stacked block system where the top block rotation is a function of that of the bottom block. The two stacked block system can further be evolved into a single equivalent rocking block for the case with symmetrical eccentricity. It is concluded that a time independent equivalent rocking block exists for rocking frames with symmetrical eccentricities but not for those with unsymmetrical ones. This study explored strategic maneuvering of the top support eccentricities to make them symmetrical, to arrive at the parameters of a merged pier that leads to a dynamically equivalent rocking block model.

It is concluded that the equation of motion of rocking frames with unsymmetrical eccentricities can be formulated representing an assembly of equivalent rocking blocks that facilitate the conversion of equation of motion of the frame into a simplified form, making it convenient to be adapted in the field (e.g., NPPs). Also, the equation of motion in form of an assembly of equivalent blocks can be instrumental in formulation of an approximate finite element model applying the techniques suggested in the literature [3-518, 26] by considering each equivalent block as a SDOF oscillator with negative stiffness.

The rocking response calculated by the procedure given in this study can be utilized in arriving at fragilities of rocking frames required to assess seismic risk of a NPP. To facilitate adoption of this study directly in the field, geometrical properties of trapezoidal block piers (common to NPPs) in terms of variables essential to obtain the response have been presented. Explicit expressions of the system slenderness, α^*, required to establish minimum acceleration to initiate rocking, and effective rotation, θ^*, that defines the effective overturning as an instability criterion were established. The responses to earthquake records for a symmetrical eccentricity example, in terms of normalized effective rotation, θ^*/α, normalized rotations, θ/α_{eq}, and θ/α^*, were verified to be equal to each other, proving self verification of concepts established in this study. The COR of unsymmetrical piers has been established and utilized in obtaining the same for a frame with unsymmetrical piers but symmetrical support conditions. Also, the COR of frames with unsymmetrical eccentricity has been established. The phenomenon of impact of the beam on piers was explained and the assumption made in the literature on equality of impulses on top of the piers during impact, for the case with symmetrical eccentricities, was validated. Rocking responses of example frames to earthquake records, with trapezoidal and rectangular piers, were obtained for

different cases of eccentricities. It was observed that for a reasonably substantial rotational response (such as 50 percent of overturning limit), the response at higher eccentricities increases for heavier frames. This is in contrast to the generalized observation in the literature [25] that the seismic response of asymmetric frames is almost identical to the symmetric ones. For rocking frames in the field, it is recommended that the unsymmetrical frame eccentricities be made symmetrical by maneuvering the support system so that the response of an equivalent block can be obtained from a rocking spectrum. If not possible to do so, the system response can be obtained by the procedure laid out in this study.

Since rocking frames result in the vertical and horizontal motion of the beam, further research is required to examine the instability of frames due to separation (or lift off) of the beam in slide restricted rocking frames. The impact of eccentricities on instability by beam separation is required to be studied. The influence of the COR on separation of beam is also required to be investigated.

3.12 References

1. EPRI. *A Methodology for Assessment of Nuclear Power Plant Seismic Margin*. Electric Power Research Institute, Report NP-6041-SL-Revision 1, Palo Alto, CA, 1991.
2. Reed J W, Kennedy R P. *Methodology for Developing Seismic Fragilities.* Report TR-103959, Electric Power Research Institute, Palo Alto, CA, 1994.
3. EPRI. *Program on Technology Innovation: The Effects of High Frequency Ground Motion on Structures, Components, and Equipment in Nuclear Power Plants*. Report 1015108, Electric Power Research Institute, Palo Alto, CA, 2007.
4. Dar A, Konstantinidis D, El-Dakhakhni WW. Impact of slenderness on the seismic response of rocking frames in Ontario nuclear power plants. *5th International Structural Specialty Conference*, London, Ontario, Canadian Society for Civil Engineering, 2016.
5. Dar A, Konstantinidis D, El-Dakhakhni W. Seismic response of rocking frames with top support eccentricity. *Earthquake Engineering and Structural Dynamics* 2018; **47**(12): 2496– 2518. https://doi.org/10.1002/eqe.3096
6. Makris N, Vassiliou MF. Planar rocking response and stability analysis of an array of free-standing columns capped with a freely supported rigid beam. *Earthquake Engineering and Structural Dynamics* 2013; **42**(3):431-449.

7. Drosos V, Anastasopoulos I. Shaking table testing of multidrum columns and portals. *Earthquake Engineering and Structural Dynamics* 2014;**43**(11):1703-23.
8. Vassiliou MF, Mackie KR, Stojadinović B. A finite element model for seismic response analysis of deformable rocking frames. *Earthquake Engineering and Structural Dynamics* 2017;**46**(3):447-66.
9. USNRC. Arkansas Nuclear One – NRC augmented inspection team follow-up inspection report 05000313/2013012 and 05000368/2013012; preliminary red and yellow findings. United States Regulatory Commission's letter to Ankansas Nuclear One. 2014, March 24. Retrieved May 9, 2021, from www.nrc.gov: https://www.nrc.gov/docs/ML1408/ML14083A409.pdf
10. American Society of Civil Engineers. *ASCE 43-19 – Seismic Design Criteria for Structures, Systems and Components in Nuclear Facilities*, Reston, 2019.
11. Housner GW. The behavior of inverted pendulum structures during earthquakes. *Bulletin of the Seismological* Society of America 1963; **53**(2):403–417.
12. Aslam M, Scalise DT, Godden WG. Earthquake rocking response of rigid bodies. *Journal of the Structural Division* 1980; **106**(2):377-392.
13. Spanos PD, Koh AS. Rocking of rigid blocks due to harmonic shaking. *Journal of Engineering Mechanics* 1984;**110**(11):1627-1642.
14. Konstantinidis D, Makris N. The dynamics of a rocking block in three dimensions. Proc., *8th Hellenic Society for Theoretical and Applied Mechanics Int. Congress on Mechanics*, Hellenic Society for Theoretical and Applied Mechanics, Athens, Greece, 2007.
15. Yim CK, Chopra A, Penzien J. Rocking response of rigid blocks to earthquakes. *Earthquake Engineering and Structural Dynamics* 1980; **8**(6):565–587.
16. Makris N, Roussos Y. *Rocking response and overturning of equipment under horizontal pulse-type motions*, Report No. 1998/05. Berkeley, 1998.
17. Shao Y, Tung C. Seismic response of unanchored bodies. *Earthquake Spectra* 1999; **15**(3):523–536.
18. Konstantinidis D, Makris N. Experimental and analytical studies on the response of 1/4-scale models of freestanding laboratory equipment subjected to strong earthquake shaking. *Bulletin of Earthquake Engineering*, 2010; **8**(6):1457–1477.
19. Priestley M, Evison R, Carr AJ. Seismic response of structures free to rock on their foundations. *Bulletin of the New Zealand National Society for Earthquake Engineering* 1978; **11**(3):141–150.
20. Wesley DA, Kennedy RP, Richter PJ. Analysis of the seismic collapse capacity of unreinforced masonry wall structures. *Proceedings of the 7th World Conference on Earthquake Engineering*, Istanbul, Turkey, 1980.
21. Makris N, Konstantinidis D. The rocking spectrum and the limitations of practical design methodologies. *Earthquake Engineering and Structural Dynamics* 2003; **32**(2):265–289.
22. Dar A, Konstantinidis D, El-Dakhakhni W. Requirement of rocking spectrum in Canadian nuclear standards. *Transactions, 22nd International Structural Mechanics in Reactor Technology Conference (SMiRT22)* San Francisco, CA, 2013.
23. Dar A, Konstantinidis D, El-Dakhakhni WW. Evaluation of ASCE 43-05 seismic design criteria for rocking objects in nuclear facilities. *Journal of Structural Engineering* 2016; **142**(11).

24. DeJong MJ, Dimitrakopoulos EG. Dynamically equivalent rocking structures. *Earthquake Engineering and Structural Dynamics* 2014; **43**:1543–1563.
25. Dimitrakopoulos, E. G., Giouvanidis, A. I. Seismic Response Analysis of the Planar Rocking Frame. J. Eng. Mech 2015; **141**(7).
26. Diamantopoulos, S., Fragiadakis, M. (2021). Modeling of rocking frames under seismic loading. *Earthquake Engng Struct Dyn,* 2021, **51**(1): 109-128.
27. Lee TH. Nonlinear dynamic analysis of a stacked fuel column subjected to boundary motion. *Nuclear Engineering and Design* 1975; **32**:337-350.
28. Ikushima, Nakazawa T. A seismic analysis method for a block column gas-cooled reactor core. *Nuclear Engineering and Design* 1979; **55**:331-342.
29. Allen RH, Oppenheim IJ, Parker AR, Bielak J. On the dynamic response of rigid body assemblies. *Earthquake Engineering and Structural Dynamics* 1986;**14**:861-876.
30. Psycharis IN. Dynamic behaviour of rocking two-block assemblies. *Earthquake Engineering and Structural Dynamics* 1990; **19**:555-575.
31. Spanos PD, Roussis PC, Nikolaos P. Dynamic analysis of stacked rigid blocks. *Soil Dynamics and Earthquake Engineering* 2001; **21**:559-578.
32. Konstantinidis D, Makris N. Seismic response analysis of multidrum classical columns. *Earthquake Engineering and Structural Dynamics* 2005; **34**:1243–1270.
33. Kounadis AN, Papadopoulos GJ, Cotsovos DM. Overturning instability of a two-rigid block system under ground excitation. *ZAMM Z. Angew. Math. Mech.* 2012; **92**(7):536 – 557.
34. Minafo G, Amato G, Stella L. Rocking behaviour of multi-block columns subjected to pulse-type ground motion accelerations. *The Open Construction and Building Technology Journal* 2016; **10**(Suppl 1: M9): 150-157.
35. Bachmann JA, Vassiliou MF, Stojadinović B. Dynamics of rocking podium structures. *Earthquake Engineering and Structural Dynamics* 2017.
36. Wittich CE, Hutchinson TC. Shake table tests of stiff, unattached, asymmetric structures. *Earthquake Engineering and Structural Dynamics* 2015; **44**(14):2425-43.
37. Wittich CE, Hutchinson TC. Shake table tests of unattached, asymmetric, dual-body systems. *Earthquake Engineering and Structural Dynamics* 2017; **46**(9):1391–1410.
38. O'Reilly, O. M. *Engineering Dynamics A Primer*. New York: Springer-Verlag New York Inc, 2001.
39. Dar A, Konstantinidis D, El-Dakhakhni WW. Seismic response of rocking frames with unsymmetrical piers. *25th Conference on Structural Mechanics in Reactor Technology*. Charlotte, NC; 2019.
40. USNRC. *Design Response Spectra for Seismic Design of Nuclear Power Plants, Regulatory Guide 1.60, Revision 1*. Washington, D.C.: United States Nuclear Regulatory Commission, 1973.
41. USNRC. *Design Response Spectra for Seismic Design of Nuclear Power Plants, Regulatory Guide 1.60, Revision 2*. Washington DC: United States Regulatory Commission, 2014.
42. Newmark, N. M., Blume, J. H., & Kapur, K. K. Seismic Design Spectra for Nuclear Power Plants. *Journal of the Power Division,* 1973;**99**(2), 287-303.
43. Tyson, H. N. *Kinematics.* New York: John Wiley & Sons, Inc, 1966.
44. PTC. Mathcad 15.0. Parametric Technology Corporation, 140 Kendrick Street, Needham, MA 02494, USA. 2012.

45. Dar, A., Konstantinidis, D., & El-Dakhakhni, W. W. Input Motion Scaling for Seismic Evaluation of Rocking Components in Canadian Nuclear Power Plants. *Proceedings of the Canadian Society of Civil Engineering Annual Conference*, CSCE, 2021.

3.13 Tables

Table 3-1 Parameters of a trapezoidal pier.

Parameter	This study	Symmetrical Piers [5] $\phi = \phi'$
μ	$1-\frac{1}{2}\left(\phi-\sqrt{4\phi'^2-3\phi^2+4\phi'+4}\right)$	2
ξ	$\frac{3(\mu+\phi+\phi')}{\mu+2\phi+2\phi'}$	$\frac{3(1+\phi)}{1+2\phi}$
$^{\dagger}I_{on}=\frac{r_o^2}{R^2}$	$\frac{\sin^2\alpha}{6(\mu+\phi+\phi')}\begin{bmatrix}(3\phi+3\phi'+\mu)(\xi^2\cot^2\alpha+1)+\cdots\\ \mu^2(\mu+\phi+1)+\phi^2(\mu+\phi+3)+\cdots\\ \phi'^2(\phi'^2-3)+2\phi\mu\end{bmatrix}$	$\frac{\sin^2\alpha}{6}\left[7+\phi^2+\frac{(1+3\phi)}{(1+\phi)}\xi^2\cot^2\alpha\right]$

$^{\dagger}r_0$ is the radius of gyration of the pier about the pivot point.

Table 3-2: Equivalent block parameters for a rocking frame with symmetrical eccentricities**.**

	Unsymmetrical piers (any geometry) This study $\eta=\mu-2+\eta'$	Symmetrical piers (any geometry) [5] $\eta=\eta',\ q_m=1,\ q_T=2q,\ q_I=1$
α_{eq}	$\tan^{-1}\left(\frac{1+(\mu-1)q_m+(1+\eta)q_T}{1+q_m+q_T\xi}\tan\alpha\right)$	$\tan^{-1}\left(\frac{1+(\eta+1)q}{1+\xi q}\tan\alpha\right)$
λ	$\sqrt{\left(1+(\mu-1)q_m+(1+\eta)q_T\right)^2\sin^2\alpha+\left(1+q_m+q_T\xi\right)^2\cos^2\alpha}$	$\sqrt{(1+(\eta+1)q)^2\sin^2\alpha+(1+\xi q)^2\cos^2\alpha}$
$^{\dagger}\psi$	$1+q_I+\frac{q_T}{I_{on}}\left[(1+\eta)^2\sin^2\alpha+\xi^2\cos^2\alpha\right]$	$1+\frac{q}{I_{on}}\left[(1+\eta)^2\sin^2\alpha+\xi^2\cos^2\alpha\right]$
R_{eq}	$\frac{\lambda}{1+q_m+q_T}R$	$\frac{\lambda}{1+q}R$
I_{eq}	ψI_o	ψI_o
p_{eq}	$p\sqrt{\lambda/\psi}$	$p\sqrt{\lambda/\psi}$

$^{\dagger}I_{on}=r_o{}^2/R^2$, where, r_o is the radius of gyration of the pier about the pivot point.

Table 3-3: Details of rocking frame with unsymmetrical eccentricities ($\boldsymbol{q_m=1}$).

Example 1 Figure 3-3(b) Unsymmetrical Trapezoidal piers

α	α'	μ	ξ	p_p(rad/s)	p_n(rad/s)	e_G^+	e_G^-	I_{on}	η_s	η_s'
0.35	0.434	2.27	2.1	1.918	1.902	0.804	0.764	1.362	0.438	0.168

R (m)	l_B (m)	I_o (m^4)	q_I	q_{OT}	α_T	R_T (m)	l_T (m)	q_{RT}	q_{IT}	q_{LT}
1.957	8.636	26.87	1.053	6.527	1.40	4.587	8.636	2.344	26.608	0.054

Grey cells contain variables that would vary with eccentricity. The listed values are for symmetrical eccentricities, η_s and η_s'.

Example 2 Figure 3-3(c) Symmetrical Rectangular piers

α	α'	μ	ξ	p_p(rad/s)	p_n(rad/s)	e_G^+	e_G^-	I_{on}	η	η'
0.149	0.149	2	2	1.545	1.545	0.967	0.967	1.333	0	1

R (m)	l_B (m)	I_o (m^4)	q_I	q_{OT}	α_T	R_T (m)	l_T (m)	q_{RT}	q_{IT}	q_{LT}
3.082	3.048	70.6	1	0.033	1.279	1.591	2.5908	0.485	0.133	0.257

Eccentricities remain as given and do not vary in this example.

Table 3-4: Details of earthquake records.

Earthquake	Year	Station	Record	PGA (g)
Aegion, Greece	1995	SMA-1 5097	AIGA9501 COMP 3	0.517
Loma Prieta, CA	1989	LGPC	LGP 000	0.563
Northridge, CA	1994	Rinaldi	RRS 228	0.838
Napa Valley, CA	2014	Crockett - Carquinez Br	Chan 3: 180	0.979
San Fernando, CA	1971	Pacoima Dam	PCD 254	1.160

3.14 Figures

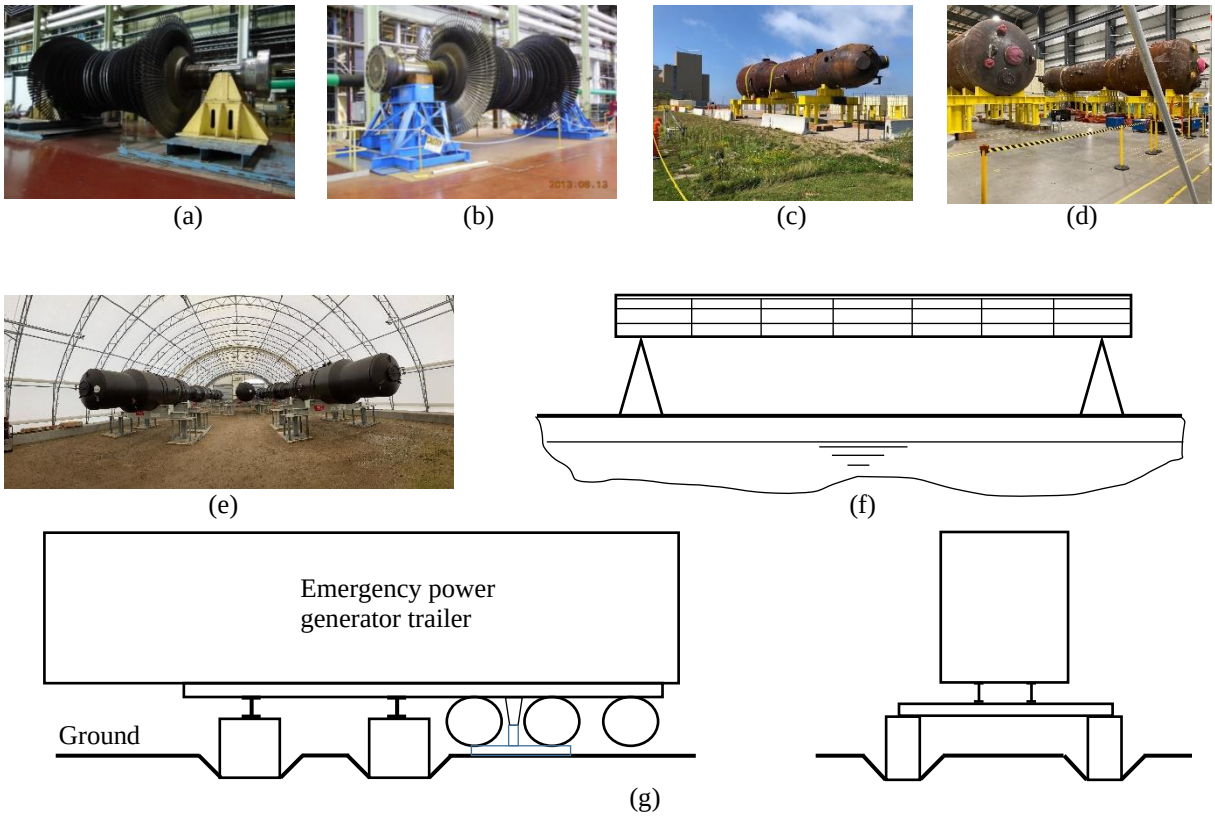

Figure 3-1: Rocking frame **e**xamples in NPPs: (a) and (b) turbine rotors supported by symmetrical and unsymmetrical piers. (c), (d), and (e), steam generators in storage. (f), schematic representation of the 4 Ton 40 feet span man bridge geometry beside the fuel bay pool resting on two triangular steel piers (g) emergency power generator resting on concrete piers with steel beams during maintenance. Photo Curtsey: Bruce Power (Ontario).

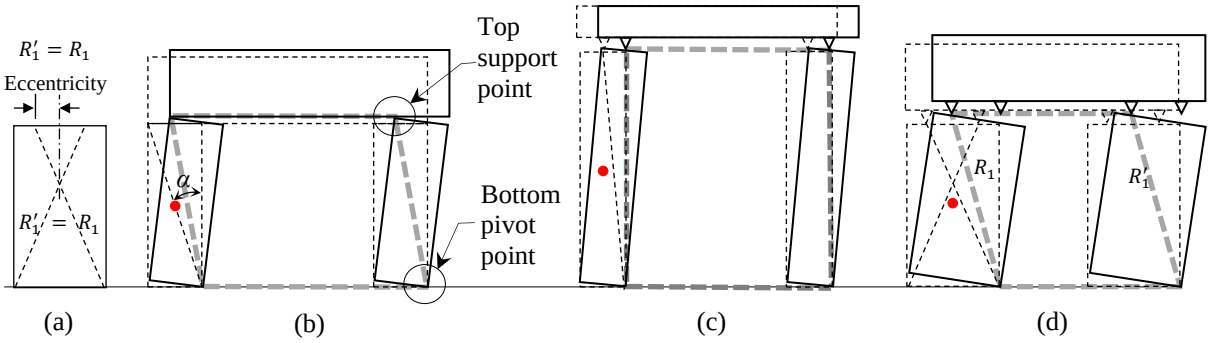

Figure 3-2: Rocking frames with symmetrical piers and symmetrical eccentricity. (a) pier schematics. Top supports at (b) pier corners, (c) pier centers, and, (d) in between the two. Thick dashed grey lines constitute the contact polygon. Red dots represent piers' CG when at rest.

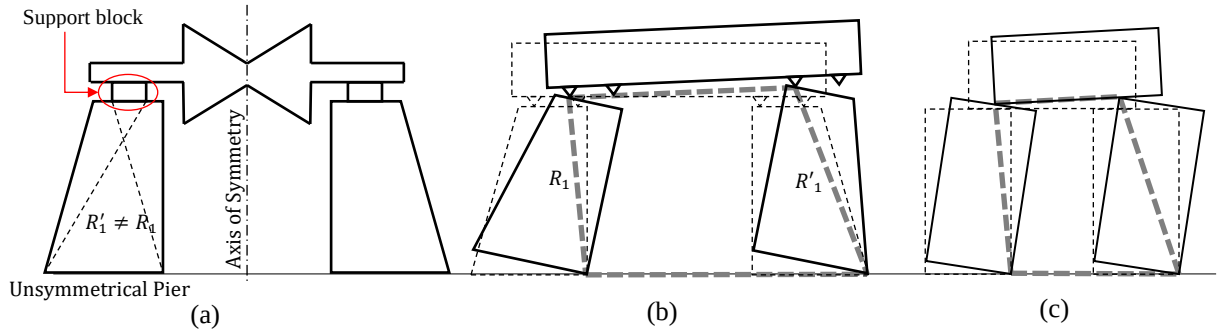

Figure 3-3 Schematics of rocking frames with unsymmetrical eccentricities (a) turbine rotor with unsymmetrical piers (b) simplified representation, and, (c) symmetrical piers

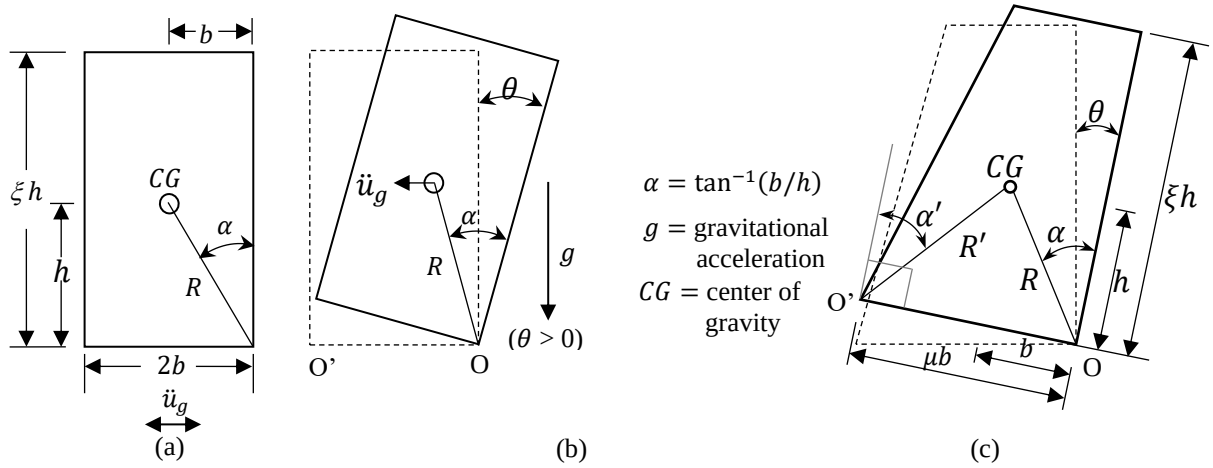

Figure 3-4 Freestanding rigid block Schematic: (a) and (b) rectangular, and, (c), non-rectangular

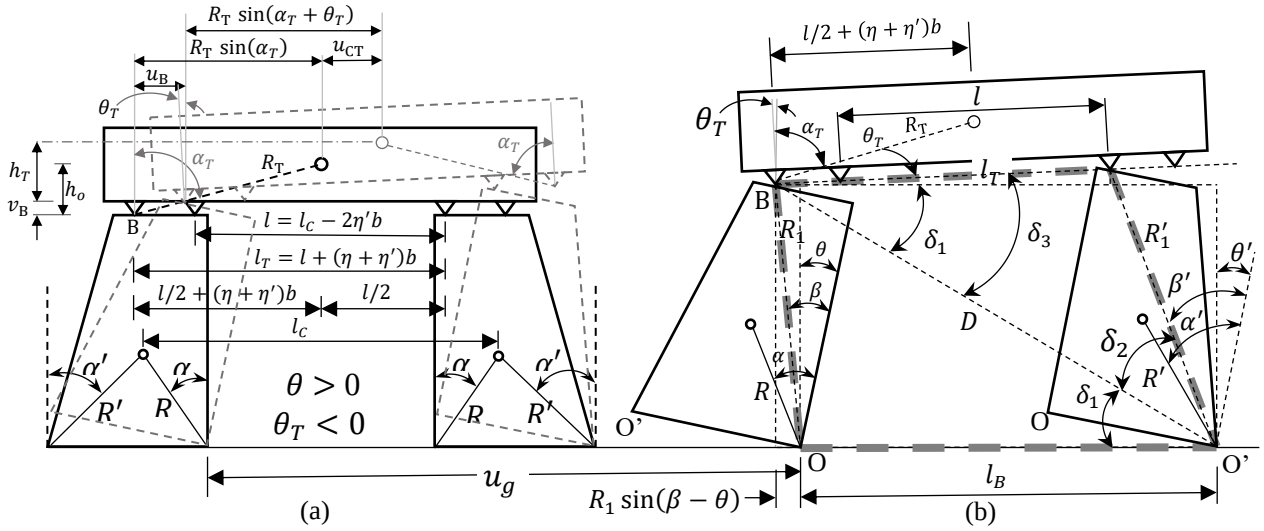

Figure 3-5 Rocking frame: (a) at rest, and, (b) in motion. Contact polygon in grey dashed lines.

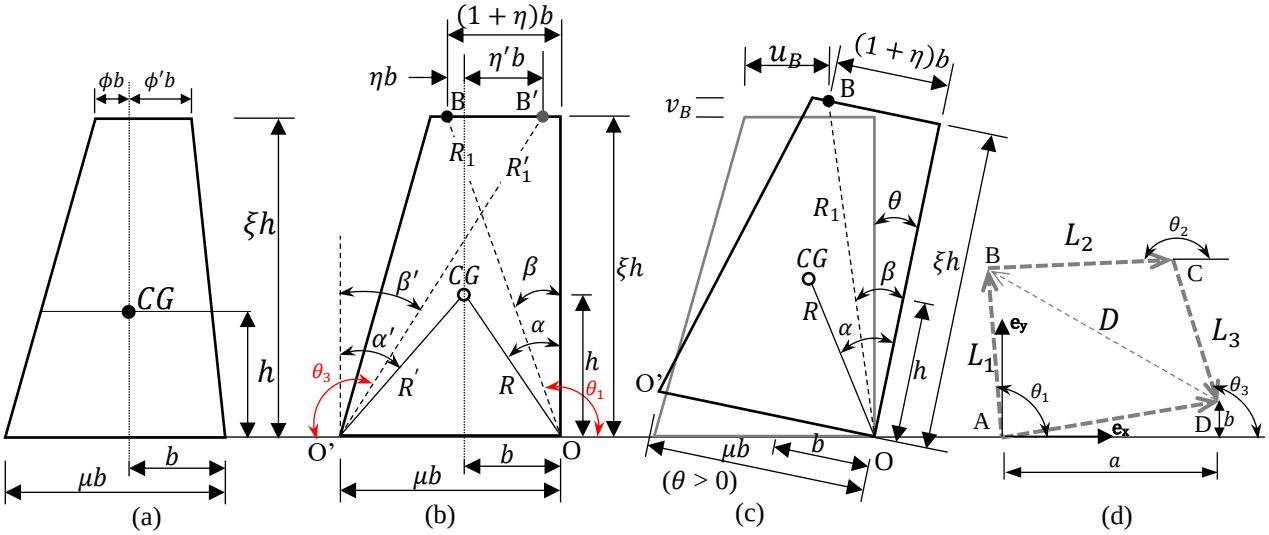

Figure 3-6 Unsymmetrical trapezoidal pier: (a) generic configuration, (b) with $\phi' = 1$ at rest and (c) under rocking motion. (d) vector geometry

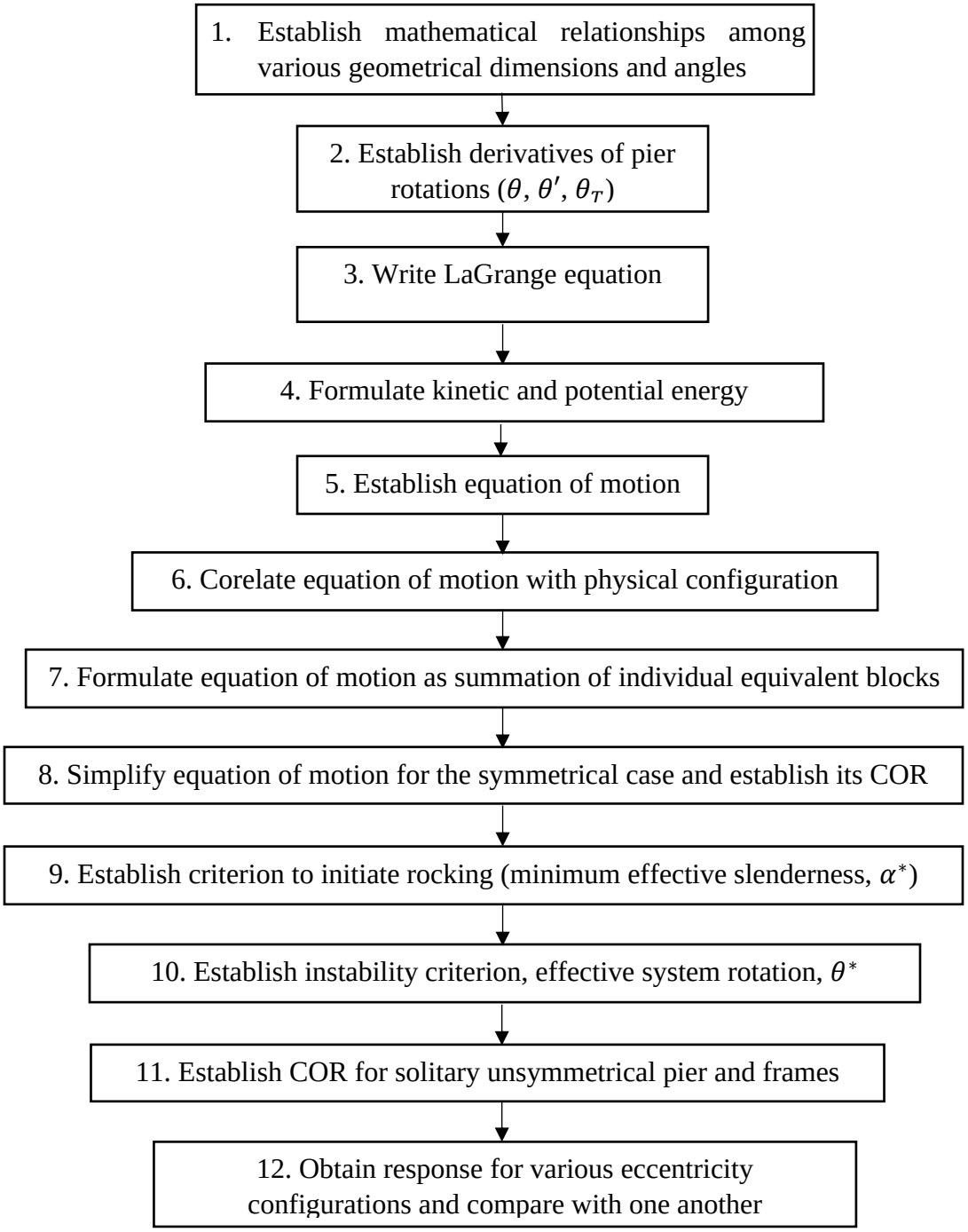

Figure 3-7 Flow chart describing various steps in analysis.

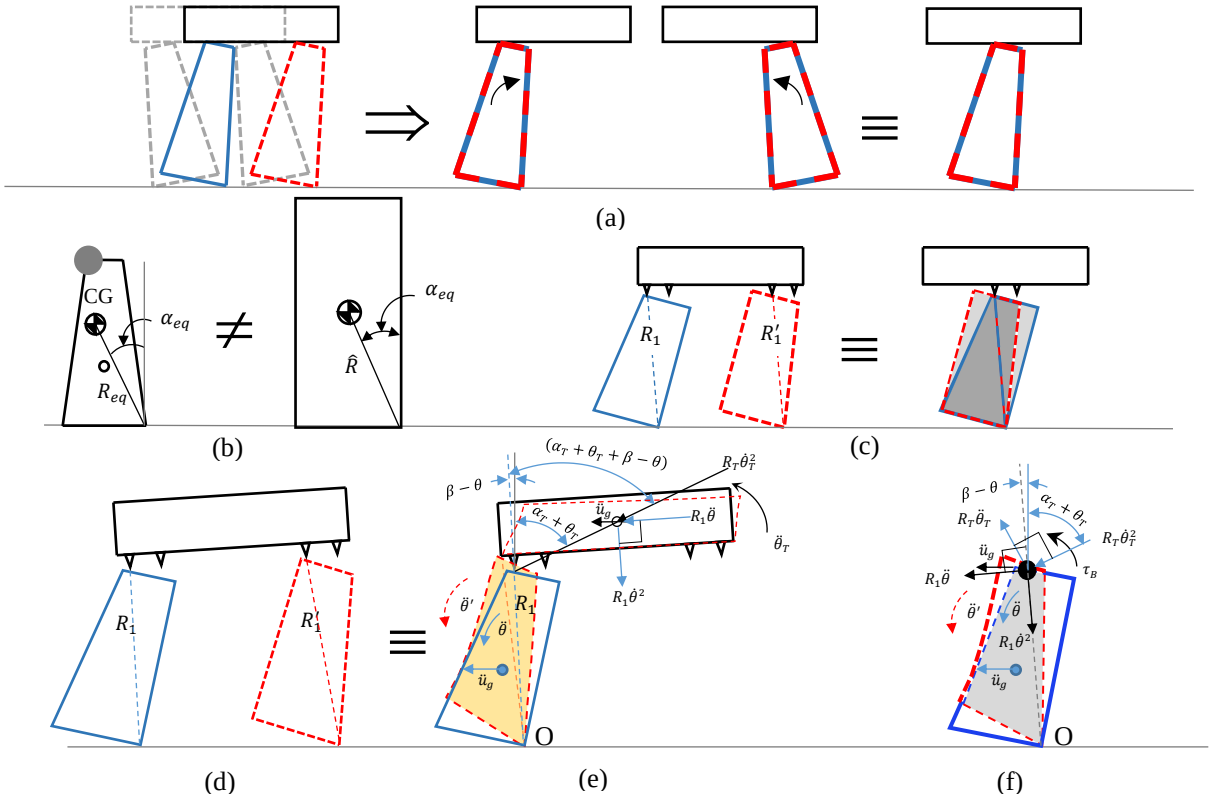

Figure 3-8 "Equivalent Block' concept in rocking frames. (a) symmetrical piers with symmetrical eccentricity (left), merging piers (middle), equivalent SDOF two-block system where top block remains horizontal. (b) equivalent lumped mass and pier system perceived as an equivalent block. (c) unsymmetrical piers with symmetrical eccentricity ($R_1 = R'_1$) and equivalent SDOF two-block system. (d) unsymmetrical eccentricities with unsymmetrical piers. (e) equivalent SDOF two block system with merged piers and beam with mathematical distortions and applicable forces. (f) instantaneous equivalent system with lumped mass, merged piers and applicable forces.

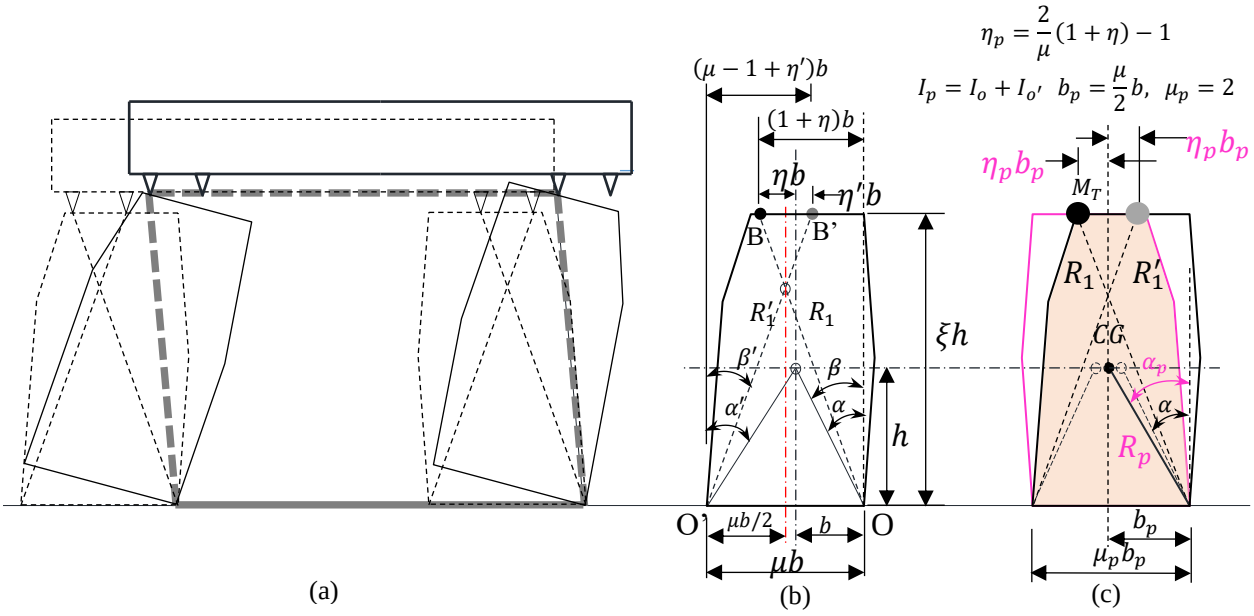

Figure 3-9 Unsymmetrical piers and symmetrical eccentricities: (a) rocking frame in motion. (b) left pier geometry. (c) equivalent system with merged piers, point mass, M_T, and $R_1 = R'_1$. Black and grey dots represent M_T under positive and negative rotations respectively.

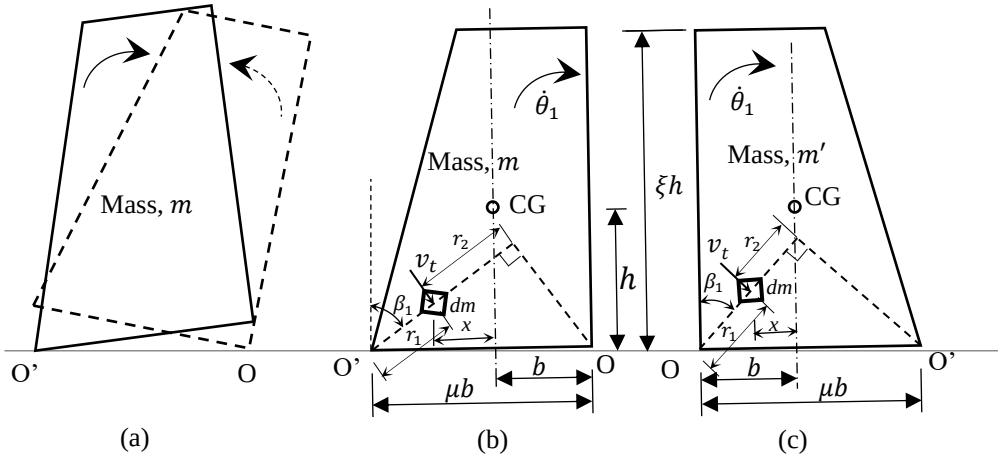

Figure 3-10 Unsymmetrical piers in rocking motion: (a) solitary, (b) left and (c) right pier of rocking frame.

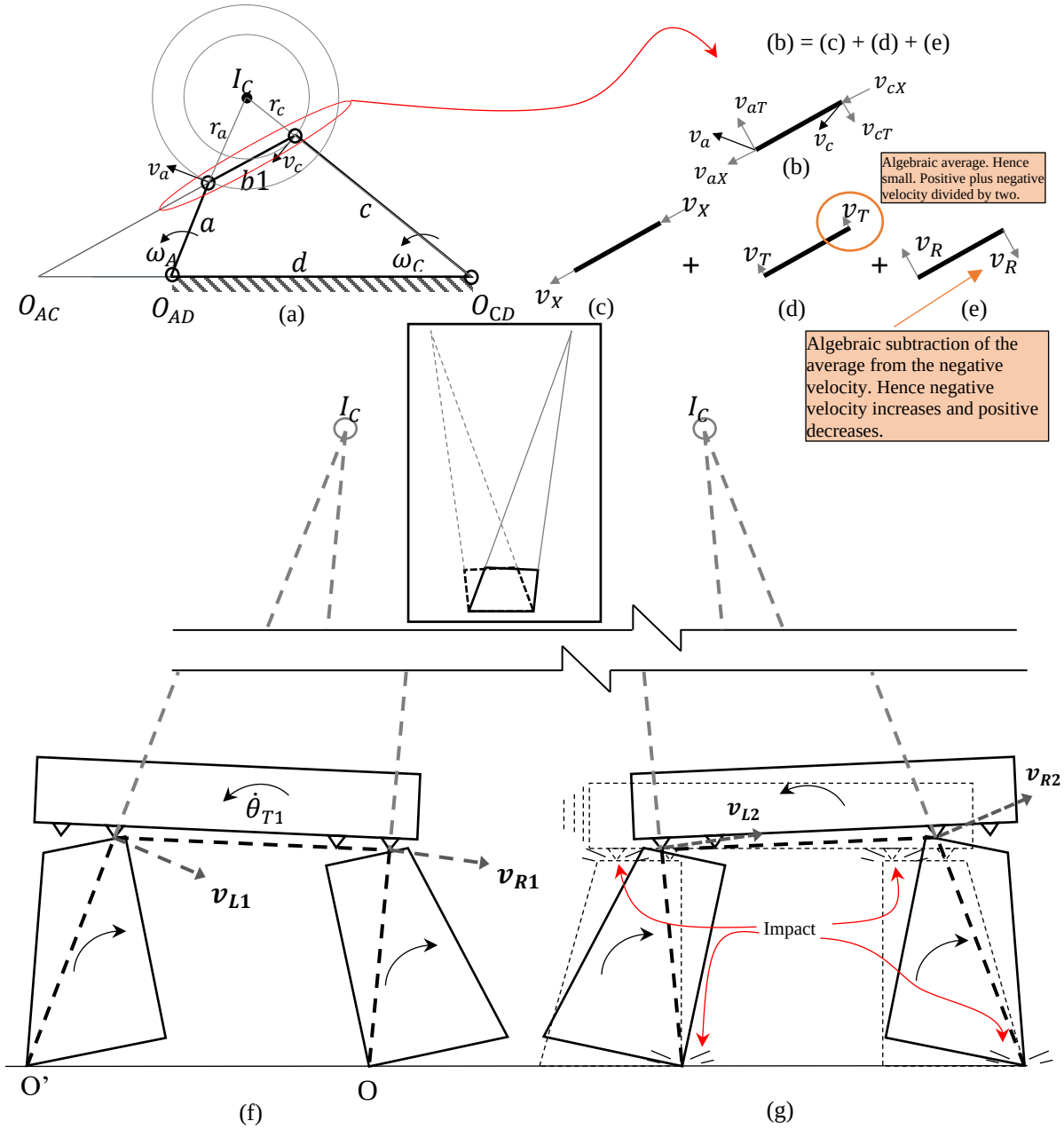

Figure 3-11 (a) Typical four-bar linkage mechanism. (b) Top link with components of velocity vectors in longitudinal and transverse directions. (c) Pure translation with longitudinal velocity components. (d) Pure translation with transverse velocity components. (e) Pure rotation with equal and opposite velocity components. (f) and (g) Rocking frame before and after impact. Inset: Pre and post impact four-links along with the respective instantaneous centers of rotation.

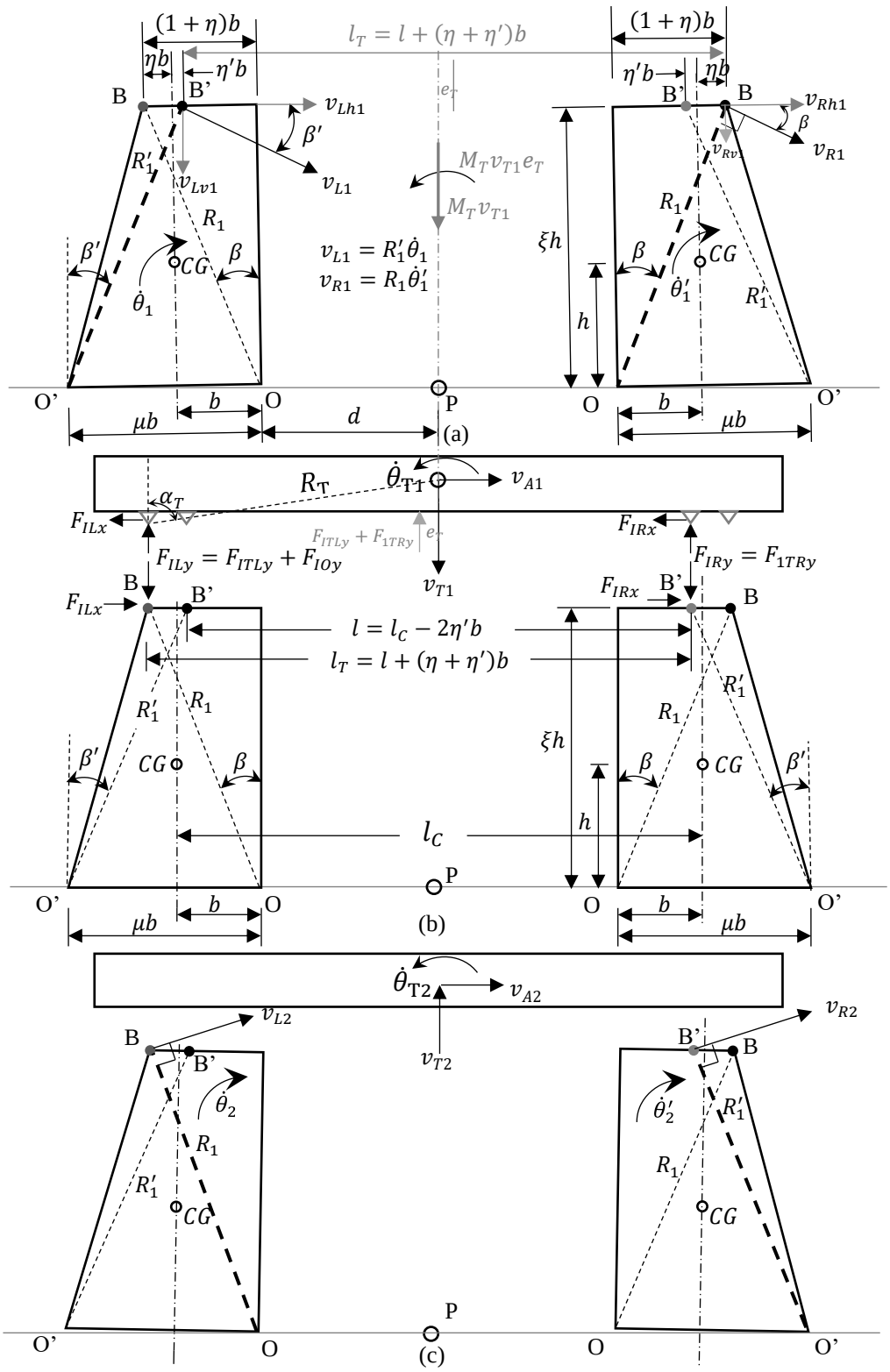

Figure 3-12 Rocking frame piers: (a) just before impact, (b) during impact the beam leaves with the velocity gained just before impact (v_{TL}, v_{TR}), and (c) just after impact.

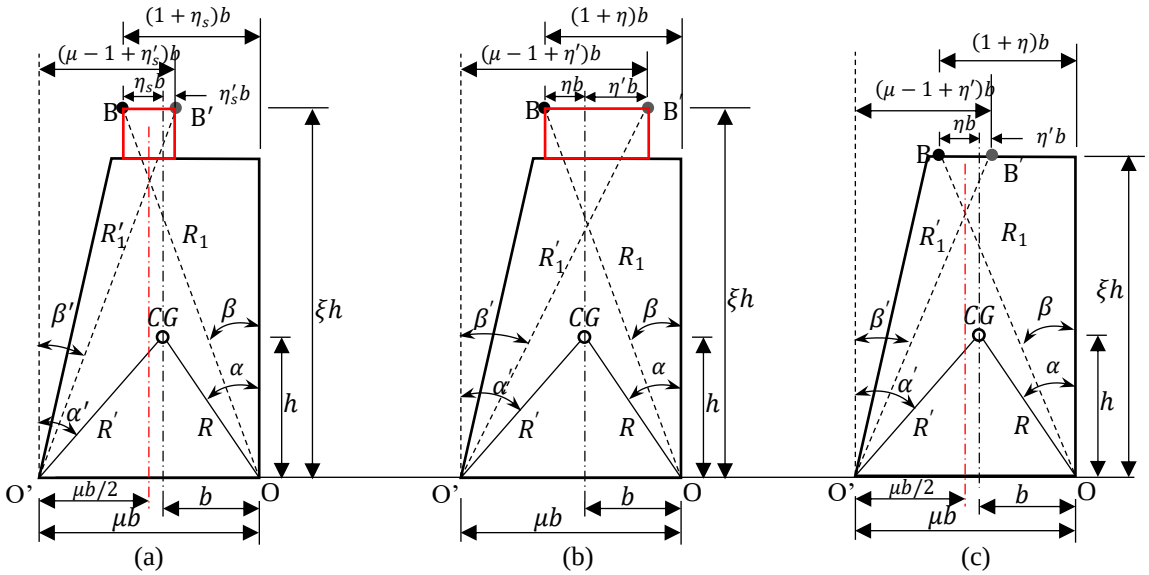

Figure 3-13 Pier with stem: (a) symmetrical, and (b) unsymmetrical eccentricities. (c) idealized configuration without stem.

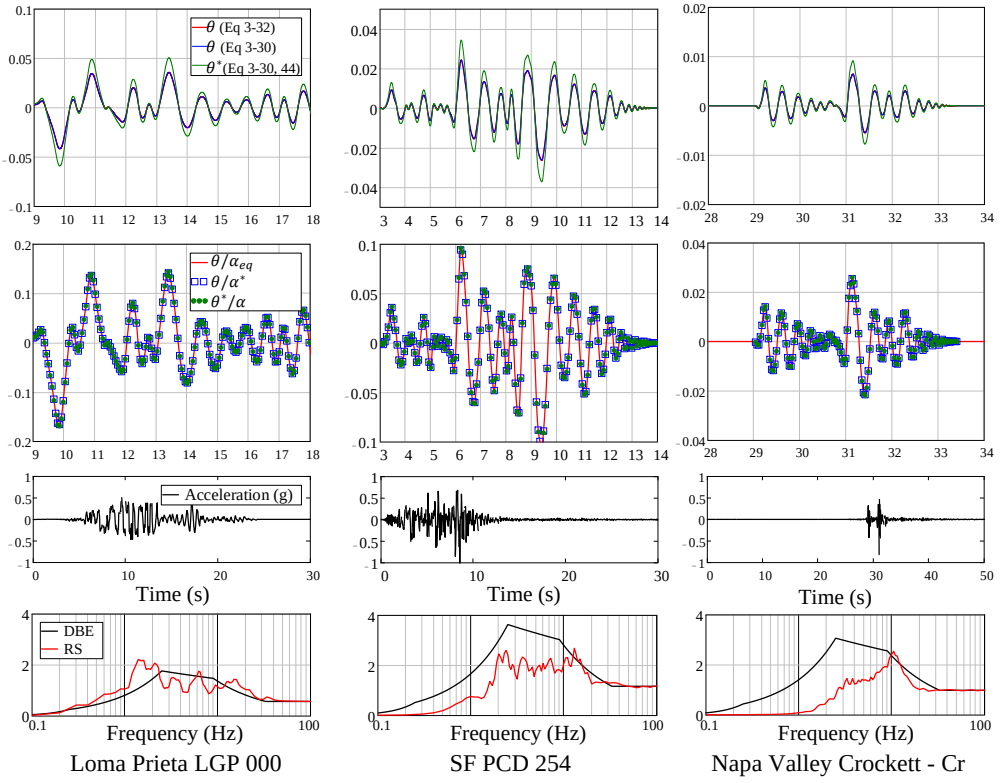

Figure 3-14 Rocking response of Example 1 (Table 3-3) with symmetrical eccentricities and $q_T = 20$. Top two rows: rotational responses by different equations and normalized responses: θ/α_{eq}, θ/α^*, and θ^*/α. Bottom two rows: Excitation time histories and response spectra. COR=0.879.

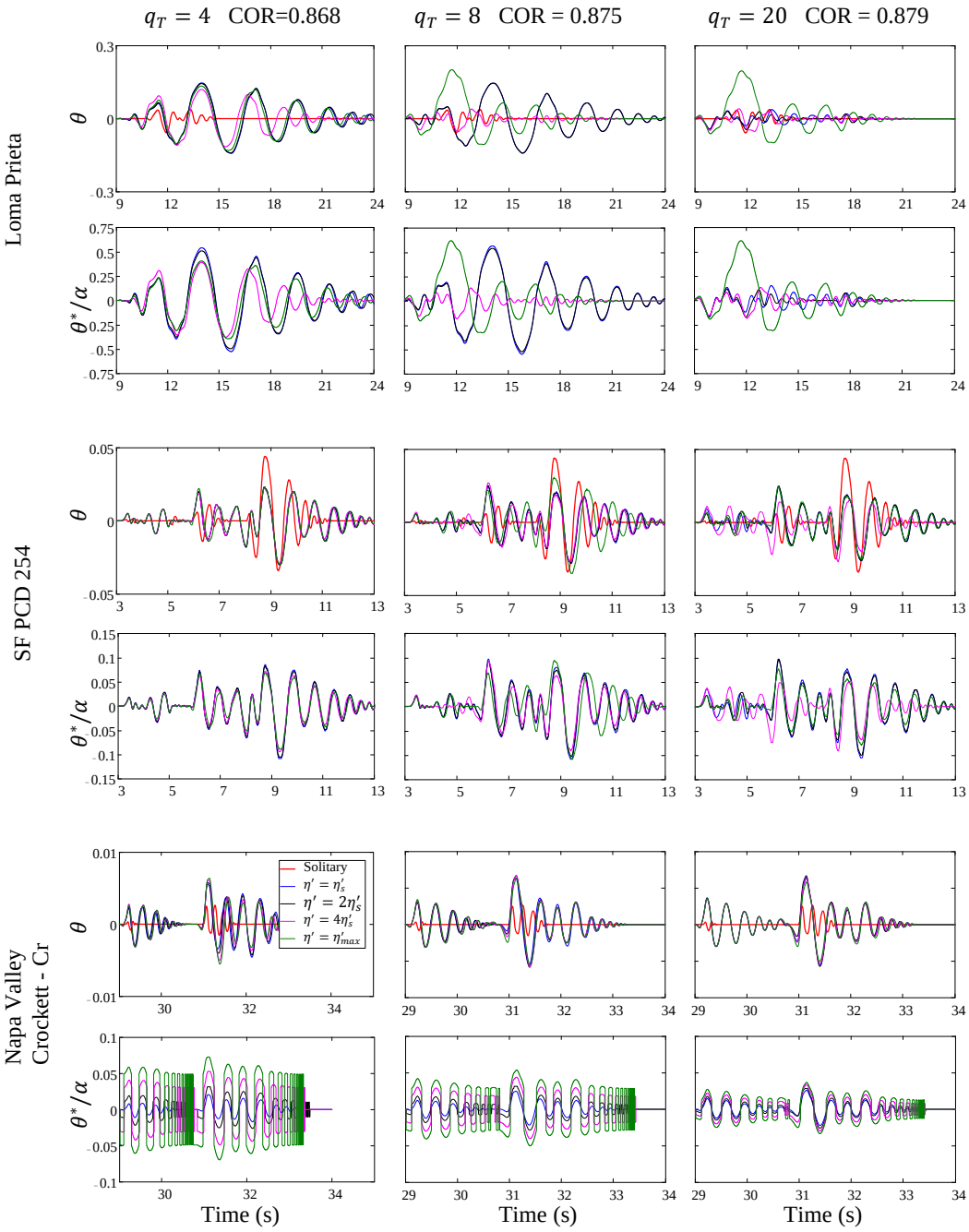

Figure 3-15 Example 1 (Table 3-3) response to earthquake records with $\eta = \eta_s$ and varying $\eta' = \eta'_s, 2\eta'_s, 4\eta'_s, \eta'_{max}$. COR for symmetrical eccentricity case applied to all.

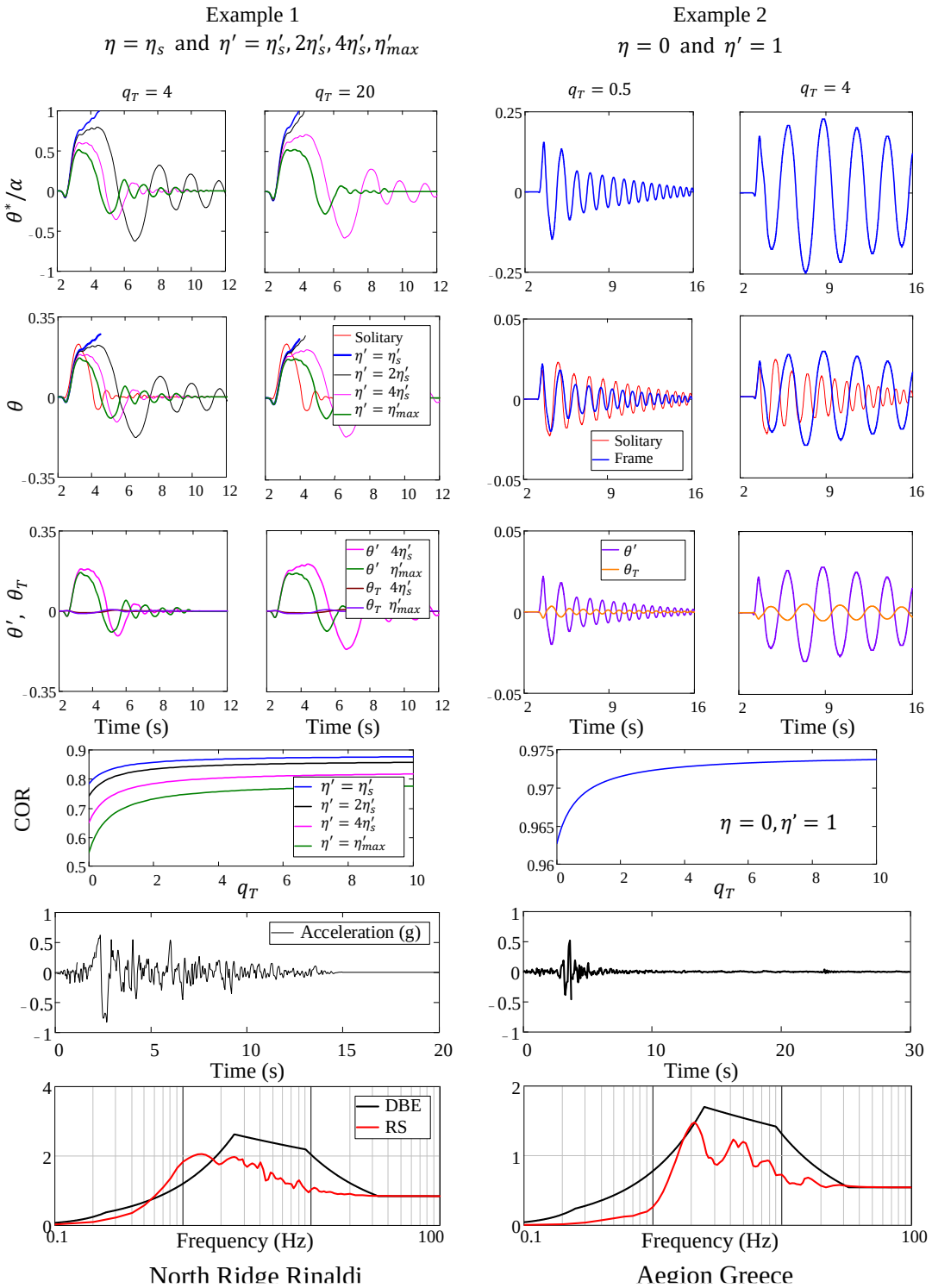

Figure 3-16 Response of rocking frames, Examples 1 and 2 (Table 3-3), to Rinaldi and Aegion records on left and right respectively. CORs are for unsymmetrical eccentricities.

CHAPTER 4

SEISMIC STABILITY OF ROCKING FRAMES UNDER HORIZONTAL EXCITATION

4.1 Abstract

Rocking frames consisting of a beam freely supported by piers, need to be kinematically constrained (or slide-restrained), to maintain frame action during rocking motion. However, in such frames, the beam remains free to lift off or separate from the pier, owing to the beam-pier contact point's downward acceleration exceeding gravity. Under slide-restrained condition, the literature has focused on *rising* blocks leading to overturning as the only mode of instability. To the best of author's knowledge, no attention has been paid to a *falling* block which is more likely to experience separation in comparison to a rising one. Since symmetrically supported rocking frames can be represented by an equivalent block, this study begins with the investigation of a block's separation while returning from its peak rotation or, falling, subjected to the excitation that augments its fall. A novel mode of instability, *Slide-restrained Rocking-induced Separation under Horizontal excitation* (SRSH), is identified and investigated. Equations of horizontal pulse excitations leading to the SRSH failure mode are derived for slender blocks. Instability of a rocking frame due to separation of its beam versus *effective* overturning of the entire system is investigated under symmetrical and unsymmetrical support conditions. Influence of support eccentricity on beam's separation is examined. Simplified semi-empirical expressions for estimating the beam's horizontal and vertical accelerations in a frame are developed. Effectiveness of beam's isolation in rocking motion is investigated. Beam separation and effective overturning of a rocking frame are treated separately, and instability is assumed when one of these exceeds the required criterion.

However, influence of one on the other in a continued rocking response is beyond the scope of this study. Rocking frames are commonly used in nuclear power plants to support heavy components. Accidental drop of such items has been reported to directly influence the nuclear risk. This study provides tools to ascertain seismic risk of a rocking frame's instability under the SRSH failure mode.

4.2 Introduction

A nuclear power plant (NPP) contains several safety systems that are vulnerable to seismic interaction by unanchored components [1] such as tool carts, portable power supply etc. Apart from individual components subject to rocking, their assemblages such as stacked containers or unanchored frames prone to rocking are also required to be studied. Starting from Housner's pioneer work [2], several studies [3-17] have focused on a rocking block's response to various types of excitations. Efforts were also made to obtain the response of a rocking block by considering an equivalent spring-mass-damped oscillator [18, 19]. However, such methodologies were found to lead to erroneous results [20-22].

Many types of rocking assemblages have been studied in the literature including rocking frames [23-31], assemblage of stacked blocks [32-40] and rocking frames as seismic isolation systems [24, 41-45]. The response of a rocking frame represented by an equivalent block [23-25] can be obtained from a rocking spectrum [20]. However, there are some frames that cannot be represented by an equivalent rocking block as discussed by Dimitrakopoulos and Giouvanidis [30]. The authors focused on piers of asymmetric frames with unequal heights but without any consideration of beam separation. Diamantopoulos and Fragiadakis [31] proposed finite element modelling of rocking frames with symmetrical piers as a single-degree-of-freedom (SDOF)

oscillator with negative stiffness based on the equivalent block model and its equation of motion presented in [24]. However, the authors did not discuss the instability of frames due to beam separation.

In NPPs rocking frames are commonly used to support heavy components that may drop down in case of the frame's failure. The drop of a heavy turbine stator in Arkansas Nuclear One was investigated by the United States Nuclear Regulatory Commission (USNRC) [46] and concluded to impact the nuclear risk of the entire NPP. Therefore, all types of failure modes of a rocking frame including the separation of the beam are required to be studied.

A rigid block's rocking motion is influenced by size and slenderness. While the size of a block is represented by its *radius*, the distance of the blocks' geometric center from the pivot, its slenderness is measured in terms of the inclination angle of the radius from the vertical. Stockier blocks with large radius are more stable than slender small blocks. Therefore, if a rocking frame can be converted to an equivalent block with equivalent slenderness, α_{eq} and equivalent radius, R_{eq}, its stability can be compared with that of any other block. However, these two parameters are highly influenced by the support's eccentricity parameter, η, depicted in Figure 4-1(a), defined as the ratio of the distance of the top mass from the center of gravity (CG) of the pier divided by its half base-width [25]. As depicted, equal eccentricity for both piers results in equal distances of top support points from the pivots, $R_1 = R_1'$. Figure 4-1 (b) shows rocking frames analyzed by Makris and Vassiliou [24] with symmetrical piers supporting the top beam at their corners ($\eta = 1$) during rocking motion. Assuming no sliding, the authors established parameters of an equivalent block concluding that a heavier beam results in reduced response. Dar et al. [25] discovered the reason behind this behaviour attributing it to the location of the geometric center of the lumped mass of

the beam and the pier depicted by the red dot in Figure 4-1 (b), being collinear with pivot points in rocking motion, resulting in a higher location of the geometric center (larger size of an equivalent block) with no change in slenderness parameter (α). The authors analyzed frames as shown in Figure 4-1 (c) where the pier's CG is not collinear with pivot points ($\eta \neq 1$). Also, they proved that such systems can be represented by an equivalent block that is a pier-plus-lumped-mass system where the lumped mass represents the beam mass per pier. Figure 4-1 (d) shows the equivalent block or pier-plus-lumped-mass system where the blue dot indicates the system CG with the system radius and slenderness parameters, R_{eq} and α_{eq} respectively.

For both cases shown in Figure 4-1 (b) and (c), because $R_1 = R_1'$, the beam remains horizontal during rocking motion, assuming no sliding. Thus, all sides of the contact polygon shown in thick dashed grey lines remain invariant. Figure 4-1 (e) exhibits application of rocking frames in the context of a podium (e.g., a rigid mobile office), resting on comparatively smaller piers (e.g., triangular shape as shown), quite common to construction projects in NPPs. Figure 4-1 (f) shows a rocking frame having symmetrical pier and unsymmetrical support conditions where the top beam rotates during rocking motion because $R_1 \neq R_1'$. The symmetrical and unsymmetrical support conditions are referenced here onwards as symmetrical and unsymmetrical eccentricities. Figure 4-2 shows more examples of unsymmetrical eccentricities ($R_1 \neq R_1'$) such as a rocking frame in a NPP, consisting of turbine rotors freely supported by unsymmetrical piers in Figure 4-2(a) and its idealized representation in Figure 4-2(b). Figure 4-2(c) illustrates an example of a rocking frame as a temporary support to an emergency power generator (EPG) trailer during maintenance.

Assuming no sliding, rocking frames in the literature [24, 25] are subjected to only one instability criterion, i.e., overturning (rotation > equivalent slenderness parameter, α_{eq}). However, during rocking motion, the beam would separate if the beam-pier contact point's vertical acceleration is less than -g (e.g., if the pier contact point moves downward with acceleration $-1.2g$, the beam being unanchored to the pier will not be able to follow it and separate). Since such frames can be represented by an equivalent block, it is important to understand the phenomenon of separation of an individual block during rocking motion. Several studies have discussed multiple response modes (rocking, sliding, rock-sliding, bouncing etc.) of a rocking block [8-15]. However, separation was considered in the context of sliding or resulting from vertical excitation and not under pure horizontal excitation with restrained sliding conditions achieved by high friction, shear keys or wheel-rail configuration found in movable trolleys or work platforms common to NPPs. Figure 4-2(d) shows mobile elevated work platforms (that move on rails) in fully retracted and extended configurations. When fully retracted, they behave as rigid blocks. Since restricted by rails, their lateral stability is influenced by the SRSH failure mode under transverse horizontal excitation. Figure 4-2(e) shows the picture of an overturned train during 1906 San Francisco earthquake that was analyzed in [13]. This example is revisited in this study.

Pompei et al. [10] examined the possibility of separation (or *jump* as referred therein) for a falling block under free vibration but a rising block under horizontal rectangular pulse excitation. The authors concluded the separation of a slender block to be impossible under free vibration and highly 'unlikely' under forced excitation because sliding precedes, or safeguards against, separation. The authors did not derive conclusive relationships among various parameters such as excitation amplitude and its duration, block's size and slenderness that may lead to separation.

Taniguchi [14] considered vertical reaction of a block resulting from vertical and horizontal excitation but in the context of initiation of sliding response of a rising wide block. Zhang and Makris [13] explored the example of a locomotive, slide-restrained due to engagement of wheels, that overturned during 1906 San Francisco Earthquake without considering the SRSH mode and surmising the overturning to be the only failure mode leading to instability.

Studies on rocking frames as seismic isolation systems [24, 41-45] focused on the horizontal and vertical displacements of the beam. Horizontal acceleration of the top load of a rocking block was obtained in [42] but not in the context of a frame with varying top load and its impact on equivalent radius and slenderness. However, none of these studies explored the vertical acceleration of the beam under horizontal excitation leading to separation. In this study horizontal acceleration response at beam location is obtained along with vertical acceleration and the phenomenon of isolation has been revisited as applicable to the examples considered. As noted by Bachmann et al [41] slender ($\alpha \leq 0.3$) piers in a rocking frame are more suitable for seismic isolation, this study devotes special attention to the SRSH failure mode in slender pier frames. Regarding rocking frames, no evidence could be found in the literature that included obtaining the vertical acceleration of the beam to evaluate the possibility of separation.

Seismic response of rocking frames is influenced by seven parameters: 1. COR, 2. Overturning condition, 3. Separation of the beam from the pier(s) during rocking motion, 4. Pier slenderness, 5. Pier geometry, 6. Beam/pier mass ratio, 7. Eccentricities. This study begins with the investigation of a rocking block's separation under pulse excitations, followed by frames with symmetrical and unsymmetrical eccentricities subjected to pulse excitations and earthquake records that are compatible with the seismic design basis of NPPs prescribed in the USNRC

regulatory guide 1.60 [47, 48] based on the design response spectrum given by Newmark, Blume and Kapur [49]. Semi empirical relationships to ascertain separation of beam in frames are established and compared with the factor of safety of 2, recommended by the nuclear standard, ASCE 43-19 [50]. Sufficient friction including the presence of shear keys is assumed at all support points and no sliding is envisaged but separation of the beam from piers due to vertical acceleration being less than -g is accounted for. Failures by overturning and separation are treated separately and on the failure of anyone of the two modes, the rocking block or system is rendered unstable. The support profile (such as rail and wheel combination or shear keys) is assumed to restrict sliding. Continued rocking motion after separation, and the impact of support profile configuration, e.g., bulged rail top in contact with a worn-out curved wheel surface or any other mechanism such as shear keys, on sliding restriction are beyond the scope of this study. The response of rocking blocks and frames subjected to various pulse excitations and earthquake records is obtained through nonlinear response analysis of equivalent rocking blocks, using a state-space formulation [20] and the AdamsBDF solver [51].

4.3 Review of a Rocking Block and Rocking Frame

Figure 4-3(a) shows a rigid rectangular block with its properties and base excitation defined therein. Figure 4-3(b) shows the rectangular block in positive rotation, θ, with applicable accelerations and reactions. Considering clockwise rotation as positive, the equation of motion of the rocking block is [6]:

$$\ddot{\theta} = -p^2 \left\{ \sin[\alpha \, \mathrm{sgn}(\theta) - \theta] + \frac{\ddot{u}_g}{g} \cos[\alpha \, \mathrm{sgn}(\theta) - \theta] \right\} \tag{4-1}$$

where, sgn(·) is the *signum* function, and $p = \sqrt{mgR/I_o}$ is the natural frequency of the block under free vibration when suspended as a pendulum from its pivot. The parameter p is an indicator of the block size, referenced as size parameter here onwards. Larger the p, smaller is the block. The coefficient of restitution (COR) as the ratio of post-impact and pre-impact velocities, $\dot{\theta}_2$ and $\dot{\theta}_1$is given as [25],

$$e_G = \frac{\dot{\theta}_2}{\dot{\theta}_1} = 1 - \frac{2}{I_{on}} \sin^2 \alpha \tag{4-2}$$

where, I_{on} is the normalized moment of inertia ($I_{on} = I_o/(mR^2) = r_o^2/R^2$), where r_o is the radius of gyration of the block about O.

Figure 4-3(c) shows a vertically unsymmetrical trapezoidal block where the bottom and top width are μb, and $(\mu - \phi - \phi')b$ respectively. Various parameters for this block defined in Chapter 3 are reproduced in Table 4-1. For a symmetrical pier, $\phi = \phi'$. Size parameters for the unsymmetrical configuration are $p_p = \sqrt{mgR/I_o}$, for $\theta > 0$, and, $p_n = \sqrt{mgR'/I_{o\prime}}$, for $\theta < 0$, where R' and $I_{o\prime}$ are computed with respect to the pivot point O'. The equation of motion for this block is

$$\begin{aligned} \ddot{\theta} &= -p_p^2 \left\{ \sin[\alpha - \theta] + \frac{\ddot{u}_g}{g} \cos[\alpha - \theta] \right\} && \text{for } \theta > 0 \\ \ddot{\theta} &= -p_n^2 \left\{ \sin[-\alpha' - \theta] + \frac{\ddot{u}_g}{g} \cos[-\alpha' - \theta] \right\} && \text{for } \theta < 0 \end{aligned} \tag{4-3}$$

Figure 4-3(d) shows a rocking frame with symmetrical trapezoidal piers ($\phi = \phi'$) with mass, m, supporting a beam (mass M_T) and symmetrical eccentricities ($\eta = \phi$) and an idealized

representation of shear keys illustrated as recesses in the beam and the floor (similar to those in [24] for rectangular piers). The horizontal and vertical distance travelled by the beam during rocking motion are depicted as u and v respectively. Figure 4-3(e) shows an equivalent block system for the frame with trapezoidal piers where the point mass, qm, (q = beam mass divided by the number of piers) rests on top of the pier with eccentricity, η [25]. The parameter ϕ defines the shape of the pier. As shown in Figure 4-3(f), $\phi = 1$ represents a rectangle whereas $\phi = 0$ leads to a triangle. Figure 4-3(e) shows the CG of the pier located at distance, R, and angle, α, from the pivot, whereas the CG of the assembly, $\overline{CG}$, is located at the distance, R_{eq}, and angle, α_{eq}, that were defined in Chapter 2 [25] as the radius and slenderness of the equivalent system that represents the frame. The distance of the point mass from the pivot is R_1 (defined in Chapter 2). The ratio, R_1/R_{eq}, is defined as R_{ratio} in this study. As q approaches infinity, R_{ratio} approaches 1. The size parameter of a pier is referred to as p whereas for the equivalent block it is referenced as p_{eq}.

4.4 Stability of a Rocking Block

The overturning condition of a rocking block in the literature [e.g. 20] is considered to be achieved beyond the stage when its potential energy is at its maximum, i.e., $\theta/\alpha = 1$. Apart from overturning, another stability criterion was proposed by Pompei et al [10] that the block may separate from its base, or become *weightless* due to its vertical acceleration becoming less than -g. Differentiating the horizontal and vertical displacements of the CG (Figure 4-3(b)), $H_C = R\sin\alpha - R\sin(\alpha - \theta)$, and, $V_C = R\cos(\alpha - \theta) - R\cos\alpha$, respectively, leads to the horizontal and vertical accelerations of the CG as [10, 13]

$$\ddot{H}_C = R\ddot{\theta}\cos(\alpha\mathrm{sgn}(\theta) - \theta) + R\dot{\theta}^2\sin(\alpha\mathrm{sgn}(\theta) - \theta)$$
$$\ddot{V}_C = R\ddot{\theta}\sin(\alpha\mathrm{sgn}(\theta) - \theta) - R\dot{\theta}^2\cos(\alpha\mathrm{sgn}(\theta) - \theta) \quad (4\text{-}4)$$

The two expressions in Equation (4-4) represent combinations of horizontal and vertical components of tangential ($R\ddot{\theta}$) and centripetal accelerations ($R\dot{\theta}^2$) acting on the block's CG shown in grey in Figure 4-3(b). Equation (4-4) leads to the horizontal reaction, F_x, normal N, and the coefficient of friction demand (COFD), μ_D, as

$$F_x = m(\ddot{u}_g + \ddot{H}_C)$$
$$N = m(g + \ddot{V}_C) \quad (4\text{-}5)$$
$$\mu_D = \frac{|F_x|}{N} = \frac{\ddot{H}_C + \ddot{u}_g}{\ddot{V}_C + g}$$

At an instant during rocking motion, if $\ddot{V}_C = -g$, $N = 0$ and the block would separate from its base. In other words, if the acceleration demand at the CG is less than $-g$, the block would separate. It is to be noted that the COFD in this study is considered as the ratio between the absolute value of F_x and N rather than the absolute value of the entire ratio, $|F_x/N|$, as expressed by Zhang and Makris [13]. Although, $N = 0$ causes the COFD to be infinite and the instability renders further analysis futile, considering the absolute value of the ratio would leave a negative N (representing separation) unrecognized, resulting in an incorrect mathematical model. Also, since exact $N = 0$ may not be captured in numerical analysis owing to the time steps not matching the instant of separation, a negative μ_D would be an indicator of separation. Recognizing, $R = g/p^2 I_{on}$ for a rectangular block, and substituting it in Equation (4-4) gives

$$\ddot{H}_{Cn} = \frac{\ddot{H}_C}{g} = \frac{1}{I_{on}}\left[\frac{\ddot{\theta}}{p^2}\cos(\alpha\text{sgn}(\theta) - \theta) + \left(\frac{\dot{\theta}}{p}\right)^2 \sin(\alpha\text{sgn}(\theta) - \theta)\right]$$
$$\ddot{V}_{Cn} = \frac{\ddot{V}_C}{g} = \frac{1}{I_{on}}\left[\frac{\ddot{\theta}}{p^2}\sin(\alpha\text{sgn}(\theta) - \theta) - \left(\frac{\dot{\theta}}{p}\right)^2 \cos(\alpha\text{sgn}(\theta) - \theta)\right] \quad (4\text{-}6)$$

where $\ddot{H}_{Cn}$, $\ddot{V}_{Cn}$, $\ddot{\theta}/p^2$ and $\dot{\theta}/p$ are the dimensionless or normalized horizontal, vertical, angular accelerations, and angular velocity, respectively. Since the centripetal acceleration would always act downwards (towards the pivot), it is evident that the best opportunity for separation ($\ddot{V}_{Cn} = -1$) exists when the block is falling rather than rising. This situation is represented by the vector schematics shown in Figure 4-3(b). Although, this study assumes sufficient friction (aided by shear keys in a rocking frame) to resist the horizontal force, the COFD is still tracked as a proof of concept because, as demonstrated later, its exponential rise is caused by reduction in $\ddot{V}_C$ rather than the increase in $\ddot{H}_C$. Considering small angle approximation for a slender block turns the expression for $\ddot{V}_{Cn}$ in Equation (4-6) into

$$\ddot{V}_{Cn} = \frac{\alpha^2}{I_{on}}\left[\frac{\ddot{\theta}_n}{p^2}(\text{sgn}(\theta) - \theta_n) - \left(\frac{\dot{\theta}_n}{p}\right)^2\right] \quad (4\text{-}7)$$

Where, $\theta_n = \theta/\alpha$, is normalized rotation. The possibility of separation ($\ddot{V}_{Cn} = -1$) is investigated below for slender blocks subjected to pulse excitations with special attention on a falling block. Zhang and Makris [13] investigated overturning of unrestrained blocks caused by cycloidal pulses resembling shapes in earthquake records [7]. The cases reported therein demonstrated that overturning took considerable time (≈3s) after the pulse expiry because a block teeters for a while when close to its maximum rotation before eventually overturning. Since

earthquake records continue long after the expiry of a pulse integrated within, a teetering block may return to stability, undergo stable vibration, or eventually overturn in a realistic scenario once the pulse has expired. Since the focus is on the excitation that augments the fall of a block, the best opportunity for separation exists within the pulse duration rather than after its expiry. Therefore, the response to a pulse within the pulse duration leading to separation is likely to be closer to reality rather than after its expiry in an earthquake record especially looking at the sensitivity of the response "to the nonlinear nature of the problem" [7]. Hence, the focus in this section is on a block's separation before the pulse expiry.

According to Makris and Vassiliou [16], the rectangular pulse is the most conservative of all pulse excitations to arrive at the minimum slenderness of a block that ensures stability against overturning. Therefore, the rectangular pulse is chosen for the conceptual study of a falling block. For the ease of segregation of a block's response pertaining to the slenderness parameter, α, rectangular blocks are categorized as: 1. Slender ($\alpha \leq 0.3$), 2. Wide, ($0.3 < \alpha < 0.95$) and 3. Super wide ($\alpha \geq 0.96$). The threshold of 0.96 emanates from the COR being negative (for $\alpha = 0.955$ in Equation (4-2)). The negative COR was considered as zero in [25]. Figure 4-4(a) shows a falling slender block under free vibration rotating counter clockwise, having slenderness parameter as α_1 and it compliment as α_2. In this condition, the tangential acceleration acts downwards towards left. Figure 4-4(b) shows a rising slender block subjected to a rectangular pulse excitation resulting in clockwise rotation and upward tangential acceleration. The clockwise overturning of this block is illustrated in Figure 4-4(c) where it turns into a super wide block of slenderness parameter, α_2 ($= \pi/2 - 0.3 = 1.271$ for $\alpha_1 = 0.3$). Applying small angle approximation turns Equation (4-1) into to the following

$$\ddot{\theta}_n = -p^2\left\{\text{sgn}(\theta_n) - \theta_n + \ddot{u}_{gn}\right\} \tag{4-8}$$

Where, $\theta_n = \theta/\alpha$ and $\ddot{u}_{gn} = \ddot{u}_g/\alpha g$ (normalized excitation).

The focus is on a falling block while retreating in free vibration regime from its peak rotation, $\theta = \alpha^-$ (where $\dot{\theta} = 0$), and reaching $\theta = 0^-$. Several instances of pulse application that augments the fall of the block are possible between the two extremes: 1. $\theta = 0^-$, i.e., just before impact, and 2. $\theta = \alpha^-$, i.e., just before overturning. Figure 4-4(d) shows a block under free vibration returning from the peak rotation (or falling), struck by a rectangular pulse just before impact. Figure 4-4(e) shows the block as in (a), under free vibration rotating anticlockwise just short of overturning, at $\theta = \alpha^-$, that is struck by a rectangular pulse that aids to its fall. The analysis below relates to the stages of the slender block shown in Figure 4-4. The impact timing is referenced as 'just before' or 'just after' in the context of angular velocity and acceleration because of the jump-discontinuities caused by impact. The jump-discontinuities in rotational acceleration ($\ddot{\theta}$) are demonstrated in Figure 4-4(f) that illustrates the normalized response of a rectangular slender block excited by a rectangular acceleration pulse shown in green causing it to rise up to the expiry of the pulse, followed by its free vibration regime. Figure 4-4(f) is included at this stage only for reference to demonstrate a slender block's behavior during and after the pulse excitation. As illustrated, the vertical acceleration is positive when the block is rising but instantly becomes negative at the expiry of the pulse.

4.4.1 Free vibration (Figure 4-4(a))

Housner's free vibration solution of Equation (4-8) for $\ddot{u}_{gn} = 0$, subject to the initial conditions, $\theta(0) = \theta_o$ and $\dot{\theta}(0) = 0$, and the normalized time of impact, pt_i, are given as [2]

$$\theta_n = 1 - \left(1 - \frac{\theta_o}{\alpha}\right)\cosh pt \qquad pt_i = \cosh^{-1}\frac{1}{\left(1 - \frac{\theta_o}{\alpha}\right)} \tag{4-9}$$

Equation (4-9) leads to the angular velocity and acceleration just before impact when the block is released from the initial normalized rotation θ_o/α, as

$$\dot{\theta}\big|_{pt=pt_i} = -\alpha p\sqrt{2\frac{\theta_o}{\alpha} - \left(\frac{\theta_o}{\alpha}\right)^2} \quad \text{and} \quad \ddot{\theta}\big|_{pt=pt_i} = -\alpha p^2 \tag{4-10}$$

For $\theta_o = \alpha$, Equation (4-10) yields $\dot{\theta}/p = \ddot{\theta}/p^2 = -\alpha$. Substituting $\theta_n = 0$ (just before impact), $\dot{\theta}_n/p = \ddot{\theta}_n/p^2 = -1$, in Equation (4-7) gives the vertical acceleration at the CG of the block as

$$\text{For } \theta_o = \alpha \qquad \ddot{V}_{Cn1} = -\frac{2\alpha^2}{I_{on}} \qquad\qquad \text{For } \ddot{V}_{Cn1} = -1, \quad \alpha = \sqrt{\frac{I_{on}}{2}} \tag{4-11}$$

The subscript 1 is used to denote the vertical acceleration under free vibration. Substituting $I_{on} = 4/3$ for rectangular blocks leads to $\alpha = \sqrt{2/3} = 0.81$, a large value not applicable to slender blocks, indicating that separation of a slender block is impossible under free vibration as observed in [10]. It is interesting to note that while angular velocity depends on θ_o, the angular acceleration is independent of any such constraint. Hence, at extremely small rotation under free vibration ($\theta_o \approx 0$ for each cycle), the normalized angular acceleration switches back and forth between αg, and, $-\alpha g$, and the normalized angular velocity $\dot{\theta}/p \approx 0$, results in the vertical acceleration (Equation (4-7)) remaining practically constant at $-\alpha^2 g/I_{on}$, till the rotation reaches zero at infinite time. This is verified later in the section on response to pulse excitation.

4.4.2 Rectangular pulse excitation (rising block in Figure 4-4(b))

Housner [2] provided the following solution of Equation (4-8), $\theta_n = \theta/\alpha$, for a rectangular pulse excitation, $\ddot{u}_g = -a_p$, with initial conditions $\theta_n = \dot{\theta}_n = 0$, as

$$\theta_n = (a_n - 1)(\cosh pt - 1) \tag{4-12}$$

Where, $a_n = a_p/\alpha g$, addressed as normalized amplitude hereinafter. According to Dar et al [25], the relationship between a_n and pulse duration, pT_p, required to achieve $\theta_n = 1$, as given in [2] can be expressed as

$$pT_p = -\ln\left(1 - \frac{1}{a_n}\right) \tag{4-13}$$

As the block rises under pulse excitation, velocity increases and $\ddot{V}_C$ decreases. Substituting the derivatives of Equation (4-12) in Equation (4-7) and considering $\ddot{V}_{Cn} = 0$ first and then $\ddot{V}_{Cn} = -1$ gives the following relationships between the normalized amplitude and duration of the rectangular pulse.

$$\text{For } \ddot{V}_{Cn} = 0 \qquad pT_{pz} = \cosh^{-1}\left[\frac{a_n + \sqrt{a_n^2 + 8(a_n - 1)^2}}{4(a_n - 1)}\right]$$

$$\text{For } \ddot{V}_{Cn} = -1 \qquad pT_{ps} = \cosh^{-1}\frac{1}{4(a_n - 1)}\left[a_n + \sqrt{a_n^2 + 8(a_n - 1)^2 + \frac{8I_{on}}{\alpha^2}}\right] \tag{4-14}$$

Figure 4-5(a) compares Equation (4-13), depicted as Housner's overturning limit, and Equation (4-14) as zero vertical acceleration ($\ddot{V}_{Cn} = 0$) and separation timing ($\ddot{V}_{Cn} = -1$),for various values of α for a rectangular block ($I_{on} = 4/3$). As evident, the minimum pulse duration required to cause

instability represented by the Housner limit governs. While this situation may be ignored when overturning is considered as a 'failure', it may influence the analysis based on [13] and [15] where the 'survival' of rocking blocks beyond overturning criterion ($\theta_n > 1$) has been reported because such blocks may become unstable due to separation if not accounted for in analysis that assumes no sliding. The Housner limit represents the duration of the pulse after which the block overturns in its free vibration regime [25]. However, for a pulse to cause separation before overturning in a rising block it will have to continue beyond Housner limit with an extremely large amplitude as explained below. Substituting Equation (4-14) in (4-12) leads to

$$\text{For } \ddot{V}_{Cn} = 0 \qquad \theta_{nz} = \frac{1}{4}\left(\sqrt{a_n^2 + 8(a_n - 1)^2} - 3a_n + 4\right)$$

$$\text{For } \ddot{V}_{Cn} = -1 \qquad \theta_n = \frac{1}{4}\left(\sqrt{a_n^2 + 8(a_n - 1)^2 + \frac{8I_{on}}{\alpha^2}} - 3a_n + 4\right) \tag{4-15}$$

Equation (4-15) is plotted in Figure 4-5(b) illustrating that zero vertical acceleration is achieved at $\theta_n = 1/3$ for almost all amplitudes, a_n, except for small ones. Dashed red lines depict $\theta_n = 1$, where separation and overturning occur concurrently for $\alpha = 0.3$, subjected to $a_n = 8$. At $\theta_n = 1$, the tangential acceleration ($R\ddot{\theta}$) being horizontal, plays no role in vertical acceleration. Substituting $\theta = \alpha$, and $\ddot{V}_C = -g$, and considering the terms of $\ddot{\theta}$ as zero, in Equation (4-4) leads to the tangential velocity, $R\dot{\theta} = \sqrt{gR}$ which is the same as the minimum velocity required for an automobile to jump over a bump of radius R, as a classical physics example. Substituting $\theta_n = 1$ in Equation (4-15) for $\ddot{V}_{Cn} = -1$ leads to the relationship between the rectangular pulse amplitude and a block's slenderness for coinciding separation with overturning as,

$$a_{nso} = \frac{1}{2}\left(\frac{I_{on}}{\alpha^2} + 1\right) \tag{4-16}$$

Equation (4-17) is plotted as the middle curve in Figure 4-5(c) for a rectangular block ($I_{on} = 4/3$).

4.4.3 Secondary pulse excitation during free vibration (falling block)

This section investigates a falling block struck by a rectangular pulse that augments its fall. Two extremes of excitation application are discussed below, just before impact, with initial condition $\theta = 0^-$, and just before overturning, at $\theta = \alpha^-$ as depicted in Figure 4-4(d) and (e).

4.4.3.1 Secondary rectangular pulse excitation just before impact at $\theta = 0^-$ (Figure 4-4(d))

If the block is struck by a pulse when at rest, it would pivot around O'. But in this case, the block is already pivoting around O. Since the pulse strikes just before impact, its own time of occurrence is considered as $t = 0$. Substituting $-a_n$ in place of a_n in Equation (4-12), gives the velocity and acceleration experienced by the block just at the beginning of the pulse excitation, at time $t = 0^+$, as

$$\frac{\dot{\theta}_n}{p} = -(a_n + 1)(\sinh pt)|_{t=0^+} = 0, \qquad \left.\frac{\ddot{\theta}_n}{p^2}\right|_{t=0^+} = -(a_n + 1) \tag{4-17}$$

Substituting Equation (4-17) in Equation (4-7) yields additional vertical acceleration caused by the new pulse just before impact as

$$\ddot{V}_{Cn2} = -\frac{\alpha^2}{I_{on}}(a_n + 1) \tag{4-18}$$

Under the free vibration before the pulse strike, the block has its own vertical acceleration due to the free fall given by Equation (4-11). Adding the two vertical accelerations: Equation (4-11) and Equation (4-18), and considering $\ddot{V}_{Cn} = \ddot{V}_{Cn1} + \ddot{V}_{Cn2} = -1$, leads to the following relationship between pulse amplitude and slenderness of a rectangular block ($I_{on} = 4/3$).

$$\ddot{V}_{Cn} = \ddot{V}_{Cn1} + \ddot{V}_{Cn2} = -\frac{\alpha^2}{I_{on}}(a_n + 3) \quad \Rightarrow \quad a_n = \frac{I_{on}}{\alpha^2} - 3 \tag{4-19}$$

Equation (4-19) is plotted as the top curve in Figure 4-5(c) where, slenderness limit of $\alpha = 0.3$ is marked by a dashed line.

4.4.3.2 Secondary rectangular pulse excitation just before overturning at $\theta = \alpha^-$ (Figure 4-4(e))

Figure 4-4(e) depicts a rectangular pulse striking the block that just begins retreating from the verge of overturning at $\theta = \alpha^-$ under free vibration. The solution to such excitation subject to the initial conditions $\theta(0) = \alpha^-$ and $\dot{\theta}(0) = 0$ is obtained as

$$\theta_n = a_n(1 - \cosh pt) + 1 \tag{4-20}$$

And the normalized time of impact with a continued pulse is

$$pT_{pi} = \cosh^{-1}\left(1 + \frac{1}{a_n}\right) \tag{4-21}$$

The normalized time of separation with a continued pulse is obtained as

$$pT_{ps} = \cosh^{-1}\left(\frac{1}{4} + \sqrt{\frac{I_{on}}{2\alpha^2 a_n^2} + \frac{9}{16}}\right) \tag{4-22}$$

Equating the timing of impact with that of separation in Equations (4-21) and (4-22) gives the minimum amplitude of the pulse (applied at $\theta = \alpha^-$) required to cause separation just before impact as

$$a_{ns} = \frac{1}{3}\left(\frac{I_{on}}{\alpha^2} - 2\right) \tag{4-23}$$

Equation (4-23) is plotted in Figure 4-5(c) as the lower curve for a rectangular block ($I_{on} = 4/3$). Figure 4-5(c) compares the slenderness required for separation to occur just before impact due to two extremes of excitation application: just before impact and just before overturning depicted by the top and bottom curves respectively. The gap between the two below the slenderness limit, $\alpha = 0.3$, (dashed red line) denotes several possibilities of excitation amplitudes applicable to various values of slenderness that would cause separation just before impact of a slender block. As illustrated by the bottom curve in Figure 4-5(c) for $\alpha = 0.3$, the amplitude of the pulse required to cause separation just before impact, is $a_n \approx 4$. This is about half of that required for a rising block, $a_n \approx 8$, as shown in Figure 4-5(b) to achieve $\ddot{V}_{Cn} = -1$ at overturning ($\theta_n = 1$). Beyond $a_n = 8$ in Figure 4-5(c), the gap between the top and the bottom curve is practically bisected by the middle curve that belongs to a rising block depicting Equation (4-16). Still, several possibilities of separation exist between the middle and the bottom curve. For example, at $\alpha = 0.2$, the lower curve leads to $a_n \cong 10$, whereas the middle curve leads to $a_n \cong 18$. Thus, Figure 4-5(c) demonstrates that much lesser acceleration is required to achieve separation of a falling block in comparison to a rising one.

Substituting derivatives of Equation (4-20) into Equation (4-7) gives the equation for vertical acceleration caused by a pulse excitation just before overturning as

$$\ddot{V}_{Cn} = \frac{1}{I_{on}}\left(\frac{a_p}{g}\right)^2 [\cosh pt - \cosh(2pt)] \tag{4-24}$$

Equations (4-14) and (4-22) relate to the normalized moment of inertia, I_{on}. Larger the I_{on}, longer is the timing of separation. Vertical acceleration in Equations (4-19) and (4-24) is inversely proportional to I_{on}. Thus, two blocks with equal slenderness (α) and size (p) but different geometry, will experience an identical rotational response (obtained from Equation (4-1)) to a given excitation but the one with smaller I_{on} would be more at risk due to separation than the other. In case of a symmetrically supported frame by slender rectangular piers with eccentricity $\eta = 1$, having the beam mass much larger than the pier mass (Figure 4-3(e)) would render its equivalent block's $I_{on} \approx 1$, resembling a stick-mass system. Hence, a top-heavy frame (with $\eta = 1$) would be less stable than the solitary pier under the SRSH failure mode. The general conclusion in [24] that top-heavy frames are always more stable than their lighter counterparts (considering overturning as a failure mode) was proven by Dar et al [25] to be not necessarily true when $\eta \neq 1$. However, as shown above, it cannot be considered true even for $\eta = 1$ when the SRSH is considered as a failure mode. This is demonstrated later in Section 4.6.3 with an example. Table 4-2 lists the summary of Equations in Sections 4.4.1 and 4.4.3.

4.4.4 Hybrid Excitation: Combination of rectangular pulses for slender blocks

The analysis so far consisted of individual pulses where the block rises to overturning limit (under free vibration after pulse expiry) caused by one pulse and while retreating, is struck by another in the direction opposite to the first one. However, since the duration of the first pulse to

cause overturning is less than that required for the block to overturn, there will be considerable time gap between the two pulses. Figure 4-6(a) shows this scenario where part 1 of excitation makes the block rise and reach the overturning limit when part 2 strikes in the opposite direction. Such piecemeal excitation is not compatible with a practical realistic scenario of continuous excitation. Figure 4-6(b) shows continuous excitation as a combination of rectangular pulses where a negative amplitude $(-a_{p1})$ pulse makes the block rise in positive rotation. The second pulse (amplitude a_{p2}) strikes at time, t_{p1}, the end of the first pulse. The block keeps rising to the brink of overturning ($\theta = \alpha^-$) up to time, $t_{p1} + t_{pk}$, reaches peak rotation and starts falling back. Separation occurs at time t_s relative to the overturning or peak rotation stage. A third pulse with amplitude, $-a_{p2}$, strikes that would make the block rise again. While analyzing such scenario under restricted sliding condition, if the SRSH failure mode is ignored, the analysis would render the block as safe but in reality, it would separate from its base. Combination of pulses with different periods and magnitudes is referred hereinafter as hybrid excitation or hybrid pulse. Figure 4-6 shows the falling block's rotation and the excitation (part 2) as positive. Meaning, to augment a block's fall, the excitation should carry the same sign as of the rotation. This is verified later for earthquake records in Section 4.8.3.

Equation (4-12) is applicable as the solution for the first pulse (part 1) up to time t_{p1}. For part 2, the pulse with amplitude, a_{p2}, with its initial normalized time $pt = 0$, would begin at the expiry of part 1 at time, t_{p1}. Considering the initial conditions $\theta(t_{p1})$ and $\dot{\theta}(t_{p1})$, at $pt = 0$, the solution of Equation (4-8) for the second pulse (part 2 in Figure 4-6(b)) is derived as

$$\theta_n = -a_{2n}(\cosh pt - 1) + \left[(a_{1n} - 1)\cosh\left(p\left(t_{p1} + t\right)\right) - a_{1n}\cosh(pt)\right] + 1$$

$$\frac{\dot{\theta}_n}{p} = \left[(a_{1n} - 1)\cosh pt_{p1} - a_{1n} - a_{2n}\right]\sinh pt + (a_{1n} - 1)\sinh pt_{p1}\cosh pt \tag{4-25}$$

Where, $a_{1n} = a_{p1}/\alpha g$, and $a_{2n} = a_{p2}/\alpha g$. The block reaches its peak rotation, at time, t_{pk}, when $\dot{\theta}_n = 0$. Substituting, $\dot{\theta}_n = 0$, in Equation (4-25) gives the normalized peak rotation time, pt_{pk}, as

$$pt_{pk} = \tanh^{-1}\left[\frac{\sinh pt_{p1}}{\frac{a_{1n} + a_{2n}}{a_{1n} - 1} - \cosh pt_{p1}}\right] \tag{4-26}$$

Equation (4-23) gives, a_{ns}, the minimum pulse amplitude (applied at $\theta = \alpha^-$) required to cause separation of a falling block upon impact. Considering $a_{2n} = a_{ns}$, and $\theta_n = 1$ in Equations (4-25) and (4-26), the two equations can be numerically solved to determine a_{1n} and t_{p1}.Thus, for a given value of a_{2n}, a continuous pulse excitation can be obtained that leads to separation at the end of the second pulse just before impact. The angular velocity at the end of the second pulse is expected to be large enough to cause overturning which can be offset by adding an equally strong pulse in the opposite direction. For a given $a_{2n} > a_{ns}$, several combinations of a_{1n} and t_{p1} can be numerically determined that would cause separation before the end of the second pulse or before impact. Piecemeal closed form solutions from Equation (4-12) and Equation (4-25) can be combined to arrive at full solution.

4.4.5 Hybrid excitation: Combination of half sine pulses for slender blocks

Similar to the rectangular pulses in the previous section, the concept of hybrid excitation can be applied to combination of half sine pulses. Figure 4-6(c) shows piecemeal excitation where application of part 1 rises the block to just short of overturning when part 2 strikes in the opposite direction. Before going further, it is essential to delve into individual solutions to sine pulse excitations, part 1 and 2 in Figure 4-6(c). The initial conditions for part 1 of excitation are $\theta(0) = 0$ and $\dot{\theta}(0) = 0$, whereas for part 2, $\theta(0) = \alpha^-$ and $\dot{\theta}(0) = 0$.

The solution of Equation (4-8) by Housner [2] for the sine pulse excitation (part 1 in Figure 4-6(c)), $-a_{p1}\sin(\omega_{p1}t + \psi)$, (where, $a_{p1}\sin\psi = g\sin\alpha$, or, $\psi = \sin^{-1}(\alpha g/a_{p1})$), is given as

$$\frac{\theta - \alpha}{\alpha} = \frac{1}{1 + \left(\frac{\omega_{p1}}{p}\right)^2}\left[\frac{\omega_{p1}}{p}\frac{\sinh pt}{\tan\psi} - \left(\frac{\omega_{p1}}{p}\right)^2\cosh pt - \frac{\sin(\omega_{p1}t + \psi)}{\sin\psi}\right] \tag{4-27}$$

Approximate relationship between a_{p1} and ω_{p1} that make the block overturn in free vibration regime after the end of the pulse is given as [25]

$$a_n = 0.84 + \frac{1}{2}\omega_n \quad \text{for} \quad \omega_n > 0.32 \tag{4-28}$$

Where, $a_n = a_p/\alpha g$ and $\omega_n = \omega_p/p$ are normalized amplitude and frequency respectively.

Applying the half sine pulse excitation, $a_p\sin(\omega_p t)$ in the opposite direction (part 2 in Figure 4-6(c)) at the brink of overturning with the initial conditions, $\theta(0) = \alpha^-$ and $\dot{\theta}(0) = 0$, leads to the following solution of Equation (4-8)

$$\theta_n = \frac{a_n}{1+\omega_n^2}[\sin(\omega_n pt) - \omega_n \sinh pt] + 1 \tag{4-29}$$

Substituting Equation (4-29) into Equation (4-7) and considering $\ddot{V}_{Cn} = -1$ leads to the following transcendental giving relationship between normalized amplitude and frequency of the pulse that causes separation upon impact at the end of the pulse, i.e., normalized time, $pt = \pi/\omega_n$.

$$\cosh\frac{\pi}{\omega_n} = \frac{1}{2}\left[\sqrt{1 + 2\frac{I_{on}}{\alpha^2 a_n^2 \omega_n^2}(1+\omega_n^2)^2} - 1\right] \tag{4-30}$$

Numerical solution of Equation (4-30) leads to the following approximate relationship

$$\alpha a_n = 0.60\omega_n - 0.5 \quad \text{for} \quad \omega_n > 0.83 \tag{4-31}$$

It is to be noted that Equation (4-31) leads to an approximate timing that may not necessarily match with the pulse end but close to it. Reducing the frequency or increasing the amplitude of the second pulse would lead to separation before impact. Equations (4-28) and (4-31) provide amplitudes for given frequencies (or vice versa) of the first and second pulse that cause overturning and separation respectively, which are approximate but useful as a starting point of the iterative numerical analysis for the continuous excitation in Figure 4-6(d) as explained below.

Figure 4-6(d) shows combination of sine pulses with the first half sine pulse excitation ($a_{p1}\sin(\omega_{p1}t)$) resulting in positive rotation of the block. The second pulse, $a_{p2}\sin(\omega_{p2}t)$ strikes at the end of the first pulse. The block keeps rising to brink of overturning and experiences separation during its downward path. The solution of Equation (4-8) for the first pulse is given by Equation (4-27). Initial conditions for the second pulse $\theta(t_{p1})$ and $\dot{\theta}(t_{p1})$, obtained from Equation (4-27), lead to the solution for the second pulse excitation as

$$\theta_n = \frac{1}{1+\omega_{2n}^2}(a_{2n}\sin\omega_{2n}pt - a_{2n}\omega_{2n}\sinh pt) + \frac{1}{1+\omega_{1n}^2}\left[\frac{\omega_{1n}}{\tan\psi}\sinh\left(\frac{\pi-\psi}{\omega_{1n}}+pt\right) - \omega_{1n}^2\cosh\left(\frac{\pi-\psi}{\omega_{1n}}+pt\right) + \frac{\omega_{1n}}{\sin\psi}\sinh pt\right] + 1$$

$$\frac{\dot{\theta}_n}{p} = \frac{1}{1+\omega_{2n}^2}\omega_{2n}(a_{2n}\cos\omega_{2n}\,pt - a_{2n}\cosh pt) + \frac{1}{1+\omega_{1n}^2}\left[\frac{\omega_{1n}}{\tan\psi}\cosh\left(\frac{\pi-\psi}{\omega_{1n}}+pt\right) - \omega_{1n}^2\sinh\left(\frac{\pi-\psi}{\omega_{1n}}+pt\right) + \frac{\omega_{1n}}{\sin\psi}\cosh pt\right] \quad (4\text{-}32)$$

Where, $\psi = \sin^{-1}(1/a_{1n})$, $a_{1n} = a_{p1}/\alpha g$, $\omega_{1n} = \omega_{p1}/p$, $a_{2n} = a_{p1}/\alpha g$, $\omega_{2n} = \omega_{p2}/p$. The normalized time at peak rotation, pt_{pk} corresponds to zero velocity. For this condition, Equation (4-32) for $\dot{\theta}_n = 0$, leads to a transcendental that can be numerically solved for $\theta_n = 1$ and $\ddot{V}_{Cn} = -1$ (Equation (4-7)). Amplitudes for given frequencies (or vice versa) obtained from Equations (4-28) and (4-31) as starting points, and applied to Equation (4-32) lead to a host of normalized amplitude-frequency combinations (a_{1n}, ω_{1n}, a_{2n}, ω_{2n}) of a hybrid pulse that would make a block rise to just short of the peak rotation, $\theta_n = 0.99$, for example, and fall to separate just before impact. Figure 4-6(e) shows combinations of sine pulses in real earthquake records which resemble those in Figure 4-6(d), where a low-amplitude and low-frequency half sine wave is followed by a high-amplitude high-frequency one.

The analysis above points out several possibilities of separation when pulse excitation is applied to a falling slender block. This contrasts with the observation by Pompei et al [10] that "*separation usually occurs for wide blocks that is not so interesting from the practical point of view*". Fragilities of rocking blocks in NPPs [52] are expressed in terms of the peak acceleration of the excitation time history or the zero-period acceleration (ZPA) of the corresponding response spectrum that causes overturning. Separation is not recognized as a failure mode in [50] and [52]. In risk analysis, a new fragility criterion can be introduced named as 'separation fragility' for the

SRSH failure mode. A block undergoing minimum vertical acceleration, for example -0.7g, would be more at risk in comparison to the one with -0.5g. Fragility of a rocking frame with symmetrical eccentricities can be represented by that of an equivalent rocking block. However, frames with unsymmetrical eccentricities that cannot be represented by a rocking block needs to be examined as explained below.

4.5 Stability of Rocking Frame with Symmetrical and Unsymmetrical Eccentricities

4.5.1 Rocking frames with symmetrical eccentricities

A rocking frame with symmetrical eccentricities can be represented by an equivalent block (Chapter 2). Table 4-3 lists the parameters of such frames essential to obtain the response of an equivalent block by solving Equation (4-1). In order to ascertain the COFD at the beam level (Figure 4-3(d)), the horizontal and vertical accelerations of the beam ($\ddot{u}$ and $\ddot{v}$) can be obtained by multiplying those at the CG of the equivalent block, with R_{ratio} (Figure 4-3(e)). Similar to Equation (4-5), the COFD at the beam location in Figure 4-3(e) would be

$$\mu_{DS} = \frac{|\ddot{u}_T|}{\ddot{v} + g} \tag{4-33}$$

Where, $\ddot{u}_T = \ddot{u} + \ddot{u}_g$

4.5.2 Rocking Frame with unsymmetrical eccentricities

This section provides a brief review of the equation of motion of rocking frame with unsymmetrical eccentricities, as established in Chapter 3. Figure 4-7(a) shows a rocking frame with unsymmetrical piers with unsymmetrical support eccentricities and Figure 4-7(b) shows it in

rocking motion where the left pier pivots about O and the right one about O'. While the piers are vertically unsymmetrical, the frame by itself is symmetrical about its central axis. In rocking motion, rotations of the left and right piers, and, the beam are denoted as θ, θ', and θ_T, respectively. Rotation, θ, is the generalized coordinate representing the rotation of the left pier when the frame swings to the right and of the right pier when the frame swings to the left. The masses of the left pier, right pier and the beam are m, m', and M_T, and their moments of inertia about point O, O' and point B are, I_o, $I_{o'}$ and I_{TB}, respectively. The beam's moment of inertia about its CG is I_T. Figure 4-8(a) shows details of an unsymmetrical pier. Figure 4-8(b) shows various angles and dimensions. Figure 4-8(c) shows the left pier and the beam. The relationships among angles and their derivatives that are required for the equation of motion, as established in Chapter 3, are listed in Table 4-4.

The equation of motion of rocking frame was derived in Chapter 3 as

$$\begin{aligned}\ddot{\theta} = &-p_L^2\left[\sin(\mathrm{sgn}(\theta)\alpha_L - \theta) + \frac{\ddot{u}_g}{g}\cos(\mathrm{sgn}(\theta)\alpha_L - \theta)\right] \\ &-p_R^2\left[\sin(\mathrm{sgn}(\theta)\alpha_R - \theta') + \frac{\ddot{u}_g}{g}\cos(\mathrm{sgn}(\theta)\alpha_R - \theta')\right] \\ &-p_T^2\left[\sin(-\mathrm{sgn}(\theta)\alpha_T - \theta_T) + \frac{\ddot{u}_g}{g}\cos(-\mathrm{sgn}(\theta)\alpha_T - \theta_T)\right] - \frac{\tau}{\psi}\dot{\theta}^2\end{aligned} \tag{4-34}$$

Where, p_L, p_R., p_T, α_L, α_R., λ_L, λ_R, τ and ψ, are listed in Table 4-4 along with the COR of rocking frame, $\check{e}$, that was derived in Chapter 3. Various dimensionless ratios as defined in Chapter 3, applicable to the contents of Table 4-4 are $q_I = I_{o'}/I_o$, $q_{IT} = I_{TB}/I_o$, $q_T = M_T/m$, $q_m = m'/m$, $q_R = R'/R$, $q_{RT} = R_T/R$, $q_{OT} = I_T/I_o$, $q_{LT} = I_T/I_o$, $q_L = b/l_C$, and $q_{LT} = 2q_L^2/(1 + 2\eta\, q_L)[1 + (\eta - \eta')\, q_L]$.

4.5.3 Minimum acceleration required to initiate rocking

As explained in Chapter 3, the minimum acceleration required to initiate rocking is

$$\ddot{u}_g = g \tan \alpha^* \tag{4-35}$$

Where,

$$\alpha^* = \tan^{-1}\left[\frac{b_0^*}{h_0^*}\right] \tag{4-36}$$

$$b_0^* = b\left[1 + (\mu - 1)q_m + (1 + \eta)q_T - q_T \frac{R_T \sin \alpha_T}{R \sin \alpha}\left[\frac{R_1 \sin(\beta - \beta')}{l_T \cos(\beta')}\right]\right]$$

$$h_0^* = h\left[1 + q_m + q_T \xi + q_T \frac{R_T \cos \alpha_T}{R \cos \alpha}\left[\frac{R_1 \sin(\beta - \beta')}{l_T \cos(\beta')}\right]\right]$$

4.5.4 Stability Condition for the Rocking Frame with Unsymmetrical Eccentricities

Two types of stability conditions are applicable: effective rotation reaching its limit and separation of the beam.

4.5.4.1 Effective rotation of the frame

As established in Chapter 3, the instability is reached when

$$\theta^* = \alpha \operatorname{sgn} \theta \tag{4-37}$$

Where,

$$\theta^* = \tan^{-1} \frac{\left((1 + q_T \xi)\sin \theta + q_m \frac{d\theta'}{d\theta} \sin \theta' + q_T \sin \theta_T \frac{R_T \cos \alpha_T}{R \cos \alpha} \frac{d\theta_T}{d\theta}\right)}{\left(\cos \theta + q_m \frac{d\theta'}{d\theta}(\mu - 1) \cos \theta' + (1 + \eta)q_T - q_T \cos \theta_T \frac{R_T \sin \alpha_T}{R \sin \alpha} \frac{d\theta_T}{d\theta}\right)} \tag{4-38}$$

The rotation, θ^*, a function of θ, in Equation (4-37) is defined as *effective* rotation of the system.

4.5.4.2 Separation of the beam

Vertical acceleration

In Figure 4-8(c), considering point B as reference, the vertical displacement of the beam's CG, v_{TU}, from its position at rest, would be the sum of its displacement relative to point B (v_{TB}) and the displacement of point B (v_B). The vertical discplacement of the beam and its second derivative are given as

$$v_{TU} = v_{TB} + v_B = R_T[\cos(\text{sgn}(\theta)\,\alpha_T + \theta_T) - \cos\alpha_T] + R_1\cos(\beta\,\text{sgn}(\theta)\, - \theta) - \xi h$$

$$\begin{aligned}\ddot{v}_{TU} = \ddot{v}_{TB} + \ddot{v}_B = &\left[R_1\ddot{\theta}\sin(\beta\,\text{sgn}(\theta) - \theta) - R_1\dot{\theta}^2\cos(\beta\,\text{sgn}(\theta) - \theta)\right] \\ &-\left[R_T\ddot{\theta}_T\sin(\text{sgn}(\theta)\alpha_T + \theta_T) - R_T\dot{\theta}_T^2\cos(\text{sgn}(\theta)\alpha_T + \theta_T)\right]\end{aligned} \quad (4\text{-}39)$$

Where, $\dot{\theta}_T = \dot{\theta}(d\theta_T/d\theta)$, and $\ddot{\theta}_T = \ddot{\theta}(d\theta_T/d\theta) + \dot{\theta}^2(d^2\theta_T/d\theta^2)$. The subscript U is added to differentiate the acceleration in frames with unsymmetrical eccentricities with those having symmetrical. If $\ddot{v}_{TU}$ is equal to $-g$, the beam would become *weightless* and separate.

Horizontal acceleration

Similar to Equation (4-39), the total horizontal displacement and its derivative would be

$$u_{TU} = u_{TB} + u_B + u_g$$

$$u_{TU} = (1+\eta)R\sin(\alpha\text{sgn}(\theta)) - R_1\sin(\beta\text{sgn}(\theta) - \theta) + R_T[\sin(\text{sgn}(\theta)\,\alpha_T + \theta_T) - \sin(\text{sgn}(\theta)\,\alpha_T)] + u_g$$

$$\begin{aligned}\ddot{u}_{TU} = \ddot{u}_g + R_1&\left[\cos(\beta\text{sgn}(\theta) - \theta)\ddot{\theta} + \sin(\beta\text{sgn}(\theta) - \theta)\,\dot{\theta}^2\right] + \\ &R_T\left[\cos(\text{sgn}(\theta)\alpha_T + \theta_T)\,\ddot{\theta}_T - \sin(\text{sgn}(\theta)\alpha_T + \theta_T)\,\dot{\theta}_T^2\right]\end{aligned} \quad (4\text{-}40)$$

Where, $\ddot{u}_g$ is ground acceleration $\dot{\theta}_T = \dot{\theta}(d\theta_T/d\theta)$, and $\ddot{\theta}_T = \ddot{\theta}(d\theta_T/d\theta) + \dot{\theta}^2(d^2\theta_T/d\theta^2)$. Equations (4-39) and (4-40) can also be obtained by differentiating the vertical and horizontal velocities, $\dot{v}_T$ and $\dot{u}_T$, of the beam in Equation (3-15) in Chapter 3.

The corresponding COFD for the beam in a rocking frame with unsymmetrical eccentricities would be

$$\mu_{DU} = \frac{|\ddot{u}_{TU}|}{\ddot{v}_{TU} + g} \tag{4-41}$$

4.6 Response to Pulse Excitation

4.6.1 Response of a rigid block to rectangular hybrid pulse (Figure 4-9)

Table 4-5 lists details of three rectangular hybrid normalized acceleration pulses and a procedure to derive pulse No.1 from the equations marked therein for a rectangular block with slenderness parameter, $\alpha = 0.3$. Each hybrid pulse is made of three parts as depicted in Figure 4-6(b). Pulse No. 1 represents 'balanced' loading that achieves separation coinciding with impact and allow rocking to continue in free vibration mode after the pulse expiry with the maximum possible rotation without overturning ($|\theta| \approx \alpha$). Pulse No.2 contains the amplitude of Part 2 (Figure 4-6(b)) higher but its duration lower than that in Pulse No. 1, causing separation before impact but allowing rocking to continue with amplitude $|\theta| < \alpha$. Pulse No. 3 is the same as pulse No. 2 but with the duration of part 2 longer than that in pulse No. 1 resulting in separation before impact and also after impact during overturning.

Figure 4-9 shows linear numerical normalized response over normalized time (pt) to the pulse excitations obtained by linear numerical analysis, starting from the top row for the first pulse in Table 4-5. The first column contains normalized rotation, normalized angular velocity and acceleration along with the excitation acceleration plots. Various parts of excitation 1, 2 and 3 (Figure 4-6(c)) are marked in the left column. The right column shows normalized rotation,

horizontal and vertical accelerations, and, the COFD. Linear numerical solutions in all rows are in agreement with the linear analytical solutions. Such agreement is depicted only in the second row for brevity. Timing of peak acceleration, zero velocity and separation match with those predicted in Table 4-5 in all rows. The COR is assumed as 1 in all cases.

The top row depicts a 'balanced' condition where the excitation acceleration in part 2 of the excitation is just enough to coincide separation with impact. Part 3 excitation acceleration is just enough to continue rocking with maximum allowable rotation close to overturning ($|\theta_n| \approx 1$). As shown in the left column, with the start of excitation part 1, normalized angular rotation (θ/α) starts increasing. Normalized angular velocity ($\dot{\theta}/p$) increases to reach its peak at the end of part 1 and then starts reducing to zero (while normalized rotation reaches its peak) and then to its peak in the negative direction up to impact where onwards it starts increasing again to zero at the end of excitation. The normalized angular acceleration ($\ddot{\theta}/p^2$) increases in the positive direction under excitation part 1 with a sudden change to negative at the start of excitation part 2 followed by the second sudden shift back to positive caused by impact and application of excitation part 3. The second column shows that separation (vertical acceleration = -1g) coincides with impact. Post impact, the vertical acceleration behavior is opposite to that during part 2 of excitation. The exponential rise in COFD is not because of the increase in horizontal but decreasing vertical acceleration. It is observed that this exponential rise begins after the vertical acceleration starts decreasing below -0.5g. Assuming no effect caused by zero vertical acceleration, rocking continues in its free vibration regime with a large period.

The middle row shows response to excitation Pulse No. 2 in Table 4-5 where the acceleration of part 2 is more than its counter part in the top row but with a comparatively lesser duration,

allowing separation to be achieved before impact. The left column shows the response of normalized rotation, angular velocity and acceleration similar to the top row except for a brief stint of a small step in the angular acceleration. Acceleration of excitation part 3 is enough to suppress the response below the maximum allowable with continued rocking. Results obtained from Equations (4-12), (4-25) and (4-24) are depicted to be in agreement with numerical analysis. The right column shows occurrence of separation (vertical acceleration equal to -1g, at normalized time 3.17) before impact (at 3.20). Under the excitation part 2, vertical acceleration keeps decreasing up to -1g till part 3 strikes in the opposite direction causing a sudden increase. Unlike the top row, after the strike of excitation part 3, the rotation is still positive and hence there is a small gap between two extremes of vertical acceleration, between separation and impact. Post impact, the block starts rotating in the opposite direction. The COFD is observed to increase exponentially once the vertical acceleration drops below -0.5g.

The bottom row depicts the response to Pulse No. 3 in Table 4-5 which is the same as Pulse No. 2 but with an increased duration of part 2. The left column shows that after peak rotation, the negative velocity reaches its peak and starts increasing at the end of excitation part 2. But, since the excitation part 3 is not strong and long enough to sustain the increase in velocity, it starts decreasing again at the end of excitation part 3. Thus, the rotation continues to be negative leading to overturning. The left column shows sudden reduction in angular acceleration during excitation part 2 upon impact (at normalized time, 3.20), followed by a sudden switch from negative to positive at the end of part 2. Right column shows two instances of separation: 1. before impact, and, 2. during overturning in the opposite direction as shown in the right column depicted by brown dashed lines. Line 1 represents impact, line 2 is marked at vertical acceleration reaching -1g and

line 3 is marked where the rotation reaches its maximum allowable limit with vertical acceleration $\approx -1.5g$. Slight difference between the separation and impact timings is accompanied with a huge decrease in vertical acceleration during overturing. Separation during overturning, especially with vertical acceleration at $-1.5g$, may extend the reach of an overturned block and thus increase the risk of its seismic interaction with nearby seismically qualified components. Therefore, safe distances from unanchored objects marked in typical NPP procedures need to be revisited for the SRSH failure mode.

4.6.2 Response of a rigid block to hybrid sine pulse (Figure 4-10 and Figure 4-11)

Table 4-6 lists details of hybrid sine pulses with normalized amplitudes and frequencies of various parts of the pulse as depicted in Figure 4-6(d). Figure 4-10 shows non-linear normalized response of a block with slenderness parameter $\alpha = 0.25$, $p = 2.14/s$ and the COR as 0.91, same as the locomotive example shown in Figure 4-2(e) considered in [13]. The top row shows the normalized response to pulse 1. As shown in the left column, due to part 1 of excitation the block reaches its peak normalized rotation (not far from overturning limit =1) in normalized time, 2.14, experiences impact before the end of excitation part 2, survives the overturning limit on the other side, returns to experience one more impact and overturns (after two impacts) after the expiry of the entire excitation in its free vibration regime. Agreement between linear analytical and nonlinear numerical solutions with minor differences is exhibited. The normalized angular acceleration varies similar to excitation acceleration but with the opposite sign. The right column shows horizontal acceleration following a trend opposite to excitation and vertical acceleration reaching less than -1g before impact. Upon impact vertical acceleration experiences a sudden rise and then drops again. The timings of separation and impact are highlighted by brown lines overlapping with

the COFD asymptotes. The COFD remains positive as long as vertical acceleration is > -1g. The COFD's exponential rise begins after the vertical acceleration falls below -0.5g.

The bottom row shows response to Pulse No. 2 (Table 4-6). As shown in the left column, peak rotation occurs at normalized time 3.54 followed by the impact leading to overturning before the end of part 2 of excitation. The right columns shows vertical acceleration reaching less than -1g before impact and also during overturning at normalized time, 4.18. Again, once the vertical acceleration falls below -0.5g, COFD is observed to increase exponentially. The bottom row exhibits that it is possible for the locomotive example considered in [13] to overturn with negative acceleration, a failure mode different from that considered therein as detailed below.

Figure 4-11(a) shows real time response of the locomotive example [13] ($\alpha = 0.25, p = 2.14/s$), to Pulse No. 2 with amplitude 2.34g (a_{2n} x α = 9.36x0.25), and angular frequency (ω_{2n} x p =3.01x2.14) as 6.44 rad/s (~1Hz). Figure 4-11(b) shows the response to a single sine pulse with amplitude 2.2g and angular frequency of 15.7 rad/s (~2/5Hz) as considered in [13]. According to the testimony in [53], the train experienced "a great lurch to the east, followed by another to the west, which threw the whole train on its side" and "The fireman turned to jump from the engine to the west when the return shock came. He then leaped to the east". From the narration it appears that more time was spent in the first leap. Figure 4-11(a) shows a large leap on one side consuming large time in comparison to that in Figure 4-11(b). The timings of reaching the peak rotation and impact are 1.65s and 1.85s respectively. Figure 4-11(b) (representing the analysis in [13]) depicts the impact timing as 0.815s which is less than half of that in Figure 4-11(a). The overturning timings in both cases are not too far from each other, 1.95s and 2.2s in Figure 4-11(a) and (b) respectively. Separation occurs twice in Figure 4-11(a), just before impact at 1.85s and

during overturning at 1.95s. No separation occurs in Figure 4-11(b). The overturning in Figure 4-11(a) accompanied with vertical acceleration lower than -1g, is a SRSH failure mode which is different from simple and smooth overturning in Figure 4-11(b). Thus, the possibility of the crane overturning with the hybrid sine pulse excitation depicted in Figure 4-11(a) cannot be ruled out.

Figure 4-11(c) shows response to the sine pulse as in Figure 4-11(b) but with a preceding half sine pulse excitation with -0.27g amplitude and 3.391 rad/s angular frequency. As shown, in this case no overturning occurs and the block enters free vibration regime after the end of the pulse. Figure 4-11(d) depicts the free vibration mode after the pulse expiry. Here, as predicted by Equations (4-7) and (4-10), the normalized angular acceleration switches back and forth between α (=0.25), and, $-\alpha$, the normalized angular velocity is comparatively quite small (almost zero), and, as predicted in Section 4.4.1, the vertical acceleration (in g's) remains constant at $-\alpha^2/I_{on} = -0.25^2/(4/3) = -0.047$. Thus, the response to a single sine pulse as predicted in [13] can be easily influenced by a preceding half sine pulse that appears to be comparatively insignificant but turns out to be highly effective in transforming the response from overturning to continued rocking. Also, a hybrid pulse is closer to reality in an earthquake record rather than a single sine pulse.

4.6.3 Response of rocking frame with slender rectangular piers to hybrid sine pulse excitation with $\eta = 1$ (Figure 4-12)

Per Equation (4-6), the horizontal and vertical accelerations are inversely proportional to the normalized moment of inertia of a rigid block. In order to derive the equivalent block system of a frame, it is essential to obtain the normalized moment of inertia of the system.

Table 4-3 lists various parameters reproduced from Chapter 3 except for those that are greyed out including the normalized moment of inertia of an equivalent block (or system), denoted as I_{ons}. Utilizing these relationships for a rectangular pier frame ($\phi = \phi' = 1$, $I_{on} = 4/3$, $\xi = 2$), with symmetrical eccentricities ($\eta = 1$), the normalized moment of inertia of an equivalent block comes out to be

$$I_{ons}|_{\text{Rectangle}} = \frac{4}{3}\frac{(1+3q)(1+q)}{(1+2q)^2} \tag{4-42}$$

As q approaches infinity, Equation (4-42) would asymptote to 1. For a rectangular pier shown in Figure 4-3(f) with $\eta = 1$, $R_{eq} \approx 2R$ for a large beam mass. Therefore, for slender rectangular piers, as q approaches infinity, the equivalent block would resemble a stick mass system with the entire mass at $2R$ from the pivot and the normalized moment of inertia of the equivalent block system, $I_{ons} \cong 1$.

According to Figure 8 in [25] (Chapter 2, Figure 2-8), for a rectangular slender piers frame with $\eta = 1$, the ratio of the equivalent block's and pier's size parameters, p_{eq}/p, asymptotes to 0.816, with increase in q. For $\eta = 1$, the slenderness parameter of the equivalent block, $\alpha_{eq} = \alpha$. The top diagram in Figure 4-12 shows a rocking frame with its equivalent block system consisting of a pier ($I_{on} = 4/3, p = 1$) with a top mass [25]. Also shown is the equivalent block system with $q = \infty$, $I_{ons} = 1$ and $p = 0.816$, resembling an equivalent stick mass system that rocks between two angular limits, α and $-\alpha$ on either side depicted by red triangles; rising from position 1 to 2 and back to 1 with impact, instantly switching its position to 3 to rise to 2 and then back to 3 and so on. The middle and bottom rows illustrate response to the hybrid sine pulse No. 1 and 2 in Table 4-6 respectively. The left column depicts the response of a solitary pier and the equivalent block

of the frame for normalized excitation. Meaning, the excitation for the frame and solitary pier is not the same but suited to their size to make them rise to the same maximum positive rotation resembling a 'self-similar' response [54]. The normalized response of a pier and the frame is identical but the vertical acceleration of the frame before impact is much lesser than that of the pier, owing to $I_{ons} = 1$ for the frame but $I_{on} = 4/3$ for the pier. Since the equivalent block of the frame consists of a point mass at the top representing the beam, vertical acceleration being less than -1g will cause the beam to lift off or separate from the pier. Also, during negative rotation, the frame experiences vertical acceleration $= -1g$ at $\theta_n \approx 0.5$, depicted by brown dashed line, causing separation much prior to impact resulting in the lift-off of the beam. The frame's vertical acceleration after impact is less than that of the pier. Similar trend is visible in the bottom row first column where the frame experience separation before and after impact.

The second column shows the response of the pier and the frame subject to the same excitation as applied to the pier. Here, the frame size being larger (smaller p_{eq}), causes the frame rotation response to be less than that of the pier in both rows. However, in the middle row, the minimum vertical acceleration of the frame before impact is less than that of the pier. Also, the frame achieves vertical acceleration = -1g prior to impact causing the beam to lift-off. In the bottom row, both the pier and the frame overturn and the frame's minimum vertical acceleration is slightly less than that of the pier rendering it less stable in the SRSH failure mode.

Figure 4-12 proves that a frame is more susceptible to instability due to negative vertical acceleration than the pier under the SRSH failure mode. Makris and Vassiliou [24] claimed that the top-heavy frames are more stable than their lighter counter parts. Dar et al [25] proved that this is true only for frames with $\eta = 1$ when overturning is considered as a stability criterion. The

above analysis proves that a top-heavy frame with $\eta = 1$ is more susceptible to separation than its lighter counterpart under the SRSH failure mode. Thus, a top-heavy frame being more stable than its lighter counterpart depends on support eccentricity and the applicability of the SRSH failure mode.

4.6.4 Response of rocking frame with symmetrical trapezoidal piers and symmetrical eccentricities to hybrid sine pulse excitation (Figure 4-13)

Trapezoidal piers are used in NPPs to support heavy turbine rotors weighing almost 12 to 25 times the weight of the pier. Such piers are not slender, and the case considered herein is of a frame with symmetrical stocky trapezoidal piers with $\alpha = 0.806$, and, $\phi = \phi'$ (Figure 4-8(a)), as listed in Table 4-7 along with the details of a hybrid sine pulse excitation that corelates to Figure 4-6. The radius of an equivalent block, R_{eq} is the same as shown in Figure 4-3(e). Since, for a solitary pier the radius can be expressed as, $R = g/p^2 I_{on}$, the radius of the equivalent block comes out to be, $R_{eq} = g/p_{eq}^2 I_{ons}$, that can be obtained with the help of Table 4-1 and Table 4-3. Figure 4-13 shows the response of solitary trapezoidal pier and equivalent blocks of frames with symmetrical eccentricities. Two values of q, are considered: 0.5 and 20. For the solitary pier, $q = 0$. Eccentricity varies as $\eta = 0, 0.5\phi, 0.8\phi$, and ϕ. The pier-mass system or equivalent block schematics is shown as an inset in the top row of the right column. The response of this system at $q = 0$ represents a solitary pier and its response is marked as 'solitary' in the top row, left column. The COR for the solitary pier is 0.21 whereas for the fame it varies between 0.49 and 0.42 corresponding to two extremes of η: 0 and ϕ.

The top row depicts the normalized rotation and vertical acceleration responses of the solitary pier and rocking frames with $q = 0.5$ and various values of η. The excitation pulse, shown in green, corresponds to the right scale. The normalized responses in all cases (left column, top row) experience two impacts within the pulse duration followed by free vibration regime. Jump-discontinuities in vertical accelerations coincide with impacts. The vertical accelerations under free vibration (right column, top row) reach their respective constant values, similar to the illustration in Figure 4-11(d) (and as predicted in Section 4.4.1 albeit for a slender block) which will approach zero at infinite time when the block comes to complete rest. Although the normalized rotation in all cases is not too significant, still, the vertical acceleration reaches -1g before each of the two impacts within the pulse duration. Pompei et al [10] reported separation of a wide block under free vibration close to impact when the wide block is released from its overturning limit, $\theta = \alpha$. Figure 4-13 shows that separation can be achieved at rotations much smaller than α when subjected to hybrid pulse excitation, in the case of a falling block.

The left column in middle row shows the response of frames with $\eta = 0$ and $q = 0.5$, and the right column shows the same for $\eta = \phi$ and $q = 0.5$. Vertical acceleration is depicted at two locations: CG of the pier-mass system, or equivalent block, and the location of the point mass (beam). As shown, the rotational response is not too significant, yet separation occurs at both locations: CG of the system and the beam. The rotational response at $\eta = \phi$ is less than that for $\eta = 0$ but the vertical acceleration shows an opposite trend. In the entire middle row, the vertical acceleration separation occurs before impact.

The bottom row shows response for $q = 20$ and, $\eta = 0$ and ϕ. In this case, since the beam is much heavier than the pier, the system CG is quite close to the beam and consequently, the vertical

acceleration plots at the system CG and the beam overlap. In the left column the system overturns. Vertical acceleration remains above -1g till the occurrence of overturning. Contrasting to this, in the right column the overturning does not occur, but the vertical acceleration falls below -1g at the end of the pulse excitation.

Figure 4-13 demonstrates that despite the low rotational response, separation is possible in wide blocks under hybrid pulse excitations. All cases depicted in Figure 4-13 show SRSH failure mode even in those that do not overturn.

4.7 Seismic Isolation of the Beam in Rocking Frames with Symmetrical Eccentricities Subjected to Hybrid Pulse Excitations

4.7.1 Isolation versus separation (Figure 4-14)

The horizontal accelerations (at the pier CG), relative to the pivot, derived from Equation (4-4), plotted in Figure 4-9 and Figure 4-10 for rectangular blocks and in Figure 4-13 for trapezoidal blocks are practically mirror images of their corresponding excitation plots, albeit smaller in amplitude. This indicates seismic isolation of a rigid block due to rocking action implying that the base shear magnitude, or, absolute value of reaction, F_x, in Equation (4-5), would be less than that caused purely by the excitation acceleration. In a rocking frame, the seismic isolation of the beam caused by piers acting together as an isolation device would be much more pronounced in comparison to the pier's CG.

Similar to the vertical acceleration plots in Figure 4-13, for a lighter frame, the horizontal acceleration of the beam would be more than that at the equivalent block's CG because of the beam contact point being farther from the pivot than equivalent block's CG. For a heavier frame,

the two would be quite close. The absolute horizontal accelerations at the equivalent block's CG and the beam are

$$\text{Absolute horizontal acceleration at equivalent block's CG} = \ddot{H}_c + \ddot{u}_g$$
$$\text{Absolute horizontal acceleration at beam} = \ddot{u} + \ddot{u}_g \quad (4\text{-}43)$$

Figure 4-14 shows two examples of rocking isolation of light frames: slender pier frame in top row and wide trapezoidal pier frame in the bottom row. The top row shows the response of a frame with slender rectangular piers ($\alpha = 0.25$ and $p = 1$) and $q = 0.6$ subjected to Pulse No 3 in Table 4-6. The absolute horizontal acceleration at the beam (Equation (4-33)) is much lesser than the excitation indicating nearly perfect isolation. However, as shown in the left column, the beam achieves vertical acceleration less than -1g, prior to impact indicating separation and hence instability. If separation is ignored, as shown in the right column, the frame continues to rock in free vibration regime after the expiry of the excitation pulse. The bottom row shows the response of a frame with wide trapezoidal piers subject to the excitation as given in Table 4-7 with $q = 1.5$. Similar to the first row, the beam's absolute horizontal acceleration is much less than the excitation acceleration but separation of the beam occurs before impact, causing instability. If instability is ignored, rocking solution continues in free vibration regime.

Figure 4-14 demonstrates that despite achieving seismic isolation, the top beam is vulnerable to the SRSH failure mode under hybrid pulse excitation. This is in contrast to the conclusion by Makris and Vassilou [24] and Makris [45] that by making the beam heavier, a rocking frame becomes more stable implying seismic isolation.

4.7.2 Horizontal and vertical accelerations of the beam (Figure 4-15 and Figure 4-16)

Figure 4-15 shows numerical responses (rotation of piers, and, horizontal and vertical accelerations experienced by the beam) of two symmetrical rocking frames with slender rectangular piers subjected to hybrid pulse No. 4 and 5 in Table 4-6 followed by continuous excitations mentioned as part 4 therein. Both cases are for piers with $\alpha = 0.25$ and $\eta = 1$. The top row in Figure 4-15 shows the excitation pulse No. 4 followed by the second row illustrating the response of a heavily loaded frame ($q = 20$) with large piers ($p = 1$ or radius = 7.36m). The third and fourth (bottom) rows respectively show the excitation pulse No. 5 followed by the response of a lightly loaded frame ($q = 1$) with small piers ($p = 6$, or radius = 0.204m). As evident, despite the difference in size and loading of the frames, during the excitation after the pulse expiry and despite continued excitation, the horizontal acceleration experienced by the beam varies between two extremes: αg and $-\alpha g$, achieving seismic isolation. The reason for this behaviour is explained below.

As shown in Figure 4-3(e) the horizontal and vertical displacements of the point mass would be the same as beam displacements, u and v. The distance of the top mass from the pivot, R_1' ($= R_1$), and the radius of the equivalent block, R_{eq}, are obtained by following the relationships in Table 4-3. The ratio between the two distances, R_1, and R_{eq}, defined as R_{ratio}, comes out to be

$$R_{ratio} = \frac{\nu}{\lambda}(1+q) \tag{4-44}$$

Where, $\nu = \sqrt{(1+\eta)^2 \sin^2\alpha + \xi^2 \cos^2\alpha}$ $\lambda = \sqrt{(1+(\eta+1)q)^2 \sin^2\alpha + (1+\xi q)^2 \cos^2\alpha}$

For a rectangular pier with $\eta = 1$ and $\xi = 2$, giving $\nu = 2$, leads to,

$$R_{ratio} = 2\left(\frac{1+q}{1+2q}\right) \tag{4-45}$$

R_{ratio} is useful as a multiplier in obtaining horizontal and vertical accelerations at the beam location (point mass as depicted in Figure 4-3(e)) from those at the CG of the equivalent block given by Equations (4-4) or (4-6). As evident, R_{ratio} approaches 1 as q approaches infinity, turning the equivalent block into a stick-mass system. Applying small angle approximation to the horizontal acceleration in Equation (4-6) leads to the horizontal acceleration at the CG of the block and mass system, or equivalent block, relative to the pivot point as

$$\ddot{H}_{CSn} = \frac{\ddot{H}_{CS}}{g} = \frac{1}{I_{ons}}\left[\frac{\ddot{\theta}}{p_{eq}^2} + \left(\frac{\dot{\theta}}{p_{eq}}\right)^2\left(\alpha_{eq}\text{sgn}(\theta) - \theta\right)\right] \tag{4-46}$$

Where, the system's (or equivalent block's) normalized moment of inertia, I_{ons}, is given by Equation (4-42) and p_{eq} is given in Table 4-3. Substituting, $\ddot{\theta}/p_{eq}^2$, from Equation (4-1) with small angle approximation leads to

$$I_{ons}\ddot{H}_{CSn} + \frac{\ddot{u}_g}{g} = \left[\left(\frac{\dot{\theta}}{p_{eq}}\right)^2 - 1\right]\left(\alpha_{eq}\text{sgn}(\theta) - \theta\right) \tag{4-47}$$

As illustrated in Figure 4-15, the normalized velocity squared horizontal component (NVHC), depicting $\left(\dot{\theta}/p_{eq}\right)^2 \sin[\alpha(\text{sgn}\,\theta) - \theta]$ is almost zero. Also, as observed in Figure 4-11, Figure 4-14, and Figure 4-15, the horizontal and vertical accelerations' maxima coincide with impact, when $\theta = 0$. Considering $\theta = 0$ and neglecting $\alpha_{eq}\left(\dot{\theta}/p_{eq}\right)^2$, gives

$$I_{ons}\ddot{H}_{CSn} + \frac{\ddot{u}_g}{g} = -\alpha_{eq}\text{sgn}(\theta) \tag{4-48}$$

Multiplying the horizontal acceleration at the CG of the equivalent block, $\ddot{H}_{CSn}$, with the multiplier, R_{ratio}, in Equation (4-45) leads to the horizontal acceleration at the beam, $\ddot{H}_{Bn} = R_{ratio}\ddot{H}_{CSn}$. Manipulating Equation (4-48) gives

$$I_{BR}\ddot{H}_{Bn} + \frac{\ddot{u}_g}{g} = -\alpha_{eq}\text{sgn}(\theta) \tag{4-49}$$

Where, $\ddot{H}_{Bn} = R_{ratio}\ddot{H}_{CSn}$ and $I_{BR} = I_{ons}/R_{ratio}$, given in Table 4-3. For a frame with rectangular pier and symmetrical eccentricity I_{BR} comes out to be

$$I_{BR}|_{\text{Rectangle}} = \frac{I_{ons}}{R_{ratio}} = \frac{2}{3}\frac{(1+3q)}{(1+2q)} \tag{4-50}$$

As evident, Equation (4-50) asymptotes to 1 as q approaches infinity. Figure 4-16 shows similar variation in I_{BR}, obtained from relationships listed in Table 4-1 and Table **4-3**, for rectangular, trapezoidal and triangular piers with different eccentricities and slenderness parameters. As evident from Figure 4-16, for $q > 1$, $I_{BR} > \sim 0.9$ for all cases. The horizontal acceleration of the beam relative to the pivot, $\ddot{u} = I_{BR}\ddot{H}_{Bn}g$. Considering $I_{BR} \cong 1$, and the general case when $\eta \neq 1$, Equation (4-49) leads to total or absolute acceleration at beam, $\ddot{u}_T = \ddot{u} + \ddot{u}_g$, expressed as $\ddot{u}_{TA}$ with the additional subscript 'A' denoting approximation as given below.

$$\ddot{u}_{TA} \cong -\alpha_{eq}\text{sgn}(\theta)g \tag{4-51}$$

Figure 4-15 demonstrates the validity of Equation (4-51) for a frame with $\eta = 1$, and $\alpha_{eq} = \alpha$. As shown for a large q (=20), the absolute horizontal acceleration varies between $-\alpha g$ and αg,

whereas for a small q (=1), it slightly exceeds these limits. Equation (4-51) also concludes that for a symmetrically supported rocking frame on slender piers with eccentricity parameter, $\eta = 1$, that survives a given excitation, the horizontal acceleration received by the beam would be αg. This behaviour is verified for earthquake records in the sequel.

Regarding the vertical acceleration, normalized velocity squared vertical component (NVVC), $\left(\dot{\theta}/p_{eq}\right)^2 \cos\alpha[(\operatorname{sgn}\theta) - \theta]$, plays significant role and cannot be neglected. Also, the vertical acceleration's sudden decrease to the lowest value shows up as a spike as depicted in Figure 4-15 (top set of diagrams) for heavier frame ($q = 20$). However, $\left(\dot{\theta}/p_{eq}\right)^2$ plays a significant role only when there is a steep variation in rotation as visible therein. However, for the lighter frames shown in the bottom set of diagrams in Figure 4-15, it is not so. The analysis below attempts to obtain a conservative approximate solution of vertical acceleration received by the beam in a frame.

Substituting $\ddot{\theta}/p_{eq}^2$ from Equation (4-1) in Equation (4-6) gives normalized vertical acceleration at CG of the equivalent block system as

$$\ddot{V}_{CSn} = \frac{\ddot{V}_{CS}}{g} = \frac{1}{I_{ons}}\left[\frac{\ddot{\theta}}{p_{eq}^2}\sin\left(\alpha_{eq}\operatorname{sgn}(\theta) - \theta\right) - \left(\frac{\dot{\theta}}{p_{eq}}\right)^2 \cos\left(\alpha_{eq}\operatorname{sgn}(\theta) - \theta\right)\right]$$

Where, $\ddot{V}_{CS}$ is the vertical acceleration at the CG of the equivalent block system and $\ddot{V}_{CSn}$ is its normalized version. In the bottom row of Figure 4-15, vertical acceleration achieves its minimum at low period of oscillations where angular velocity is small. Neglecting $\left(\dot{\theta}/p_{eq}\right)^2$ and applying small angle approximation gives

$$I_{ons}\ddot{V}_{CSn} = \left[-\left[\alpha_{eq}\,\mathrm{sgn}(\theta) - \theta\right]^2 - \left[\alpha_{eq}\,\mathrm{sgn}(\theta) - \theta\right]\frac{\ddot{u}_g}{g}\right] \tag{4-52}$$

Multiplying the normalized vertical acceleration at the CG of the equivalent block, $\ddot{V}_{CSn}$, with the multiplier, R_{ratio}, leads to the normalized vertical acceleration at the beam, $\ddot{V}_{Bn} = R_{ratio}\ddot{V}_{CSn}$. Vertical acceleration is minimum at low period of oscillation which also implies low rotation amplitude because high amplitudes result in high period. Hence, considering $\alpha_{eq}\,\mathrm{sgn}(\theta) - \theta \cong \alpha_{eq}$, or, substituting $\theta = 0$ in Equation (4-52) while recognizing $I_{BR} = I_{ons}/R_{ratio}$, leads to the approximate vertical acceleration at beam, $\ddot{v}_A$

$$\ddot{v}_A = I_{BR}\ddot{V}_{Bn}g = -{\alpha_{eq}}^2 - \alpha_{eq}\,\mathrm{sgn}(\theta)\frac{\ddot{u}_g}{g} \tag{4-53}$$

Considering $I_{BR} \cong 1$ as before for frames with $q > 1$, gives

$$\ddot{v}_A = -{\alpha_{eq}}^2 g - \alpha_{eq}\,\mathrm{sgn}(\theta)\ddot{u}_g \tag{4-54}$$

Equation (4-54) does not lead to values that are too close to the vertical acceleration in the case of steep rise or decline of rotation in the pulse excitation case in the second row in Figure 4-15. However, in the bottom row, it leads to results that are close to the vertical acceleration obtained from nonlinear analysis. It also provides close approximation to the numerical solutions in the case of actual earthquake records as observed later. Regarding the strong high amplitude pulse excitations as in the second row of Figure 4-15, applying the factor of safety = 2 as recommended by ASCE 43-19 to Equation (4-54) would lead to conservative conclusion on separation (-0.75g x 2 = -1.5g which is less than -1.25g). Thus, Equation (4-54) can be extremely useful in quick assessment on beam separation in the case of strong pulse like excitations and the other

comparatively lower amplitude excitations. It is to be noted that Equations (4-51) and (4-54) appear to be independent of pier size and dependent only on slenderness. However, while Equation (4-51) offers two extremes (positive and negative) and can be considered as size independent, Equation (4-54) contains $\mathrm{sgn}(\theta)$ associated to a term that is added to a constant making it dependent on the rotational response of the equivalent block which in turn depends on the size of the pier. Moreover, the equations are subject to the condition that the equivalent block survives the excitation and cannot be applied to a block that overturns. Hence, if the equivalent block response is obtained from a rocking spectrum where, the response time history (or $\mathrm{sgn}\theta$) is unknown, a conservative possibility of beam separation can be ascertained directly from the excitation by considering the minimum of the vertical acceleration obtained from positive and negative of the time history as given below.

$$\ddot{v}_{\min} = \min\left[\min\left(-\alpha_{eq}^2 g - \alpha_{eq}\,\ddot{u}_g\right), \min\left(-\alpha_{eq}^2 g + \alpha_{eq}\,\ddot{u}_g\right)\right] \tag{4-55}$$

Substituting Equations (4-51) and (4-53) into (4-41) leads to the COFD for the beam as

$$\breve{\mu}_{DU} = \frac{\alpha_{eq}}{\frac{\ddot{v}_{\min}}{g} + 1} \tag{4-56}$$

Although the above explains the seismic isolation of the beam, the effectiveness of this isolation is required to be understood in terms of the response of mass-spring-dashpot oscillators and also of rocking blocks to the horizontal acceleration of the beam. As evident in Figure 4-15, the second row shows the beam's horizontal acceleration as a combination of large period rectangular pulses, whereas in the bottom row they are of much shorter duration. The two scenarios lead to drastically different responses to the beam's horizontal acceleration response time history

as discussed in the next section. The rectangular pulse that is "not physically realizable on the ground" [16] is always present in rocking isolation.

4.8 Response to Earthquake Records

Table 4-8 lists the earthquake records considered in this study. First, symmetrically supported frame responses are studied with regard to seismic isolation and separation of the beam. Later, responses of unsymmetrically supported frames to earthquake records are obtained.

4.8.1 Response of a symmetrically supported frame with rectangular piers (Figure 4-17)

Figure 4-17 shows the response of three sample rocking frames depicted in Figure 4-1 (b) with: 1. $\alpha = 0.165, p = 1.23, q = 4$, 2. $\alpha = 0.3, p = 3.3, q = 1$, and, 3. $\alpha = 0.4, p = 3, q = 2$ in the left, middle and right columns respectively to the San Fernando PCD 164 record. The eccentricity parameter, $\eta = 1$, for all cases. As shown in Figure 4-3 (f), for $\eta = 1$, $\alpha_{eq} = \alpha$. Multiplying the horizontal and vertical displacements at the system CG (marked as $\overline{CG}$) by the ratio of the pier radii, $2R/R_{eq}$, defined as R_{ratio}, in Equation (4-45), leads to vertical and horizontal displacements, u and v, as marked in Figure 4-3 at the beam contact point. The first row from top illustrates the normalized rotation, θ/α_{eq}, the second, vertical displacement, v, and the third, vertical acceleration, $\ddot{v}$. The fourth and fifth rows depict the horizontal displacement, u and the total or absolute horizontal acceleration, $\ddot{u}_T$ respectively. The last row portrays the relative horizontal acceleration, $\ddot{u}$, and the excitation acceleration $\ddot{u}_g$. The example illustrated in left column is from [24], where horizontal and vertical displacement of the beam contact point (pier corner) were reported but without any horizontal or vertical accelerations. The rotation and displacements obtained in this study for this example are identical to those reported in [24]. In the first row, in

comparison to the left column, the normalized rotation (θ/α_{eq}) response increases in the middle but decreases in the right column. The second row shows vertical displacement of the beam to be the maximum in the left column, followed by a little decrease in the second and the least in the third. The third row shows vertical acceleration of the beam which is quite low in the left column but decreases to nearly -0.5g in the middle and less than -0.6g in the right column. The minimum vertical accelerations marked in Figure 4-17 in all columns, are close to the approximate minimum obtained from Equation (4-54) with variations as: 16.7%, 4.1% and 3.2% in the left, middle and right columns respectively. Equation (4-55) gives the same results as Equation (4-54) in the middle and right columns and is conservative in the left column. The right column depicts the lowest rotations (top row) but also the lowest vertical acceleration indicating that in comparison to the other two frames (left and middle columns) this frame is quite stable with regard to overturning but more susceptible to separation of the beam. This is because a large rotation results in a large period of 1s or more (as evident in the top row, left column) which does not match with the excitation period in most of the earthquake records. Considering an earthquake record as a series of pulses, a falling block accompanied with the excitation acceleration augmenting its fall results in the minimum vertical acceleration when the rotation period is somewhat close to the excitation pulse period during rocking motion. This concept is further verified by other examples later in this study.

The fourth row exhibits the horizontal displacement in the left column as 50 cm, which reduces to 5cm in the right column. The fifth row shows total horizontal acceleration experienced by the beam, $\ddot{u}_T$. As predicted by Equation (4-51), for slender piers, $|\ddot{u}_T| \approx \alpha g$ which indeed is the case as shown in the left and the middle columns and with minor variation in the right column. The

bottom most row in the left and middle columns, depicts the two accelerations, $\ddot{u}$ and $\ddot{u}_g$ as approximate mirror images of each other, indicating seismic isolation. The left column belongs to a non-slender pier ($\alpha = 0.4$) and hence the variations in the horizontal acceleration of the beam are pronounced more in comparison to the left and middle columns.

Figure 4-17 demonstrates that the vertical acceleration predicted by Equation (4-55) matches with the numerical cases in all cases except the left column where it is found to be conservative. Also, the rotational response leading to overturning is not the only instability criterion because the vertical acceleration is not necessarily the lowest when rotations are large because the minimum vertical acceleration occurs when the rotation period is somewhat close to the excitation pulse period during rocking motion. A vertical acceleration spectrum accompanied with a rocking spectrum provides better information on instability as explained in the sequel. But before advancing further, it is imperative to investigate the 'effectiveness' of seismic isolation.

4.8.2 Effectiveness of Seismic Isolation for Horizontal Excitation (Figure 4-18 and Figure 4-19)

It is essential to ascertain the effectiveness of seismic isolation in terms of the responses of mass-spring-dashpot SDOF oscillators and of rocking blocks to the beam's horizontal response time history. Two cases of rocking frames shown in the left and middle columns of Figure 4-17 are considered. An enlarged version of $\ddot{u}$, $\ddot{u}_T$ and $\ddot{u}_g$ for these cases is shown in Figure 4-18(a) for the slender large size heavy frame ($\alpha = 0.165$, $p = 1.23$, $q = 4$) and in Figure 4-18(b) for a comparatively less slender, smaller size lighter frame ($\alpha = 0.3$, $p = 3.3$, $q = 1$). As illustrated therein, the absolute horizontal acceleration, $\ddot{u}_T$, is effectively a periodic pulse, resembling a

rectangular one, with amplitude close to αg. In both cases, the pulse period reduces towards the end of the vibration. The acceleration, $\ddot{u}_T$, oscillates between two values even at very low rotations under free vibration and becomes zero at infinite time as explained earlier in Section 4.4.1. Figure 4-18 also illustrates the NVHC, $\left(\dot{\theta}/p_{eq}\right)^2 \sin[\alpha(\text{signum}\,\theta) - \theta]$, to be almost negligible. The plots include the COFD variation over time at the pier pivot and the beam, and vertical acceleration's comparison with that approximated by Equation (4-54). In both cases it is observed that the COFD predicted by Equation (4-56) is close the plotted maximum and the vertical acceleration from Equation (4-54) is close to the numerical solution.

Although the beam's horizontal acceleration response amplitudes are close to each other in both cases as a series of periodic pulses, there is a distinct difference between the two responses with respect to their pulse periods. The period in Figure 4-18(a) is larger than that in Figure 4-18(b). Also Figure 4-18(b) shows more frequent amplitude variation in comparison to Figure 4-18(a). Meaning, Figure 4-18(b) is comparatively richer in the frequency content in comparison to Figure 4-18(a). The difference between the frequency content is demonstrated by Figure 4-19 where the top and bottom rows show responses to the beam time histories of the slender-but-heavy and less-slender-but-lighter frames of Figure 4-18. Both frames are subjected to the same seismic excitation, San Fernando PCD 164 record referenced as the ground time history (TH). The left column compares mass-spring-dashpot SDOF oscillator response spectra for the ground TH with that corresponding to beam's horizontal acceleration TH, $\ddot{u}_T$, from Figure 4-18. Also shown is the USNRC Reg Guide 1.60 design response spectrum [47, 48] for reference. The second and third columns show rocking spectra for the ground TH and the beam TH seismic inputs. It is assumed

that the response/rocking spectra are for oscillators/rocking blocks uncoupled with the frame having insignificant influence on the frame's response.

In the left column top row of Figure 4-19, the spectral accelerations (SA) and the ZPAs in the response spectrum of the beam's TH are much lesser than those for the ground TH, indicating effective seismic isolation. The second column shows the rocking spectra for $\alpha = 0.165$ spread over the period $2\pi/p$ (or size parameter of the pier, larger the $2\pi/p$, larger the block), where, the response to the ground TH is much more than that to the beam TH. However, in the third column, for $\alpha = 0.15$, the larger blocks survive the ground TH but all sizes overturn in response to the beam TH. This means that the blocks with $\alpha = 0.15$ that survive the ground motion are unable to survive the beam acceleration.

In the bottom row, the left column shows the response spectrum for the beam TH to be somewhat close to that for the ground TH, indicating that the isolation is not effective although the ZPA of the response spectrum for the beam TH is lower than that for the ground TH. In the second and the third columns, the rocking response shows similar trend as in the top row.

This section concludes that for the top row in Figure 4-19, horizontal acceleration isolation is effective for mass-spring-dashpot SDOF oscillators but with a broader band response spectrum whereas for rocking blocks the isolation is not effective. In the bottom row isolation is neither effective for the SDOF oscillators, nor for the rocking blocks.

4.8.3 Response of symmetrically supported frames to scaled records (Figure 4-20)

Fragilities of components in NPPs [52] are expressed in terms of the peak acceleration of the excitation time history (the ZPA of the corresponding response spectrum) that leads to failure. In

this section the earthquake records are scaled to the extent that results in the SRSH failure mode but without overturning.

Figure 4-20 shows responses of equivalent blocks of different frames to three earthquake records: 1. SF PCD 164, 2. NR Sylmar and 3. Kobe, in the left, middle and the right columns respectively. The top two rows show responses to the earthquake records and the bottom two rows show responses to the records scaled by the factors 2, 2.8 and 5.6. The rocking frame parameters considered in the top two rows are, $\alpha = 0.4$, $p = 3$, $q = 2$, in the first, $\alpha = 0.4$, $p = 2.5$, $q = 1$, in the second, and $\alpha = 0.3$, $p = 1.75$, $q = 20$, in the third column. For the bottom two rows, the parameters are $\alpha = 0.4$, $p = 1.5$, $q = 2$, in the first, $\alpha = 0.4$, $p = 1$, $q = 12$, in the second, and $\alpha = 0.3$ $p = 1$, $q = 20$, in the third column. The bottom row shows the responses over a large duration whereas the top and the third rows depict them over the time range of interest when the beam's vertical acceleration reaches its minimum. Response parameters marked as 'RS' are plotted on the right scale and others on the left scale.

The left columns shows responses to the SF PCD 164 record. In this column, the top row shows similarity between the excitation time history and a hybrid sine pulse marked in magenta; low frequency and low amplitude half sine pulse followed by a high amplitude half sine pulse at a comparatively higher frequency similar to that shown for the Northridge Rinaldi record in Figure 4-6(e). Due to the initial negative excitation, positive rotation increases, reaches its peak and starts reducing (i.e. block starts falling). Because the rotation and excitation carry the same sign, the excitation augments the fall of the block. Vertical acceleration reduces and reaches its minimum, close to that predicted by Equation (4-54) is close to the numerical solution. The second row of the left column shows the COFD variation at beam to be lower than that predicted by Equation

(4-56). The third row shows the responses to the scaled record for normalized rotation, θ/α_{eq}, NVVC - $\left(\dot{\theta}/p_{eq}\right)^2 \cos\alpha[(\text{sgn}\,\theta) - \theta]$, vertical acceleration and the COFD at the base. As evident, the NVCC is close to zero when vertical acceleration is minimum. The vertical acceleration at the beam crosses the -1g limit. The COFD at the base remains close to 0.5 except for a small fraction of duration (less than 0.2s) when it spikes up exponentially owing to the vertical acceleration reaching its minimum. Here, the COFD for the beam as predicted by Equation (4-56) comes out to be negative; correctly predicting beam's separation. The COFD at beam is not shown for clarity because it asymptotes to infinity upon separation. The vertical acceleration predicted by Equation (4-54) is close to the numerical solution. The bottom row displays, the rotational response, vertical acceleration and the COFD (base) variation over a large duration. As shown, the equivalent block of the frame does not overturn but the beam undergoes separation. The COFD remains close to 0.5 throughout the response except when it spikes to a large value upon separation. Overall, the responses shown in the left column validate the assumptions made in the derivation of Equation (4-54) associated with the occurrence of the beam's minimum vertical acceleration: 1. NVVC is practically zero when the vertical acceleration reaches its minimum, 2. The minimum vertical acceleration coincides with low rotation rather than a large one, and 3. Minimum vertical acceleration occurs when the rotation period (at low rotations) is somewhat closer to that of the excitation. Large rotation results in large period (1s or more) which is not likely to result in minimum vertical acceleration crossing the -1g limit because large period implies large rotation. The minimum vertical acceleration occurs when the block is close to its peak rotation and not when it is about to impact.

The middle column shows the response to NR Sylmar record where, as shown in the top row, the equivalent block rises to its peak and begins to fall and vertical acceleration reaches its minimum. The other rows of this column show similar behavior as witnessed in the left column. The vertical acceleration is close to -1g limit resulting in an exponential rise in the COFD. Equation (4-56) conservatively predicts the COFD at the beam and the vertical acceleration by Equation (4-54) is close to the numerical solution.

The right column exhibits the response to the Kobe record illustrating similar trend as observed in the left and middle columns. The only difference in this case is that the block rises to its negative rotation and starts falling back and the vertical acceleration reaches its minimum. In the second row of this column, the COFD at the base is almost equal to that at the beam because of the heavy loading ($q = 20$) that brings the CG of the equivalent block close to the beam point mass, i.e. $R_{eq} \cong 2R$ (Figure 4-3 (f)).

This section validates the assumptions made in derivation of Equation (4-54) and demonstrates how the excitation being coincidental with the fall of a block leads to the minimum vertical acceleration and the applicability of Equation (4-54) to conservatively predict minimum vertical acceleration. Stability is governed by the separation of the beam because all examples survive the rocking motion without overturning if separation is ignored. Thus, not considering the SRSH failure mode, or assuming its absence would be detrimental to the safety of a rocking frame in a NPP. The COFD's exponential rise is influenced by the reduction in the vertical acceleration rather than the increase in the horizontal acceleration. The COFD is conservatively predicted by Equation (4-56).

4.8.4 Rocking spectra of symmetrically supported frame for rotation, horizontal and vertical accelerations (Figure 4-21)

Figure 4-21 shows rocking spectra of normalized rotations of the equivalent blocks of frame, and, horizontal and vertical accelerations of the beam, for symmetrically supported rocking frames with $\eta = 1$, subject to various earthquake records for four values of $q = 1, 2, 4, 20$, in increasing order from left to right columns. The first and the second rows from top depict response for frames with slenderness parameter, $\alpha = 0.12$, and the rest for 0.2, 0.3, 0.4 and 0.6. The normalized rotation (θ/α_{eq}) and total horizontal acceleration, $\ddot{u}_T$, are plotted on the left vertical axis of left scale, whereas, vertical acceleration, $\ddot{v}$, is plotted on right scale (RS). Out of the three, the normalized rotation and the horizontal acceleration spectra depict the maxima of their absolute response values, whereas the vertical spectral acceleration is the minimum of the entire response. The horizontal axis shows variation in the pier size parameter, p, denoted as period, $2\pi/p$. Overturning is assumed to occur when $\theta/\alpha_{eq} = 1$. Although the horizontal and vertical spectral accelerations are displayed even beyond the overturning ($\theta/\alpha_{eq} > 1$) limit, they are irrelevant because the frame is rendered unstable when $\theta/\alpha_{eq} > 1$. Since $\eta = 1$, $\alpha_{eq} = \alpha$, for all cases. Hence the size (p_{eq}) is the only parameter that impacts the rotational response with variation in q. However, as mentioned in Chapter 2, the ratio of the size parameter of the equivalent to pier is $p_{eq}/p = (1 + 2q)/(1 + 3q)$, variation in q from 1 to 20 renders the variation in p_{eq}/p from 0.866 to 0.82, a 5.3% difference which exponentially diminishes with the increase in q. Therefore, a subtle decrease in rotational response is seen with the increase in q for every $2\pi/p$ from the left column to the right in every row.

The top row in Figure 4-21 shows the response to Hollister followed by the next two rows for Elcentro, fourth row for Kobe, fifth for NR Sylmar and the bottom row for the SF PCD 164 record. As depicted, the normalized rotation and vertical acceleration decrease (from top to bottom) in all columns as α increases, or the pier becomes wider. Meaning, the beam's separation risk increases as the overturning risk decreases, as was observed in Figure 4-17. The vertical acceleration increases with the increase in q, from left to right column depicting that a heavier frame is more stable. The horizontal acceleration decreases with the increase in q for the first three rows where it matches with, αg, as predicted by Equation (4-51). In the fourth row for $\alpha = 0.3$, the maximum acceleration in the last column is within 9% range of that predicted by Equation (4-51). Whereas, in the fifth row ($\alpha = 0.4$) the variation is within 15%. Hence, it can be concluded that Equation (4-51) can predict the horizontal acceleration with good accuracy in a heavy slender pier frame (up to $\alpha = 0.2$) and within a reasonable accuracy for frames with the slenderness angle up to $\alpha = 0.4$.

Table 4-9 lists the values of maximum and minimum horizontal and vertical accelerations for all spectra. As evident from the second last column (from right), maximum vertical accelerations variation range above the prediction by Equation (4-55) is from 3 to 37 percent. However, the right most column of Table 4-9 shows that the minimum vertical accelerations obtained for various records fall 4 to 8 percent below that predicted by Equation (4-55). Since separation risk depends on the minimum vertical acceleration of the beam, it can be concluded that the vertical acceleration predicted by Equation (4-55) leads to a conservative prediction within an acceptable range. The maximum horizontal acceleration on the other hand varies from 12 to 35 percent over Equation

(4-51) but the minimum varies between 1 to 9 percent (for heavy frames, $q = 20$) for slender piers up to $\alpha = 0.3$. Figure 4-21 and Table 4-9 lead to the following conclusions:

1. Overturning and separation risks vary opposite to each other with increasing stockiness in frames with symmetrical eccentricities. As α increases the overturning risk decreases but separation risk increases.
2. Horizontal acceleration of the beam can be predicted by Equation (4-51) with good accuracy in a heavy slender pier frame ($q \geq 4$) with slenderness angle up to $\alpha = 0.2$ and within a reasonable accuracy (15%) for frames with the slenderness angle up to $\alpha = 0.4$.
3. Horizontal acceleration of the beam in lighter frames of any slenderness can be predicted by Equation (4-51) with a factor of safety of 2 (as recommended by ASCE 43 [50]).
4. The minimum vertical acceleration of the beam can be conservatively predicted by Equation (4-55) for a rocking frame subjected to an earthquake record excitation that is compatible with the DBE of NPPs per USNRC Regulatory Guide 1.60 [47, 48].

4.8.5 Effect of Eccentricity on Seismic Response of the Beam (Figure 4-22)

Figure 4-22 shows the impact on instability due to variation in the eccentricity parameter, η for four values of $q = 1, 2, 4, 20$, in four columns from left to right. The first row shows the response to the Parkfield Cholame record, of a frame with slender piers ($\alpha = 0.2$) and the size parameter, $p = 1.5$. The second row shows the response to the Northridge Rinaldi record for a frame with pier parameters, $\alpha = 0.5$, and, $p = 2$.

As evident in the first row in all columns, with the increase in η, the rotation decreases, total horizontal acceleration increases and the vertical acceleration decreases in all columns. Thus, the

stability due to rotation improves but due to separation worsens with the increase in eccentricity. However, with the increase in q, the total horizontal accelerations decrease, and vertical accelerations increase from left to right column. Or, in other words, the gap between the two accelerations widens with the increase in q rendering a heavier frame more stable in comparison to a lighter one.

In the second row, the effect of variation in η on rotation, and, horizontal and vertical acceleration of the beam is observed to be similar to that in the first row. However, comparing the difference between the two rows in a column, the gap between the horizontal and vertical acceleration narrows in the second row, indicating an overall increase in the total horizontal acceleration coupled with the overall decrease in the vertical. Thus, a beam on wider piers is more susceptible to separation.

Dar et al [25] demonstrated that a symmetrically supported rocking frame's vulnerability to overturning decreases with the increase in η as evident in Figure 4-22 where the rotations increase with the decrease in η. However, the decreasing overturning vulnerability is coupled with the increase in separation vulnerability caused by the increase in η. Thus, while the overturning stability of frames improves with the increase in η, the separation stability worsens.

4.8.6 Response of unsymmetrically supported frames on symmetrical and unsymmetrical piers to earthquake records (Figure 4-23 to Figure **4-26**)

As proven in the previous chapter, no equivalent rocking block exists for an unsymmetrically supported rocking frame. The response of such frames depends on pier slenderness, its geometry, and two eccentricities, η and η' (Figure 4-8(b)). Table 4-10 lists parameters for two examples,

marked as Example 1 and 2. Figure 4-23 (a) illustrates Example 1 for symmetrical eccentricities (marked as η_s and η'_s) and Figure 4-23 (b) for varying eccentricities. Example 2 is illustrated in Figure 4-23 (c) for only one case of eccentricity, $\eta = 0$ and $\eta' = 1$. An additional case of symmetrical eccentricities for Example 2, $\eta = 0$ and $\eta' = 0$, has also been considered in analysis.

Figure 4-24 shows responses of Example1 to Chi Chi Taiwan record (Table **4-8**). The time history and the corresponding response spectrum (RS) along with the DBE spectrum [47] are shown in the bottom row. Various responses, rotation, acceleration etc., exhibited therein are obtained through numerical solution of Equation (4-34) with the help of Table 4-4. Three cases of the beam to pier weight ratios are worked out: $q_T = 2, 4, 20$ exhibited in the left, middle and right columns respectively. The first row from top shows the rotation, followed by the normalized effective rotation, θ^*/α, horizontal vertical accelerations at the beam, $\ddot{u}_{TU}$ (Equation (4-40)) and $\ddot{v}_{TU}$ (Equation (4-39)), and the COFD at beam, μ_{DU} (Equation (4-41)). Four types of responses are considered: solitary pier, symmetrical eccentricity, η_s and η'_s, and two cases of unsymmetrical eccentricities, $\eta' = 4\eta'_s$ and $\eta' = \eta'_{max} = 1$. The solitary pier is included in the first row as a reference but not in the rest. The first and second row depict the peak response of symmetrical eccentricity case as maximum. It is noticed that the solitary pier response is the least in all columns in the first row and the peak rotational response is maximum in the middle column for the symmetrical eccentricity case. The focus of this study is on beam accelerations and hence the discussion on rotational response covered in Chapter 3, is kept at bare minimum. The third row shows the horizontal acceleration of the beam for all cases in three columns to be bounded by the acceleration, $\alpha^* g$ (replacing α_{eq} by α^* in Equation (4-51); $\alpha^*$is defined in Equation (4-36)) for the maximum eccentricity case, $\eta' = 1$. Although Equation (4-51) was worked out for

symmetrical eccentricity case with slender piers, it is still applied here in the context of the system slenderness, α^* and found to be bounding. The fourth row shows the vertical acceleration of the beam, bounded by Equation (4-55) applied with system slenderness (α^*) for the symmetrical case. The fifth row shows COFD, (obtained from Equation (4-41), at the beam and the bounding lines for three cases obtained from Equation (4-56) by considering system slenderness, α^*. As evident, the COFD for the symmetrical eccentricity (from Equation (4-56)) bounds all cases as a conservative estimate.

Figure 4-25 shows the responses of Example 1 to Loma Prieta record (Table **4-8**). The first row from the top exhibits the solitary pier response to be the least but the overall response of the symmetrical eccentricity case to be dominating and increasing from the left to the right column. Other responses and their corresponding bounding cases are similar to that in Figure 4-24.

Figure 4-26 shows the responses of Example 2 to SF PCD 254 record. Here the beam to pier weight ratio $q_T = 0.5, 4, 20$, in left, middle and right columns respectively. Only two cases of eccentricity are considered: 1. Symmetrical with $\eta = \eta' = 0$, and 2. Unsymmetrical, $\eta = 0$ and $\eta' = 1$. According to the top two rows, the symmetrical case dominates the response. The horizontal acceleration in the first column (third row) is not bounded by Equation (4-51) because as discussed earlier, Equation (4-51) is applicable when $q_T \geq 1$. The bounding cases for the rest of the responses in all columns are the same as in Figure 4-25.

This section demonstrates that the bounding cases of horizontal and vertical accelerations, and the COFD at the beam, are governed by Equations (4-51) for the maximum eccentricity, and, Equations (4-55) and (4-56) for the symmetrical eccentricity cases respectively when the system slenderness (α^*) is considered in these equations rather than the pier slenderness (α).

4.9 Summary, Verification, Conclusions and Recommendations

4.9.1 Summary

This study investigated the instability of slide restrained rocking frames caused by the lift-off, or separation, of the beam owing to its downward acceleration being more than that due to gravity (or its negative acceleration being less than -g) under horizontal excitation. This mode of instability was identified as Slide-restrained-Rocking-induced-Separation-under-Horizontal-excitation or the SRSH mode. Because the beam's rotational acceleration is more than that at the CG of the entire system, the beam's separation from the piers (rather than the piers' separation from the base) is considered as the governing mode of separation instability in rocking frames. Semi empirical expressions for the beam's horizontal and vertical accelerations, and the COFD were developed for frames with symmetrical eccentricity which were found to be bounding on rocking frames with the beam/piers mass ratio, $q \geq 1$. The response spectra of the earthquake records utilized in this study are similar to the DBE response spectrum recommended by the USNRC Regulatory Guide 1.60 applicable to NPPs [47, 48]. For two- pier frames with unsymmetrical eccentricities the mass ratio between the left and the right pier was considered as, $q_m = 1$, for the two examples in Table 4-10.

4.9.2 Verification of analysis on Working Model 2D and at higher elevations

Finite Element verification of a single block's and frames' responses to hybrid pulse excitation and earthquake records was carried out on the software Working Model 2D [55]. The details of verification are given in APPENDIX B. Verification of semi empirical expressions (Equations 4-51, 4-54, 4-55, and 4-56) was carried out for the time history at higher elevations in a building subject to the USNRC spectrum seismic input. APPENDIX C contains details for this verification.

4.9.3 Conclusions

4.9.3.1 Rigid blocks

Since a symmetrically supported rocking frame can be represented by an equivalent block, the study began with the separation of a rigid block under horizontal excitation. The following conclusions were reached for a slide restrained rigid rocking block.

- According to the literature [10], sliding precedes or safeguards against separation of a rigid block. However, in the case of a slide restrained block (e.g. mobile trolley on rails or a block with shear keys) separation is possible.
- Separation can be achieved in a hybrid-horizontal-pulse excitation consisting of a long period and low amplitude rectangular or half-sine pulse that makes the block rise to its peak rotation, followed by a shorter period and higher amplitude one in reverse direction that accelerates its fall. Thus, separation is likely in the case of a falling block retreating from its peak rotation when the algebraic signs of excitation and block rotation are the same.
- The low-frequency-low-amplitude half sine pulse that often precedes the main sine pulse in an earthquake record was discovered to make a considerable difference in a block's response. Such pre-excitation half sine pulse has been ignored in the literature [13].
- In contrast to the literature [10], the SRSH instability mode was demonstrated to be possible for slender blocks and separation to be achievable at rotations much smaller than α (block's slenderness) for wide blocks.

- Closed form solutions for a falling slender block struck by a rectangular or half-sine pulse while retreating from its peak rotation were derived and numerically verified.
- Equations of hybrid pulse excitations (combination of pre-excitation and the main excitation pulse) were derived that lead to the separation of a slender block without overturning. These equations were utilized (and numerically verified) to generate pulse excitations leading to separation.
- A block's normalized moment of inertia (representative of its geometry) was discovered to influence separation. Lesser the normalized moment of inertia, larger is the absolute value of the block's downward vertical acceleration.
- A rocking spectrum is not a true indicator of the stability of a slide restrained rigid block. It must be accompanied not only with the corresponding vertical acceleration spectrum but also the information on the block's geometry or its normalized moment of inertia.
- In a typical seismic probabilistic risk study [52], only the overturning risk is considered in the case of a rocking block. Consideration of separation risk is warranted for slide restrained blocks.

4.9.3.2 Rocking frames with symmetrical eccentricities

Several cases of rocking frames with symmetrical eccentricities and different pier geometries subjected to various types of hybrid pulse excitations and earthquake records were studied giving rise to the following conclusions regarding the separation of the beam in a rocking frame.

- Overturning and separation risks vary opposite to each other with increasing pier stockiness. As α increases the overturning risk decreases but separation risk increases.

- The response of rocking frames to earthquake records leading to the beam's minimum negative vertical acceleration was found to be similar to that caused by a hybrid pulse excitation, i.e., the occurrence of the beam's minimum negative acceleration coinciding with the portion of excitation that resembles a hybrid sine pulse.
- Fundamental difference between the two modes of instability, overturning and the separation of the beam under the SRSH mode, is that the former is caused by high amplitude large rotations (or large period) but the latter by low amplitude small period rotations.
- Large rotations lead to larger period response in rocking systems (1s or more) which was not found to be a match for the excitation duration in any of the studied cases. However, a low rotational response provides an opportunity for the excitation period to match with that of a falling block helping the beam reach its minimum negative vertical acceleration.
- In all cases, frames' responses to earthquake records considered in this study, the beam's negative vertical acceleration was found to be minimum when the equivalent block system was falling rather than rising. In none of the cases, although a theoretical possibility at a high amplitude excitation, a rising system was found to lead to separation.

4.9.3.3 Seismic isolation in rocking frames with symmetrical eccentricities

Seismic isolation of a rigid beam due to rocking is similar to the seismic isolation of a rigid podium freely supported by piers reported in the literature [41] to be achievable for slender piers with $\alpha \leq 0.3$. The following conclusions were reached in this study with regard to seismic isolation.

- Although the rocking induced seismic isolation may be successful for the beam in a frame, it may still be susceptible to the SRSH instability mode. This is in contrast to the conclusion in [24] and [45] that by making the beam heavier, a rocking frame becomes more stable implying seismic isolation. In reality, making a frame heavier reduces the overturning risk but increases the beam's separation risk because of the low rotational response of the heavier frame at a lower period which is likely to match with a portion of excitation that augments its fall. Therefore, instability due to separation deserves attention in rocking induced seismic isolation.
- The total or absolute horizontal acceleration of the beam in a frame resembles a series of rectangular pulses with the acceleration amplitude being close to $\alpha_{eq}g$ for frames with slender piers.
- A rectangular pulse is the most conservative (or damaging) form of pulse excitation for a rocking block which is not found in real earthquake records but always present in a seismically isolated rigid beam or a rigid podium. Therefore, a large variety of rocking blocks inside an isolated podium would overturn. This behavior was verified for earthquake records.
- The effectiveness of seismic isolation of the beam was evaluated on two counts: 1. The response of SDOF oscillators represented by a response spectrum and, 2. The response of rigid rocking blocks represented by a rocking spectrum, to the response time history of the isolated beam. It was found that the isolation achieved by rocking differs from case to case and may or may not be always effective. The spectral peaks of response spectrum of the isolated time history were found to be somewhat identical to that of the base excitation for

a small pier frame indicating insignificant reduction in seismic demand. Rocking spectrum of the isolated time history was found to be worse than that for the base excitation.

- The seismic isolation and separation of the beam in rocking frames with rectangular piers were discovered to be susceptible to eccentricities varying from $\eta = 0$ to 1. The beam's horizontal acceleration was found to be the maximum and the negative vertical acceleration to be the minimum at $\eta = 1$, a worst-case scenario for the SRSH mode of instability. According to the literature [25] (Chapter 2), the eccentricity, $\eta = 1$, leads to the minimum rotational response and hence the least overturning risk but as established in this study, this condition also leads to the worst case for the SRSH instability mode. Thus, a top-heavy frame being more stable than its lighter counterpart depends on the applicability of the SRSH failure mode. Similar trend was observed for the trapezoidal piers where, the rotational response at $\eta = \phi$ is less than that for $\eta = 0$ but the vertical acceleration shows an opposite trend.

4.9.3.4 Semi-empirical expressions for accelerations and the COFD in rocking frames with symmetrical eccentricities

The response of symmetrically supported rocking frames to earthquake records with different pier geometries led to the development of semi empirical equations, which were found to provide conservative estimates of beam's vertical acceleration and the COFD for the beam at higher loadings, i.e., the beam to piers' cumulative mass ratio, $q \geq 1$. Four relationships (Equations (4-51), (4-54), (4-55) and (4-56)) were established for slender piers which were found to be applicable to frames with equivalent block's slenderness up to, $\alpha_{eq} = 0.4$. The expressions for the beam's horizontal and vertical accelerations, and the COFD respectively are given by Equations

(4-51), (4-55) and (4-56). Equation (4-54) provides an approximate estimation of beam's vertical acceleration response over the entire duration of the excitation that closely resembles the numerical response at its minimum. However, because Equation (4-54) contains $\mathrm{sgn}(\theta)$, the rotational response (θ) is required to be known beforehand. Nevertheless, Equation (4-54) leads to Equation (4-55) that is helpful when the rotational response is unknown. The symmetrically supported rocking frames response to earthquake records leads to the following conclusions:

- The maximum horizontal acceleration of the beam can be predicted by Equation (4-51) with good accuracy in a heavy slender pier frame ($q \geq 4$) with slenderness up to $\alpha = 0.2$ and within a reasonable accuracy for frames with the slenderness angle up to $\alpha = 0.4$.
- Since rocking frames in NPPs are generally used to support heavy beams, the semi empirical expressions developed in this study are found to be applicable to NPPs.
- The maximum horizontal acceleration of the beam in lighter frames of any slenderness can be conservatively predicted by Equation (4-51) by multiplying it with a factor of 2.
- The minimum vertical acceleration of the beam can be conservatively predicted by Equation (4-55).
- The beam's approximate COFD is expressed by Equation (4-56). The COFD's exponential rise, under the SRSH mode, is caused by the reduction in vertical acceleration rather than the increase in horizontal acceleration which is practically constant, $\alpha_{eq} g$, due to isolation.

4.9.3.5 Rocking frames with unsymmetrical eccentricities

The semi empirical expressions were found to be applicable to the response of rocking frames with unsymmetrical eccentricities to earthquake records but by replacing the equivalent block's

slenderness, α_{eq}, with the system slenderness, α^* in Equations (4-51), (4-55) and (4-56). Where, α^* is as given in Equation (4-36) that varies with eccentricities, η and η'. The symmetrical eccentricity case in such fames is denoted by eccentricities, $\eta = \eta_s$ and $\eta' = \eta'_s$. Equations (4-51), (4-55) and (4-56) were found to be bounding on all conditions of unsymmetrical eccentricities for the beam to the generalized rotation pier mass ratio, $q_T \geq 2$, as described below:

- Beam's horizontal acceleration by Equation (4-51) with, $\alpha_{eq} = \alpha^*$, for eccentricities $\eta = \eta_s$ and $\eta' = \eta'_{max} = 1$.
- Beam's vertical acceleration by Equation (4-55) for the symmetrical eccentricity case $\eta = \eta_s$ and $\eta' = \eta'_s$.
- Beam's COFD by Equation (4-56) for the symmetrical eccentricity case $\eta = \eta_s$ and $\eta' = \eta'_s$.

4.9.4 Recommendations for future research

This study considered separation and overturning separately and the occurrence of either is considered as a failure. IN a practical scenario if the separation duration is too small, the rocking may continue once the beam separates and rejoins the piers. However, in such situation, the frame geometry may be altered since the beam-pier contact point may move from its original configuration, and thus altering frame parameters. Post separation continued response is beyond the scope of this study and is a subject of future research.

It was discovered that the separation of slide restrained block can coincide with overturning causing its interaction with nearby seismically qualified components in a NPP. The safe distance of an unanchored object from seismically qualified component is governed by its height because

sliding precedes or safeguards against separation. However, for slide restrained blocks such as mobile trolleys on rails, separation may coincide with overturning causing the safe distance to be larger than that required in an unrestrained block. Future research in this direction is required.

In rocking induced isolation, the isolated time history consists of series of pulses approximately resembling a rectangular shape whose period depends on the pier size of the frame. Larger piers lead to a larger pulse period. On the contrary, smaller piers lead to smaller period directly impacting the effectiveness of seismic isolation. Determination of pier size leading to seismic isolation is beyond the scope of this study and is a subject of future research.

Further research is also required on verification of semi empirical expressions for earthquake records with the response spectra dissimilar to the USNRC spectrum [47, 48]. Nonetheless, for higher elevations in a building subjected to the USNRC spectrum seismic input, the semi empirical expressions developed herein have been verified as detailed in APPENDIX C.

4.10 References

1. EPRI. *A Methodology for Assessment of Nuclear Power Plant Seismic Margin*. Electric Power Research Institute, Report NP-6041-SL-Revision 1, Palo Alto, CA, 1991.
2. Housner GW. The behavior of inverted pendulum structures during earthquakes. *Bulletin of the Seismological Society of America*, 1963; **53**(2):403–417.
3. Aslam M, Scalise DT, Godden WG. Earthquake rocking response of rigid bodies. *Journal of the Structural Division* 1980; **106**(2):377-392.
4. Spanos PD, Koh AS. Rocking of rigid blocks due to harmonic shaking. *Journal of Engineering Mechanics*, 1984; **110**(11):1627-1642.
5. Konstantinidis D, Makris N. The dynamics of a rocking block in three dimensions. Proc., *8th Hellenic Society for Theoretical and Applied Mechanics Int. Congress on Mechanics*, Hellenic Society for Theoretical and Applied Mechanics, Athens, Greece, 2007.
6. Yim CK, Chopra A, Penzien J. Rocking response of rigid blocks to earthquakes. *Earthquake Engineering and Structural Dynamics* 1980; **8**(6):565–587.
7. Makris N, Roussos Y. *Rocking response and overturning of equipment under horizontal pulse-type motions*, Report No. 1998/05. Berkeley, 1998.

8. Ishiyama, Y. “Motions of rigid bodies and criteria for overturning by earthquake excitations.” *Earthquake Engineering and Structural Dynamics*, 1982; **10**(5), 635–650
9. Shenton, H. W. (1996). “Criteria for initiation of slide, rock, and slide-rock rigid-body modes.” Journal of Engineering Mechanics, 1996; **122**(7), 690–693.
10. Pompei, A., Scalia, A., & Sumbatyan, M. A. Dynamics of rigid block due to horizontal ground motion. *Journal of Engineering Mechanics,* 1998; **7**(124), 713-717.
11. Shao Y, Tung C. Seismic response of unanchored bodies. *Earthquake Spectra,* 1999; **15**(3):523–536.
12. Soong, T. T., Yao, G. C., and Lin, C. C. “Near-fault seismic vulnerability of nonstructural components and retrofit strategies.” *Earthquake Engineering &Engineering Seismology*, 2000; **2**(2), 67–76.
13. Zhang, J.and Makris, N. Rocking response of free-standing blocks under cycloidal pulses, *Journal of Engineering Mechanics* 2001; **127**(5), 473-483
14. Taniguchi, T. “Non-linear response analyses of rectangular rigid bodies subjected to horizontal and vertical ground motion.” *Earthquake Engineering and Structural Dynamics*, 2002; **31**(8), 1481–1500
15. Linde, S. A., Konstantinidis, D., & Tait, M. J. Rocking response of unanchored building contents considering horizontal and vertical excitation. *Journal of Structural Engineering,* 2020; **146**(9).
16. Makris, N., & Vassiliou, M. Sizing the slenderness of free-standing rocking columns to withstand earthquake shaking. *Archive of Applied Mechanics*, 2012; **82**(10), 1497–1511
17. Konstantinidis D, Makris N. Experimental and analytical studies on the response of 1/4-scale models of freestanding laboratory equipment subjected to strong earthquake shaking. *Bulletin of Earthquake Engineering*, 2010; **8**(6):1457–1477..
18. Priestley, M., Evison, R., & Carr, A. J. Seismic response of structures free to rock on their foundations. *Bulletin of the New Zealand National Society for Earthquake Engineering*, 1978; **11**(3) 141–150.
19. Wesley, D. A., Kennedy, R. P., & Richter, P. J. Analysis of the seismic collapse capacity of unreinforced masonry wall structures. *Proc. 7th World Conference on Earthquake Engineering,* Istanbul, Turkey, 1980.
20. Makris N, Konstantinidis D. The rocking spectrum and the limitations of practical design methodologies. *Earthquake Engineering and Structural Dynamics* 2003; **32**(2):265–289.
21. Dar A, Konstantinidis D, El-Dakhakhni W. Requirement of rocking spectrum in Canadian nuclear standards. *Transactions, 22nd International Structural Mechanics in Reactor Technology Conference (SMiRT22)* San Francisco, CA, 2013.
22. Dar A, Konstantinidis D, El-Dakhakhni WW. Evaluation of ASCE 43-05 seismic design criteria for rocking objects in nuclear facilities. *Journal of Structural Engineering* 2016; **142**(11).
23. Dar A, Konstantinidis D, El-Dakhakhni WW. Impact of slenderness on the seismic response of rocking frames in Ontario nuclear power plants. *5th International Structural Specialty Conference*, London, Ontario, Canadian Society for Civil Engineering, 2016.
24. Makris N, Vassiliou MF. Planar rocking response and stability analysis of an array of free-standing columns capped with a freely supported rigid beam. *Earthquake Engineering and Structural Dynamics* 2013; **42**(3):431-449.

25. Dar A, Konstantinidis D, El-Dakhakhni W. Seismic response of rocking frames with top support eccentricity. *Earthquake Engineering and Structural Dynamics* 2018;**47**(12):2496–2518. https://doi.org/10.1002/eqe.3096
26. Drosos V, Anastasopoulos I. Shaking table testing of multidrum columns and portals. *Earthquake Engineering and Structural Dynamics* 2014;**43**(11):1703-23.
27. Vassiliou MF, Mackie KR, Stojadinović B. A finite element model for seismic response analysis of deformable rocking frames. *Earthquake Engineering and Structural Dynamics* 2017;**46**(3):447-66.
28. Allen , R. H., Oppenheim , I. J., Parker, A. R., & Bielak, J. On the dynamic response of rigid body assemblies. *Earthquake Engineering and Structural Dynamics*, 1986;(**14)**:861-876.
29. DeJong MJ, Dimitrakopoulos EG. Dynamically equivalent rocking structures. *Earthquake Engineering and Structural Dynamics* 2014;**43**:1543–1563.
30. Dimitrakopoulos, E. G., Giouvanidis, A. I. Seismic Response Analysis of the Planar Rocking Frame. *J. Eng. Mech* 2015;**141**(7).
31. Diamantopoulos, S., Fragiadakis, M. Modeling of rocking frames under seismic loading. *Earthquake Engng Struct Dyn*, 2021;**51**(1):109-128.
32. Lee TH. Nonlinear dynamic analysis of a stacked fuel column subjected to boundary motion. *Nuclear Engineering and Design* 1975; **32**:337-350.
33. Ikushima, Nakazawa T. A seismic analysis method for a block column gas-cooled reactor core. *Nuclear Engineering and Design* 1979; **55**:331-342.
34. Psycharis IN. Dynamic behaviour of rocking two-block assemblies. *Earthquake Engineering and Structural Dynamics* 1990; **19**:555-575.
35. Spanos PD, Roussis PC, Nikolaos P. Dynamic analysis of stacked rigid blocks. *Soil Dynamics and Earthquake Engineering* 2001; **21**:559-578.
36. Konstantinidis D, Makris N. Seismic response analysis of multidrum classical columns. *Earthquake Engineering and Structural Dynamics* 2005; **34**:1243–1270.
37. Kounadis AN, Papadopoulos GJ, Cotsovos DM. Overturning instability of a two-rigid block system under ground excitation. *ZAMM Z. Angew. Math. Mech.* 2012; **92**(7):536 – 557.
38. Minafo G, Amato G, Stella L. Rocking behaviour of multi-block columns subjected to pulse-type ground motion accelerations. *The Open Construction and Building Technology Journal* 2016; **10**(Suppl 1: M9): 150-157.
39. Wittich CE, Hutchinson TC. Shake table tests of stiff, unattached, asymmetric structures. *Earthquake Engineering and Structural Dynamics* 2015;**44**(14):2425-43.
40. Wittich CE, Hutchinson TC. Shake table tests of unattached, asymmetric, dual-body systems. *Earthquake Engineering and Structural Dynamics* 2017;**46**(9):1391–1410.
41. Bachmann, J. A., Vassiliou, M. F., & Stojadinović, B. Dynamics of rocking podium structures. *Earthquake Engng Struct. Dyn*. 2017; **46**, 2499– 2517. doi:10.1002/eqe.2915
42. Chen, Y.-H., Liao, W.-H., Lee, C.-L., & Wang, Y.-P. Seismic isolation of viaduct piers by means of a rocking mechanism. *Earthquake Engng. Struct. Dyn.*, 2006;**35**(6),713-736.
43. Cheng, C.-W., & Chao, C.-H. (2017). Seismic behavior of rocking base-isolated structures. *Engineering Structures*, **139**, 46-58.
44. Lu, L.-Y., & Hsu, C.-C. Experimental study of variable-frequency rocking bearings for near-fault seismic isolation. *Engineering Structures*, 2013;**46**,116-129.

45. Makris, N. Dynamics of Rocking Isolation . *Recent Advances in Earthquake Engineering in Europe - 16th European Conference on Earthquake Engineering*, 2018;**46**:289-307. Thessaloniki: Springer.
46. USNRC. Arkansas Nuclear One – NRC augmented inspection team follow-up inspection report 05000313/2013012 and 05000368/2013012; preliminary red and yellow findings. United States Regulatory Commission's letter to Ankansas Nuclear One. 2014, March 24. Retrieved May 9, 2021, from www.nrc.gov: https://www.nrc.gov/docs/ML1408/ML14083A409.pdf
47. USNRC. Design Response Spectra for Seismic Design of Nuclear Power Plants, Regulatory Guide 1.60, Revision 1. Washington, D.C.: United States Nuclear Regulatory Commission, 1973.
48. USNRC. Design Response Spectra for Seismic Design of Nuclear Power Plants, Regulatory Guide 1.60, Revision 2. Washington DC: United States Regulatory Commission, 2014.
49. Newmark, N. M., Blume, J. H., & Kapur, K. K. Seismic Design Spectra for Nuclear Power Plants. *Journal of the Power Division,* 1973;**99**(2), 287-303.
50. American Society of Civil Engineers. ASCE 43-19 – Seismic Design Criteria for Structures, Systems and Components in Nuclear Facilities. Reston, Virginia, USA, 2019.
51. PTC. Mathcad 15.0. Parametric Technology Corporation, 140 Kendrick Street, Needham, MA 02494, USA. 2012.
52. Reed, J. W., & Kennedy, R. P. *Methodology for Developing Seismic Fragilities EPRI TR-103959.* Palo Alto, California: Electric Power Research Institute, 1994.
53. USGS. (n.d.). *1906 Earthquake. How fast did the ground move?* Retrieved 9 25, 2022, from earthquake.usgs.gov: https://earthquake.usgs.gov/earthquakes/events/1906calif/18april/howfast.php
54. Dar, A., Konstantinidis, D., & El-Dakhakhni, W. W. Input Motion Scaling for Seismic Evaluation of Rocking Components in Canadian Nuclear Power Plants. *Proceedings of the Canadian Society of Civil Engineering Annual Conference*, CSCE, 2021.
55. Working Model 2D Version 9.0.3.806. Design Simulations Technologies Inc. 43311 Joy Road, #237 Canton, MI 48187. www.workingmodel.com .

4.11 Tables

Table 4-1 Parameters of a trapezoidal pier (reproduced from Chapter 3)

Parameter	Chapter 3	Symmetrical Piers [25] $\phi = \phi'$
μ	$1-\frac{1}{2}\left(\phi-\sqrt{4\phi'^2-3\phi^2+4\phi'+4}\right)$	2
ξ	$\frac{3(\mu+\phi+\phi')}{\mu+2\phi+2\phi'}$	$\frac{3(1+\phi)}{1+2\phi}$
$^{*}I_{on}=\frac{{r_0}^2}{R^2}$	$\frac{\sin^2\alpha}{6(\mu+\phi+\phi')}\left[\begin{matrix}(3\phi+3\phi'+\mu)(\xi^2\cot^2\alpha+1)+\cdots\\ \mu^2(\mu+\phi+1)+\phi^2(\mu+\phi+3)+\cdots\\ \phi'^2(\phi'-3)+2\phi\mu\end{matrix}\right]$	$\frac{\sin^2\alpha}{6}\left[7+\phi^2+\frac{(1+3\phi)}{(1+\phi)}\xi^2\cot^2\alpha\right]$

* r_0 is the radius of gyration of the pier.

Table 4-2 Response of a rigid slender rectangular block under free vibration and rectangular pulse ($\boldsymbol{I_{on} = 4/3}$)

Excitation	Initial conditions		Normalized rotation ($\theta_n = \theta/\alpha$)	Vertical acceleration just before impact	Impact timing (pT_{pi})	Separation timing (pT_{ps})	$a_n = a_p/\alpha g$ (separation just before impact)
	$\theta(0)$	$\dot{\theta}(0)$					
Free Vibration	θ_o	0	$1-\left(1-\frac{\theta_o}{\alpha}\right)\cosh pt$	$-\frac{2\alpha^2}{I_{on}}$	$\cosh^{-1}\frac{1}{\left(1-\frac{\theta_o}{\alpha}\right)}$	NA	NA
Pulse just before impact	0	0	NA	$-\frac{\alpha^2}{I_{on}}(a_n+3)$	NA	Same as impact	$\frac{4}{3\alpha^2}-3$
Pulse just before overturning	α^-	0	$a_n(1-\cosh pt)+1$	$\frac{1}{I_{on}}\left(\frac{a_p}{g}\right)^2[\cosh pt-\cosh(2pt)]^*$	$\cosh^{-1}\left(1+\frac{1}{a_n}\right)$	$\cosh^{-1}\left(\frac{1}{4}+\sqrt{\frac{2}{3\alpha^2 a_n^2}+\frac{9}{16}}\right)$	$\frac{4-6\alpha^{2\dagger}}{9\alpha^2}$

*a_p = Pulse amplitude.

†Obtained by equating impact time with separation time.

NA = Not Applicable

Table 4-3 Equivalent block parameters for a rocking frame with symmetrical eccentricities

	Unsymmetrical piers (any geometry) Chapter 3 $\eta = \mu - 2 + \eta'$	Symmetrical piers (any geometry) [25] $\eta = \eta',\ q_m = 1,\ q_T = 2q,\ q_I = 1$
α_{eq}	$\tan^{-1}\left(\frac{1+(\mu-1)q_m+(1+\eta)q_T}{1+q_m+q_T\xi}\tan\alpha\right)$	$\tan^{-1}\left(\frac{1+(\eta+1)q}{1+\xi q}\tan\alpha\right)$
λ	$\sqrt{(1+(\mu-1)q_m+(1+\eta)q_T)^2\sin^2\alpha+(1+q_m+q_T\xi)^2\cos^2\alpha}$	$\sqrt{(1+(\eta+1)q)^2\sin^2\alpha+(1+\xi q)^2\cos^2\alpha}$
ν	$\sqrt{(1+\eta)^2\sin^2\alpha+\xi^2\cos^2\alpha}$	$\sqrt{(1+\eta)^2\sin^2\alpha+\xi^2\cos^2\alpha}$
R_1	νR	νR
$^*\psi$	$1+q_I+\nu^2\frac{q_T}{I_{on}}$	$1+\nu^2\frac{q}{I_{on}}$
R_{eq}	$\frac{\lambda}{1+q_m+q_T}R$	$\frac{\lambda}{1+q}R$
I_{eq}	ψI_o	ψI_o
$^\dagger p_{eq}$	$p\sqrt{\lambda/\psi}$	$p\sqrt{\lambda/\psi}$
$^{**}E_{eq}$	$\frac{1}{\psi}\left(e_{GL}+q_I e_{GR}+\frac{q_T}{I_{on}}(\xi^2\cos^2\alpha-(\eta+1)^2\sin\alpha^2)\right)$	$\frac{1}{\psi}\left[e_G+\frac{q}{I_{on}}\left[\xi^2\cos^2\alpha-(1+\eta)^2\sin^2\alpha\right]\right]$
$^{\dagger\dagger}I_{ons}$	$\frac{I_{eq}}{(1+q_m+q_T)mR^2}=\frac{1+q_m+q_T}{\lambda^2}\psi I_{on}$	$\frac{1+q}{\lambda^2}\psi I_{on}$
R_{ratio}	$\frac{R_1}{R_{eq}}=\frac{\nu}{\lambda}(1+q_m+q_T)$	$\frac{R_1}{R_{eq}}=\frac{\nu}{\lambda}(1+q)$
I_{BR}	$\frac{I_{ons}}{R_{ratio}}=\frac{\psi}{\nu\lambda}I_{on}$	$\frac{I_{ons}}{R_{ratio}}=\frac{\psi}{\nu\lambda}I_{on}$

*$I_{on} = {r_o}^2/R^2$, where, r_o is the radius of gyration of the pier about the pivot point.

**Coefficient of restitution. e_G is defined in Equation (4-2), and, e_{GL} and e_{GR}, in Table 4-4.

†p, the size parameter of the pier about the pivot point O (towards the frame's interior)

††I_{ons} = normalized moment of inertia of the equivalent block.

Greyed area depicts parameters defined in this study.

Table 4-4 Parameters for frames with unsymmetrical eccentricities (Chapter 3)

α_L	$\tan^{-1}\left(\frac{1+(1+\eta)q_T}{1+q_T\xi}\tan\alpha\right)$	α_R	$\tan^{-1}\big((\mu-1)\tan\alpha\big)$
λ_L	$\sqrt{(1+(1+\eta)q_T)^2\sin^2\alpha+(1+q_T\xi)^2\cos^2\alpha}$	λ_R	$q_m\sqrt{(\mu-1)^2\sin^2\alpha+\cos^2\alpha}$
p_L^2	$\frac{\lambda_L}{\psi}p^2, \quad p=mgR/I_o$	p_R^2	$p_R^2=\frac{\lambda_R}{\psi}\frac{d\theta'}{d\theta}p^2$
p_T^2	$\frac{q_Tq_{RT}}{\psi}\frac{d\theta_T}{d\theta}p^2$	δ_1	$\tan^{-1}\left[\frac{R_1\cos(\beta-\lvert\theta\rvert)}{l_B+R_1\sin(\beta-\lvert\theta\rvert)}\right]$
δ_2	$\cos^{-1}\left[\frac{D^2+R'^2_1-l_T^2}{2DR'_1}\right]$	δ_3	$\cos^{-1}\left[\frac{D^2+l_T^2-R'^2_1}{2Dl_T}\right]$
θ'	$\operatorname{sgn}\theta\left(\delta_1+\delta_2+\beta'-\frac{\pi}{2}\right)$	θ_T	$-\operatorname{sgn}\theta\,(\delta_3-\delta_1)$
$\frac{d\theta'}{d\theta}$	$\left[\frac{R_1\cos(\theta_T-\theta+\operatorname{sgn}(\theta)\beta)}{R'_1\cos(\theta_T-\theta'+\operatorname{sgn}(\theta)\beta')}\right]$	$\frac{d\theta_T}{d\theta}$	$-\operatorname{sgn}\theta\,(\delta_3-\delta_1)$
$\frac{d^2\theta'}{d\theta^2}$	$\frac{d\theta'}{d\theta}\left[\tan(\theta_T-\theta'+\operatorname{sgn}(\theta)\beta')\left(\frac{d\theta_T}{d\theta}-\frac{d\theta'}{d\theta}\right)-\tan(\theta_T-\theta+\operatorname{sgn}(\theta)\beta)\left(\frac{d\theta_T}{d\theta}-1\right)\right]$		
$\frac{d^2\theta_T}{d\theta^2}$	$\frac{d\theta_T}{d\theta}\left[\tan(\theta_T-\theta'+\operatorname{sgn}(\theta)\beta')\left(\frac{d\theta_T}{d\theta}-\frac{d\theta'}{d\theta}\right)+\cot\big(\theta'-\theta+\operatorname{sgn}(\theta)(\beta-\beta')\big)\left(\frac{d\theta'}{d\theta}-1\right)\right]$		
ψ	$1+q_I\left(\frac{d\theta'}{d\theta}\right)^2+q_{IT}\left(\frac{d\theta_T}{d\theta}\right)^2+\frac{q_T\nu}{I_{on}}\left[\nu+2q_{RT}\frac{d\theta_T}{d\theta}\cos(\operatorname{sgn}(\theta)\alpha_T+\theta_T+\operatorname{sgn}(\theta)\beta-\theta)\right]$ Where, $\nu=\sqrt{(1+\eta)^2\sin^2\alpha+\xi^2\cos^2\alpha}$		
τ	$q_I\left(\frac{d\theta'}{d\theta}\right)\frac{d^2\theta'}{d\theta^2}+q_{IT}\left(\frac{d\theta_T}{d\theta}\right)\frac{d^2\theta_T}{d\theta^2}+\frac{\nu q_Tq_{RT}}{I_{on}}\left[\frac{d^2\theta_T}{d\theta^2}\cos(\operatorname{sgn}(\theta)\alpha_T+\theta_T+\operatorname{sgn}(\theta)\beta-\theta)+\left(\frac{d\theta_T}{d\theta}\right)\sin(\operatorname{sgn}(\theta)\alpha_T+\theta_T+\operatorname{sgn}(\theta)\beta-\theta)\left[1-\left(\frac{d\theta_T}{d\theta}\right)\right]\right]$		
$\check{e}$	$\frac{1}{\check{\psi}}\left(e_{GL}+q_Ie_{GR}+\frac{q_T}{4I_{on}}(4\xi^2\cos^2\alpha-(\mu+\eta+\eta')^2\sin\alpha^2)-(1+\eta)q_{OT}q_{LT}(\mu+\eta'-\eta-2)\right)$		
$\check{\psi}$	$\left[1+q_I+\frac{q_T}{4I_{on}}(4\xi^2\cos^2\alpha+(\mu+\eta+\eta')^2\sin\alpha^2)+(1+\eta)q_{OT}q_{LT}(\mu+\eta'-\eta-2)\right]$		
e_{GL}	$q_I-\frac{\mu(\mu-1)}{I_{on}}\sin^2\alpha$		
e_{GR}	$\frac{1}{q_I}\left(1-\frac{\mu q_m}{I_{on}}\sin^2\alpha\right)$		

Table 4-5 Normalized amplitudes and timings of rectangular pulse excitation applied to rectangular block ($\alpha = 0.3$)

Pulse No	Part 1		Part 2					Overall timing			Part 3
								Peak time	Separation	Impact	Amplitude ($= a_{2n}$)
	Amplitude (a_{1n})	Duration (pt_{p1})	[1]Amplitude (a_{2n})	[2]Peak (pt_{pk})	Separation (pt_s) Eq(4-22)	Impact (pt_i) Eq(4-21)	Duration $pt_{pk} + pt_s$	$pt_{p1} + pt_{pk}$	$pt_{p1} + pt_{pk} + pt_s$	$pt_{p1} + pt_{pk} + pt_i$	Duration less than Eq(4-21)
1	1.2	2.36	4.272	0.24	0.67	0.67	0.91	2.6	3.27	3.27	0.67
2	1.2	2.37	5	0.21	0.59	0.62	0.80	2.58	3.17	3.20	0.60
3	Same as No. 2 except for the increased duration of Part 2						1.2	Same as pulse 2.			

Procedure for pulse No.1:
[1]Step 1: Determine a_{2n} from Eq (4-23)
[2]Step 2: Determine a_{1n}, pt_{p1} and pt_{pk} numerically from Equations (4-25) and (4-26) for $\theta_n = 1$ and $\dot{\theta}_n = 0$.
[3]Step3: Part 3 amplitude is the same as of part 2 but opposite in sign. Assign enough duration to lift the block to its free vibration mode without overturning in the other direction.

Table 4-6 Normalized amplitudes and frequencies of sine pulse excitation applied to rectangular block, $\alpha = 0.25$

Pulse No	Part 1		Part 2		Part 3		Part 4		Normalized peak time (pt_{pk})
	Amplitude (a_{1n})	Frequency (ω_{1n})	Amplitude (a_{2n})	Frequency (ω_{2n})	Amplitude (a_{3n})	Frequency (ω_{3n})	Amplitude (a_{3n})	Frequency (ω_{3n})	
1	1.5	1.2	13.28	5.64	Same as Part 2		NA	NA	2.14
2	1.2	0.65	9.36	3.01	Same as Part 2		NA	NA	3.54
3	1.2	0.65	11	5.2	Same as Part 2		NA	NA	3.474
4	1.2	0.65	11	5.2	Same as Part 2		1.38	30	NA
5	1.2	3.8	2	28	Same as Part 2		1	56	NA

Table 4-7 Parameters of solitary symmetrical trapezoidal pier and pulse excitation

ϕ	ξ	ξh (m)	h (m)	b (m)	R (m)	α (rad)	p (rad/s)	e_G	Hybrid Sine Pulse (Figure 4-6)			
									Part 1		Parts 2 & 3	
									a_{1p}	ω_{1p}(rad/s)	a_{2p}	ω_p(rad/s)
0.25	2.5	2.4	0.96	1.00	1.921	0.806	2.32	0.207	$1.2\, g \tan\alpha$	4	$2.4\, g \tan\alpha$	8

Table 4-8 Details of earthquake records

Earthquake	Year	Station	Record	PGA (g)
Hollister, Calif.	1961	Hollister	B-HCH271	0.195
Imperial Valley, CA	1940	117 El Cento Array #9	I-ELC180	0.313
Parkfield, CA	1966	1013 CHOLAME #2	C02065	0.476
Loma Prieta, CA	1989	LGPC	LGP 000	0.563
Kobe	1995	Takarazuka	000	0.69
Northridge, CA	1994	Rinaldi	RRS 228	0.838
Northridge, CA	1994	Sylmar	360	0.843
Chi Chi Taiwan	1999	TCU084	East	1.00
San Fernando, CA	1971	Pacoima Dam	PCD 254	1.16
San Fernando, CA	1971	Pacoima Dam	PCD 164	1.226

Table 4-9 Horizontal and vertical acceleration response of frames with symmetrical eccentricities

Earthquake Record	α	Horizontal Acceleration					Vertical Acceleration				
		Max (g) $q=1$	Min (g) $q=20$	Equation (4-51)	Variation over Eq (4-51) Max (%)	Variation over Eq (4-51) Min (%)	Max (g) $q=20$	Min (g) $q=1$	Equation (4-55)	Variation over Eq (4-55) Max (%)	Variation over Eq (4-55) Min (%)
Hollister	0.12	0.146	0.121	0.12	22	1	-0.028	-0.031	-0.038	26	18
El Centro	0.12	0.16	0.121	0.12	33	1	-0.044	-0.054	-0.052	15	-4
El Centro	0.20	0.243	0.206	0.2	22	3	-0.1	-0.111	-0.103	3	-8
Kobe	0.30	0.335	0.326	0.3	12	9	-0.187	-0.243	-0.298	37	18
NR Sylmar	0.4	0.458	0.433	0.4	15	8	-0.466	-0.521	-0.497	6	-5
PCD164	0.6	0.854	0.811	0.6	42	35	-0.795	-0.889	-1.096	27	19

Greyed cells: Maximum values belong to $q = 20$ and minimum to $q = 1$.

Table 4-10 Details of rocking frame examples

Example 1 Figure 4-23(a) Unsymmetrical Trapezoidal piers

α	α'	μ	ξ	p_p(rad/s)	p_n(rad/s)	e_G^+	e_G^-	I_{on}	η_s	η_s'
0.441	0.540	2.270	2.386	2.141	2.113	0.696	0.643	1.361	0.438	0.168

R (m)	l_B (m)	I_o (m^4)	q_I	q_{OT}	α_T	R_T (m)	l_T (m)	q_{RT}	q_{IT}	q_{LT}
1.573	8.636	1.34E+01	1.082	13.079	1.490	4.536	8.636	2.884	52.431	0.054

Grey variables would vary with eccentricity. The listed values are for symmetrical eccentricities, η_s and η_s'.

Example 2 Figure 4-23 (c) Symmetrical Rectangular piers

α	α'	μ	ξ	p_p(rad/s)	p_n(rad/s)	e_G^+	e_G^-	I_{on}	η	η'
0.359	0.359	2	2	2.377	2.377	0.815	0.815	1.333	0	1

R (m)	l_B (m)	I_o (m^4)	q_I	q_{OT}	α_T	R_T (m)	l_T (m)	q_{RT}	q_{IT}	q_{LT}
1.302	3.048	5.04E+00	1.000	0.467	1.279	1.591	2.591	1.222	1.866	0.257

Greyed variables are for the given eccentricity. They will be different for the symmetrical case.

4.12 Figures

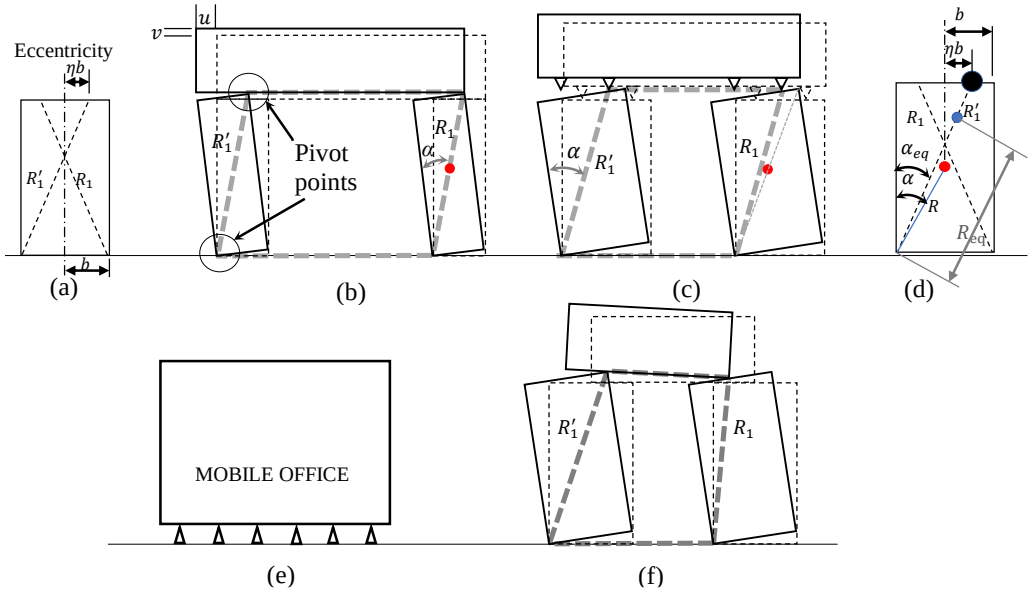

Figure 4-1 Rocking frames: (a) pier schematics, (b) top supports at pier corners ($R_1 = R_1'$), (c) in between the pier corners and centers ($R_1 = R_1'$), (d) equivalent block system, (e) mobile office on triangular piers, (f) dissimilar top support condition with unsymmetrical eccentricities ($R_1 = R_1'$).

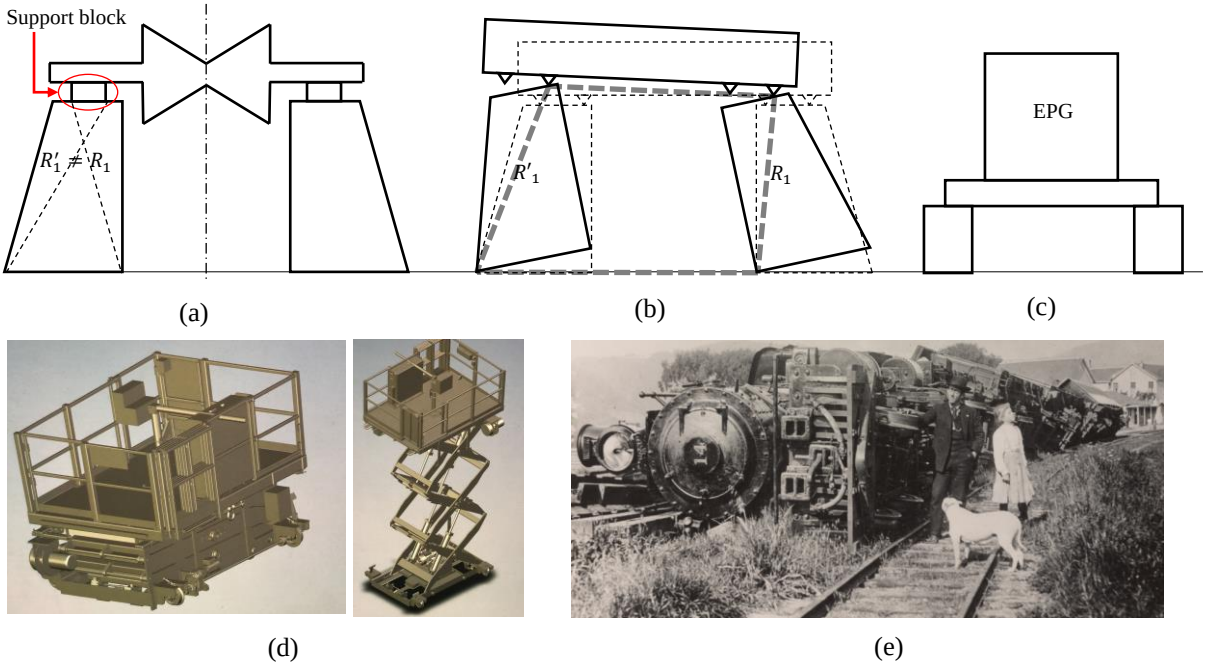

Figure 4-2 (a) schematics of a turbine rotor, (b) simplified representation of (a) in rocking motion, (c), emergency power generator (EPG) trailer on temporary supports. (d) & (e) mobile elevated work platform in NPPs and an overturned train due to 1906 San Francisco earthquake (Roy D. Graves Collection, The Bancroft Library, UC, Berkeley).

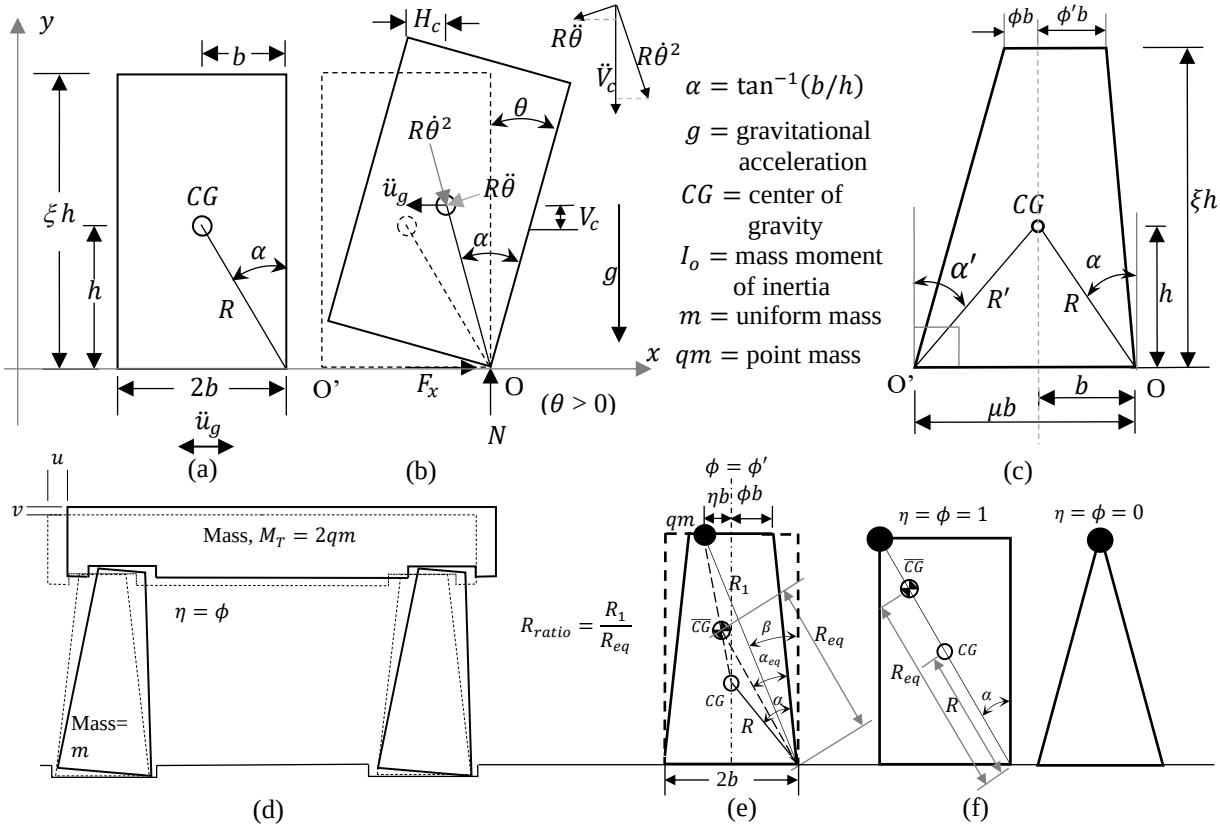

Figure 4-3 Schematic of a freestanding rigid block: (a) and (b), rectangular, and, (c) non-rectangular. (d) rocking frame on trapezoidal piers. (e) equivalent block system of trapezoidal. (f) rectangular and triangular piers.

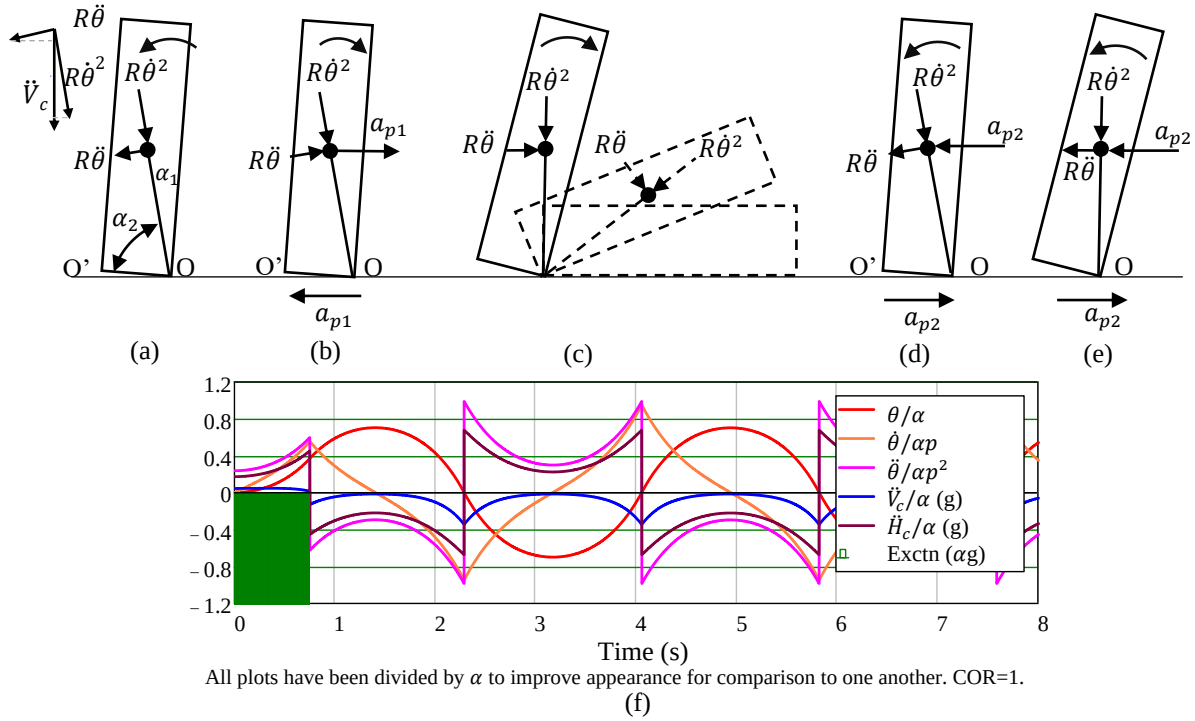

Figure 4-4 Tangential and centripetal accelerations for a block with slenderness parameter, α_1, and its compliment, α_2: (a) under free vibration, (b) with excitation pulse applied towards left resulting in clockwise rotation, (c) overturned slender block turns into to a wide block with slenderness, α_2, accelerating downwards, (d) and (e) excitation pulse applied toward right to the slender block in (a), just before impact and just before overturning respectively. (f) Response of a slender rectangular block to a rectangular pulse (green rectangle) with normalized amplitude, $a_p/\alpha g$ =1.2. All plots are divided by α to improve visibility. COR=1.

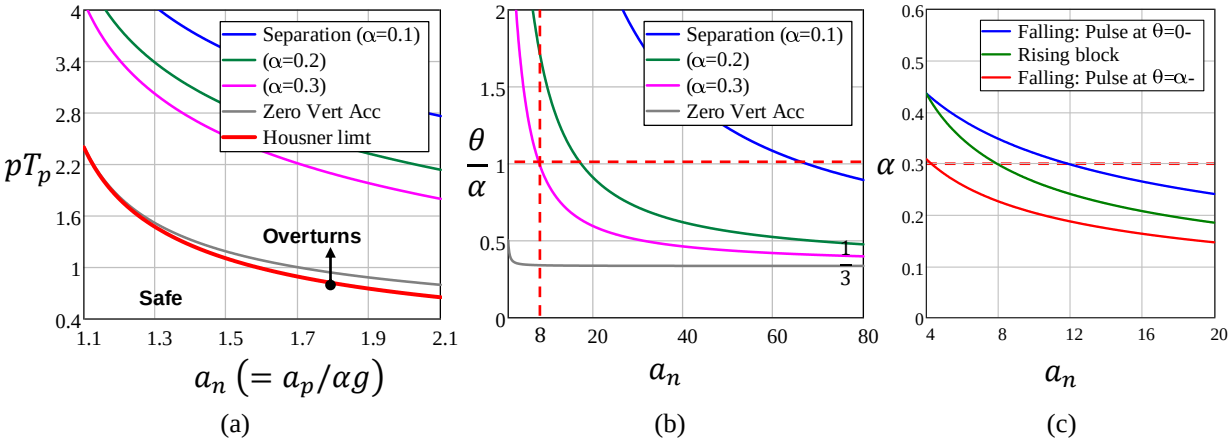

Figure 4-5 (a) Rising block: normalized pulse duration v/s amplitude. (b) Rising block: normalized rotation at zero vertical acceleration and separation (c) Falling block: slenderness required to cause separation for two extremes of pulse application: just before impact ($\theta = 0^-$) and just before overturning.

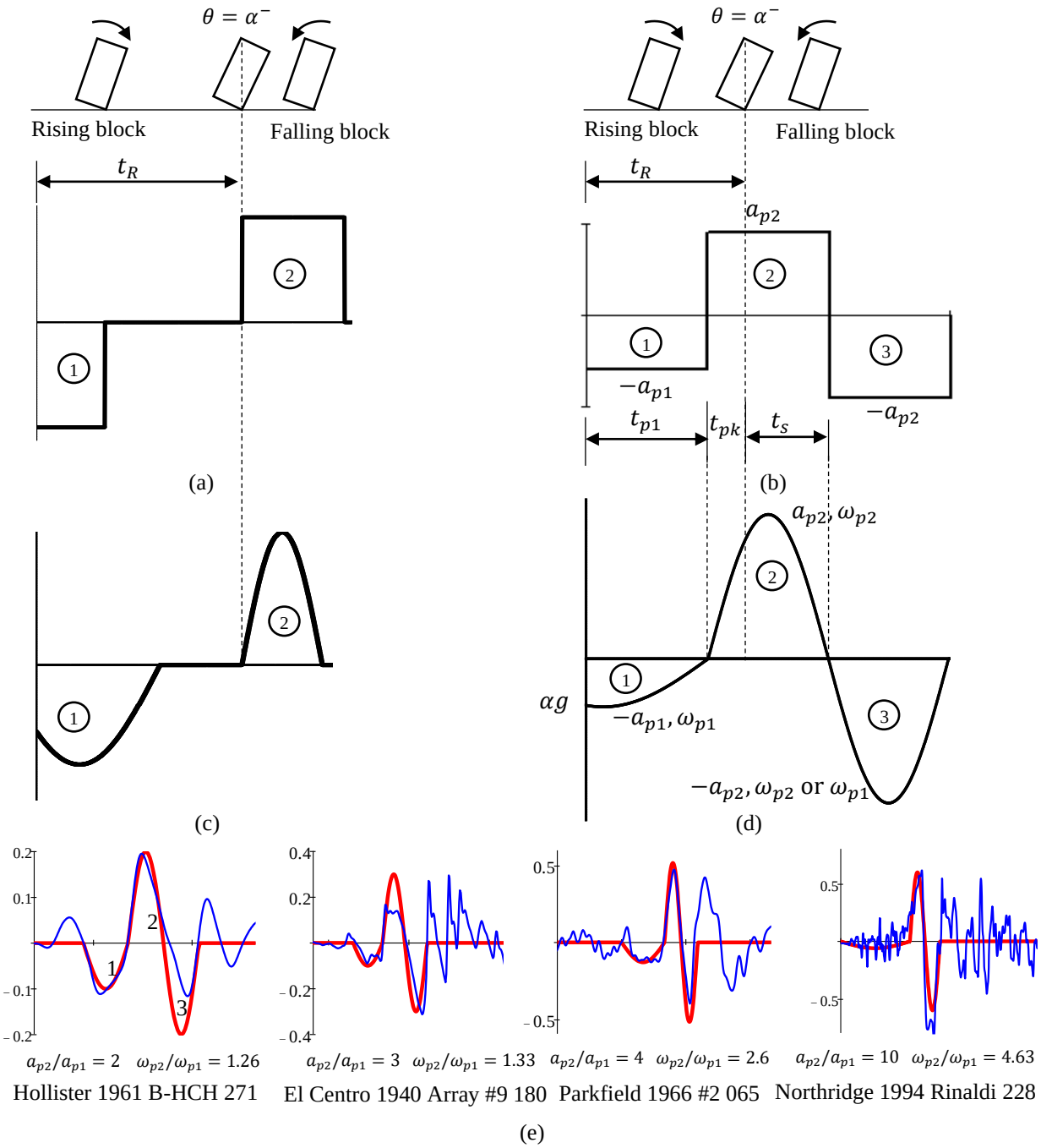

Figure 4-6 Rectangular and sine pulse excitations: (a) and (b), Part 1 expires, block rises to overturning limit, Part 2 strikes, causes separation. (c) and (d): Part 1 strikes, block rises. Part 2 strikes, block keeps rising up to overturning limit and then retreats. Separation at time, t_s. Part 3 strikes in the opposite direction. (e) Examples of earthquake records with pulse excitation similar to that in (d).

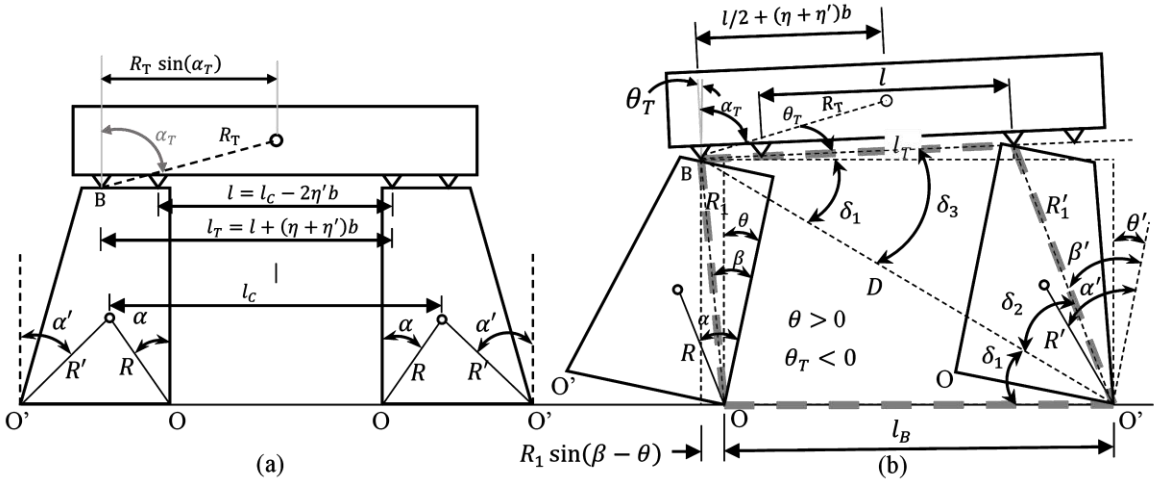

Figure 4-7 Rocking frame: (a) at rest, and (b) rocking. Contact polygon in grey dashed lines.

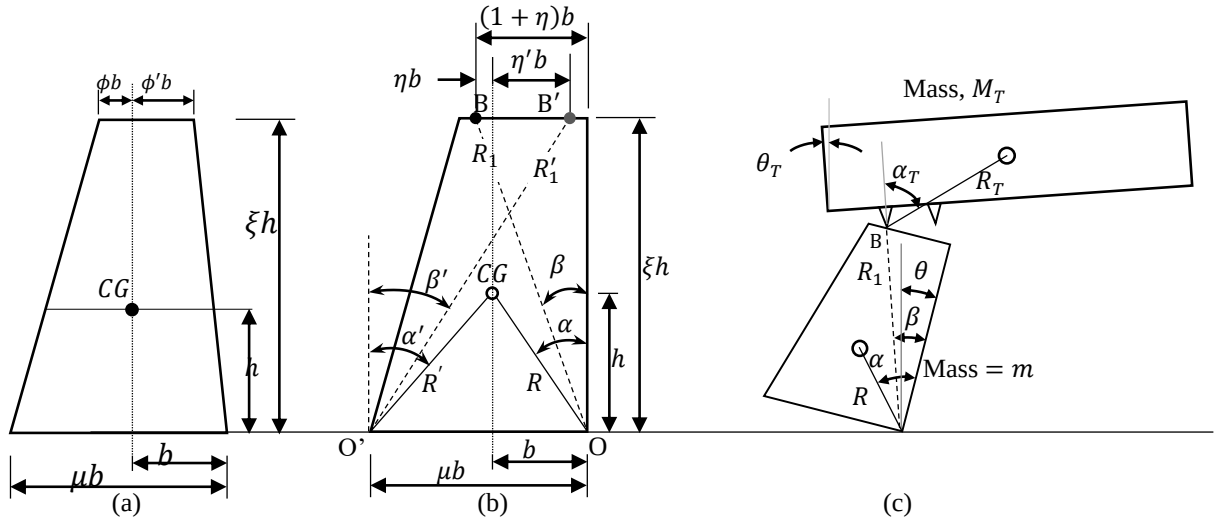

Figure 4-8 Unsymmetrical trapezoidal piers: (a) generic configuration, (b) various dimensions, and (c) left pier with beam under rotation.

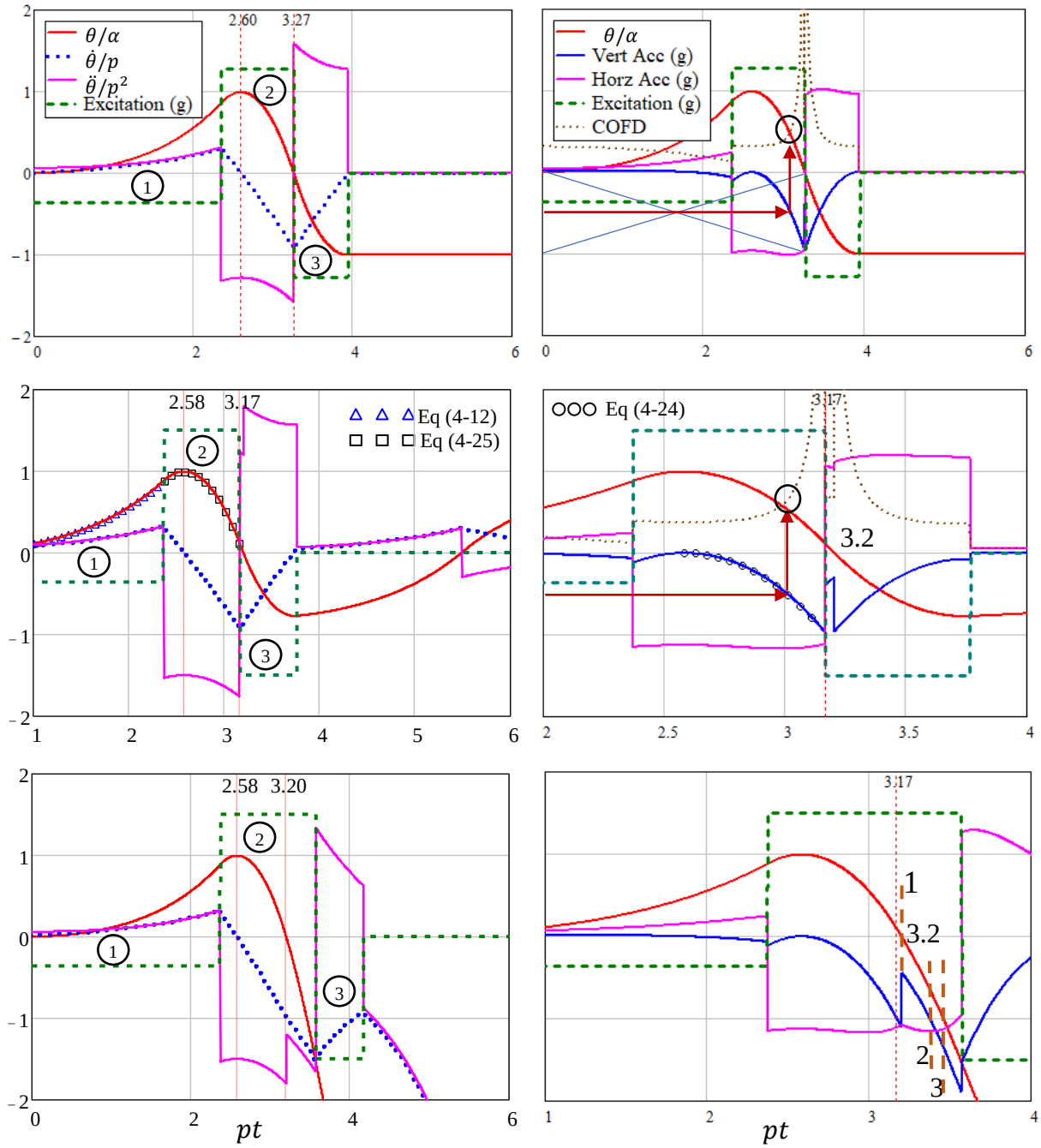

Figure 4-9 Numerical linear response to rectangular pulses (Table 4-5) over normalized time for $\alpha = 0.3$. Top row: Pulse 1, equal separation and impact timings. Free vibration at maximum amplitude limit. Middle row: Pulse 2, separation (3.17) before impact (3.2) followed by free vibration (ignoring separation). Agreement between analytical and numerical solutions. Bottom row: Pulse 3, two instances of separation (brown dashed vertical lines): 1. before impact and, 2. while overturning. Third brown dashed line shows vertical acceleration <-1.5g at $\theta = \alpha$, implying separation while overturning. COR=1 in all cases.

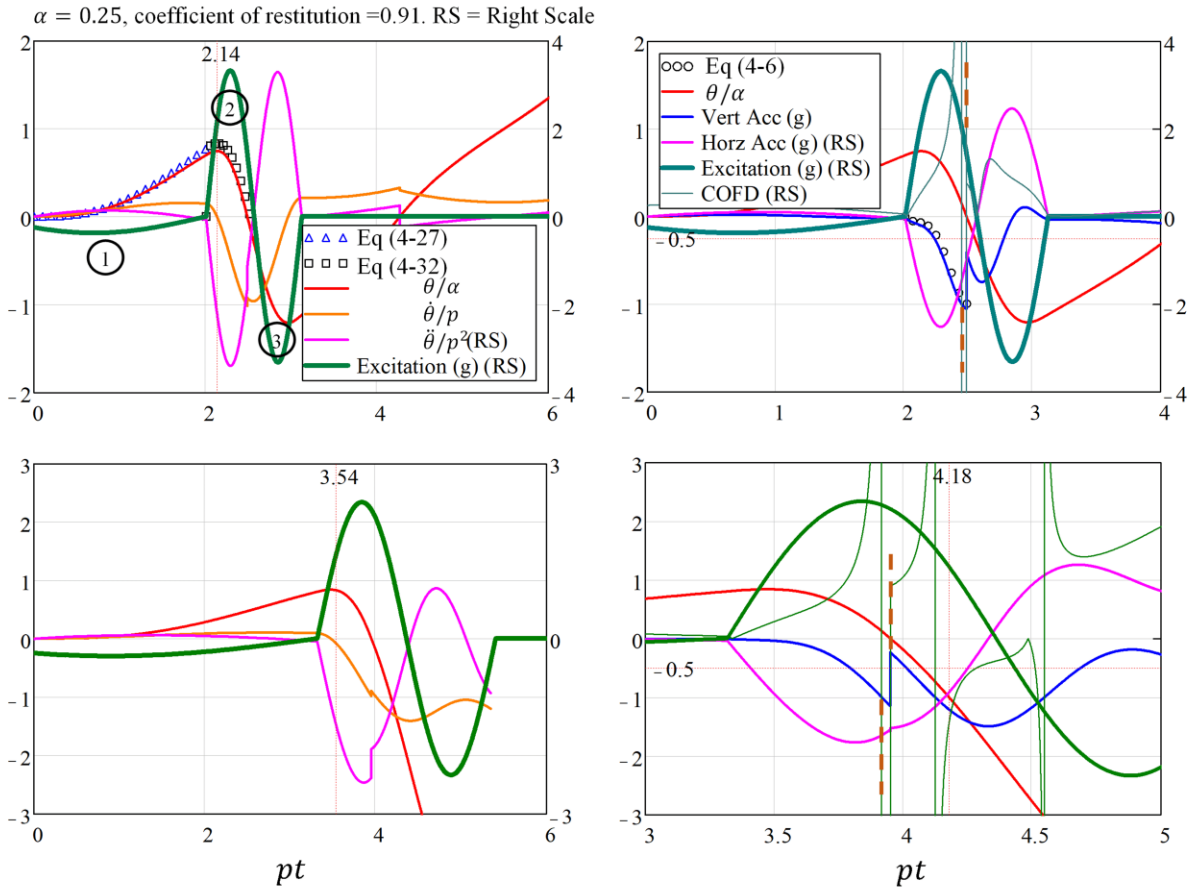

Figure 4-10 Nonlinear numerical response to sine pulses (Table 4-6) over normalized time for $\alpha = 0.25, p = 2.14/s$. Top row, Pulse No. 1: Close agreement between analytical and numerical solutions. Bottom row, Pulse No. 2. In the right column for both rows, dashed brown lines depict the impact and separation timing. Exponential increase in positive, and decrease in negative, COFD once the vertical acceleration drops below -0.5g. Coefficient of restitution in all cases = 0.91.

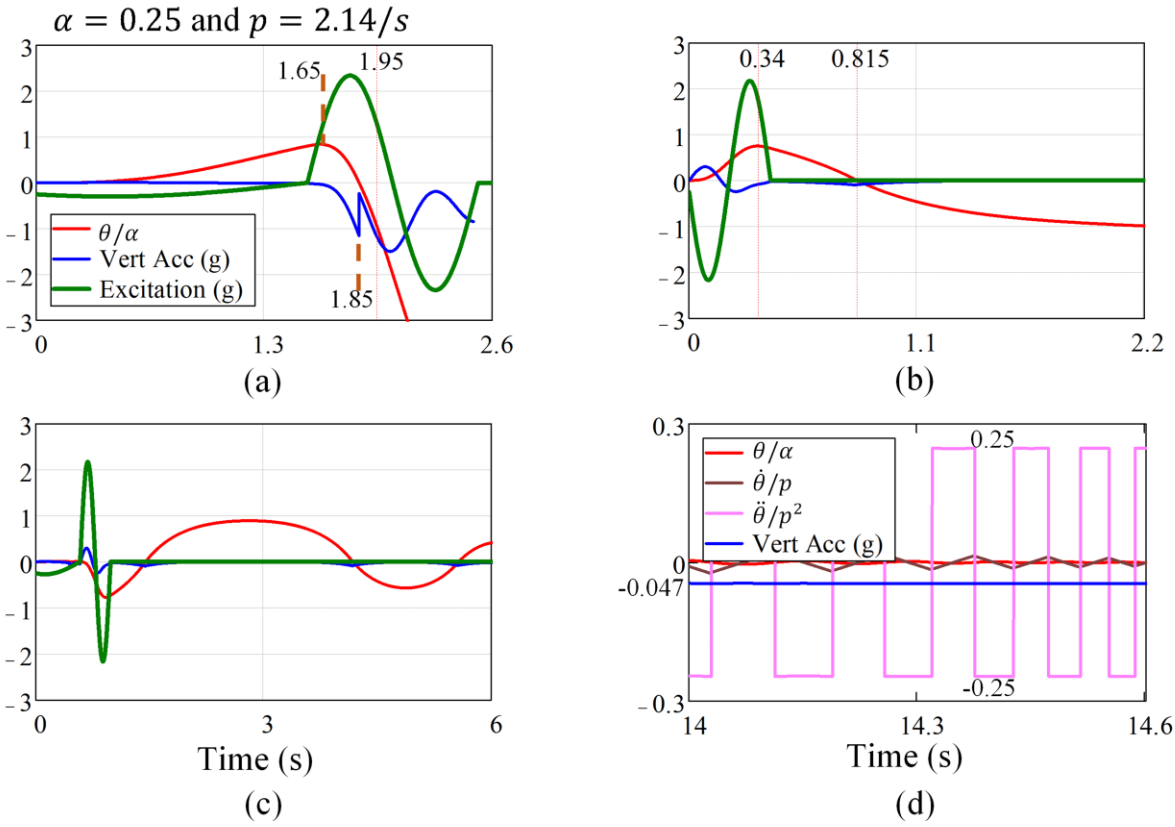

Figure 4-11 Comparison of nonlinear numerical response for the locomotive example considered in [13]: (a) Response to Pulse No. 2 in Table 4-6. (b) Response to sine pulse in [13] with amplitude, 2.2g and angular frequency, 15.7 rad/s. (c) response to the sine pulse excitation as in (b) but preceded by half pulse with amplitude, -0.27g and angular frequency, 3.391 rad/s leading to free vibration. (d) free vibration response where vertical and normalized angular accelerations reach constant values as predicted in Equations (4-7) and (4-10). COR = 0.91.

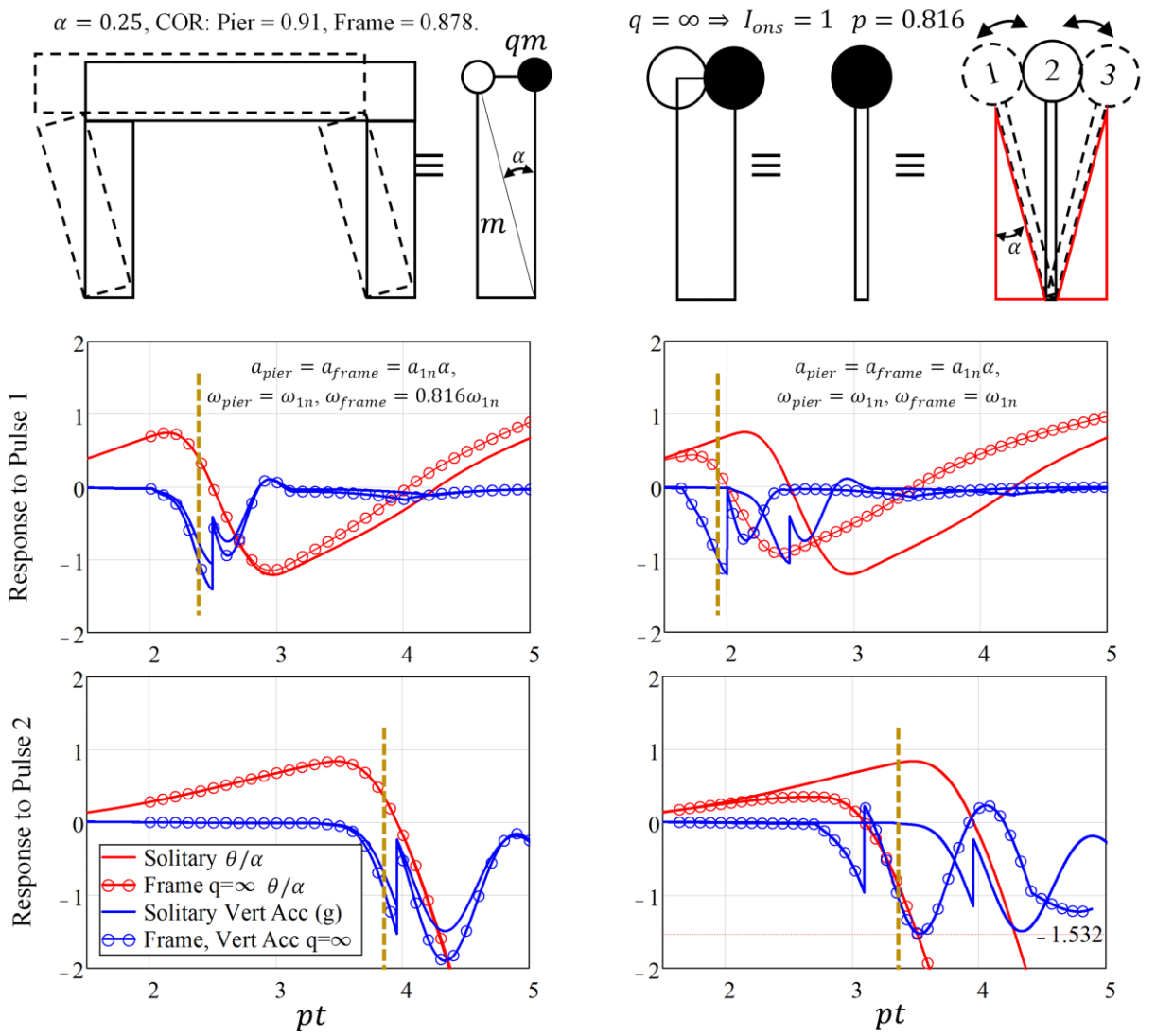

Figure 4-12 Numerical nonlinear response over normalized time to sine pulses (Table 4-6) with two extremes of top loading: a solitary rectangular pier, $q = 0$ ($\alpha = 0.25$, $I_{on} = 4/3$, and $p = 1$), and, the frame with $q = \infty$ ($\eta = 1$, $\alpha_{eq} = 0.25$, $I_{ons} = 1$, and $p_{eq} = 0.816$). CORs for the pier and the frame are 0.91, and 0.878 respectively. Top left: Frame under vibration and its equivalent block instantly switching position upon impact from the black dot to white. Top right: Pier and large mass combination equivalent to a stick mass model rocking between two extremes represented by the red triangles: between 2 and 1, and, 2 and 3, with instant switch upon impact from 1 to 3 and 3 to 1. Middle and bottom rows: responses to Pulse No. 1 and 2 (Table 4-6) respectively: Left column, the solitary pier and the frame both rise to their peaks exhibiting self-similar response to the normalized excitation. Right column, the frame experiences the same excitation as of the solitary pier. Brown dashed line marks the time for vertical acceleration = -1g for the frame.

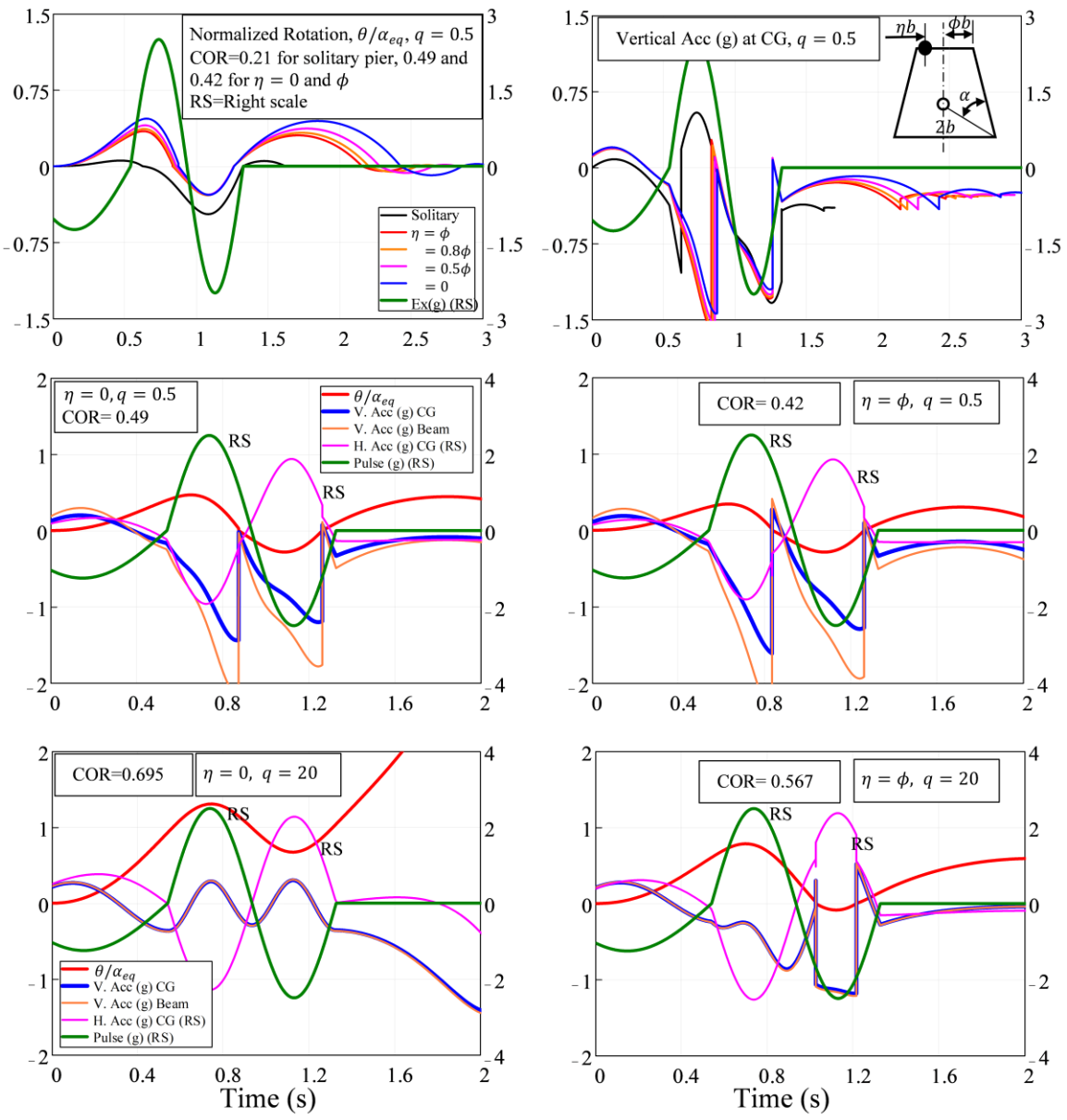

Figure 4-13 Comparison of nonlinear numerical response of a symmetrical trapezoidal pier ($\alpha = 0.806$, and $\phi = 0.25$) to the hybrid sine pulse, as listed in Table 4-7 and corresponding frames with various eccentricities ($\eta = 0,\ 0.5\phi, 0.8\phi$ and ϕ). Top row: Response of the CG of equivalent blocks. Middle row: comparison of vertical acceleration at equivalent block CG and the beam for $q = 0.5, \eta = 0$, and, $\eta = 0.5\phi$. Bottom row: The same for, $q = 20$. COR varies with eccentricity and the beam weight. RS = right scale.

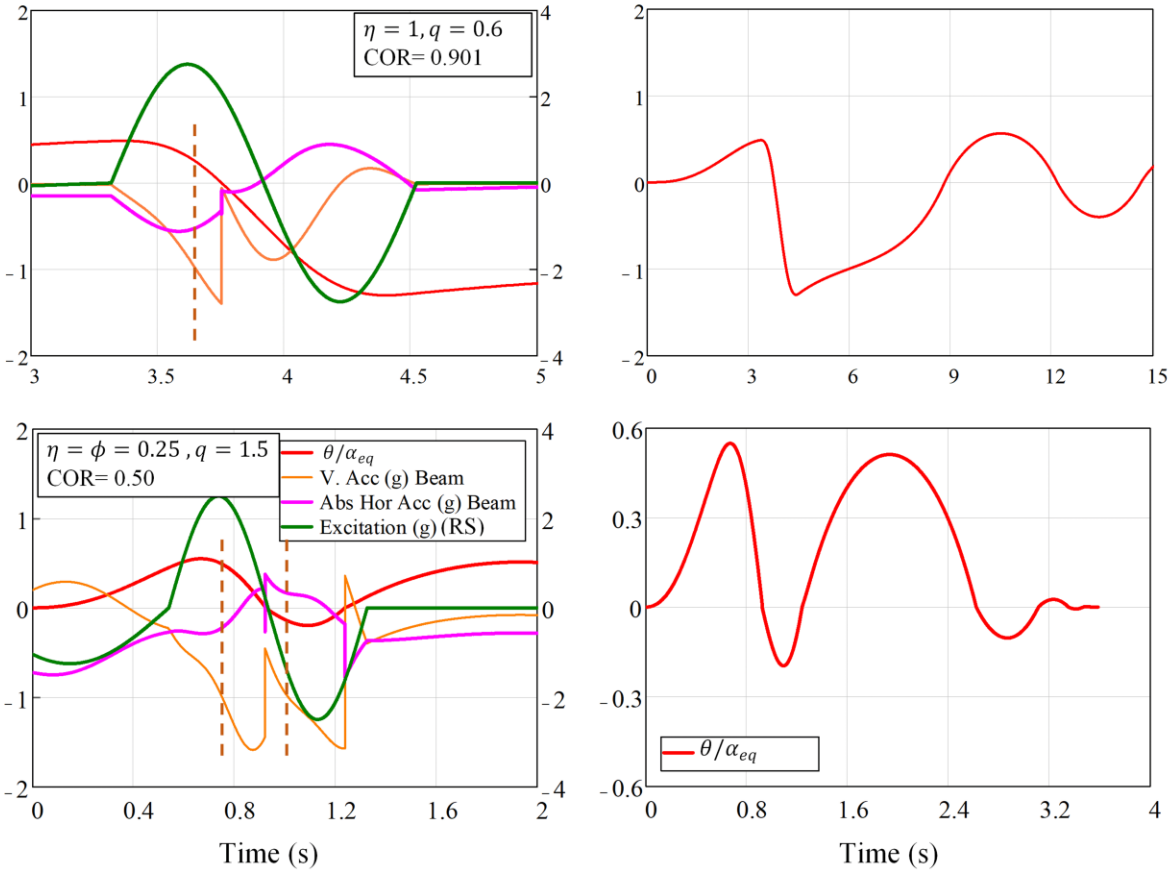

Figure 4-14 Comparison of seismic isolation of horizontal and vertical acceleration in the response of equivalent blocks of frames subjected to the excitation Pulse 3 in Table 4-6 depicted on right scale (RS): Top row, frame with slender rectangular piers ($\alpha = 0.25$ and $p = 1$) and $q = 0.6$. Bottom row, frame with wide trapezoidal piers subjected to the pulse excitation given in Table 4-7 and $q = 1.5$. COR and eccentricity are as noted. The left column shows amplified view close to impact. The right column shows normalized rotation over a large time interval.

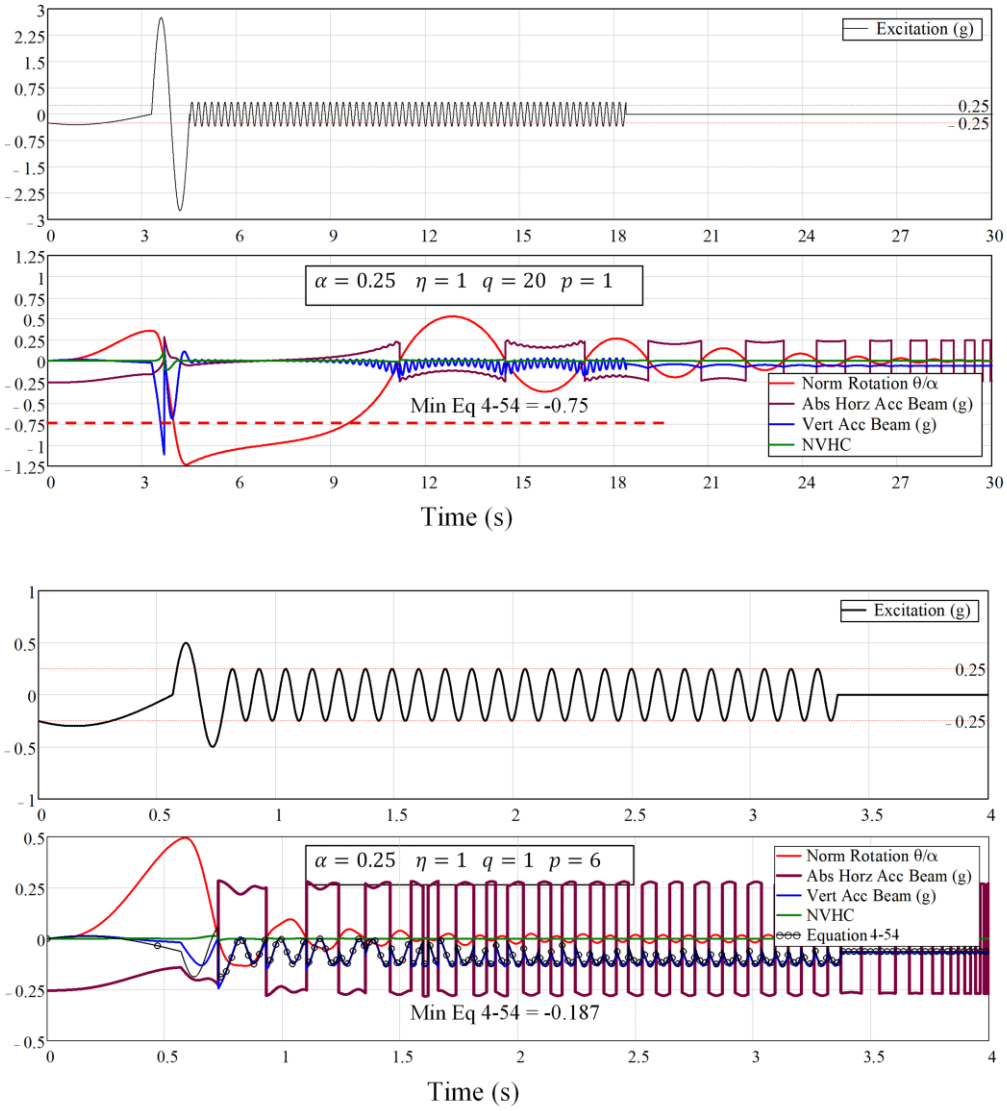

Figure 4-15 Numerical response (at beam) of rocking frames with slender rectangular piers under hybrid pulse followed by continuous excitation. Top and bottom sets: Excitation pulses 4 and 5 in Table 4-6 respectively and corresponding responses.

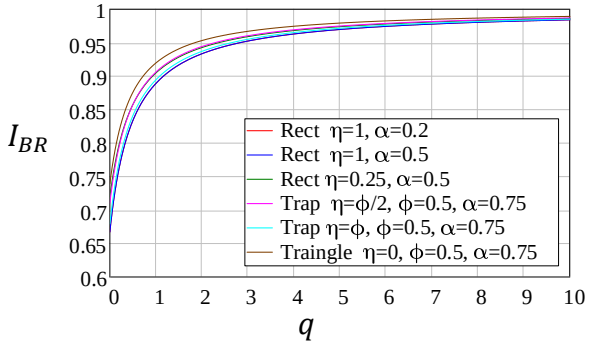

Figure 4-16 Variation in I_{BR} with respect to q

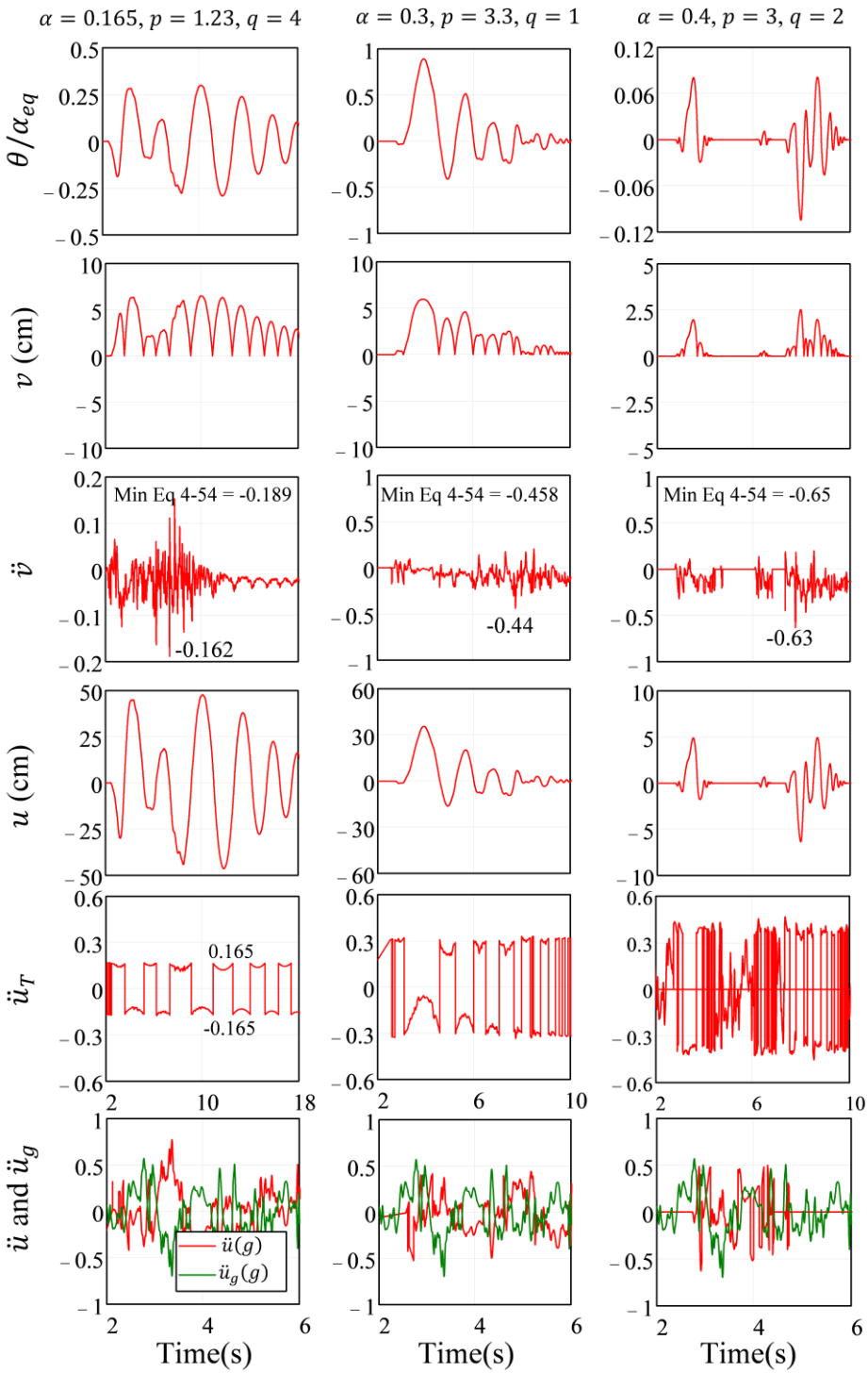

Figure 4-17 Response of symmetrically supported frame to San Fernando PCD 164 record: Left column, $\alpha = 0.165$, $p = 1.23$, $q = 4$. Middle column: $\alpha = 0.3$, $p = 3.3$, $q = 1$. Right column: $\alpha = 0.4$, $p = 3$, $q = 2$. For this frame, $\alpha_{eq} = \alpha$, because $\eta = 1$.

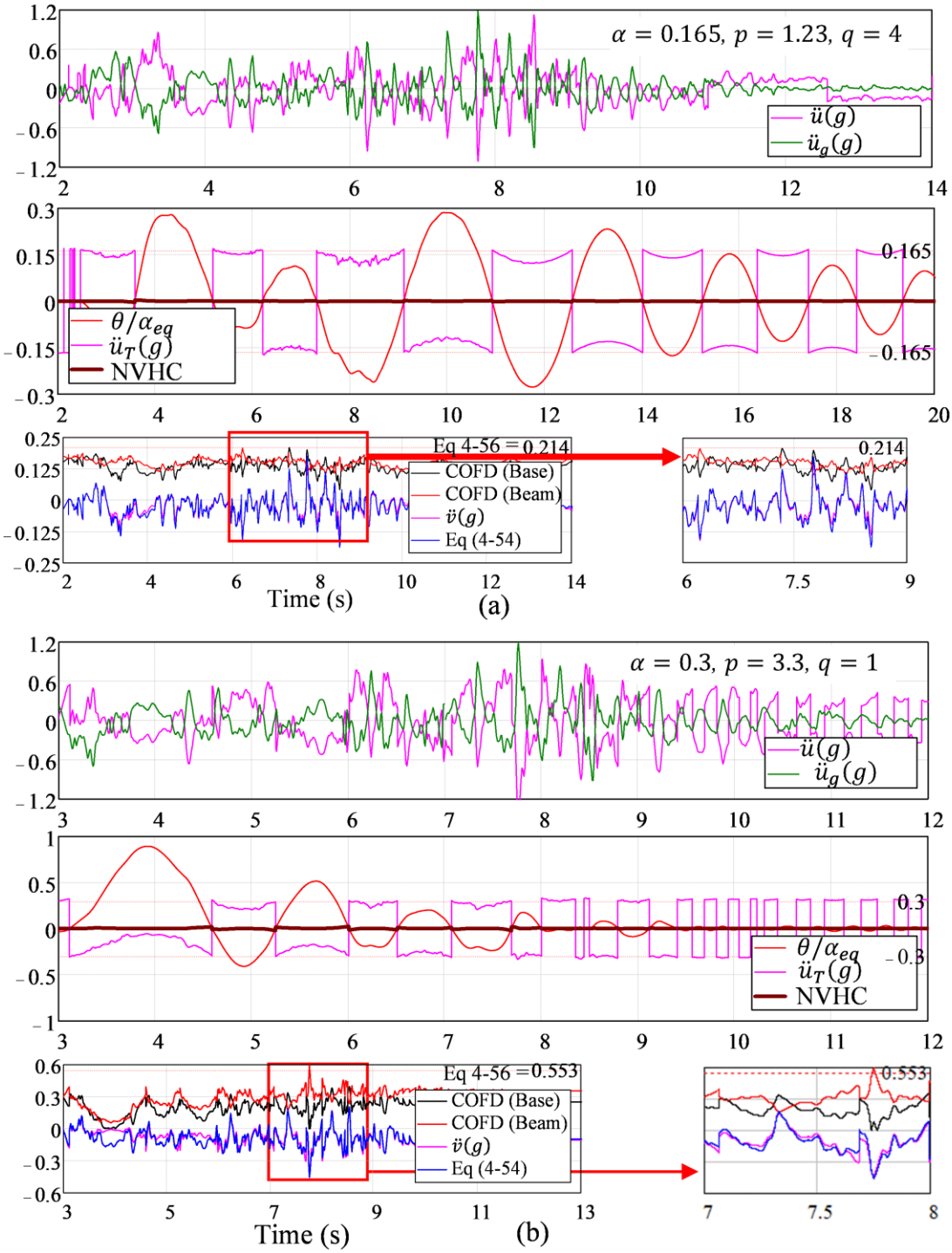

Figure 4-18 Relative and absolute horizontal acceleration responses at beam to San Fernando PCD 164 record in symmetrically supported frames on slender rectangular piers (same as the first two columns of Figure 4-17). (a) $\alpha = 0.165, p = 1.23, q = 4$. (b) $\alpha = 0.3, p = 3.3, q = 1$.

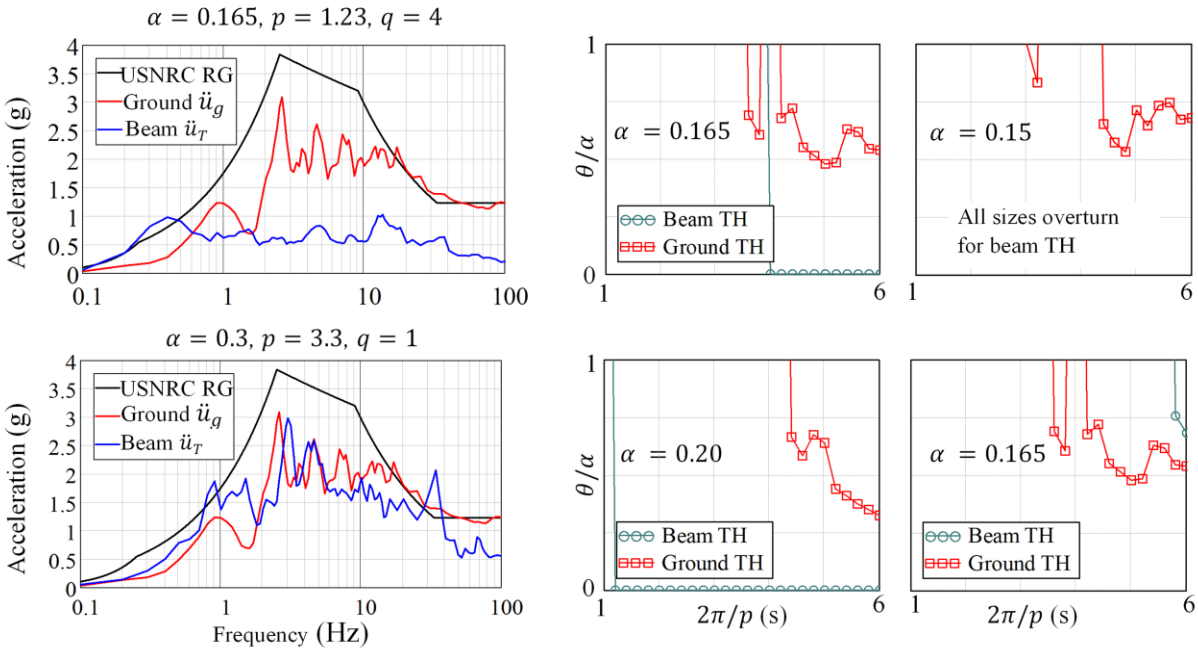

Figure 4-19 Comparison of SDOF spring-mass-dashpot oscillator response spectra (left column) and rocking spectra (middle and right columns) for the excitation TH ($\ddot{u}_g$) and beam response ($\ddot{u}_T$). The first and second rows correspond to $\ddot{u}_g$ and $\ddot{u}_T$, from Figure 4-18(a) and (b) respectively. The design basis earthquake spectrum from the USNRC Regulatory Guide 1.60 is shown only for reference.

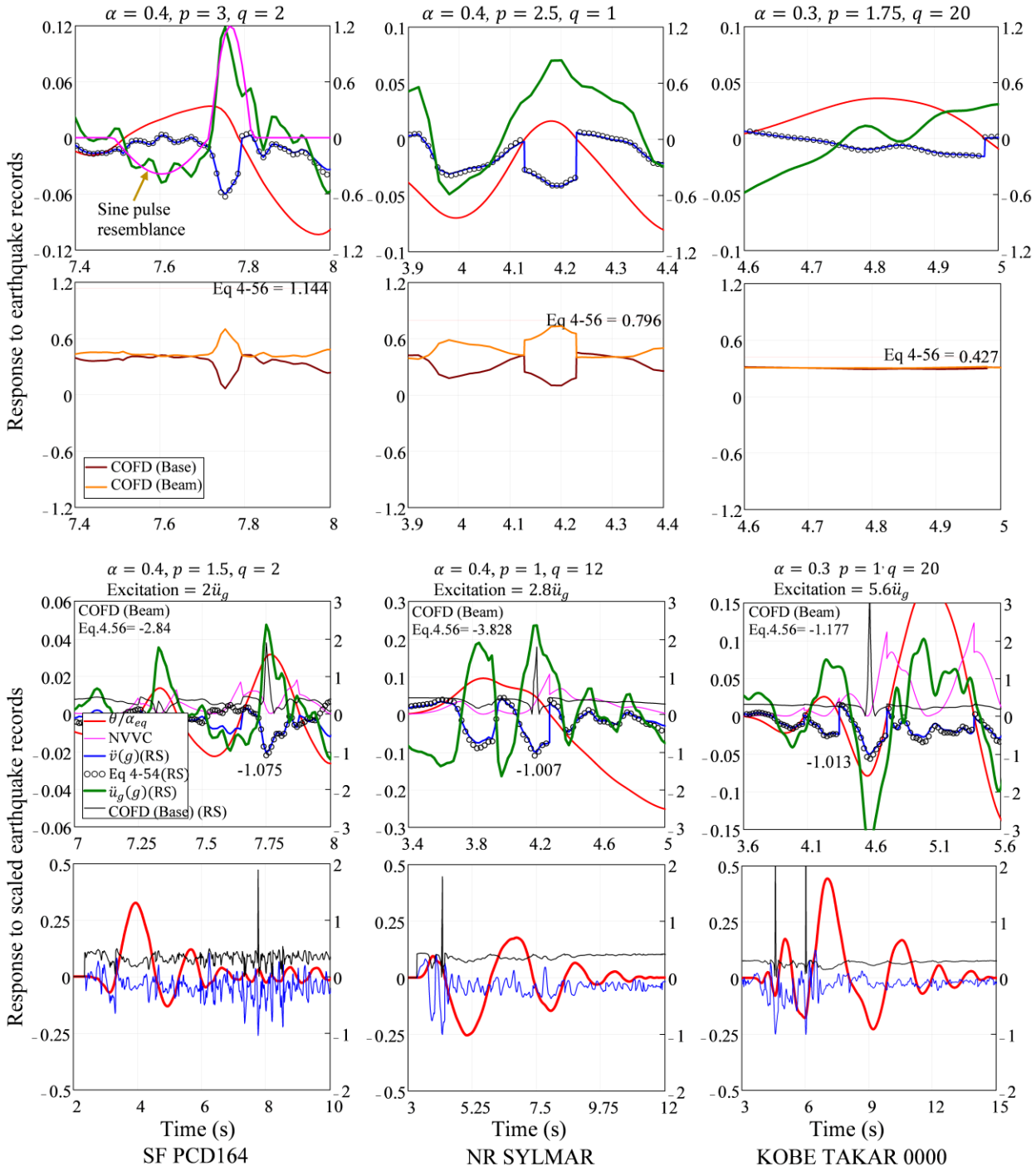

Figure 4-20 Examples of ground acceleration augmenting the fall of an equivalent block system. Top two rows: Responses to earthquake records. Bottom two rows: Responses to scaled records. The third row shows the amplified version of the bottom row at the timing of the maximum COFD at the base. Parameters marked as (RS) are plotted on the right scale. $\eta = 1$ for all cases.

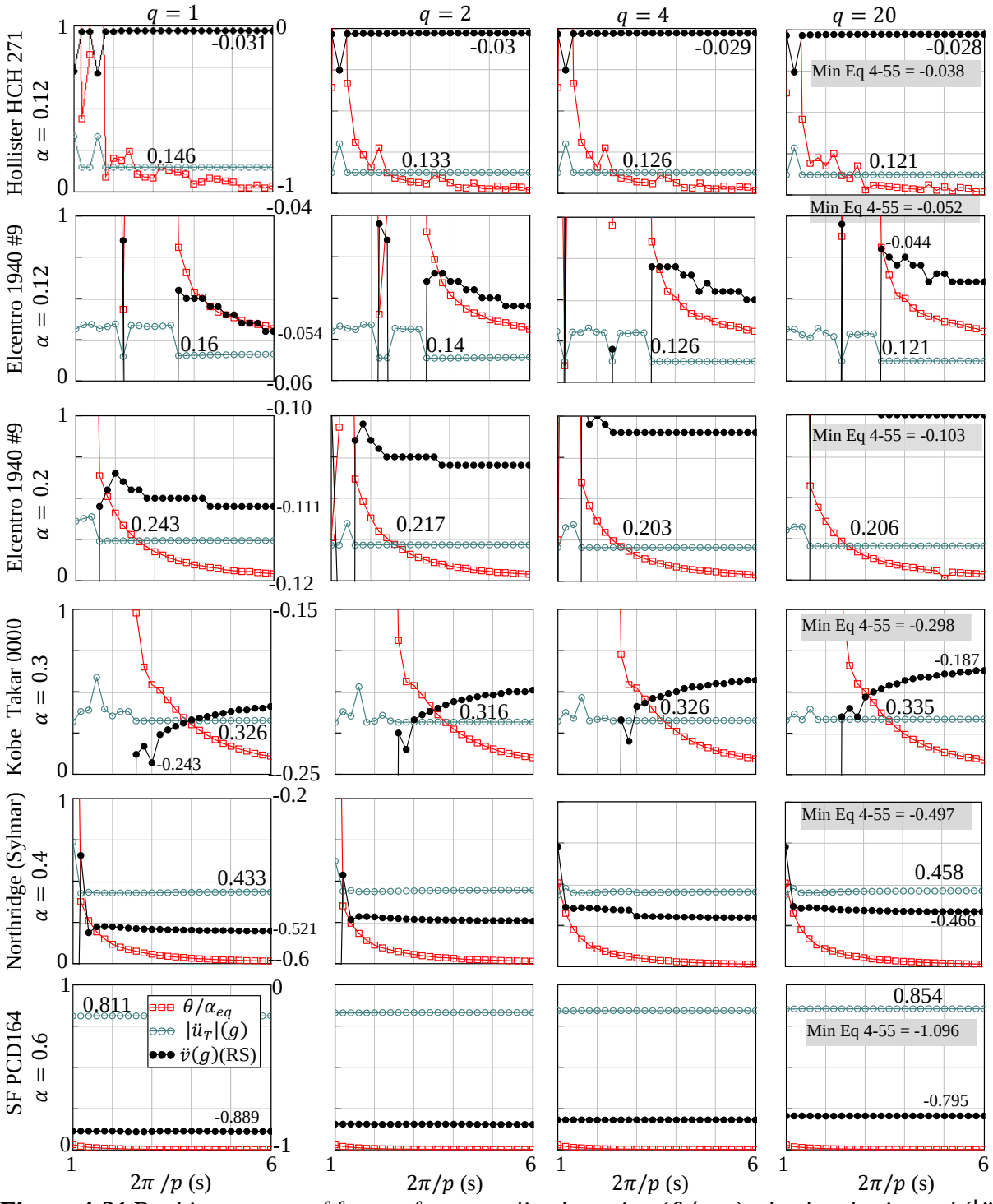

Figure 4-21 Rocking spectra of frames for normalized rotation (θ/α_{eq}), absolute horizontal ($|\ddot{u}_T|$) and minimum vertical ($\ddot{v}$) accelerations of the beam, with variations in q and pier slender parameter (α) against the pier period, $2\pi/p$. For all cases, $\eta = 1$ and therefore, $\alpha_{eq} = \alpha$. All variables are plotted on left scale except $\ddot{v}$ on right scale (RS).

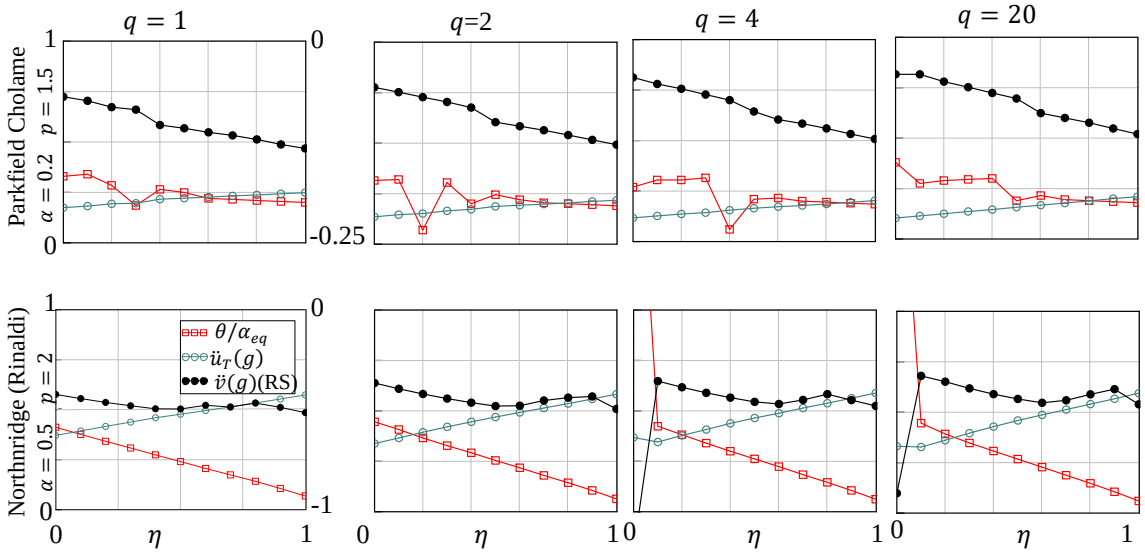

Figure 4-22 Rocking spectra of symmetrically supported frames over varying eccentricity for normalized rotation (θ/α_{eq}), total horizontal ($|\ddot{u}_T|$) and minimum vertical ($\ddot{v}$) accelerations of the beam, with variations in beam/piers weight ratio (q). All variables are plotted on left scale except $\ddot{v}$ on right scale (RS). Top row: $\alpha = 0.2 \quad p = 1.5$. Bottom row: $\alpha = 0.5 \quad p = 2$

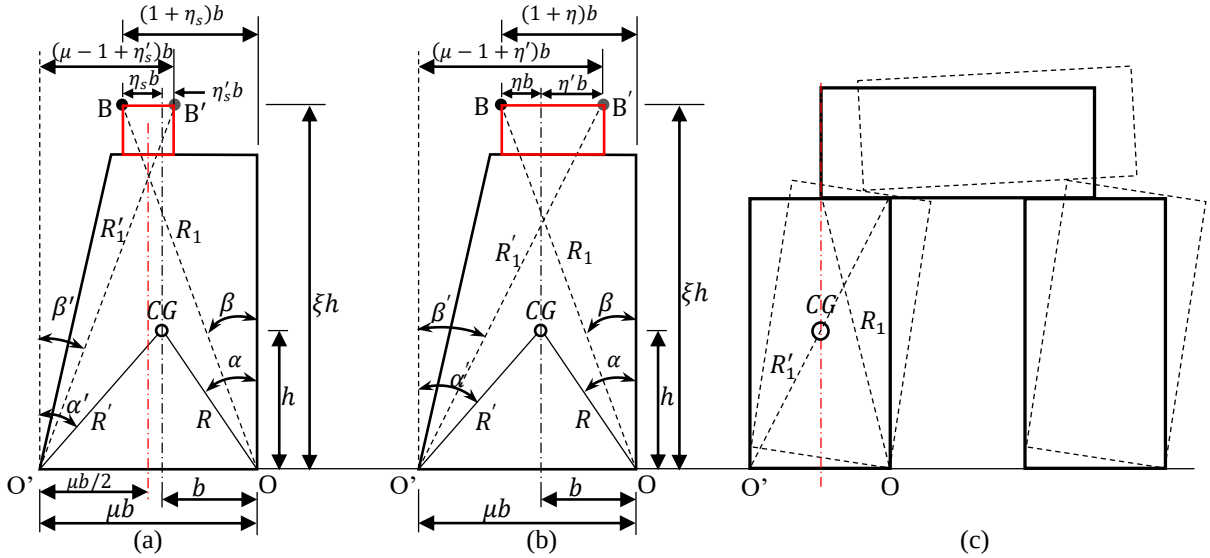

Figure 4-23 Configurations of pier supports: (a) symmetrical, $\eta = \eta_s$ and $\eta' = \eta'_s$, lead to $R_1 = R'_1$, (b) unsymmetrical, $R_1 \neq R'_1$ and (c) rectangular piers with unsymmetrical support condition, $\eta = 0$, $\eta' = 1$ and $R_1 \neq R'_1$.

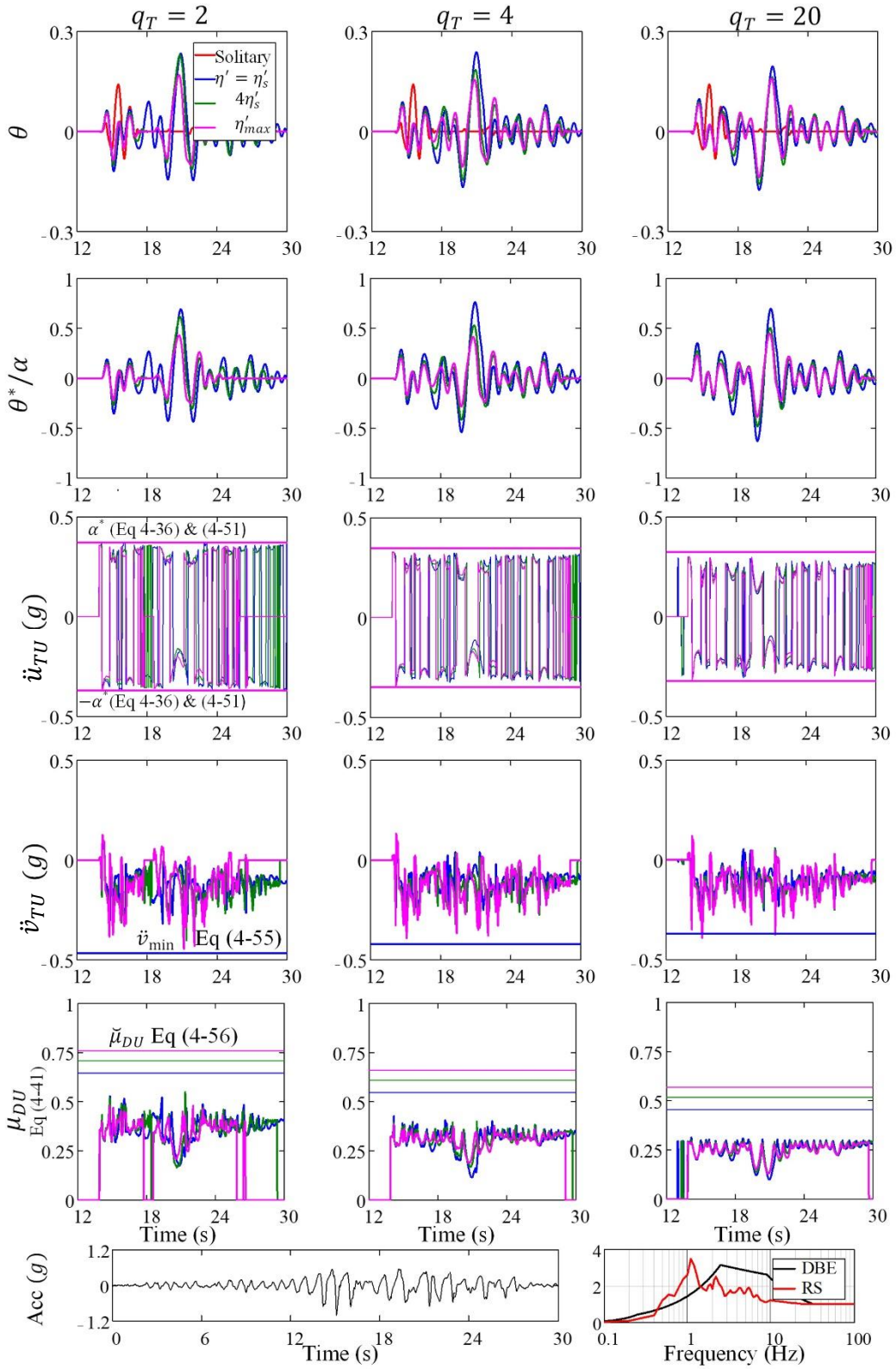

Figure 4-24 Response of Example 1 (Table 4-10) to Chi Chi Taiwan record (Table 4-8)

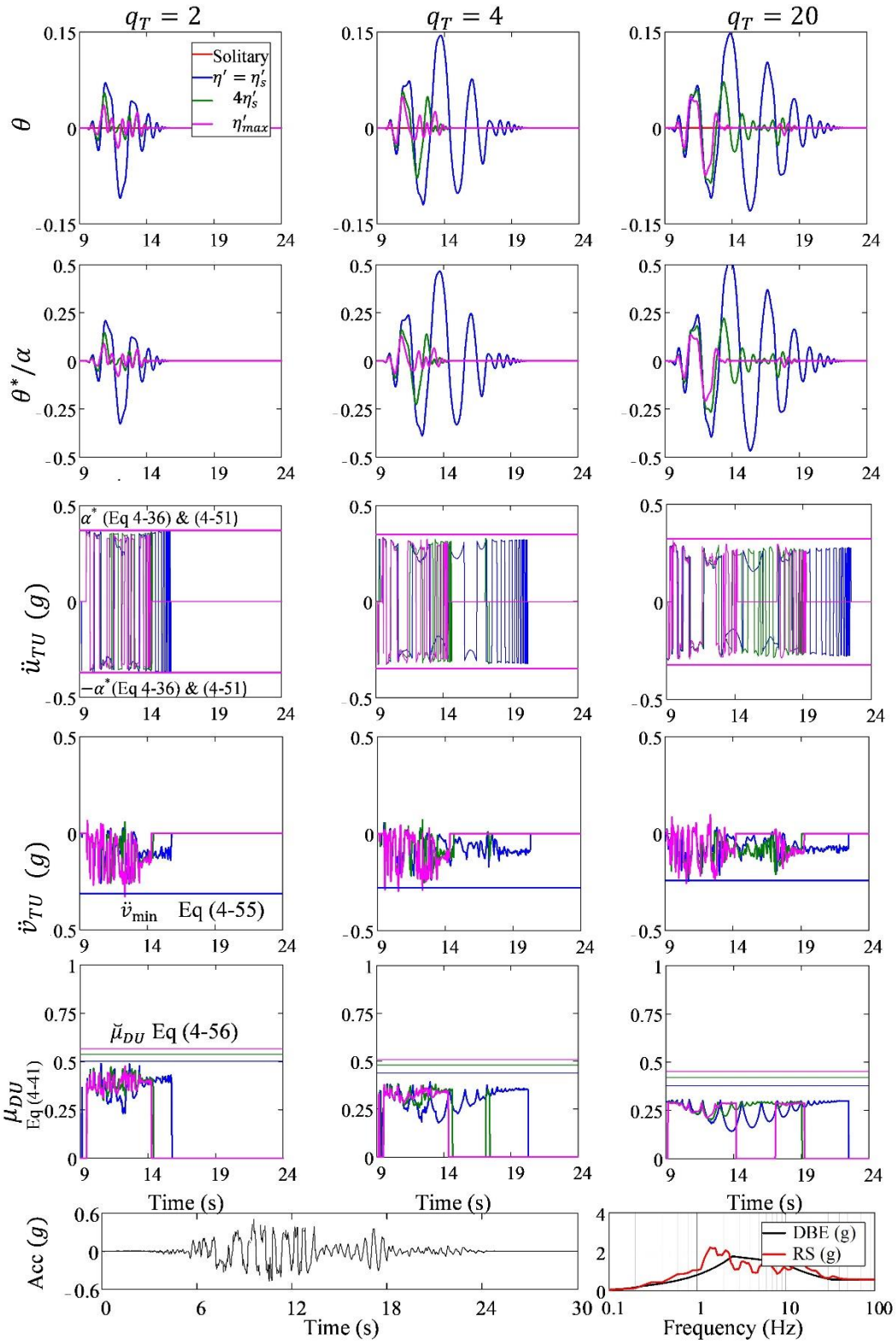

Figure 4-25 Response of Example 1 (Table 4-10) to Loma Prieta record (Table 4-8)

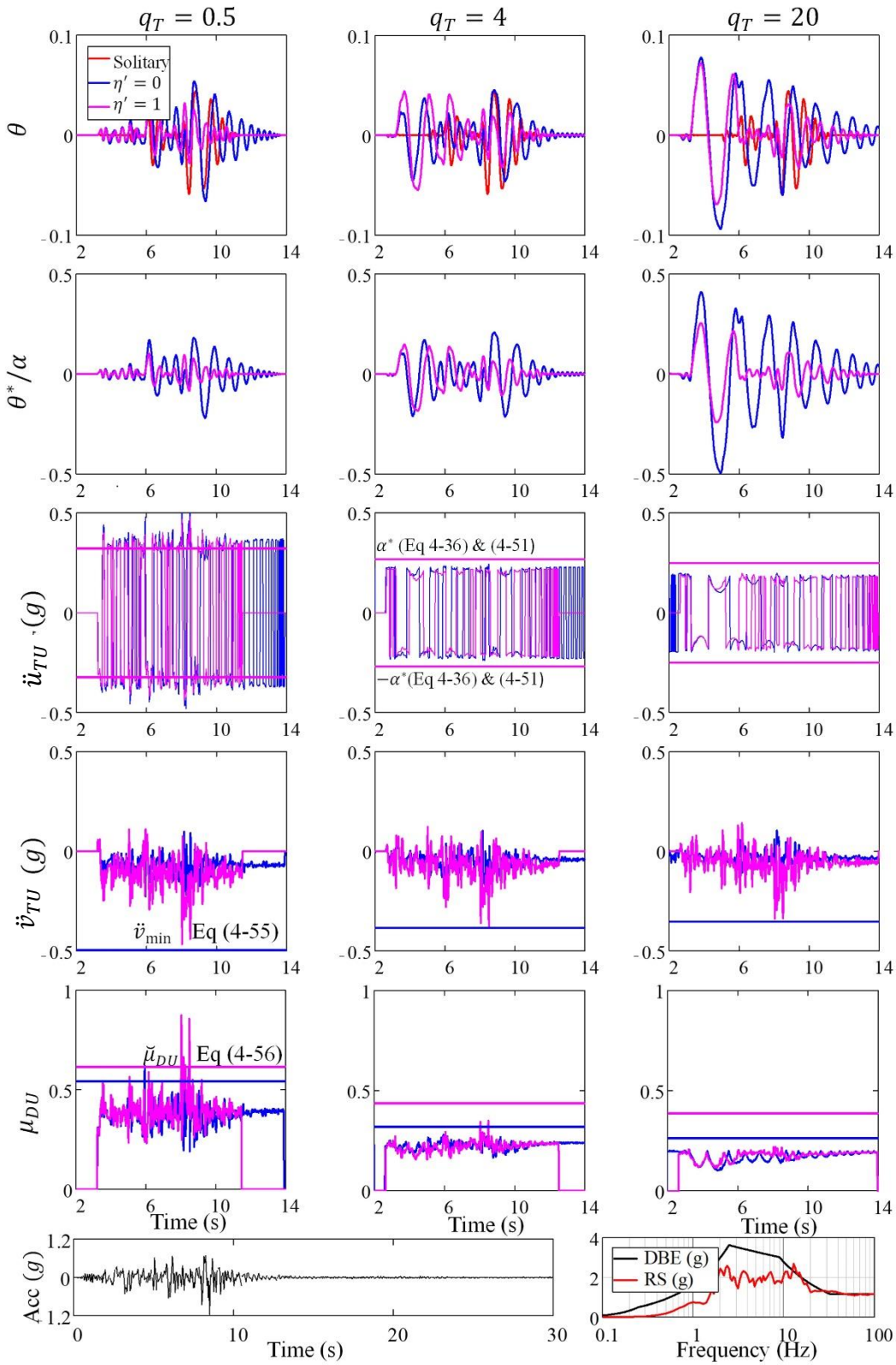

Figure 4-26 Response of Example 2 (Table 4-10) to SF PCD 254 record (Table 4-8)

CHAPTER 5

SUMMARY, LIMITATIONS, CONCLUSIONS AND RECOMMENDATIONS

5.1 Summary

Rocking frames, consisting of a beam freely supported by unanchored piers, are a convenient way of storing long and heavy passive components in NPPs. Lessons learned from the ANO accident indicate that a heavy object's drop on the structure housing safety components may impact the nuclear risk of the entire NPP. In a seismic event, a rocking frame may destabilize and drop the load that it carries. Current nuclear standards provide no guidance on rocking frames and the literature on rocking frames is scarce, covering only one configuration type with rectangular piers and maximum eccentricity, whereas the rocking frames in NPPs consist of pier geometries other than rectangular carrying the top beam with varying support eccentricities. As a result, the seismic risk of rocking frames in NPPs remains unknown.

For the continued frame action, the contact points of the pier and the beam are to remain kinematically constrained, allowing no sliding. Even if shear keys are assumed, the beam can still break its contact with the piers by lifting-off owing to its downward acceleration being more than that due to gravity and destabilize the frame action. A novel mode of instability, the SRSH failure mode was introduced. Occurrence of any of the two possible failure modes, overturning and SRSH, is considered as failure and no further analysis is required. Cross coupling of the two modes of failure is beyond the scope of this study. Assuming no sliding, this dissertation delved into the dynamics of rocking frames in the following manner:

1. Analysis of rocking frames with symmetrical eccentricities on symmetrical piers.

2. Analysis of rocking frames with unsymmetrical eccentricities on unsymmetrical and symmetrical piers.
3. Rocking frames with symmetrical eccentricity on unsymmetrical piers
4. Stability of rocking frames described above with respect to the separation of the beam.

For frames with symmetrical eccentricity, the masses of all piers are equal. For the two-pier frames with unsymmetrical eccentricity, equal mass piers are utilized in the field. Therefore, the examples for such frames were worked out with $q_m = 1$.

5.2 Limitations

Vertical excitation may significantly impact the overall response of frames especially on separation of the beam. Similarly, two perpendicular horizontal excitations would influence the frame response. This study is limited to only pure planar horizontal excitation primarily because the excitations in other directions including vertical are highly likely to complexify the response that would mask the impact of pure horizontal excitation. The purpose of this study was to investigate the impact of pure horizontal planar excitation on frames. Nevertheless, future research might consider studying the impact of multi directional excitations.

5.3 Conclusions and Contributions

This dissertation intensively investigated the previously outlined research objectives and provided practical tools for industrial use by obtaining the seismic response of rocking frames that can be utilized in establishing their seismic risk and included in the nuclear codes and standards governing nuclear facilities. The following conclusions highlight the main findings and

contributions of the research presented in Chapters 2 to 4. The references mentioned below in each section belong to the referenced list of the chapter being addressed.

5.3.1 SEISMIC RESPONSE OF ROCKING FRAMES WITH TOP SUPPORT ECCENTRICITY (CHAPTER 2)

- The effect of the boundary conditions of the contact points between the piers and the rigid beam on the response of the rocking frame was studied. The size and slenderness parameters (p_{eq} and α_{eq}) of an equivalent rocking block, the response of which is equal to that of a rocking frame, were established.

- It was concluded that that the response of a top-heavy rocking frame is markedly affected by the location of the points that serve as pivots between the top beam and the piers when the frame is rocking. This location is characterized through an eccentricity parameter, η, which varies between 0 and 1, representing the two extremes of the contact point between the pier and beam being at the top center and the top corner, respectively.

- The closed form solutions for the response of an equivalent rocking block (for frames with slender piers) to rectangular-pulse and half-sine pulse base excitations were revisited, utilizing a simpler approach than the one reported in the literature. It is noted that the peak response of such equivalent blocks to the defined pulse loading depends on a combination of α_{eq} and p_{eq}. In comparison to a rectangular solitary pier (without a top beam) with slenderness α and frequency parameter p, any eccentricity other than η = 1 results in a reduction in the slenderness parameter ($\alpha_{eq} < \alpha$) but increase in

size ($p_{eq} < p$) of the equivalent block. To maintain the stability of the equivalent block whose equivalent slenderness parameter (α_{eq}) is reduced, its size has to be larger than the size required for a particular pulse excitation, i.e., $p_{eq} < p_{Req}$. Thus, the size and slenderness parameters are found to be complementary to each other.

- To investigate the effect of eccentricity, η, the study further examined the normalized peak rotation of three examples of rocking frames with rectangular piers to a suite of earthquake records. It was found that the coefficient of restitution of an equivalent block depends on η, and hence its peak response to the earthquake records is influenced by the location of the top beam supports on the pier. The concept of critical eccentricity η_{cr} was introduced, below which the coefficient of restitution of an equivalent rocking block increases with increasing beam-to-pier mass ratio but decreases for $\eta > \eta_{cr}$. Rocking frames consisting of rectangular flat-top piers in full contact with the top rigid beam ($\eta = 1$) are found to be more stable than a solitary pier, confirming the observation of Makris and Vassiliou [3]; but rocking frames are found to be less stable than the solitary piers as the bearing points move inward toward the centerline ($\eta = 0$) of the pier. The peak response is influenced by the combination of the size and slenderness parameters along with the coefficient of restitution of the equivalent rocking block representing the frame.

5.3.2 DYNAMIC ANALYSIS OF TWO-PIER ROCKING FRAMES WITH ECCENTRIC TOP SUPPORTS AND BEAM ROTATION (CHAPTER 3)

- Analysis of two-pier rocking frames with unsymmetrical piers of equal height was carried out and its equation of motion was established for two types of top support eccentricities: symmetrical and unsymmetrical, assuming no sliding.
- Physical interpretation of the equation of motion led to the discovery that a rocking frame with equal height piers is essentially a SDOF two stacked block system where the top block rotation is a function of that of the bottom block. The two stacked block system can further be evolved into a single equivalent rocking block for the case with symmetrical eccentricity.
- It was concluded that a time independent equivalent rocking block exists for rocking frames with symmetrical eccentricities but not for those with unsymmetrical ones. This study explored strategic maneuvering of the top support eccentricities to make them symmetrical, to arrive at the parameters of a merged pier that leads to a dynamically equivalent rocking block model.
- It is concluded that the equation of motion of rocking frames with unsymmetrical eccentricities can be formulated representing an assembly of equivalent rocking blocks that facilitate the conversion of equation of motion of the frame into a simplified form, making it convenient to be adapted in the field (e.g., NPPs). Also, the equation of motion in form of an assembly of equivalent blocks can be instrumental in formulation of an approximate finite element model applying the techniques suggested in the

literature [8, 26] by considering each equivalent block as a SDOF oscillator with negative stiffness.

- Explicit expressions of the system slenderness, α^*, required to establish minimum acceleration to initiate rocking, and effective rotation, θ^*, that defines the effective overturning as an instability criterion were established. The responses to earthquake records for a symmetrical eccentricity example, in terms of normalized effective rotation, θ^*/α, normalized rotations, θ/α_{eq}, and θ/α^*, were verified to be equal to each other, proving self verification of concepts established in this study.

- The COR of unsymmetrical piers has been established and utilized in obtaining the same for a frame with unsymmetrical piers but symmetrical support conditions. Also, the COR of frames with unsymmetrical eccentricity has been established. The phenomenon of impact of the beam on piers was explained and the assumption made in the literature on equality of impulses on top of the piers during impact, for the case with symmetrical eccentricities, was validated.

- For rocking frames in the field, it is recommended that the unsymmetrical frame eccentricities be made symmetrical by maneuvering the support system so that the response of an equivalent block can be obtained from a rocking spectrum. If not possible to do so, the system response can be obtained by the procedure laid out in this study.

5.3.3 SEISMIC STABILITY OF ROCKING FRAMES UNDER HORIZONTAL EXCITATION (CHAPTER 4)

Conclusions of this chapter are divided into two categories: rigid blocks and frames.

5.3.3.1 Rigid blocks

Since a symmetrically supported rocking frame can be represented by an equivalent block, the study began with the separation of a rigid block under horizontal excitation. The following conclusions were reached for a slide restrained rigid rocking block.

- According to the literature [10], sliding precedes or safeguards against separation of a rigid block. However, in the case of a slide restrained block (e.g. mobile trolley on rails or a block with shear keys) separation is possible.
- Separation can be achieved in a hybrid-horizontal-pulse excitation consisting of a large period and small amplitude rectangular or half-sine pulse that makes the block rise to its peak rotation, followed by a shorter period and larger amplitude one in reverse direction that accelerates its fall. Thus, separation is likely in the case of a falling block retreating from its peak rotation when the algebraic signs of excitation and block rotation are the same.
- The large-period-low-amplitude half sine pulse that often precedes the main sine pulse in an earthquake record was discovered to make a considerable difference in a block's response. Such pre-excitation half sine pulse has been ignored in the literature [13].
- In contrast to the literature [10], the SRSH instability mode was demonstrated to be possible for slender blocks and separation to be achievable at rotations much smaller than α (block's slenderness) for wide blocks.

- Closed form solutions for a falling slender block struck by a rectangular or half-sine pulse while retreating from its peak rotation were derived and numerically verified.
- Equations of hybrid pulse excitations (combination of pre-excitation and the main excitation pulse) were derived that lead to the separation of a slender block without overturning. These equations were numerically verified and utilized to generate pulse excitations leading to separation.
- A block's normalized moment of inertia (representative of its geometry) was discovered to influence separation. Lesser the normalized moment of inertia, larger is the absolute value of the block's downward vertical acceleration.
- A rocking spectrum is not a true indicator of the stability of a slide restrained rigid block. It must be accompanied not only with the corresponding vertical acceleration spectrum but also the information on its normalized moment of inertia.
- In a typical seismic probabilistic risk study [52], only the overturning risk is considered in the case of a rocking block. Consideration of separation risk is warranted for slide restrained blocks.

5.3.3.2 Rocking frames with symmetrical eccentricities

Several cases of rocking frames with symmetrical eccentricities and different pier geometries subjected to various types of hybrid pulse excitations and earthquake records were studied giving rise to the following conclusions regarding the separation of the beam in a rocking frame.

- Overturning and separation risks vary opposite to each other with increasing pier stockiness. As α increases the overturning risk decreases but separation risk increases.

- The response of rocking frames to earthquake records leading to the beam's minimum negative vertical acceleration was found to be similar to that caused by a hybrid pulse excitation, i.e., the occurrence of the beam's minimum negative acceleration coinciding with the portion of excitation that resembles a hybrid sine pulse.
- Fundamental difference between the two modes of instability, overturning and the separation of the beam under the SRSH mode, is that the former is caused by high amplitude large rotations (or large period) but the latter by low amplitude small period rotations.
- Large rotations lead to larger period response in rocking frames (1s or more) which was not found to be a match for the continued excitation period in any of the studied cases. However, a low rotational response provides an opportunity for the excitation period to match with that of a falling block helping the beam reach its minimum negative vertical acceleration.
- In all cases rocking frames' responses to earthquake records considered in this study, the beam's negative vertical acceleration was found to be minimum when the equivalent block system was falling rather than rising. In none of the cases, although a theoretical possibility at a high amplitude excitation, a rising system was found to lead to separation.

5.3.3.3 Seismic isolation in rocking frames with symmetrical eccentricities

Seismic isolation of a rigid beam due to rocking is similar to the seismic isolation of a rigid podium freely supported by piers reported in the literature [41] to be achievable for slender piers with $\alpha \leq 0.3$. The following conclusions were reached in this study with regard to seismic isolation.

- Although the rocking induced seismic isolation may be successful for the beam in a frame, it may still be susceptible to the SRSH instability mode. This is in contrast to the conclusion in [24] and [45] that by making the beam heavier, a rocking frame becomes more stable implying seismic isolation. In reality, making a frame heavier reduces the overturning risk but increases the beam's separation risk because of the low rotational response of the heavier frame at a lower period which is likely to match with a portion of excitation that augments its fall. Therefore, instability due to separation deserves attention in rocking induced seismic isolation.
- The total or absolute horizontal acceleration of the beam in a frame resembles a series of rectangular pulses with the acceleration amplitude being close to $\alpha_{eq}g$ for frames with slender piers.
- A rectangular pulse is the most conservative (or damaging) form of pulse excitation for a rocking block which is not found in real earthquake records but always present in a seismically isolated rigid beam or a rigid podium. Therefore, a large variety of rocking blocks inside an isolated podium would overturn. This behavior was verified for earthquake records.
- The effectiveness of seismic isolation of the beam was evaluated on two counts: 1. The response of SDOF oscillators represented by a response spectrum and, 2. The response of rigid rocking blocks represented by a rocking spectrum, to the response time history of the isolated beam. It was found that the isolation achieved by rocking differs from case to case and may or may not be always effective. The spectral peaks of response spectrum of the isolated time history were found to be somewhat identical to that of the base excitation for

a small pier frame indicating insignificant reduction in seismic demand. Rocking spectrum of the isolated time history was found to be worse than that for the base excitation.

- The seismic isolation and separation of the beam in rocking frames with rectangular piers were discovered to be susceptible to eccentricities varying from $\eta = 0$ to 1. The beam's horizontal acceleration was found to be the maximum and the negative vertical acceleration to be the minimum at $\eta = 1$, a worst-case scenario for the SRSH mode of instability. According to the literature [25] (Chapter 2), the eccentricity, $\eta = 1$, leads to the minimum rotational response and hence the least overturning risk but as established in this study, this condition also leads to the worst case for the SRSH instability mode. Thus, a top-heavy frame being more stable than its lighter counterpart depends on the applicability of the SRSH failure mode. Similar trend was observed for the trapezoidal piers where, the rotational response at $\eta = \phi$ is less than that for $\eta = 0$ but the vertical acceleration shows an opposite trend.

5.3.3.4 Semi-empirical expressions for accelerations and the COFD in rocking frames with symmetrical eccentricities

The response of symmetrically supported rocking frames to earthquake records with different pier geometries led to the development of semi empirical equations, which were found to provide conservative estimates of beam's vertical acceleration and the COFD for the beam at higher loadings, i.e., the beam to piers' cumulative mass ratio, $q \geq 1$. Four relationships (Equations (4-51), (4-54), (4-55) and (4-56)) were established for slender piers which were found to be applicable to frames with equivalent block's slenderness up to, $\alpha_{eq} = 0.4$. The expressions for the beam's maximum horizontal and minimum vertical accelerations, and the COFD respectively are

given by Equations (4-51), (4-55) and (4-56). Equation (4-54) provides an approximate estimation of beam's vertical acceleration response over the entire duration of the excitation that closely resembles the numerical response at its minimum. However, because Equation (4-54) contains $\mathrm{sgn}(\theta)$, the rotational response (θ) is required to be known beforehand. Nevertheless, Equation (4-54) leads to Equation (4-55) that is helpful when the rotational response is unknown. The symmetrically supported rocking frames response to earthquake records leads to the following conclusions:

- The maximum horizontal acceleration of the beam can be predicted by Equation (4-51) with good accuracy in a heavy slender pier frame ($q \geq 4$) with slenderness up to $\alpha = 0.2$ and within a reasonable accuracy for frames with the slenderness angle up to $\alpha = 0.4$.
- Since rocking frames in NPPs are generally used to support heavy beams, the semi empirical expressions developed in this study are found to be applicable to NPPs.
- The maximum horizontal acceleration of the beam in lighter frames of any slenderness can be conservatively predicted by Equation (4-51) by multiplying it with a factor of 2.
- The minimum vertical acceleration of the beam can be conservatively predicted by Equation (4-55).
- The beam's approximate COFD is expressed by Equation (4-56). The COFD's exponential rise, under the SRSH mode, is caused by the reduction in vertical acceleration rather than the increase in horizontal acceleration which is practically constant, $\alpha_{eq} g$, due to isolation.

5.3.3.5 Rocking frames with unsymmetrical eccentricities

The semi empirical expressions were found to be applicable to the response of rocking frames with unsymmetrical eccentricities to earthquake records but by replacing the equivalent block's slenderness, α_{eq}, with the system slenderness, α^* in Equations (4-51), (4-55) and (4-56). Where, α^* is as given in Equation (4-36) that varies with eccentricities, η and η'. The symmetrical eccentricity case in such fames is denoted by eccentricities, $\eta = \eta_s$ and $\eta' = \eta'_s$. Equations (4-51), (4-55) and (4-56) were found to be bounding on all conditions of unsymmetrical eccentricities for the beam to the generalized rotation pier mass ratio, $q_T \geq 2$, as described below:

- Beam's horizontal acceleration by Equation (4-51) with, $\alpha_{eq} = \alpha^*$, for eccentricities $\eta = \eta_s$ and $\eta' = \eta'_{max} = 1$.
- Beam's vertical acceleration by Equation (4-55) for the symmetrical eccentricity case $\eta = \eta_s$ and $\eta' = \eta'_s$.
- Beam's COFD by Equation (4-56) for the symmetrical eccentricity case $\eta = \eta_s$ and $\eta' = \eta'_s$.

5.4 Verification of analysis on Working Model 2D and at higher elevations

Verification of a single block's and frames' responses to hybrid pulse excitation and earthquake records was carried out on the Finite Element Analysis (FEA) software Working Model 2D [55]. The details of verification are given in APPENDIX B. Verification of semi empirical expressions (Equations 4-51, 4-54, 4-55, and 4-56) was carried out for the time history at higher elevations in a building subject to the USNRC spectrum seismic input. APPENDIX C contains details for this verification.

5.5 Step-by-step procedure to obtain the response of rocking frames

The procedures below utilize the techniques developed in Chapters 2 through 4. Therefore, they cannot be included in individual chapters. As a precursor to obtain the rocking response of frames, it is essential to develop rocking spectra at various floors of the building where such frames are located.

5.5.1 Develop rocking spectra for various floors of a building

1. Develop time history responses at various floors in a building through an appropriate dynamic analysis methodology or through an applicable commercial software. This step is well known in the literature and does not need further elaboration.
2. For the time histories obtained above, develop rocking spectra for various floors in a building for various CORs (e.g., 0.95, 0.9 etc. up to 0.7) by casting Equation (2-1) in $\dot{\mathbf{y}} = f(\mathbf{y}, t)$ format where $\mathbf{y} = [\theta, \dot{\theta}]$ and solving it through an appropriate solver. A flow chart for generating rocking spectrum is given in Appendix F of [1].

5.5.2 Frames with symmetrical eccentricity on symmetrical piers

1. Obtain the equivalent rocking block parameters, p_{eq} α_{eq} and the COR, E_{eq}, from Table 2-2.
2. Read the response for the rocking frame at the desired floor from the corresponding rocking spectrum (developed in Section 5.5.1) applying the parameters developed in step 1.
3. Obtain approximate peak horizontal beam acceleration as $\alpha_{eq} g$ per Equation (4-51).
4. Obtain approximate minimum vertical acceleration from Equation (4-55) by considering $\ddot{u}_g$ as the floor time history obtained in Section 5.5.1. This is the minimum vertical acceleration of the beam. This value being less than -g, is an indicator of beam separation.
5. Determine approximate COFD from Equation (4-56) and compare with the available COF between the beam and the pier.

5.5.3 Frames with symmetrical eccentricity on usymmetrical piers

1. Obtain the equivalent rocking block parameters, p_{eq} α_{eq} from Equation (3-32) and the COR, e_{sm}, from Equation (3-35).
2. Read the response for the rocking frame at the desired floor from the corresponding rocking spectrum developed in step 1 applying the parameters developed in step 2.
3. Obtain the approximate horizontal and vertical accelerations, and, the COFD per steps 3, 4 and 5 in Section 5.5.2.

5.5.4 Frames with unsymmetrical eccentricities

1. Convert the unsymmetrical eccentricity condition to a symmetrical one by manipulating the eccentricities as explained in Section 3.5. Once symmetrical eccentricities are obtained, follow the steps given in Section 5.5.2 or 5.5.3 as applicable. If it is not possible to manipulate the eccentricities, follow the steps as given below.
2. Follow steps elaborated in Section 3.9. It is strongly recommended to obtain the derivatives of the right pier and the beam rotation from Equations (3-12) and (3-13) rather than obtaining them numerically to avoid floating point errors due to jump discontinuities (especially in $\ddot{\theta}$ as depicted in Figure 4-4 (f)) caused by impacts.

5.6 Recommendations for Future Research

This dissertation established equivalent block parameters for rocking frames with symmetrical eccentricity on symmetrical piers, equation of motion for the frames with unsymmetrical eccentricity on unsymmetrical piers, and the stability of two in the SRSH failure mode. Semi-empirical equations to obtain the horizontal and vertical accelerations of the beam, and, its COFD were established and found to be conservative when compared with the numerically obtained response of frames to the earthquake records. The following areas of future research are identified:

- For frames with symmetrical eccentricities on symmetrical pier, future research is required to study the impact of the eccentricity parameter η on the fragility of the frames.
- This dissertation is limited to the piers that are either prismatic or wide at the bottom and narrow at the top. Piers that are wider at the top in comparison to their base might need to be investigated in the future.
- This study considered separation and overturning separately and the occurrence of either is considered as a failure. Post separation continued response is beyond the scope of this study and is a subject of future research.
- It was discovered that the separation of slide restrained block can coincide with overturning causing its interaction with nearby seismically qualified components in a NPP. The safe distance of an unanchored object from seismically qualified component is governed by its height because sliding precedes or safeguards against separation. However, for slide restrained blocks such as mobile trolleys on rails, separation may coincide with overturning causing the safe distance to be larger than that required in an unrestrained block. Future research in this direction is required.
- In rocking induced isolation, the isolated time history consists of series of pulses approximately resembling a rectangular shape whose period depends on the pier size of the frame. Larger piers lead to a larger pulse period. On the contrary, smaller piers lead to smaller period directly impacting the effectiveness of seismic isolation. Determination of pier size leading to ideal seismic isolation is beyond the scope of this study and is a subject of future research.
- Further research is also required on verification of semi empirical expressions for earthquake records with the response spectra dissimilar to the USNRC spectrum. Nonetheless, verification for the time histories at higher elevations was carried out in a

building subjected to the USNRC spectrum seismic input. APPENDIX C contains all necessary details.

- Experimental investigations on rocking frames are required to be carried out in the future especially to verify the semi empirical expressions in Equations 4-51, 4-54, 4-55 and 4-56.
- Future research might consider studying a rocking frame's response to excitations in two horizontal directions. Also, the impact of vertical excitation (especially on separation) might be studied.

5.7 References

References mentioned in Section 5.3 belong to the reference list of Chapters 2, 3 and 4 being addressed in Sections 5.3.1, 5.3.2 and 5.3.3 respectively. No separate reference list is given for this chapter except the only reference applicable particularly to this chapter.

1. Dar A. Evaluation of seismic design criteria for rocking objects in nuclear facilities. 2015: p107. https://macsphere.mcmaster.ca/handle/11375/16778

APPENDIX A

SUPPLEMENTAL INFORMATION TO CHAPTER 3

A.1 Scaling of area and moment of inertia

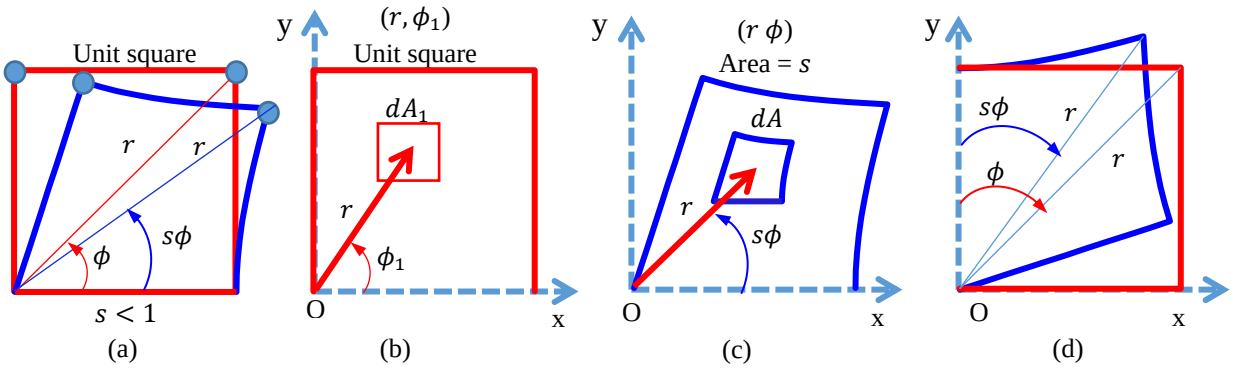

Figure A1: (a) rotation of angular coordinates in the red unit square measured anticlockwise from x-axis. (b) unit square in (r, ϕ_1) space. (c) deformed shape in (r, ϕ) space. (d) shape resulting from reduction of angular coordinates measured from y-axis. The blues shapes in (c) and (d) are identical, except for the orientation.

Figure A1(a) shows a unit square in red and a shape in blue that is the outcome of reduction in the angular coordinates of the red square by a factor, s. The angular coordinate is measured from the x-axis in counter clockwise direction. It can be shown that if the angular coordinates of all points on the unit square are reduced or scaled by a factor, s, the area of the deformed shape would be s. Figure A1(b) shows an infinitesimally small area dA_1, in the unit square enclosure at a distance, r, in the (r, ϕ_1) space, where $\phi_1 = s\phi$. Figure A1(c) shows the deformed shape due to the reduction in angular coordinates along with the infinitesimally small dA, at a distance, r. Since one unit of ϕ_1, is equal to s units of ϕ, the diagram in Figure A1(c) is in (r, ϕ) space. The scaling from (r, ϕ_1) to (r, ϕ) space is given by the Jacobian

$$J = \begin{vmatrix} \frac{dr}{dr} & \frac{dr}{d\phi} \\ \frac{d\phi}{dr} & \frac{d\phi_1}{d\phi} \end{vmatrix} = \begin{vmatrix} 1 & 0 \\ 0 & \frac{d\phi_1}{d\phi} \end{vmatrix} = s$$

In Figure A1(b), the moment of area of the unit square about O, is $Mo_1 = \sum r dA_1$. Moment of area of the shape in (r, ϕ) space in Figure A1C is

$$Mo = \sum r\, dA = \sum r\, s dA_1 = sMo_1$$

Similarly, the moment of inertia of the shape in (r, ϕ) space in Figure A1C is

$$I = \sum r^2\, dA = \sum r^2\, s dA_1 = sI_1$$

Thus, angle scaling by s leads to the scaling of the moment of area and moment of inertia in the same proportion. The right pier distortion in Figure 3-8(e) is based on the angle reduction shown in Figure A1(d) because its rotation is measured counterclockwise from the vertical. The beam distorted shape in Figure 3-8 (e) is based on Figure A1(c) since its rotation is measured clockwise from the horizontal. This concept was verified on AutoCAD® on an example trapezoidal shape and on Mathcad® for several cases.

A.2 Similarity of rocking frame and two stacked blocks configuration

The case of the rocking frame shown in Figure 3-5(b) is similar to two blocks rocking pattern with the bottom and top block undergoing rotations in opposite directions given in Figure 3-8(e). Figure A2 shows the rocking frame (without the right pier) on the left and the two-block system on the right which is the same as Pattern B(b) as discussed by Kounadis et al. in Figure 3(b) of [32]. Equivalent parameters of the two systems are described in the text box in the middle.

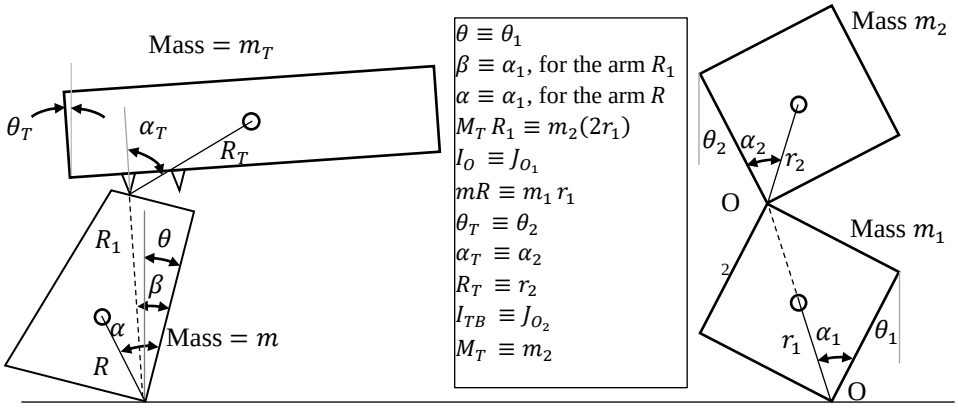

Figure A2: Equivalence of rocking frame without the right pier with two stacked blocks system in [RA-1].

The CGs of blocks are depicted by tiny circles. It is to be noted that the dynamics of the assemblages in both diagrams depends on the geometry of the lines joining: 1. the upper block pivot point to that of the lower block (R_1 and $2r_1$), 2. the upper block pivot point to its CG (R_T and r_2), and, 3. the lower block pivot point to its CG (R and r_1). Thus, the distance, R_1, in the rocking frame is equivalent to, $2r_1$, in the stacked blocks configuration. The rotation of the bottom block and the arm joining O_1 and O_2, in the stacked block configuration is the same, $(\alpha_1 - \theta_1)$, but in the rocking frame configuration, it is $(\alpha - \theta)$ for the pier and $(\beta - \theta)$ for the beam leading to the following equivalencies in the two models

$$m_2(2r_1)\cos(\alpha_1 - \theta_1) \equiv M_T R_1 \cos(\beta - \theta)$$
$$m_2(2r_1)\sin(\alpha_1 - \theta_1) \equiv M_T R_1 \sin(\beta - \theta)$$
$$m_1 r_1 \cos(\alpha_1 - \theta_1) \equiv mR \cos(\alpha - \theta)$$
$$m_1 r_1 \sin(\alpha_1 - \theta_1) \equiv mR \sin(\alpha - \theta) \quad \text{(A1)}$$

Equations (81) and (82) from [32] are reproduced below as Equations (A2) and (A3) respectively.

$$J'_{O_1}\ddot{\theta}_1 + r_1(m_1 + 2m_2)\ddot{u}_g \cos(\alpha_1 - \theta_1) + 2m_2 r_2 r_1\left[\ddot{\theta}_2 \cos(\alpha_1 + \alpha_2 + \theta_2 - \theta_1) - \dot{\theta}_2^2 \sin(\alpha_1 + \alpha_2 + \theta_2 - \theta_1)\right]$$
$$+(m_1 + 2m_2) g\, r_1 \sin(\alpha_1 - \theta_1) = 0 \quad \text{(A2)}$$

$$J_{O_2}\ddot{\theta}_2 + m_2\ddot{u}_g\, r_2 cos(\alpha_2 + \theta_2) + 2m_2 r_2 r_1\left[\ddot{\theta}_1 \cos(\alpha_1 + \alpha_2 + \theta_2 - \theta_1) + \dot{\theta}_1^2 \sin(\alpha_1 + \alpha_2 + \theta_2 - \theta_1)\right]$$
$$-m_2 g\, r_2 \sin(\alpha_2 + \theta_2) = 0 \quad \text{(A3)}$$

Where, $J'_{O_1} = 4(m_1/3 + m_2)r_1^2 = J_{O_1} + m_2(2r_2)^2$ which is the moment of inertia of the lower block plus that of the point mass at the upper pivot point. Equations (A2) and (A3) represent, the sum of moments about point O_1 and O_2 of the lower and upper block respectively. Since, for the case under this study, the upper block rotation is a function of that of the lower block, the two blocks configuration turns into a SDOF system. Hence, both equations can be rewritten by considering θ_2 as a function of θ_1 leading to $\dot{\theta}_2 = (d\theta_2/\, d\theta_1)\dot{\theta}_1$ and $\ddot{\theta}_2 = \ddot{\theta}_1(d\theta_2/d\theta_1) + \dot{\theta}_1^2(d^2\theta_2/d\theta_1^2)$. Also, there would be scaling of J_{O_2} and m_2 by $d\theta_2/d\theta_1$, in those terms that include the rotation, θ_2,

or its derivatives. Hence, the entire equation (A3) would be scaled by $d\theta_2/d\theta_1$ because all terms therein include the rotation, θ_2. In Equation (A2), the third term will be scaled. Thus, replacing θ_2, $\dot{\theta}_2^2$, and $\ddot{\theta}_2$, in terms of θ_1 and multiplying (or scaling) J_{O_2} and m_2 by the Jacobian $d\theta_2/d\theta_1$ in the entire equation (A3) and the second term in Equation (A2) leads to the following equations

$$\ddot{\theta}_1\left(J_{O_1} + m_2(2r_1)^2\right) + \left(m_1 r_1 + m_2(2r_1)\right)\ddot{u}_g \cos(\alpha_1 - \theta_1) + m_2 r_2(2r_1)\left[\left(\ddot{\theta}_1\left(\frac{d\theta_2}{d\theta_1}\right) + \dot{\theta}_1^2\left(\frac{d^2\theta_2}{d\theta_1^2}\right)\right)\cos(\alpha_1 + \alpha_2 + \theta_2 - \theta_1) - \left(\frac{d\theta_2}{d\theta_1}\dot{\theta}_1\right)^2 \sin(\alpha_1 + \alpha_2 + \theta_2 - \theta_1)\right] + \left(m_1 r_1 + m_2(2r_1)\right) g \sin(\alpha_1 - \theta_1) = 0 \quad \text{(A4)}$$

$$J_{O_2}\left(\frac{d\theta_2}{d\theta_1}\right)\left(\ddot{\theta}_1\left(\frac{d\theta_2}{d\theta_1}\right) + \dot{\theta}_1^2\left(\frac{d^2\theta_2}{d\theta_1^2}\right)\right) + m_2\left(\frac{d\theta_2}{d\theta_1}\right)\ddot{u}_g r_2 \cos(\alpha_2 + \theta_2) + m_2\left(\frac{d\theta_2}{d\theta_1}\right) r_2(2r_1)\left[\ddot{\theta}_1 \cos(\alpha_1 + \alpha_2 + \theta_2 - \theta_1) + \dot{\theta}_1^2 \sin(\alpha_1 + \alpha_2 + \theta_2 - \theta_1)\right] - m_2\left(\frac{d\theta_2}{d\theta_1}\right) g r_2 \sin(\alpha_2 + \theta_2) = 0 \quad \text{(A5)}$$

Adding Equations (A4) and (A5) and replacing, $2r_1$, r_1, θ_1, α_1, J_{O_1}, α_T, θ_2, r_2, J_{O_2} with R_1, R, θ, β, I_O, α_2, θ_T, R_T, I_{TB} respectively along with equivalent entities from Equation (A1) gives

$$\ddot{\theta}\left[I_o + M_T R_1^2 + I_{TB}\left(\frac{d\theta_T}{d\theta}\right)^2 + 2M_T R_1 R_T \frac{d\theta_T}{d\theta}\cos(\alpha_T + \theta_T + \beta - \theta)\right] = -g\left[mR\sin(\alpha - \theta) + M_T\left[R_1 \sin(\beta - \theta) - R_T \sin(\alpha_T + \theta_T)\frac{d\theta_T}{d\theta}\right]\right] - \ddot{u}_g\left[mR\cos(\alpha - \theta) + M_T\left[R_1\cos(\beta - \theta) + R_T\cos(\alpha_T + \theta_T)\frac{d\theta_T}{d\theta}\right]\right] - \dot{\theta}^2 I_{TB}\left(\frac{d\theta_T}{d\theta}\right)\frac{d^2\theta_T}{d\theta^2} - \dot{\theta}^2\left[M_T R_1 R_T\left[\frac{d^2\theta_T}{d\theta^2}\cos(\alpha_T + \theta_T + \beta - \theta) + \left(\frac{d\theta_T}{d\theta}\right)\sin(\alpha_T + \theta_T + \beta - \theta)\left[1 - \left(\frac{d\theta_T}{d\theta}\right)\right]\right]\right] \quad \text{(A6)}$$

Equation (A6) is nothing but Equation (3-23) but without the terms for the right pier. Adding the right pier (or merging its distorted shape with the left pier leads to the gemoetry shown in Figure 3-8(e). This proves the fact that the rocking frame under consideration in this study with the merged pier and the top beam at an instant constitutes a two stacked blocks mechanism but as a single degree of freedom system.

The entire concept can also be understood by considering it as a combination of piers and lumped beam mass with applicable forces. Figure A3(a) shows the system with merged piers and beam. As a result of scaling by Jacobians, i.e., the shape distortions, of the right pier and the beam are shown in dashed lines. The angular accelerations for the left and right piers, and, the beam are, $\ddot{\theta}$, $\ddot{\theta}'$, $\ddot{\theta}_T$, respectively. The beam is a rotating rigid body pivoting on top of another, the pier. Hence, it would experience two centripetal accelerations, 1. its own, and 2. due to the pier. The centripetal acceleration on the beam is $R_T\dot{\theta}_T^2$ and the centripetal and tangential accelerations due to the pier are, $R_1\dot{\theta}^2$and $R_1\ddot{\theta}$ respectively. Including the ground acceleration and the self weight, four moments are caused at point B due to: 1. the beam's roational acceleration, $\ddot{\theta}_T$, 2. the pier's centripetal ($R_1\dot{\theta}^2$), and 3. tangential acceleration ($R_1\ddot{\theta}$), and 4. ground and graviational acceleration. Because all accelerations act at the beam, the total moment at B after scaling by $d\theta_T/d\theta$ comes out to be,

$$\tau_B = \tau_{B1} + \tau_{B2} + \tau_{B3} + \tau_{B4}$$

Where,

$$\tau_{B1} = -I_{TB}\,\ddot{\theta}_T\frac{d\theta_T}{d\theta} = -I_{TB}\left[\ddot{\theta}\left(\frac{d\theta_T}{d\theta}\right) + \dot{\theta}^2\left(\frac{d^2\theta_T}{d\theta^2}\right)\right]\frac{d\theta_T}{d\theta}$$

$$\tau_{B2} = M_T R_1 R_T \frac{d\theta_T}{d\theta}\left[\sin(\alpha_T + \theta_T + \beta - \theta)\,\dot{\theta}^2\right]$$

$$\tau_{B3} = -M_T R_1 R_T \frac{d\theta_T}{d\theta}\left[\cos(\alpha_T + \theta_T + \beta - \theta)\ddot{\theta}\right]$$

$$\tau_{B4} = M_T g R_T \frac{d\theta_T}{d\theta}\left[\sin(\alpha_T + \theta_T) - \frac{\ddot{u}_g}{g}\cos(\alpha_T + \theta_T)\right]$$

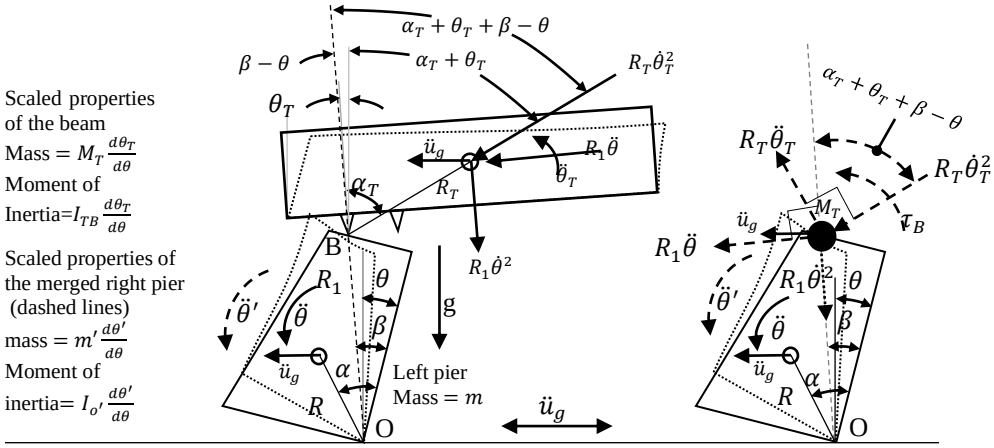

Figure A3: (a) Merged piers and beam with distortions shown in dashed lines. (b) Free body diagram of the equivalent system.

Figure A3(b) shows the equivalent system with the lumped mass (solid circle) that represents the beam along with the forces caused by reaction of the beam on the pier (at point B in Figure A3A): 1. Centripetal force, 2. Tangential forces, and 3. Moment, τ_B, depicted by dashed arrows.

The moment caused by the left pier (solid lines) at point O

$$\tau_{LP} = -\left(I_o\ddot{\theta} + mgR\left(\sin(\alpha - \theta) + \frac{\ddot{u}_g}{g}\cos(\alpha - \theta)\right)\right)$$

The moment casued by the right pier (dashed lines) at point O, including gravitational moment, scaled by $d\theta'/d\theta$, is

$$\tau'_{RP} = -\left(I'_o\ddot{\theta}' + m'gR'\left(\sin(\alpha' - \theta') + \frac{\ddot{u}_g}{g}\cos(\alpha' - \theta')\right)\right)\left(\frac{d\theta'}{d\theta}\right)$$

$$\tau'_{RP} = -\left[I'_o\left[\ddot{\theta}\left(\frac{d\theta'}{d\theta}\right) + \dot{\theta}^2\left(\frac{d^2\theta'}{d\theta^2}\right)\right] + m'gR'\left(\sin(\alpha' - \theta') + \frac{\ddot{u}_g}{g}\cos(\alpha' - \theta')\right)\right]\left(\frac{d\theta'}{d\theta}\right)$$

The inertial acceleration on the lumped mass would be $-R_1\ddot{\theta}$. Moment caused by the forces on the lumped mass due to the beam (dotted arrows)

$$\tau_M = M_T R_1\left[-R_1\ddot{\theta} - R_T\ddot{\theta}_T\cos(\alpha_T + \theta_T + \beta - \theta) - R_T\dot{\theta}_T^2\sin(\alpha_T + \theta_T + \beta - \theta)\right] - M_T g R_1\left[\sin(\beta - \theta) + \frac{\ddot{u}_g}{g}\cos(\sin(\beta - \theta))\right]$$

$$\tau_M = -M_T R_1^2\ddot{\theta} - M_T R_1 R_T\left[\left[\ddot{\theta}\left(\frac{d\theta_T}{d\theta}\right) + \dot{\theta}^2\left(\frac{d^2\theta_T}{d\theta^2}\right)\right]\cos(\alpha_T + \theta_T + \beta - \theta) + \dot{\theta}^2\left(\frac{d\theta_T}{d\theta}\right)^2\sin(\alpha_T + \theta_T + \beta - \theta)\right]$$
$$- M_T g R_1\left[\sin(\beta - \theta) + \frac{\ddot{u}_g}{g}\cos(\sin(\beta - \theta))\right]$$

The sum of the moments including that of the left pier at point O gives

$$\ddot{\theta}\begin{pmatrix} I_o + I_o'\left(\frac{d\theta'}{d\theta}\right)^2 + M_T R_1^2 + .. \\ I_{TB}\ddot{\theta}\left(\frac{d\theta_T}{d\theta}\right)^2 \end{pmatrix} = -mgR\left(\sin(\alpha-\theta) + \frac{\ddot{u}_g}{g}\cos(\alpha-\theta)\right) - m'gR'\left(\frac{d\theta'}{d\theta}\right)\left(\sin(\alpha'-\theta') + \frac{\ddot{u}_g}{g}\cos(\alpha'-\theta')\right)$$

$$+M_T g R_T \frac{d\theta_T}{d\theta}\left[\sin(\alpha_T+\theta_T) - \frac{\ddot{u}_g}{g}\cos(\alpha_T+\theta_T)\right]$$
$$-M_T g R_1\left[\sin(\beta-\theta) + \frac{\ddot{u}_g}{g}\cos(\sin(\beta-\theta))\right]$$
$$+M_T R_1 R_T \frac{d\theta_T}{d\theta}\left[\sin(\alpha_T+\theta_T+\beta-\theta)\,\dot{\theta}^2\right]$$
$$-M_T R_1 R_T \frac{d\theta_T}{d\theta}\left[\cos(\alpha_T+\theta_T+\beta-\theta)\ddot{\theta}\right]$$
$$-M_T R_1 R_T\left[\left[\ddot{\theta}\left(\frac{d\theta_T}{d\theta}\right) + \dot{\theta}^2\left(\frac{d^2\theta_T}{d\theta^2}\right)\right]\cos(\alpha_T+\theta_T+\beta-\theta) + \dot{\theta}^2\left(\frac{d\theta_T}{d\theta}\right)^2\sin(\alpha_T+\theta_T+\beta-\theta)\right]$$
$$-\dot{\theta}^2\left[I_o'\left(\frac{d^2\theta'}{d\theta^2}\right)\left(\frac{d\theta'}{d\theta}\right) + I_{TB}\left(\frac{d^2\theta_T}{d\theta^2}\right)\frac{d\theta_T}{d\theta}\right]$$

$$\ddot{\theta}\begin{pmatrix} I_o + I_o'\left(\frac{d\theta'}{d\theta}\right)^2 + M_T R_1^2 + .. \\ I_{TB}\ddot{\theta}\left(\frac{d\theta_T}{d\theta}\right)^2 \end{pmatrix} = -mgR\left(\sin(\alpha-\theta) + \frac{\ddot{u}_g}{g}\cos(\alpha-\theta)\right) - m'gR'\left(\frac{d\theta'}{d\theta}\right)\left(\sin(\alpha'-\theta') + \frac{\ddot{u}_g}{g}\cos(\alpha'-\theta')\right)$$

$$+M_T g R_T \frac{d\theta_T}{d\theta}\left[\sin(\alpha_T+\theta_T) - \frac{\ddot{u}_g}{g}\cos(\alpha_T+\theta_T)\right]$$
$$-M_T g R_1\left[\sin(\beta-\theta) + \frac{\ddot{u}_g}{g}\cos(\sin(\beta-\theta))\right]$$
$$-M_T R_1 R_T\ddot{\theta}\frac{d\theta_T}{d\theta}\cos(\alpha_T+\theta_T+\beta-\theta)$$
$$-M_T R_1 R_T\dot{\theta}\frac{d\theta_T}{d\theta}\cos(\alpha_T+\theta_T+\beta-\theta)$$
$$-M_T R_1 R_T\dot{\theta}^2\left[\left(\frac{d^2\theta_T}{d\theta^2}\right)\cos(\alpha_T+\theta_T+\beta-\theta) + \left(\frac{d\theta_T}{d\theta}\right)^2\sin(\alpha_T+\theta_T+\beta-\theta) - \frac{d\theta_T}{d\theta}[\sin(\alpha_T+\theta_T+\beta-\theta)]\right]$$
$$-\dot{\theta}^2\left[I_o'\left(\frac{d^2\theta'}{d\theta^2}\right)\left(\frac{d\theta'}{d\theta}\right) - I_{TB}\left(\frac{d^2\theta_T}{d\theta^2}\right)\frac{d\theta_T}{d\theta}\right]$$

$$\ddot{\theta}\begin{pmatrix} I_o + I_o'\left(\frac{d\theta'}{d\theta}\right)^2 + M_T R_1^2 + .. \\ I_{TB}\ddot{\theta}\left(\frac{d\theta_T}{d\theta}\right)^2 + .. \\ 2M_T R_1 R_T\frac{d\theta_T}{d\theta}\left[\cos(\alpha_T+\theta_T+\beta-\theta)\ddot{\theta}\right] \end{pmatrix} = -g\begin{bmatrix} mR\sin(\alpha-\theta) + m'R'\left(\frac{d\theta'}{d\theta}\right)\sin(\alpha'-\theta') \\ -M_T R_T\frac{d\theta_T}{d\theta}sin(\alpha_T+\theta_T) + M_T g R_1\sin(\beta-\theta) \end{bmatrix}$$
$$-\frac{\ddot{u}_g}{g}\begin{bmatrix} mR\cos(\alpha-\theta) + m'R'\cos(\alpha'-\theta') + \\ M_T g R_T\cos(\alpha_T+\theta_T) + M_T g R_1\cos(\sin(\beta-\theta)) \end{bmatrix}$$
$$-M_T R_1 R_T\dot{\theta}^2\left[\left(\frac{d^2\theta_T}{d\theta^2}\right)\cos(\alpha_T+\theta_T+\beta-\theta) + \frac{d\theta_T}{d\theta}\sin(\alpha_T+\theta_T+\beta-\theta)\left[1-\frac{d\theta_T}{d\theta}\right]\right]$$
$$-\dot{\theta}^2\left[I_o'\left(\frac{d^2\theta'}{d\theta^2}\right)\left(\frac{d\theta'}{d\theta}\right) + I_{TB}\left(\frac{d^2\theta_T}{d\theta^2}\right)\frac{d\theta_T}{d\theta}\right]$$

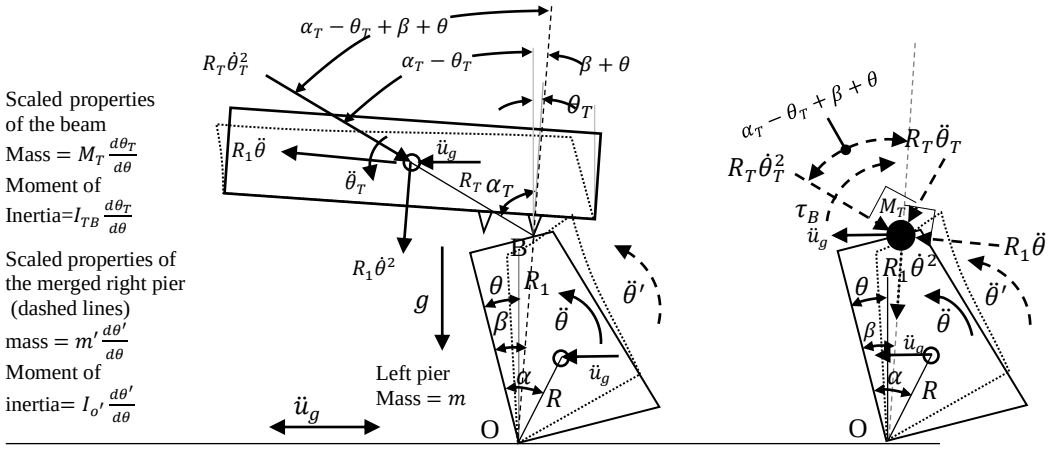

Figure A4 Mirror image of Figure A3.

A.3 Coefficient of restitution of the merged unsymmetrical equal mass piers

The coefficient of restitution of a rocking frame with symmetrical pier having slenderness angle, α, normalized moment of inertia, I_{on}, and beam to mass ratio, $q = M_T/2m$, is given as 0

$$e = \frac{1}{\psi}\left(e_G + \frac{q}{I_{on}}(\xi^2(\cos\alpha)^2 - (1+\eta)^2\sin\alpha^2)\right) \tag{A7}$$

Where, $\psi = \left[1 + \frac{q}{I_{on}}(\xi^2(\cos\alpha)^2 + (\eta+1)^2\sin\alpha^2)\right]$ and $e_G = 1 - \frac{2}{I_{on}}\sin\alpha$

Where, $\psi = \left[1 + \frac{q}{I_{on}}(\xi^2(\cos\alpha)^2 + (\eta+1)^2\sin\alpha^2)\right]$ and $e_G = 1 - \frac{2}{I_{on}}\sin\alpha$, the coefficient of restitution of an individual pier.

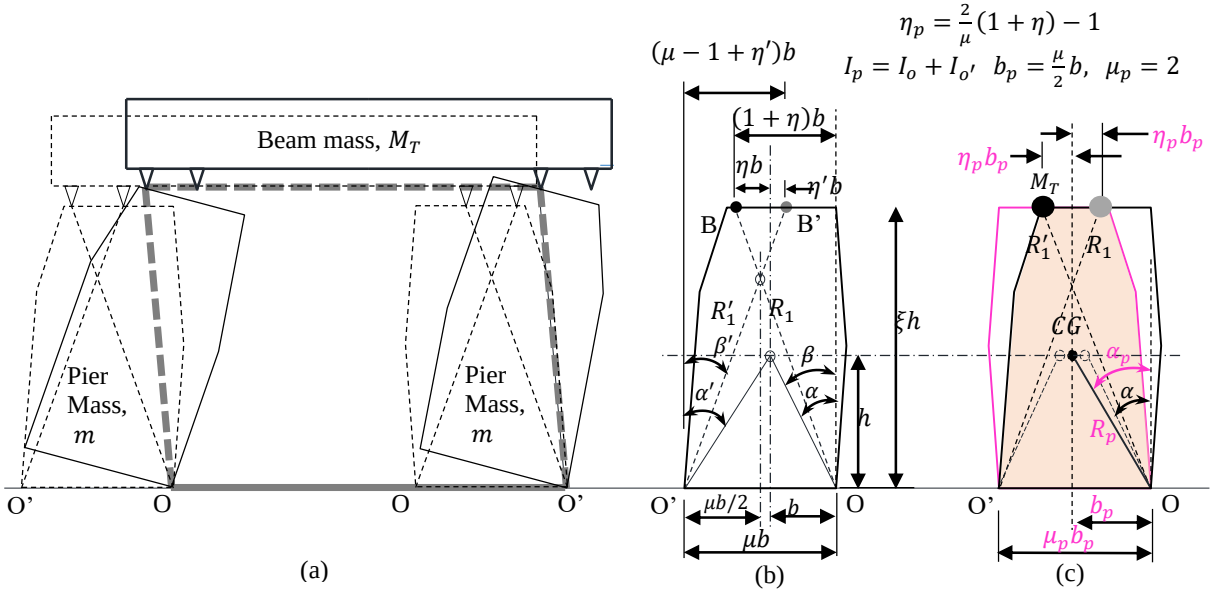

Figure A5: (a) rocking frame with unsymmetrical piers. (b) individual pier details. (c) merged piers

Figures A5(a), (b) and (c) show a rocking frame with unsymmetrical piers, details of an individual pier and merged piers respectively. Denoting the normalized moment of inertia of the merged pier as I_{pn}, the coefficient of restitution of the merged pier is given as 0

$$e_p = 1 - \frac{2}{I_{pn}}\sin^2\alpha_p \tag{A8}$$

Where, $I_{pn} = (I_o + I_o')/2mR_p^2$, the normalized moment of inertia of the merged pier, is given as

$$I_{pn} = \frac{(I_o + I_o')}{2mR_p^2} = \frac{1+q_I}{2mR_p^2}I_o \tag{A9}$$

From the pier geometry,

$$b_p = \frac{\mu b}{2}, \text{ and } \eta_p = (2/\mu)(1+\eta) - 1$$

$$(1+\eta_p)b_p = (1+\eta)b \quad \Rightarrow \quad (1+\eta_p)\sin\alpha_p = \frac{R}{R_p}(1+\eta)\sin\alpha \tag{A10}$$

$$\tan\alpha_p = \frac{b_p}{h} = \frac{\mu b}{2h} = \frac{\mu}{2}\tan\alpha \;\Rightarrow\; \alpha_p = \tan^{-1}[(\mu/2)\tan\alpha] \tag{A11}$$

Since, $\sin[\tan^{-1}[x]] = x/\sqrt{1+x^2}$, and $\cos[\tan^{-1}[x]] = 1/\sqrt{1+x^2}$

$$\sin\alpha_p = \sin[\tan^{-1}[(\mu/2)\tan\alpha]] = \frac{(\mu/2)\tan\alpha}{\sqrt{1+\left((\mu/2)\tan\alpha\right)^2}} = \frac{(\mu/2)\tan\alpha\cos\alpha}{\frac{1}{2}\sqrt{(\mu\sin\alpha)^2+4(\cos\alpha)^2}}$$

recognizing $R_p = \sqrt{b_p^2+h^2} = (R/2)\sqrt{(\mu\sin\alpha)^2+4(\cos\alpha)^2}$ gives

$$\sin\alpha_p = \frac{\mu R\tan\alpha\cos\alpha}{R\sqrt{(\mu\sin\alpha)^2+4(\cos\alpha)^2}} = \frac{\mu R}{2R_p}\sin\alpha$$

$$\cos\alpha_p = \frac{1}{\sqrt{1+\left((\mu/2)\tan\alpha\right)^2}} = \frac{\cos\alpha}{\frac{1}{2}\sqrt{(\mu\sin\alpha)^2+4(\cos\alpha)^2}} = \frac{R}{R_p}\cos\alpha \tag{A12}$$

Substituting Equations (A9) and (A12) into Equation (A8) gives

$$e_p = 1 - \frac{2}{\frac{(I_o+I_o')}{2mR_p^2}}\left[\frac{\mu R\sin\alpha}{2R_p}\right]^2 = 1 - \frac{1}{\frac{I_o(1+q_I)}{mR^2}}[\mu\sin\alpha]^2 = 1 - \frac{1}{(1+q_I)I_{on}}[\mu\sin\alpha]^2 \tag{A13}$$

Considering Equation (A7) for merged pier gives

$$e_{sm} = \frac{1}{\psi_{sm}}\left(e_p + \frac{q}{I_{pn}}\left(\xi^2\left(\cos\alpha_p\right)^2 - \left(1+\eta_p\right)^2\left(\sin\alpha_p\right)^2\right)\right) \tag{A14}$$

where

$$\psi_{sm} = \left[1 + \frac{q}{I_{pn}}\left(\xi^2\left(\cos\alpha_p\right)^2 - \left(1+\eta_p\right)^2\left(\sin\alpha_p\right)^2\right)\right]$$

Substituting, the merged pier properties, from Equations (A9), (A10) into Equation (A14) gives

$$e_{sm} = \frac{1}{\psi_{sm}}\left(e_p + \frac{q}{I_{pn}}\left(\xi^2\left(\cos\alpha_p\right)^2 - \left(\frac{R}{R_p}(1+\eta)\sin\alpha\right)^2\right)\right)$$

Substituting $\cos\alpha_p$ from Equation (A12)

$$e_{sm} = \frac{1}{\psi_{sm}}\left(e_p + \frac{q}{\frac{1+q_I}{2mR_p^2}I_o}\left(\xi^2\left(\frac{R}{R_p}\cos\alpha\right)^2 - \left(\frac{R}{R_p}(1+\eta)\sin\alpha\right)^2\right)\right)$$

The above leads to

$$e_{sm} = \frac{1}{\psi_{sm}}\left(e_p + \frac{2q}{(1+q_I)I_{on}}\left(\xi^2(\cos\alpha)^2 - \left((1+\eta)\sin\alpha\right)^2\right)\right) \tag{A15}$$

where $$\psi_{sm} = 1 + \frac{2q}{(1+q_I)I_{on}}\left(\xi^2(\cos\alpha)^2 + \left((1+\eta)\sin\alpha\right)^2\right)$$

It is to be noted that for the unmerged pier, the symmetrical eccentricity condition, $(\mu - 1 + \eta')b = (\eta + 1)b$, translates to equal distance, $\eta_p b_p$, on either side of the CG axis.

A.4 Coefficient of restitution for frames with symmetrical eccentricities

The coeffieicent of restitution equation for frames with symmetrical eccentricities depends on the treatment of impulses. The explanation below corresponds to the figures in Chapter 3 referenced in the section of coefficient of restitution.

According to Newton's second law, impact force caused by a mass, M, traveling with velocity, v, is equal to the rate of change of momentum with respect to time, i.e., $F = d(Mv)/dt$. If the mass is constant, $F = Md(v)/dt$. If the velocities before and after the impact are v_1 and v_2, integrating over the duration of impact, leads to the impulse, $\int F\,dt = M(v_1 - v_2)$, which is impulse momentum theorem. Applying it to the horizontal impact forces results in the sum of the horizontal impulses being equal to the change in linear momentum of the top beam

$$\int F_{ILx}\,dt + \int F_{IRx}\,dt = M_T\left(R_1\dot{\theta}_1\cos\beta - R_1'\dot{\theta}_2\cos\beta'\right) = M_T R_1\cos\beta\left(\dot{\theta}_1 - \dot{\theta}_2\right) = M_T\xi h\left(\dot{\theta}_1 - \dot{\theta}_2\right)$$

Since the beam remains horizontal, there is no rotation. Omitting the impulse due to rotation, F_{IOy}, in Figure 3-12 (b), the sum of vertical impulses, (noting the fact that the vertical velocities are in opposite direction), will be equal to the change in vertical momentum,

$$\int F_{ILy}\,dt + \int F_{IRy}\,dt = M_T\left(R_1\dot{\theta}_2\sin\beta + R_1'\dot{\theta}_1\sin\beta'\right) = M_T R_1\sin\beta\left(\dot{\theta}_1 + \dot{\theta}_2\right) = M_T(1+\eta)b\left(\dot{\theta}_1 + \dot{\theta}_2\right)$$

Angular momenta of the impulses about point P will be the same as their angular momenta about their pivot points (since the pivot point are stationary).

$$H_{OP_{\text{before}}} + H_{during} = H_{OP_{\text{after}}}$$

$$H_{OL_{\text{before}}} + H_{OR_{\text{before}}} + H_{\text{during}} = H_{OL_{\text{after}}} + H_{OR_{\text{after}}}$$

Since angular momentum of impact forces is the moment of linear momentum about the pivot points, the above equation leads to

$$(I_{o\prime} - \mu(\mu-1)mbR\sin\alpha)\dot{\theta}_1 + (I_o - \mu m'bR\sin\alpha)\dot{\theta}_1 + \xi h\left(\int F_{ILx}\,dt + \int F_{IRx}\,dt\right) + \Big((1+\eta)b\int F_{ILy}\,dt + (\mu - 1 + \eta')b\int F_{IRy}\,dt\Big) = (I_O + I_{O\prime})\dot{\theta}_2$$

Since $\mu - 1 + \eta' = \eta + 1$,

$$(I_{o\prime} - \mu(\mu-1)mbR\sin\alpha)\dot{\theta}_1 + (I_o - \mu m'bR\sin\alpha)\dot{\theta}_1 + \xi h\left(\int F_{ILx}\,dt + \int F_{IRx}\,dt\right) - (1+\eta)b\Big(\int F_{ILy}\,dt + \int F_{IRy}\,dt\Big) = (I_o + I_{o\prime})\dot{\theta}_2$$

$$\dot{\theta}_1\left[(I_o + I_{o\prime}) - \left(\mu q_m + \mu(\mu-1)\right)mR^2\sin^2\alpha\right] + \left(M_T\xi^2h^2\left(\dot{\theta}_1 - \dot{\theta}_2\right)\right) - (1+\eta)^2b^2M_T\left(\dot{\theta}_2 + \dot{\theta}_1\right) = (I_o + I_{o\prime})\dot{\theta}_2$$

Substituting $h = R\cos\alpha$ and $b = R\sin\alpha$ gives

$$\dot{\theta}_1\left[(I_o + I_{o\prime}) - \left(\mu q_m + \mu(\mu-1)\right)mR^2\sin^2\alpha + M_T\xi^2R^2\cos^2\alpha - M_T(1+\eta)^2R^2\sin^2\alpha\right] = \dot{\theta}_2\left[(I_o + I_{o\prime}) + M_T\xi^2R^2\cos^2\alpha + (1+\eta)^2R^2\sin\alpha^2\,M_T\right]$$

$$\dot{\theta}_1 I_o\left[1 + q_I - \left(\mu q_m + \mu(\mu-1)\right)\frac{mR^2}{I_o}\sin^2\alpha + q_T\frac{mR^2}{I_o}\left(\xi^2\cos^2\alpha - (1+\eta)^2\sin^2\alpha\right)\right]\ldots = \dot{\theta}_2 I_o\left[1 + q_I + q_T\frac{mR^2}{I_o}\left(\xi^2\cos^2\alpha + (1+\eta)^2\sin\alpha^2\right)\right] \quad \text{(A16)}$$

$$\check{e} = \frac{\dot{\theta}_2}{\dot{\theta}_1} = \frac{1}{\psi}\left(e_G^+ + q_I e_G^- + \frac{q_T}{I_{on}}(\xi^2\cos^2\alpha - (1+\eta)^2\sin^2\alpha)\right) \quad \text{(A17)}$$

Where, $\psi = \left[1 + q_I + q_T\frac{mR^2}{I_o}(\xi^2\cos^2\alpha + (1+\eta)^2\sin\alpha^2)\right]$

It is to be noted that although the piers are unsymmetrical with dissimilar individual coefficients of restitution for positive and negative rotations, the coefficient of restitution of the frame is the same in both directions because of the symmetry of the frame. For symmetrical piers with equal mass, $m = m'$, and $q = M_T/(m+m')$. Substituting $q_I = 1$, $q_m = 1$, and, $q_T = 2q$, into the above equation leads to E_{eq} derived in Equation (38) of 0. Further substituting $\eta = 1$ leads to the coefficient of restitution derived for symmetrical piers with $\eta = 1$ in 6 where an assumption was made that the impact forces on top of symmetrical piers are equal. This assumption led to the fact that the coefficient of restitution of the entire system is equal to the coefficient of restitution of a solitary pier with the point mass M_T/N, where N is the number of piers. Equation (A17) with suggested substitutions below validates the assumption in 6.

$$e_G^+ + q_I e_G^- = \left(q_I - \frac{\mu(\mu-1)}{I_{on}}\sin^2\alpha\right) + \left(1 - \frac{\mu q_m}{I_{on}}\sin^2\alpha\right)$$

$$e_G^+ + q_I e_G^- = \left(1 + q_I - \frac{\mu(q_m+\mu-1)}{I_{on}}\sin^2\alpha\right)$$

Substituting, $q_m = 1,\ \mu = 2, q_I = 1$ gives

$$e_G^+ + q_I e_G^- = \left(1 + 1 - \frac{2(1+2-1)}{I_{on}}\sin^2\alpha\right) = 2\left(1 - \frac{\sin^2\alpha}{I_{on}}\right)$$

Which is twice the coefficient of restitution for a single pier, because $q_m = 1,\ \mu = 2, q_I = 1$, means that there are two piers in the equation. Hence the coefficient of restitution is twice that of a single pier. Since ψ is twice that for the single pier, the coefficient of 2 gets cancelled as explained below.

$$\psi = \left[1 + q_I + \frac{q_T}{I_{on}}(\xi^2\cos^2\alpha + (1+\eta)^2\sin\alpha^2)\right]$$

Substituting $q_I = 1, q_T = 2q$ gives

$$\psi = 2\left[1 + \frac{q}{I_{on}}(\xi^2\cos^2\alpha + (1+\eta)^2\sin\alpha^2)\right]$$

Here ψ is twice that for the symmetrical pier frame. Hence the coefficient of restitution leads to the same formula as obtained earlier for symmetrical piers.

References:

[RA-1] Kounadis AN, Papadopoulos GJ, Cotsovos DM. Overturning instability of a two-rigid block system under ground excitation. *ZAMM Z. Angew. Math. Mech.* 2012; **92**(7):536 – 557

[RA-2] Dar A, Konstantinidis D, El-Dakhakhni W. Seismic response of rocking frames with top support eccentricity. *Earthquake Engineering and Structural Dynamics* 2018; **47**(12): 2496– 2518. https://doi.org/10.1002/eqe.3096

[RA-3] Makris N, Vassiliou MF. Planar rocking response and stability analysis of an array of free-standing columns capped with a freely supported rigid beam. Earthquake Engineering and Structural Dynamics 2013; 42(3):431-449.

APPENDIX B

VERIFICATION ON WORKING MODEL 2D

B.1 Response to hybrid rectangular pulse excitation on Working Model 2D

Figure B-1 shows the rocking response of a slide restricted slender rocking block ($\alpha = 0.3$, $p = 4$ and a large coefficient of friction, 10^6) to a hybrid rectangular pulse excitation obtained by the software Working Model 2D (WM). The response is shown at two distinct stages: the top diagram depicts the block rising and reaching its peak rotation and the bottom diagram shows it falling to the stage when the normal force reduces to zero (or, its vertical acceleration reaches -g causing separation). On the right side of the diagrams, the rocking block is depicted in red on top of a shake table shown in green. The left top corner of the block is denoted as Point 32 and the bottom right corner as Point 12. On the left side of both diagrams, are shown various plots over the duration of rocking in two columns. The state of the rocking block on the shake table is denoted by a tiny black dot highlighted in red circles on various plots. The top three plots in the left column show vertical velocity, acceleration (in g's) and position of the block's CG. The vertical position of the block's CG is with respect to its initial position, i.e., the half height of the block. The bottom row in the left column shows the rotation of the block. The top row of the right column depicts the hybrid rectangular excitation in terms of αg. The second row from the top in the right column shows rotation (θ), angular velocity ($\dot{\theta}$), and angular acceleration ($\ddot{\theta}$) of the block. This plot is similar to those in Figure 4-9. The third row in the right column shows vertical acceleration (in g's) of the top left corner (Pt 32) of the block. The fourth row in the right column shows x and y positions of the block's bottom corner (Pt 12) relative to its initial position. As shown, the x position of Pt 12 does not change depicting no sliding. The y position starts increasing upon impact and comes back to zero on the second impact. This plot is not shown in the bottom diagram. As shown in the top diagram, the black dot (inside the red circle) shows the block to be at peak rotation whereas in the bottom diagram it is shown at separation where the normal force is zero. The normal force is shown at its peak in the top diagram but in the bottom diagram it disappears because the vertical acceleration of the block's CG reaches -1 (g). Thus, Figure B1 is a proof of a slide restricted slender block's separation under a hybrid rectangular pulse excitation. It appears that the WM obtains acceleration by numerically differentiating the velocity causing large spikes due to the jump discontinuities in the velocity plot. Improving the accuracy limit in the WM may remove the spikes but at the cost of computing time which looks elegant but is of little practical use. Once the rotation and velocity are known, the rest can be computed through the equation of motion and of horizontal and vertical accelerations presented in Chapter 4 (Equations (4-1) and (4-6)) as demonstrated later in this appendix.

Figure B-2 shows two slide restricted piers with the same parameters as in Figure B-1 ($\alpha = 0.3$, $p = 4$) with a beam on top whose mass is the same as the cumulative mass of the two piers leading to $q = 1$. A large coefficient of friction (10^6) is considered for beams and piers as to represent the slide restricted condition. Since the eccentricity is symmetrical ($\eta = 1$), both piers' rotations are equal and the beam remains horizontal during rocking motion. The left pier is denoted as Blk11, the beam as Blk 36 and the left pier's top left corner as Pt 32. The response plots are shown on the left side. The first plot from top shows hybrid rectangular pulse excitation in g. The pier rotation is shown in the second plot, the pier (Blk 11) CG vertical acceleration in the third, Pt 32 vertical acceleration in the fourth, beam (Blk 36) in the fifth and the vertical position (y coordinate) of the beam with respect to Pt 32 is shown in the sixth plot at the bottom. The COFD at beam is shown in the plot towards right of the bottom plot. As depicted, close to 0.7s (before $\theta = 0$), the vertical acceleration of the pier (Blk 11) drops close to -0.5(g) causing the that of the top corner (Pt 32) to drop below -1(g). The beam's vertical acceleration (Blk 36) reaches -1(g) and remains constant indicating the pier corners (Pt 32 and the other pier corner), have left the beam. The bottom plot shows the beam's vertical position relative to Pt 32 increasing depicting separation. The COFD rises exponentially. Thus, Figure B-2 proves separation of beam from piers under slide restricted condition. Here again, there are spikes in acceleration which can be removed as explained earlier.

B.2 Response to earthquake records

Figure B-3 illustrates the rotational response of an unsymmetrical trapezoidal pier for the frame in Example 1 in Table 3-3 to the Rinaldi record (Table 3-4). A comparison of the rotation response of the solitary block from Figure 3-16 (denoted as 'Analytical') with that obtained from WM is made. The peaks and the duration of the two responses are close to each other with the first peak of the analytical response being comparatively conservative. Thus, Figure B-3 proves agreement between the Analytical and the WM plots in a trapezoidal block's response.

Figure B-4 compares the responses obtained from the analytical solution and the WM for a frame (with unsymmetrical eccentricities) in Example 2 of Table 3-3 to the Aegion record (Table 3-4). The analytical solution is the same as that in Figure 3-16 for Example 2. The first three peaks of the generalized, beam and system rotations (θ, θ_T, θ^*) of the two solutions are in agreement.

Figure B-5 illustrates the comparison of the analytical and the WM responses of a rectangular block ($p = 1.679$ and $\alpha = 0.291$) to the Rinaldi record (Table 4-8). The left most diagram shows that the rotational responses are in agreement with each other except for a minor time shift. The middle diagram shows the vertical acceleration of the block obtained from WM directly and by applying Equation (4-1), which is the equation of motion (EOM), and Equation (4-6) to the WM rotational and velocity responses. As evident, the spikes in the WM plot disappear. The diagram on right compares this response with that from the analytical solution. The rotation and vertical acceleration responses are in agreement up to 8s, which is the range of peak responses.

Figure B-6 shows the responses of a frame with rectangular piers ($p = 1.679$ and $\alpha = 0.291$) with $q = 10$ to the Rinaldi record (Table 4-8). As shown the analytical and the WM responses are in agreement. The top diagram shows that the peaks of the two responses match and the analytical response is more conservative than the WM response. The second diagram from the top shows the vertical acceleration of the beam from the WM response (with spikes) and that obtained by applying Equations (4-1) and (4-6) to the WM data. The third diagram shows the beam's vertical acceleration where the two responses are in agreement especially at the peak. The fourth diagram shows the vertical acceleration from Equation (4-54) being in agreement with that obtained from WM. Also, the minimum acceleration obtained from Equation (4-55) is shown to be in agreement with the minimum peak acceleration. The fifth diagram shows plots of horizontal acceleration where the peaks of both plots are in agreement. Also the prediction of the peak horizontal acceleration by Equation (4-51) is shown to be applicable. The spikes in the WM response can be ignored as explained earlier. Similarly, in the diagram at the bottom, an agreement is evident between the WM and the analytical responses. Here, maximum COFD obtained from Equation (4-56) leads to a conservative prediction of 0.434 against the peaks at ~0.3.

All figures in this appendix prove agreement between the responses to various types of excitations obtained by the analytical approach laid out in the thesis and those obtained from the WM. Also, the predictions of horizontal and vertical accelerations, and, the COFD from Equations (4-51), (4-54), (4-55), and (4-56), are shown to be in agreement with the two responses.

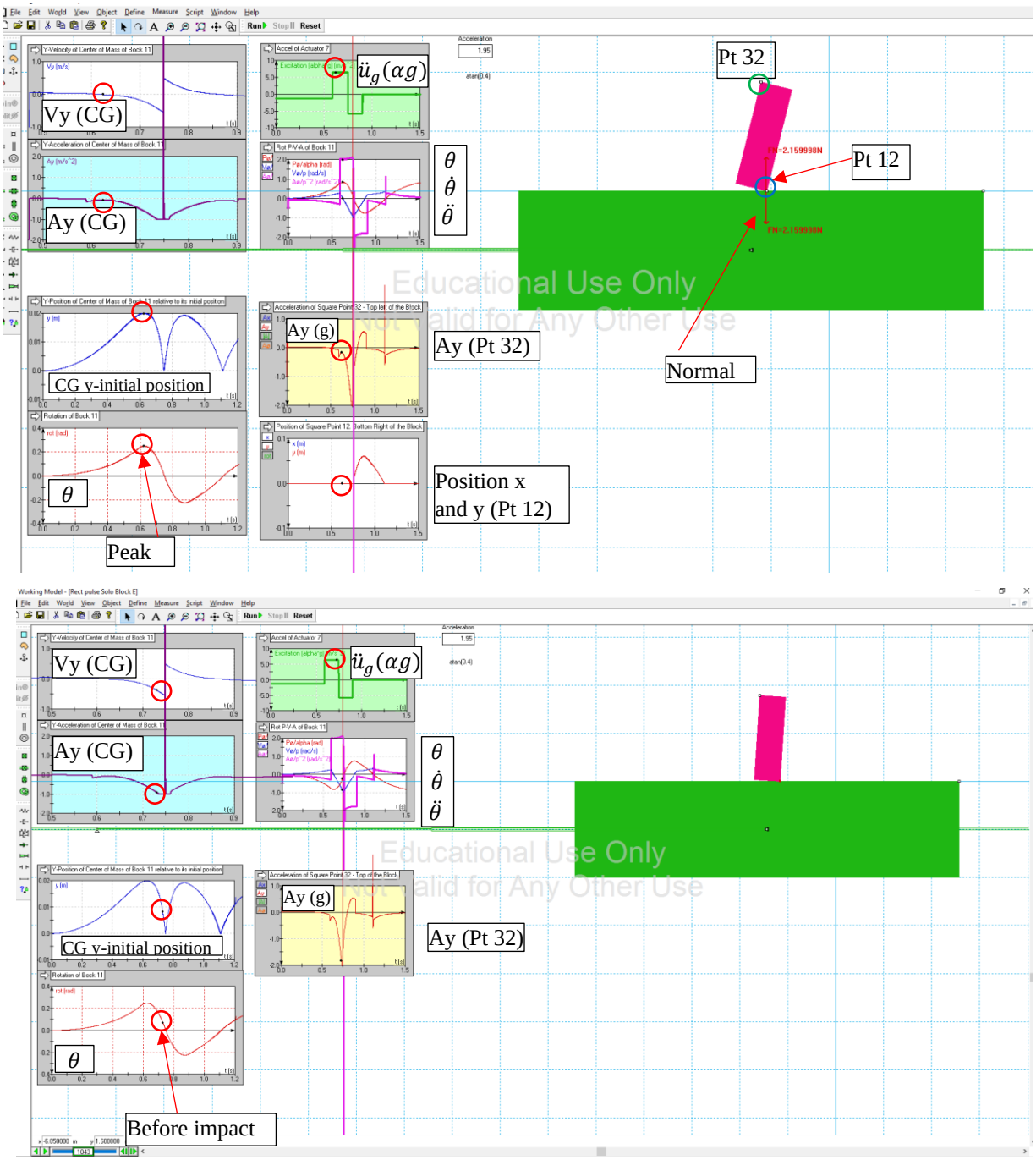

Figure B-1: Screenshots from the WM analysis of a slide restricted slender rocking block subjected to hybrid pulse rectangular excitation containing various response plots. Top: Block rises to its peak rotation where the normal force is maximum. Bottom: Block retreating from peak rotation at separation where normal force disappears.

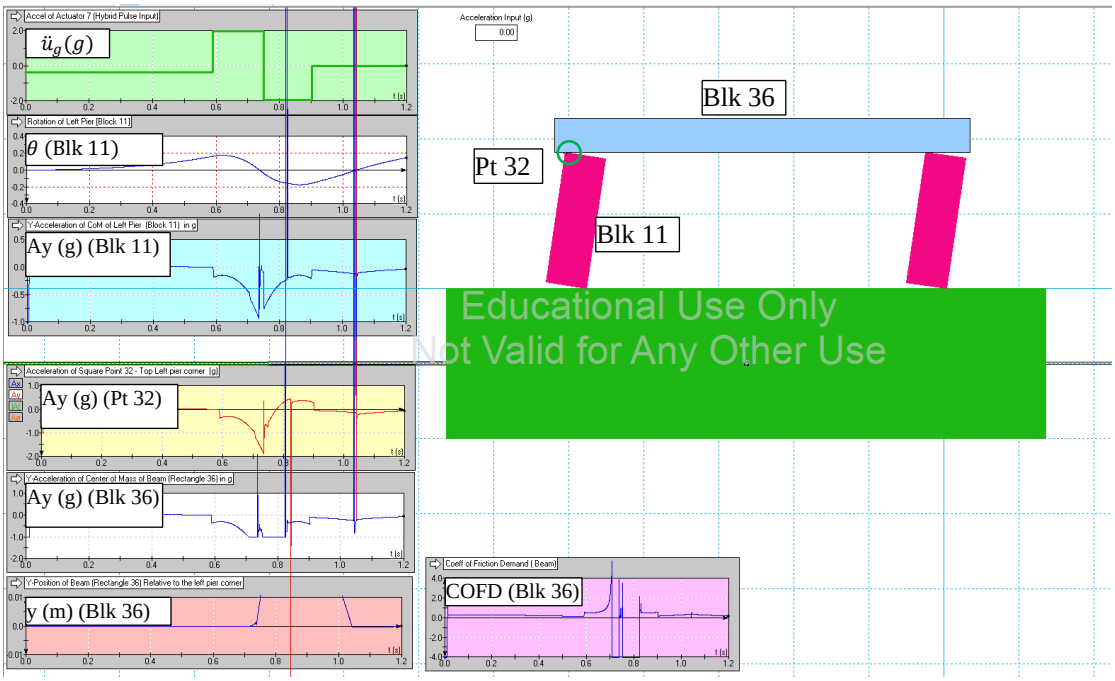

Figure B-2 WM response of a slide restricted rocking frame ($q = 1$) on slender piers to a hybrid rectangular pulse excitation

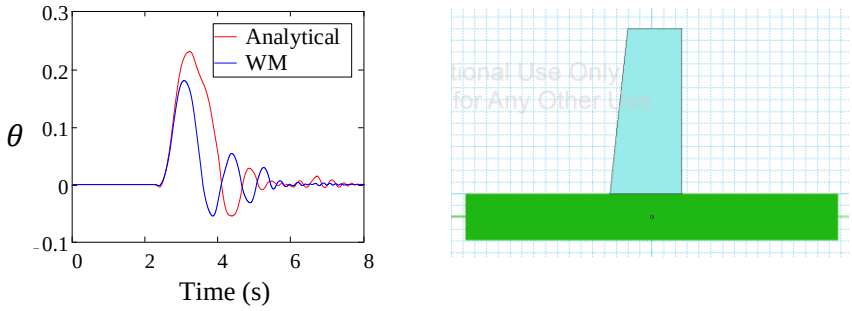

Figure B-3 Comparison of analytical and the WM response of an unsymmetrical trapezoidal block (Table 3-3, Example 1) to the Rinaldi record (Table 3-4). The analytical solution is the same as that in Figure 3-16 depicted for the solitary pier.

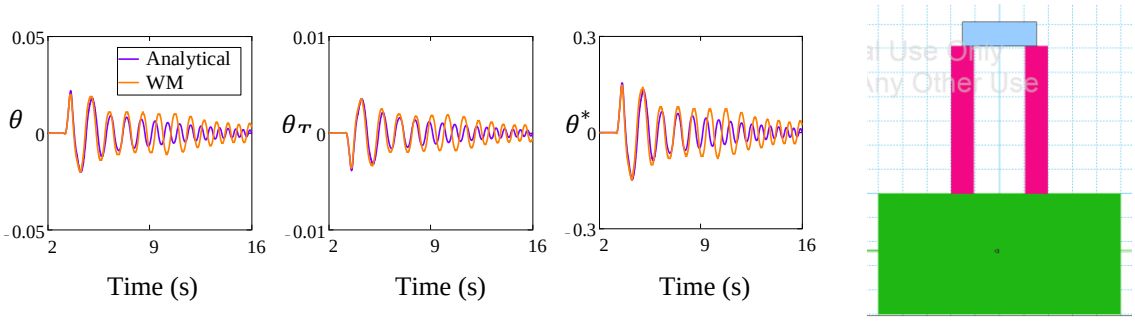

Figure B-4 Comparison of analytical and the WM response of a frame in Example 2 of Table 3-3 to the Aegion record (Table 3-4). The analytical solution is the same as that in Figure 3-16 for example 2.

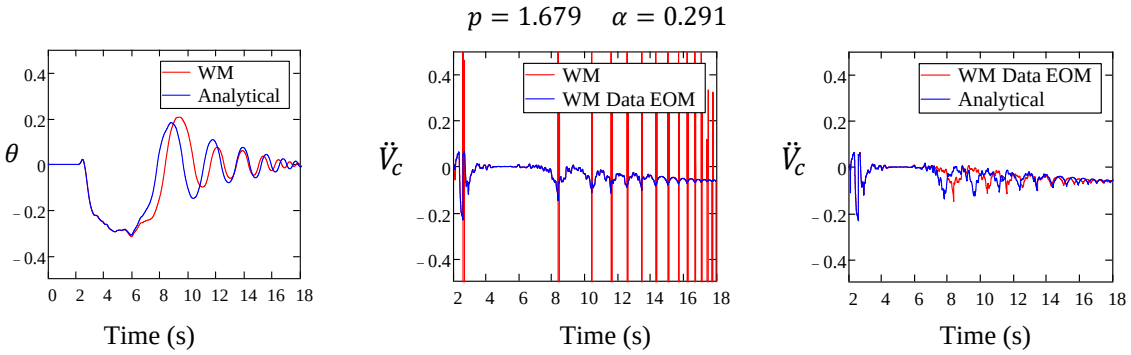

Figure B-5 Comparison of analytical and the WM response of a rectangular block ($p = 1.679$ and $\alpha = 0.291$) to the Rinaldi record (Table 4-8).

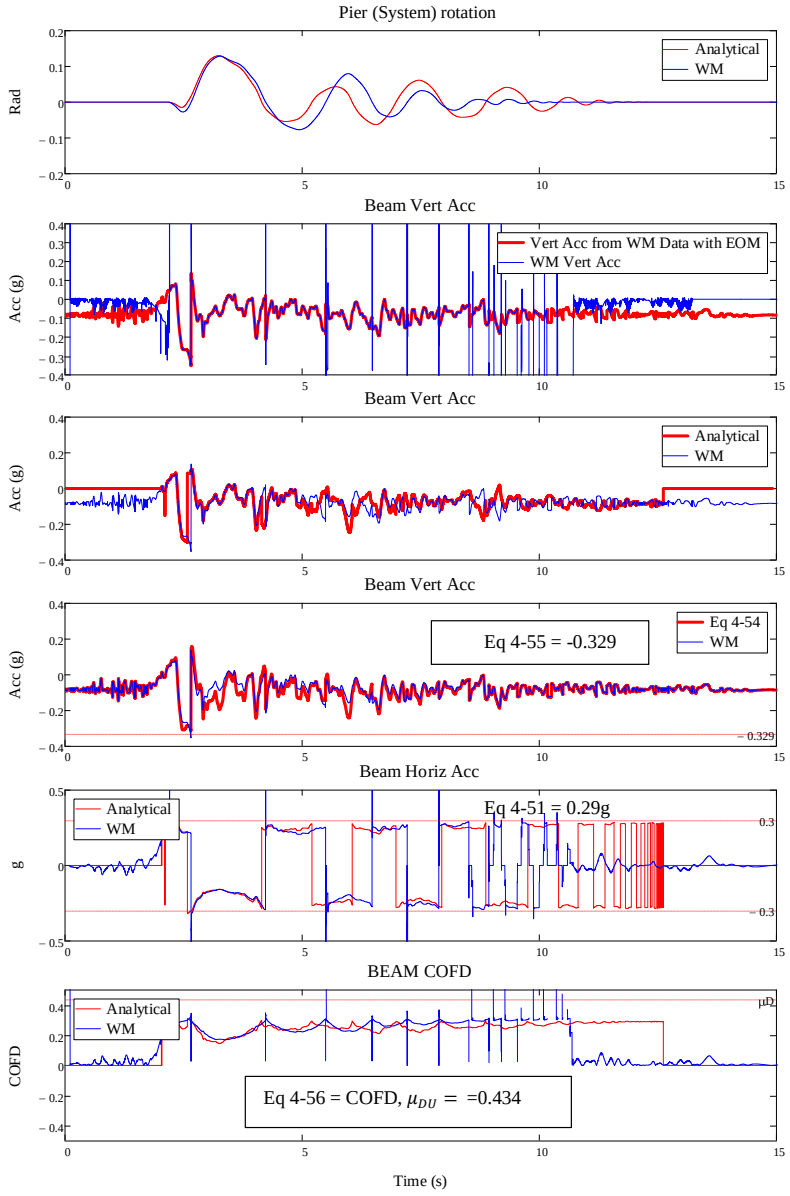

Figure B-6 Analytical and the WM responses of a two-pier frame with parameters, $\alpha = 0.291$, $p = 1.679$, $\eta = 1$ and $q = 10$ to the Rinaldi record (Table 4-8).

APPENDIX C

VERIFICATION FOR TIME HISTORY AT HIGHER ELEVATION

C.1 Verification of a frame's response to the time history at higher elevation

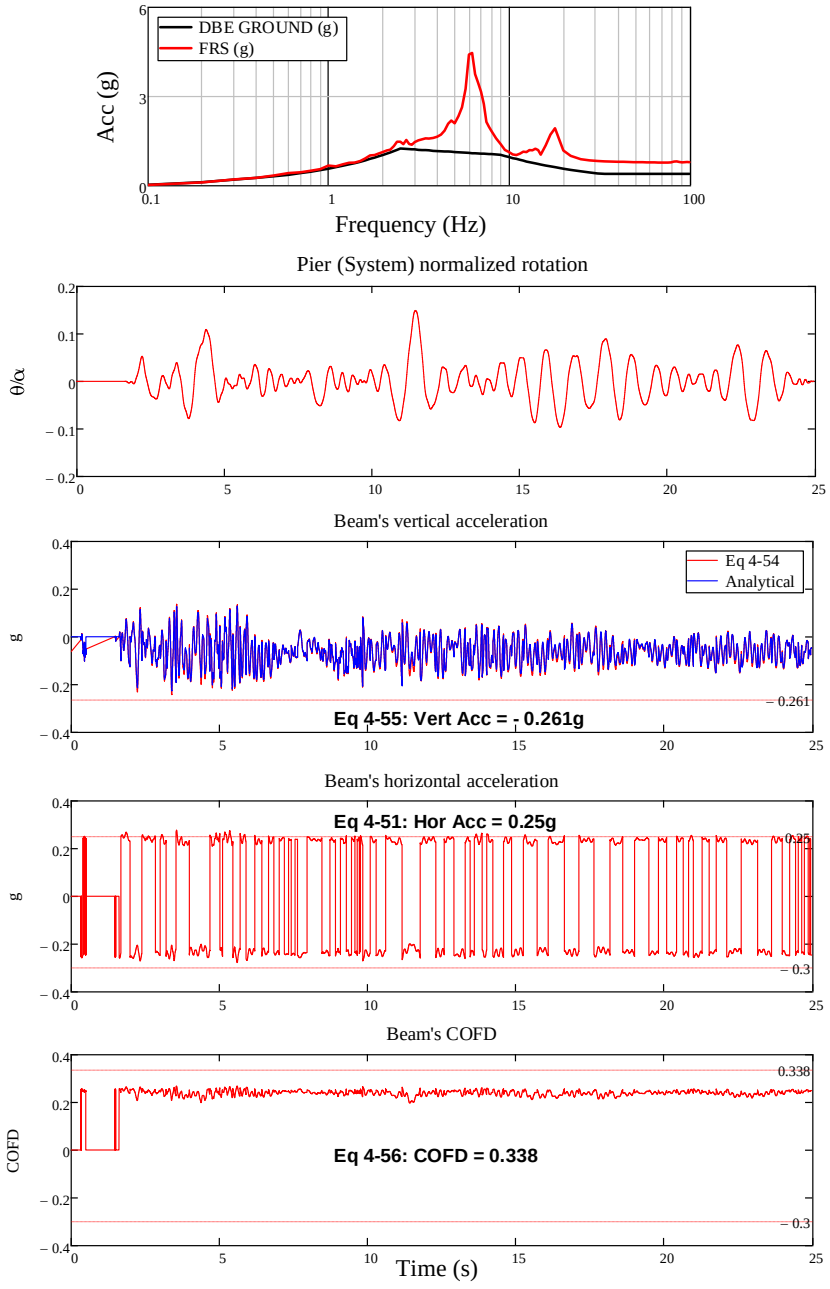

Figure C-1 Verification of Equations 4-51, 4-54, 4-55 and 4-56 for the time history corresponding to the FRS at higher elevation for a two-pier frame with parameters, $\alpha = 0.25$, $p = 2$, $\eta = 1$ and $q = 10$. The top diagram shows the DBE spectrum and the FRS.